Study on Carbonaceous Aerosols over the Central Himalayas

THESIS SUBMITTED TO THE UNIVERSITY OF DELHI
FOR THE DEGREE OF

DOCTOR OF PHILOSOPHY

By
Priyanka Srivastava

Aryabhatta Research Institute of Observational Sciences
(ARIES), Manora Peak, Nainital-263002
and
Department of Physics & Astrophysics
University of Delhi, Delhi-110007

Under the Supervision of
Prof. T. R. Seshadri and Dr. Manish K. Naja

DEPARTMENT OF PHYSICS & ASTROPHYSICS
UNIVERSITY OF DELHI
DELHI-110007, INDIA

February 2022

Department of Physics & Astrophysics
University of Delhi
Delhi - 110007, India

Date: _____

Declaration

I, Priyanka Srivastava, hereby declare that the thesis entitled "**Study on Carbonaceous Aerosols over the Central Himalayas**" is an authentic record of the research carried out by me under the joint supervision of Prof. T.R. Seshadri, Department of Physics & Astrophysics, University of Delhi and Dr. Manish K. Naja, Aryabhatta Research Institute of Observational Sciences (ARIES, Nainital). This work is original and has not been submitted for the award of any other degree in this university or any other university. The manuscript has been subjected to plagiarism checks by **Ouriginal** software. The assistance received from various sources during the course of study has been acknowledged.

Priyanka Srivastava
PhD Candidate

Prof. T. R. Seshadri
Supervisor
University of Delhi, Delhi

Dr. Manish K. Naja
Co-supervisor
ARIES, Nainital

Head, Department of Physics & Astrophysics
University of Delhi, Delhi - 110007

Department of Physics & Astrophysics
University of Delhi
Delhi - 110007, India

Date: _____

Certificate of Originality

The research work embodied in this thesis entitled "**Study on Carbonaceous Aerosols over the Central Himalayas**" has been carried out by me at the **Department of Physics & Astrophysics**, University of Delhi, New Delhi, India. The manuscript has been subjected to plagiarism checks by **Ouriginal** software. The work submitted for consideration of the award of Ph.D. is original.

Priyanka Srivastava
Name and Signature of the Candidate

Prof. T. R. Seshadri
Supervisor
University of Delhi, Delhi

Head, Department of Physics & Astrophysics
University of Delhi, Delhi - 110007

Student Approval Form

Name of the Author	*Priyanka Srivastava*
Department	*Physics & Astrophysics*
Degree	*Doctor of Philosophy*
University	*University of Delhi, New Delhi, India*
Guide	*Prof. T.R. Seshadri*
Thesis Title	*Study on Carbonaceous Aerosols over the Central Himalayas*
Year of Award	

Agreement

1. I hereby certify that if appropriate, I have obtained and attached hereto a written permission/statement from the owner(s) of each third party copyrighted matter to be included in my thesis/dissertation, allowing distribution as specified below.

2. I hereby grant to the university and its agents the non-exclusive license to archive and make accessible, under the conditions specified below, my thesis/dissertation, in whole or in part in all forms of media, now or hereafter known. I retain all other ownership rights to the copyright of the thesis/dissertation. I also retain the right to use in future works (such as articles or books) all or part of this thesis, dissertation, or project report.

   Conditions:

1. Release the entire work for access worldwide	
Release the entire work for 'My University' only for 1 Year 2 Years 3 Years and after this time release the work for access worldwide.	
3. Release the entire work for 'My University' only while at the same time releasing the following parts of the work (e.g., because other parts relate to publications) for worldwide access. a) Bibliographic details and Synopsis only b) Bibliographic details, synopsis and the following chapters	

only. c) Preview/Table of Contents/24 page only.	
4. View Only (No Downloads) (worldwide)	

Signature of the Scholar

Signature and Seal of the Guide

Place: _____

Date: _____

Dedicated to my loving parents
and brother...

Acknowledgements

The empire of a PhD degree is not built in a day and definitely not alone. Therefore, the inaugural of its royal palace – this 'Thesis', cannot be complete without duly paying acknowledgement to all those who played their parts to structure this empire in its current soul and body.

The most important role in structuring the thesis is that of the supervisor – Dr. Manish Naja and Prof. T.R. Seshadri (Sesh). I am extremely privileged to have in them, two strong pillars to constantly mentor me and shape this work. I especially look up to Manish sir who with his vast experience and knowledge introduced the subject to me. His positive scientific approach, hard work, composure, and dedication to check every microscopic detail has helped me upskill my data curation, improved my writing and presentation and helped build scientific temperament. He trusted in me since the beginning of this thesis and gave me the freedom to pursue my own scientific ideas. His encouragement and suggestions have formed the backbone of this thesis. I truly feel lucky to have Sesh, who accepted to be my doctoral supervisor. His enthusiasm to learn new subjects, time management and amiable nature is a continued source of inspiration for me. Not only did he smoothened the administrative work in university but more like a friend helped me cope in my difficult times ensuring that it didn't affect the thesis work. Thanks to both of them, the work in this dissertation could wear the feather of three awards in its making and be wrapped up today in its current composition.

I am deeply indebted to ISRO-ARFI project for funding this work.

I am also grateful to former and current Directors, ARIES - Dr. Wahab Uddin, Late Dr. Anil Kumar Pandey and Prof. Dipankar Banerjee and, ARIES and DU academic committee members who provided the necessary academic and administrative support for this work. Funding from NIES, Japan during IGAC-2018 is also greatly acknowledged. I gratefully acknowledge Dr. Suresh Babu, SPL; Prof. Shyam Lal and Prof. M. M. Sarin, PRL; Dr. Narendra Singh, Dr. D.V. Phani Kumar and Dr. U.C. Dumka, ARIES for their valuable teachings in fundamentals of the subjects. It was also my honour to have had the opportunity to discuss and work with Dr. Mukunda M. Gogoi, SPL. His wholehearted support and guidance helped me build novel perspectives for this work. Additionally, I am thankful to my seniors and collaborators in atmospheric sciences - Hema di, Srabanti di; Piyush bhaiya, Rajesh bhaiya, NCAR; Dr. T.K. Mandal, Dr. Sudhir K. Sharma and Nikki, NPL. Your support, motivation and collaboration have helped create all these publications. I further extend my gratitude to my group-mates -

Mahender, Aditya and Prajjwal for those healthy discussions and mocks, and my lab technicians - Mr. Deepak Chausali and Mr. Nitin who helped ensure the continuous operation of the instruments.

My heart overwhelms with love and gratitude for my fellow warriors - heart-and-roommate Sadhana, 'shaitan wazir' (self-acclaimed) Krishan and nerdy Arpan. While we fought our own battles at different fronts, we, especially Sadhana and Krishan found our own amusing ways to remain light. I am lucky to have found two incredible lifelong friends in both of you. Sadhana, together we saw a lot of crusts and troughs but thanks to this bond it became easier to sail through it all. Himani, my bestie, who has remained that one constant I always look out for. In our short feeling lengthy conversations, you have given me a space whereby I cannot just share myself with utmost transparency but also grow and improve. Fellow residents of ARIES hostel, my group of 'Hum-Sab', IRC group at DU, ARIES canteen and administrative staff, I thank you all for keeping this isolated place cheerful and helping me time and then. This palace will always wear the sweet fragrance of our laughter, joy, the rise after falls and our togetherness. I would also like to thank all the readers who are about to read this work. Your presence is deeply valued, and I hope this dissertation will fulfil your expectations.

Above all, my heart bows to my loving and caring parents who laid the very foundation of this empire. My ma who instilled in me the zeal to get the highest education. My father who supported my love for science and excavated every path of this empire with me. From going with me to distant places for observing the night sky, to all the places for PhD interviews. I still remember the nameplate with 'Dr. Priyanka Srivastava' written on it you gave me, the very day I said I wanted to do PhD. I thank you both for making me capable to dream and achieve this feat, for all the sacrifices you both made to keep my study going, for all the faith and patience you kept in me. Thanks for being the people I could always rely on and still couldn't thank enough. My brother, who like an empire's true guardian, responsibly took care of our parents when I was in ARIES, keeping me light and showing me always that I need not worry.

Needless to say, that you were always there in all my thick and thin and I cherish this bond to the moon and back. I thus dedicate this thesis to my small family as it is nothing but an outcome of your prayers and blessings. Lastly, I cannot end without thanking the one whom I can't know and thank enough but love the most – my Krish (Lord Krishna) and all I can say to him at the moment is that:

मेरा आपकी कृपा से, सब काम हो रहा है।

करते हो तुम कन्हैया, मेरा नाम हो रहा है॥ **Priyanka**

List of Publications

Refereed Journal

1. **Srivastava Priyanka,** Naja, M., Seshadri, T. R., Joshi, H., Dumka, U.C., Gogoi, M.M. and Babu, S.S.: Implications of Site-specific Mass Absorption Cross-section (MAC) to Black Carbon Observations at a High-altitude Site in the Central Himalaya. Asia-Pacific Journal of Atmospheric Sciences, pp.1-14, 2021.
2. **Srivastava Priyanka** and Naja, M.: Characteristics of carbonaceous aerosols derived from long-term high-resolution measurements at a high-altitude site in the central Himalayas: radiative forcing estimates and role of meteorology and biomass burning. Environmental Science and Pollution Research, 28(12), pp.14654-14670, 2021.
3. Gogoi et al., including **Priyanka Srivastava**.: Response of ambient BC concentration across the Indian region to the nation-wide lockdown: Results from the ARFINET measurements of ISRO-GBP, Current Science, Vol. 120, No. 2, 2021.
4. Sharma, S.K., Choudhary, N., **Priyanka Srivastava**, Naja, M., Vijayan, N., Kotnala, G. and Mandal, T.K.: Variation of carbonaceous species and trace elements in PM10 at a mountain site in the central Himalayan region of India. Journal of Atmospheric Chemistry, 77(3), pp.49-62, 2020.

Submitted

1. **Srivastava Priyanka**, Manish Naja, T R Seshadri.: Probing the sources of carbonaceous aerosols (OC/EC/eBC) and their dynamics over a high-altitude site in the Central Himalayas: insights from the ground based online observations, Under review in Science of the Total Environment.
2. Joshi Hema, Manish Naja, **Priyanka Srivastava**, Tarun Gupta, Mukunda M. Gogoi, S. Suresh Babu.: Long-Term Trends in Aerosol Black Carbon and Aerosol Optical Depth from a High-Altitude Site in the Central Himalayas, Under review in Frontiers in Earth Science.

To be Submitted

1. **Srivastava Priyanka et al., 2022 (To be submitted).** Quantifying fossil fuel and biomass burning fractions of ambient CO using multi-year ground-based measurements over a high-altitude Central Himalayan site.
2. **Srivastava Priyanka et al., 2022 (To be submitted).** Long term trend in carbonaceous aerosols, sources and radiative forcing at the Central Himalayas.

Conference Proceedings

1. **Srivastava Priyanka**, Manish Naja, Rajesh Kumar, Hema Joshi, U C Dumka, Mukunda M Gogoi, S. Suresh Babu.: Studies on carbonaceous aerosols from a high-altitude site in the Central Himalayas. Conference of Indian Aerosol Science and Technology Association 2018, IIT Delhi, New Delhi, 38-41.

2. **Srivastava Priyanka**, Manish Naja, Hema Joshi, Mukunda M Gogoi, S Suresh Babu.: Characterization of aerosols and trace gases at the Central Himalayas using

long-term ground and satellite observations, European Geophysical Union (EGU), 2021, Proceeding - doi: 10.5194/egusphere-egu21-7912.

Awards

1. Best Poster Award

"Tracing back carbon Aerosols: Source characterization using long term observations of EC, eBC, OC and CO from ARIES, Nainital, a high-altitude site in the Central Himalayas", International workshop on Climate Change and Extreme Events in the Himalayan Region, IIT Mandi,18-20 Apr 2019.

2. Best Video Clip Award

"Introduction to influence of carbon aerosols and their source characterization" International Global Atmospheric Chemistry Monsoon Asia Group Meeting, workshop, and training Course, Nainital, 28-30 Nov 2019.

3. Best Poster Award

"Decadal trend of black carbon aerosols over the Central Himalayas: 17 years of ground observations", 16th International Global Atmospheric Chemistry Science Conference, Online, 12-21 Sept 2021.

Oral/poster presentations in national/international conferences/symposiums/workshops:

1. International Workshop and Science Policy Dialogue, ICIMOD headquarters in Kathmandu, Nepal, 27-30 Nov, 2017.
2. 14th iCACGP - 15th IGAC International Science Conference, Takamatsu, Japan, 25-30 Sept, 2018.
3. Conference on Indian Aerosols Science and Technology Association (IASTA), IIT Delhi, 26-28 Nov, 2018.
4. National Space Science Symposium-(NSSS)-2019, Savitribai Phule Pune University, Pune, 29-31 Jan, 2019.
5. International workshop on Climate Change and Extreme Events in the Himalayan Region, IIT Mandi,18-20 Apr 2019.
6. National Centre for Polar and Ocean Research, Goa, 20-22 Aug, 2019.
7. International Global Atmospheric Chemistry Monsoon Asia Group Meeting, workshop, and training Course, Nainital, 28-30 Nov 2019.
8. International Conference on Aerosol Air Quality, Climate Change and Impact on Water Resources and Livelihoods in the Greater Himalayas, ARIES, Nainital, 14-16 Sept, 2020.
9. TROPMET-2020: National Virtual Symposium on Weather and Climate Services over Mountainous Regions, Shillong, 14-17 Dec, 2020.
10. European Geosciences Union (EGU) General Assembly, Virtual, Proceeding - doi: 10.5194/egusphere-egu21-7912, 2021.
11. 16th International Global Atmospheric Chemistry International Science Conference, 12-21 Sept, 2022.

Abstract

In this era of rapid urbanization and industrialization, large dependence on carbon-based fuel has led to a substantial increase in the concentrations of carbonaceous aerosols (organic carbon-OC and black carbon-BC), which are emitted from their incomplete combustion. These aerosols are important because of their direct adverse impacts on health and radiation budget in addition to their indirect effect in altering the properties of clouds. However, assessing their overall impact is challenging due to the large spatial and temporal variations in their emissions, types of mixing states and the dynamic atmospheric processes. Despite the scientific attention on this, continuous and high-resolution observations of carbonaceous aerosols are still very limited in South Asia and almost nonexistent in the serene yet fragile Himalayan region, which has a complex topography with largest ice mass outside the poles and lies near polluted regions like the Indo-Gangetic Plain.

Addressing the aforesaid issues, this thesis work presents results from the comprehensive analysis of the rigorous long-term online observations of OC, elemental carbon (EC), BC, CO and absorption cross-section along with results from satellite observations and model simulations over a high-altitude location in the Central Himalayas (ARIES, Nainital, 29.4^{o}N, 79.5^{o}E, 1958 a.m.s.l.). It starts with a thorough introduction of aerosols, particularly focusing on carbonaceous aerosols, the significance and challenges in their study over this region and the importance of this work to overcome these challenges. Later, it explains the *in-situ* instruments, satellite products and models used in the work for their characterization. Then it chapter-wise details the obtained results.

In Chapter 3, the first year-round diurnal variations of OC and EC over a Himalayan site are presented. Analysis of continuous high-resolution measurements from 2014 to 2017 reveals a unimodal diurnal variation in both OC and EC, in contrast to the bimodal pattern observed at any continental polluted site. Using concentration weighted trajectory (CWT) and coinciding rise in OC/EC ratio from 4.6 to 7.9 during fire events it is shown that the biomass burning in northern India is one of the major sources for the springtime maximum even at this high-altitude. Correlation between OC-EC and the boundary-layer height suggests the influence of local sources during autumn and winter. Towards the end, radiative forcing estimates at diurnal scale are derived and it is shown that the atmospheric radiative forcing due to EC during the afternoon is about 70% higher than the forenoon one.

Several studies have shown large variability in Mass Absorption Cross-section (MAC) values over distinct geographic locations and seasons. Therefore, in Chapter 4, we examine the accuracy and consistency of MAC in Aethalometer (AE-42) by deriving the foremost multispectral site-specific MAC values over the site. The results reveal that the annual mean value of MAC (5.03 ± 0.03 m^2 g^{-1} at 880 nm) is significantly lower than the constant value used in the Aethalometer (16.6 m^2 g^{-1} at 880 nm). The estimated MAC values do not show a clear diurnal variation but significant seasonal variation (e.g., 3.7 to 6.6 m^2 g^{-1} at 880 nm) owing to variation in air mass, meteorology and contribution of absorption by species other than EC. It is shown that not using the site-specific MAC, leads to an underestimation of BC by a factor of upto 3.58 and lower radiative forcing (upto ~24%).

Chapter 5 elucidates the diurnal scale phenomena with respect to emission sources, quantification of transported pollutants, the influence of biomass burning and radiative forcing. The deconvolution of OC to primary and secondary OC (POC and SOC) is performed using four methods, all of which consistently show that POC (>64%) with a prominent unimodal diurnal variation dominates over SOC (< 44%) at an annual time scale. The contribution of fossil fuel combustion (eBC_{ff}) in BC is found to be 3.5 times greater than that of biomass burning (eBC_{bb}). Radiative forcing estimates are made at diurnal scale, and it is shown that noon time eBC_{ff} contributes to more atmospheric forcing than eBC_{bb} in the same duration.

In view of the discrepancies associated with CO emissions (co-emitted with BC) and its increasing levels over the South Asian region, Chapter 6 utilizes BC measurements to provide crucial *in-situ* information to robustly constrain the relative source fractions of CO. As a novel approach, multiple linear regression based (MLR) framework is used to serve this purpose. MLR does quite well in replicating the diurnal and monthly variation of CO with a r^2 of $\geq$ 0.8 over the training period of 2014-2017, performing much better than the CO from MOPITT satellite and MERRA-2 reanalysis data. Predicted CO values for the year 2018 lie in the range of -16.1% to 16.8% of the observed average CO values in any given month. The source segregation results show that fossil fuel combustion (CO_{ff}) fractions of CO is the major contributor (27%) in CO after background CO (58%). Biomass burning (CO_{bb}) CO shows a large increase and reaches up to 28% during April as a result of increased agricultural and forest fires in the Northern Indian region. Against the MLR derived CO fractions, WRF-Chem tracer runs for source segregation are found

to underestimate the biomass burning CO emissions (-38% to -98%) while they largely overestimate the fossil fuel CO mixing ratios especially during monsoon.

Acknowledging the significance of long-term trends in aerosols for understanding the evolution of air quality and its impact over this region, Chapter 7 presents the foremost MAC corrected long-term trend in BC with 17 years of ground-based observations at the site. This analysis reveals a statistically significant, decreasing trend with a slope of ~18 ng m^{-3} $year^{-1}$ over the period of 2004–2020 which is in contrast with the trends obtained from MERRA-2 BC, AOD and BC emissions over the region which show an increasing tendency. It is also evidenced that the fossil fuel BC fraction declines faster (-20.29 ng m^{-3} $year^{-1}$) than the biomass burning (-3.77 ng m^{-3} $year^{-1}$) fraction. AOD and BC emissions over the region are found to show a positive trend. Splitting the trend into sub-periods unveils a reversal in BC trend from positive to negative after 2017 which leads to an overall negative trend.

Finally, in Chapter 8, a summary of the key results from each of the chapters is presented and future perspectives are also discussed.

The thesis thus renders a unique long-term characterization of carbonaceous aerosols in an otherwise sparsely studied complex terrain of the Central Himalayas. It shows that incorporating high-resolution measurements is particularly essential while studying aerosol-radiation interaction over this region. The work will be specifically critical to validate satellite and model results, to constraint models, to assess the regional radiation budget, for epidemiological studies and to ascertain the impact of BC in the Himalayas.

List of Figures

Figure 1.1 Schematic showing aerosol processes-source, sinks, transformation and size range (Compiled from: Hinds,1999). 3

Figure 1.2 (a) MODIS Aerosol Optical Depth at 0.55 μm averaged over 2001–2010 period (b) Pie charts showing the contribution of sulphate, BC, OC, Bio (OC and BC from biomass burning), sea salt, nitrate and Min(mineral dust) aerosol in building AOD over different regions of the globe (Extracted from:https://www.nature.com/scitable/knowledge/library/aerosols-and-their-relation-to-global-climate-102215345/; Data from Myhre et al., 2013). 5

Figure 1.3 Schematic shows the new terminologies used for the 'aerosol–radiation and cloud interactions' in AR5 and AR4.The solar and terrestrial radiation along with the couplings between the surface and the cloud layer for rapid adjustments is denoted by blue, grey and brown arrows. (Extracted from IPCC, 2013). 8

Figure 1.4 Forcings from 1880-2011 taken from Hansen et al., 2011 (Updated version extracted from- https://data.giss.nasa.gov/modelforce/)..... 13

Figure 1.5 Pie chart showing global distribution of BC and OC emissions by major source category and bar chart showing BC emissions (Gg) by World Region, 2000 (Compiled from: US EPA, 2012; Data from Lamarque et al., 2010). 16

Figure 1.6 The retreat of the Gangotri glacier retreat which is the source of the river Ganges. (Extracted from: Bachmann, 2009). 19

Figure 1.7 Schematic showing the breakup problems undertaken as part of this thesis. 21

Figure 2.1 Location of the observation site (Nainital) in the elevation map. 25

Figure 2.2 Monthly variation of (a) solar radiation, temperature and mixing-layer depth (b) wind speed and (c) relative humidity and rainfall observed at ARIES, Nainital during 2014-2017. Error bars and shaded portions in the grey show one standard deviation from the average value (Srivastava et al., 2021). 26

Figure 2.3 A flow diagram showing the working of an aethalometer, extracted from the Aethalometer manual-(https://www.arm.gov/publications/tech_reports/handbooks/aeth_-handbook.pdf). A picture of the aethalometer AE42 is shown on the right. 27

Figure 2.4 A schematic showing the working of EC-OC analyzer. A picture of the OC-EC analyser is shown on the right (Picture from: https://www.sunlab.com). 29

Figure 2.5 A schematic showing the working of Picarro trace gas analyzer. A picture of the Picarro trace gas analyser is also shown (Extracted from: https://www.picarro-.com/products/g2401_gas_concentration_analyzer). 30

Figure 2.6 Schematic showing the working of a python pipeline developed to analyse the raw data from various instruments. 31

Figure 2.7 Block diagram and image of CALIPSO payload that consists of CALIOP lidar and two passive sensors (Extracted from: https://earth.esa.int/web/eoportal/satellite-missions/c-missions/calipso). 32

Figure 2.8 MOPITT and other instruments on board Terra are shown (Extracted from: https://mopitt.physics.utoronto.ca/). 33
Figure 2.9 External view of MODIS along with its sub-systems. (Extracted from: https://commons.wikimedia.org/wiki/File:MODIS_sensor.png).....34
Figure 2.10 5-day backward, 27-member ensemble, trajectories reaching the observation site (square box) on 22 April. The black squares within trajectories are marked at interval of 24 hours. The colour bar on the left shows the height of the trajectory. 36
Figure 2.11 A flow chart showing the steps in retrieving the radiative forcing due to carbonaceous aerosols.....38
Figure 3.1 Boxplot showing diurnal variations in hourly averaged OC concentration during 2014-2017. In boxplots, the lower and upper edges of the boxes represent the 25th and 75th percentiles, respectively. The whiskers below and above are the 10th and 90th percentiles and the outliers in the boxplot show the 5th and 95th percentiles. The green triangle inside the box represents the mean and the solid lines inside the box represent the median. The monthly mean, standard deviation and number of observation counts are also mentioned for each month. 45
Figure 3.2 Same as figure 3.1 but for EC. 46
Figure 3.3 Average diurnal variations in OC and EC concentrations during winter (DJF), spring (MAM), autumn (SON) and summer-monsoon (JJA) at Nainital in 2014-2017 period. The vertical bars denote one standard deviation from the mean. 47
Figure 3.4 Percentage frequency distribution of OC and EC during winter, spring, summer-monsoon and autumn. The x-axis label of 0.0 represents the OC range 0.0-2.5 μg m^{-3}, 2.5 represents the OC range of 2.5-5.0 μg m^{-3} and so on. In the case of EC, the label of 0 represents a range of 0-0.5 μg m^{-3}, 0.5 represents a range of 0.5-1.0 μg m^{-3} and so on.....48
Figure 3.5 Boxplot showing annual variations in monthly averaged OC and EC concentration during 2014-2017. In boxplots, the lower and upper edges of the boxes represent the 25th and 75th percentiles, respectively. The whiskers below and above are the 10th and 90th percentiles and the blue-circles outliers depict the 5th and 95th percentiles. The black square inside the box represents the mean and the pink solid lines inside the box represent the median. The daily mean data points are shown as grey points. Noon (1300 - 1600 hr IST) and night (0100 - 0400 hr IST) time monthly averages are also shown. The error bars represent one standard deviation from the mean. 50
Figure 3.6 Variation of (a) OC and (b) EC with the boundary-layer height for 1130-1630 hours IST for winter, spring, summer-monsoon, and autumn. Smaller symbols show daily means and binned data are shown in the same colour scheme with a larger size. Spread in x and y axes in the binned data are one standard deviation from the mean. 54
Figure 3.7 Diurnal variation of OC, EC, RH, wind speed, temperature and solar radiation averaged for all 2014-2017. OC, temperature, solar radiation, and RH have been scaled down by factors of 3, 5, 150, 15, respectively, to fit all plots in the same graph. 55

Figure 3.8 Correlation of OC and EC concentration with the residence time of air masses in daytime and night time during 2014-2017. Backward air trajectories at 1530 and 0130 hours are correlated with the daytime (1400-1700 hours) and night time (0000-0300 hours) average OC-EC concentrations for 2014-2017. 57
Figure 3.9 Seasonal variations in MODIS fire events over northern India (24 ^{o} - 35 ^{o}N and 70^{o}- 89^{o}E) during 2014-2017. 58
Figure 3.10 (a) OC, EC, OC/EC and total fire events over northern India from 19 April to 5 May 2016. (b) and (c) show locations of fires observed from MODIS in red and 5-day backward trajectories of 5-particles in green with a square marker at every 24 hours on 22 22 April and 01 May, respectively. 58
Figure 3.11 Concentration Weighted Trajectories for OC, EC and OC/EC during low (18 - 24 Apr 2016) and high (28 Apr - 01 May 2016) fire events. 59
Figure 3.12 Correlation between the OC and EC concentrations in winter, spring, summer-monsoon and autumn during 2014-2017. Smaller points show daily means and binned data are shown in the same colour scheme with a larger size. Spread in x and y axes in the binned data is one standard deviation from the mean. 61
Figure 3.13 Clear-sky shortwave (0.25–4.0 µm) direct ARF (Wm^{-2}) at the surface (SUR), in the atmosphere (ATM) and at the top of the atmosphere (TOA) for averaged EC during forenoon (0600 - 0900 hours), and afternoon (1400 - 1700 hours). 62
Figure 4.1 Correlation between the absorption coefficient (b_{abs}) and EC concentrations at each of the wavelengths of Aethalometer observed at Nainital. Smaller points in blue show hourly mean points. The line in red shows the linear regression fit to these data points. 68
Figure 4.2 (a) The points in blue show the observed variation of MAC at seven wavelengths on a log-log scale. The red is a linear best fit. (b) Seasonal variations in MAC with wavelengths ranging from 370 – 950 nm. Error bars for each point in the plot represent errors in the slope of the regression fit made for the absorption coefficient and EC at a particular wavelength. 69
Figure 4.3 The monthly average variations (2014-2017) in MAC at seven wavelengths ranging from 370 to 950nm. Error bars for each point in the plot represent errors in the slope of the regression fit made for the absorption coefficient and EC for that month at a particular wavelength. 71
Figure 4.4 The average diurnal variations in MAC during four seasons in 2014-2017 for all the seven wavelengths. Error bar and shaded area represent the corresponding error in the slope of the line fit for each hour data. 72
Figure 4.5 Averaged diurnal variations in (a) absorption coefficient (Mm-1) at 880 nm and (b) EC (µg m^{-3}) in four seasons during 2014-2017. Average monthly variations in (c) absorption coefficient at 880 nm and (d) EC concentrations during 2014-2017. Boxplots for spring (MAM) have been shifted and line plots for winter (DJF) and autumn (SON) are plotted instead of boxplots, for clarity. In boxplots, the triangle inside the box represents the mean and the solid lines represent the median. The lower and upper edges of the boxes represent the 25th and 75th percentiles,

respectively. The lower and upper range in whiskers is 10th and 90th percentiles, respectively. Hourly data points are shown in grey in (c) and (d). 74
Figure 4.6 The correlation between MAC (for 880 nm) with Temperature and Solar Radiation for 2014-2017. The determination coefficient, slope, slope error and significance level (p) are also mentioned. Hourly data points are in small grey markers and binned data points are in black markers with error bars in the one sigma level. Red line shows the straight fit line to the binned data points..... 76
Figure 4.7 Variations in monthly average equivalent black carbon (eBC) concentrations during the 2014-2017 period using the presently derived site and month specific MAC (corrected eBC) and standard MAC of 16.6m^2 g^{-1} (uncorrected eBC). Error bars in the plot represent one sigma standard variation. Monthly variations in the percentage difference between both are also shown. 80
Figure 4.8 The seasonal correlation between eBC and EC for 2014-2017. Left-hand side correlation is with corrected eBC (using site and month specific MAC values) and right-hand side correlation is with uncorrected eBC (MAC value of 16.6 m^2 g^{-1}). 81
Figure 4.9 Diurnally averaged clear-sky shortwave (0.25–4.0 μm) direct aerosol radiative forcing (Wm^{-2}) at the surface (SUR), in the atmosphere (ATM) and at the top of the atmosphere (TOA) for corrected eBC and uncorrected eBC. 83
Figure 5.1 Seasonal variation in the percentage frequency distribution of angstrom exponent for (a) lower (370-520 nm), (b) higher (660-950 nm) and (c) total (370-950 nm) wavelengths. 89
Figure 5.2 Boxplot showing the monthly variation of angstrom exponent. Daily averages are shown in grey points. Triangles in the box represent the monthly mean and the red line shows the median. Box edges represent the 10 and 90th percentile, whiskers show the 5th and 95th percentiles. 90
Figure 5.3 The variation in SOC and POC obtained using MRS, CAB, TEN and REG methods averaged for the four seasons - winter, spring, summer-monsoon and autumn during 2014-2017. 94
Figure 5.4 The diurnal variation in SOC and POC obtained using MRS, CAB, TEN, and REG methods averaged for the four seasons winter, spring, summer-monsoon and autumn i.e., DJF, MAM, JJA and SON during 2014-2017. Error bars represent one standard deviation from the mean. 96
Figure 5.5 The diurnal variation in OC/EC ratio averaged for seasons winter, spring, summer-monsoon and autumn i.e., DJF, MAM, JJA and SON during 2014-2017. Error bars represent one standard deviation from the mean. 97
Figure 5.6 Diurnal variations of eBC and its fossil fuel (eBC_{ff}) and biomass burning (eBC_{bb}) components. Data counts in each month are also given. 101
Figure 5.7 Diurnal variation of the percentage contribution of fossil fuel (eBC_{ff}) and biomass burning (eBC_{bb}) components. 102
Figure 5.8 Monthly variations in the diurnal amplitudes of eBC_{ff} and eBC_{bb} observed in the central Himalayas during 2014-2017. The percentage difference between them is also shown. 103

Figure 5.9 Monthly averages in eBC, eBC_{ff}, and eBC_{bb}. Fire counts in the region 24-34^{o}N, 70-90^{o}E from MODIS are also shown as a bar plot in the secondary y-axes. 103
Figure 5.10 The concentrations of eBC along with fossil fuel (eBC_{ff}) and biomass (eBC_{bb}) components during four seasons over the central Himalayas during 2014-2017. Percentage contributions of eBC_{ff} and eBC_{bb} are also shown. 104
Figure 5.11 Diurnally averaged, forenoon (fn) (0600 - 0900 hours) and afternoon (an) (1400 - 1700 hours), clear-sky shortwave (0.25–4.0 µm) direct aerosol radiative forcing (Wm^{-2}) at the surface (SUR), in the atmosphere (ATM) and at the top of the atmosphere (TOA)) for eBC_{ff} and $eBC_{bb.}$ 106
Figure 5.12 Correlation of POC and SOC concentrations (obtained from four methods) with eBC, eBC_{ff}, eBC_{bb} and the boundary layer height during 2014-2017. 108
Figure 5.13 Concentration Weighted Trajectories of eBC for seasons winter, spring, summer-monsoon and autumn i.e., DJF, MAM, JJA and SON during 2014-2017. 110
Figure 5.14 (a) Fire counts, OC, EC, OC/EC, eBC, eBC_{ff}, eBC_{bb}, POC SOC from CAB, TEN, REG and MRS during 19 April - 5 May 2016. Locations of fires (red dots) observed from MODIS and 5-day backward, 27-member ensemble, trajectories reaching the observation site (orange triangle) on (b) 22 April and (c) 01 May 2016. The black squares within trajectories are marked at the interval of 24 hours. The colour bar on the left shows the height of the trajectory. 111
Figure 5.15 Aerosol subtype with altitude observed by CALIPSO near the study region encircled in red during (a) low fire (22 April) and (b) high fire (1 May) days. ... 112
Figure 6.1 Monthly averaged surface CO mixing ratios from (top) MOPITT and (bottom) MERRA-2 for a 0.5^{o}x0.5^{o} region around the site (Nainital) and those from observations are shown in red and black bars respectively. The % difference between the two is also shown on the secondary axis. 118
Figure 6.2 Monthly averaged surface (solid lines) and two km (dashed lines) CO mixing ratios from WRF-Chem for NTL-Nainital, NE1-0.1^{o} North East of NTL, NE2-0.2^{o} North East of NTL and those from in-situ observations (black line with square markers) at the site are shown. 118
Figure 6.3 Correlation between (a) CO and eBC (b) eBC_{ff} and eBC_{bb} (c)CO and eBC_{ff} (d) CO and eBC_{bb} mixing ratios in winter, spring, summer-monsoon and autumn during 2014-2017. Smaller points show daily means and binned data are shown in the same colour scheme with a larger size. Spread in x and y axes in the binned data is one standard deviation from the mean. Determination coefficient for each season is also mentioned. 121
Figure 6.4 Box plot showing the intra annual monthly mean variation in observed CO and estimated CO and their averaged for the year 2014-2017. In boxplots, the lower and upper edges of the boxes represent the 25th and 75th percentiles, respectively. The whiskers below and above are the 10th and 90th percentiles and the unfilled triangles and circles depict the 5th and 95th percentiles. The solid triangles and circles inside the boxes represent the mean and the solid lines inside the boxes represent the median. 123

Figure 6.5 Correlation between estimated and observed CO mixing ratios in winter, spring, summer-monsoon and autumn during 2014-2017. Smaller points show daily means and binned data are shown in the same colour scheme with a larger size. Spread in x and y axes in the binned data is one standard deviation from the mean. The determination coefficient for each season is also mentioned. 124
Figure 6.6 Correlation between predicted and observed CO mixing ratios in winter, spring, summer-monsoon and autumn during 2018. Smaller points show daily means and binned data are shown in the same colour scheme with a larger size. Spread in x and y axes in the binned data is one standard deviation from the mean. The determination coefficient for each season is also mentioned.....125
Figure 6.7 The monthly mean variation in observed CO and predicted CO for the year 2018 are shown. In boxplots, the lower and upper edges of the boxes represent the 25th and 75th percentiles, respectively. The whiskers below and above are the 10th and 90th percentiles and the unfilled triangles and circles depict the 5th and 95th percentiles. The solid triangles and circles inside the boxes represent the mean and the solid lines inside the boxes represent the median. The percentage difference between observed and predicted CO for the year 2018 is also shown on the secondary y-axis in grey bars.....126
Figure 6.8 Diurnal variations in hourly averaged $CO_{observed}$, $CO_{estimated}$, eBC_{ff}, and eBC_{bb} concentrations averaged for 2014-2017. $CO_{observed}$, $CO_{estimated}$ have been scaled down by a factor of 100 to fit all plots in the same graph. The vertical bars denote one standard deviation from the mean.....127
Figure 6.9 Boxplot showing diurnal variations in hourly averaged CO_{ff} mixing ratio during 2014-2017. In boxplots, the lower and upper edges of the boxes represent the 25th and 75th percentiles, respectively. The whiskers below and above are the 10th and 90th percentiles and the blue circled outliers in the boxplot show the 5th and 95th percentiles. The red triangle inside the box represents the mean and the solid lines inside the box represent the median. The diurnal amplitude and number of observations are also mentioned for each month.....128
Figure 6.10 Boxplot showing diurnal variations in hourly averaged CO_{bb} mixing ratio during 2014-2017. In boxplots, the lower and upper edges of the boxes represent the 25th and 75th percentiles, respectively. The whiskers below and above are the 10th and 90th percentiles and the blue circled outliers in the boxplot show the 5th and 95th percentiles. The red triangle inside the box represents the mean and the solid lines inside the box represent the median. The diurnal amplitude and number of observations are also mentioned for each month.....129
Figure 6.11 Boxplot showing intra annual monthly and daily mean variation in (a) fossil fuel and (b) biomass burning CO fractions for 2014-2017 are shown in black. In boxplots, the lower and upper edges of the boxes represent the 25th and 75th percentiles, respectively. The whiskers below and above are the 10th and 90th percentiles and the blue-circles outliers depict the 5th and 95th percentiles. The black square inside the box represents the mean and the pink solid lines inside the box represent the median. The daily mean data points are shown as grey points. Noon

(1300 - 1600 hours) and night (0100 - 0400 hours) time monthly averages are also shown. The error bars represent one standard deviation from the mean. 131
Figure 6.12 Monthly variations in percentage difference between WRF-Chem and MLR method for fossil fuel, biomass and background component of CO. Percentage difference is calculated with respect to the MLR method. Fossil fuel fraction of CO ranges up to +962%. To clearly illustrate the monthly variation in other fractions of CO, the y-axis scale is not extended till the full range of +962%. 134
Figure 7.1 Long-term variations in the observed BC, MERRA-2 and the bias in MERRA-2 during 2004-2020 over the observations site. 142
Figure 7.2 Monthly average variations in observed BC and BC from MERRA-2 during 2004-2020. Daily, noon and night time average values are also shown. The percentage difference between observed BC and BC from MERRA-2 is shown in the bottom panel. 143
Figure 7.3 Long-term trends in observed BC and MERRA-2 during 2004-2020 over the observational site. Scattered points in blue and red show the daily average values for observed BC and MERRA-2, respectively. Monthly moving averages in BC are shown in curved lines. Linear regression for the 365 days moving average is also shown for the entire period. Mentioned slope values are from this linear regression of 365 days moving average. 144
Figure 7.4 Long-term variations in fossil fuel and biomass burning components of BC during 2004-2020. Scattered points in black and green show the daily average values for fossil fuel and biomass burning BC, respectively. Monthly moving averages in BC are shown in curved lines. Linear regression for the 365 moving average is also shown and the slope for the same is also mentioned. 146
Figure 7.5 Long-term variations in MODIS AQUA and MODIS TERRA for the period 2006-2020. Scattered points are the daily AOD values and curved lines are monthly moving averages. Linear regression is estimated using 365 days moving average and shown by the linear fit line. 148
Figure 7.6 BC emission estimates from EDGARv5.0 during 1990-2015 for China, India, Pakistan, Nepal, Afghanistan and Bangladesh. 150

List of Tables

Table 1.1 Comparison of global mean radiative forcing in SAR, TAR, AR4 and AR5 for seven components - sulphate, nitrate, SOA, mineral dust, BC and OA from biomass burning combined and BC and OC separately in fossil fuel and biofuel due to differences in their ratios from these emissions (Compiled from: IPCC, 2013).....12

Table 1.2 Global Warming Potential for BC and OC over 20 and 100 years (Compiled from: Bachmann, 2009). 14

Table 2.1 List of parameterization schemes used in the WRF-Chem setup. 40

Table 3.1 Statistical summary of monthly and seasonal variations in EC, OC and OC/EC ratio for the period of 2014-2017 Nainital. 44

Table 3.2 Average noontime (1300 - 1600 hours) and night time (0100 - 0400 hours) concentration of OC and EC during winter, spring, monsoon (June, July, August and September) and post-monsoon (October and November) periods. The ratio of noontime to night time is also shown. 51

Table 3.3 Correlation of OC and EC with meteorological parameters observed at Nainital during 2014-2017. 56

Table 4.1 Monthly and annual MAC values at 880 nm for the 2014-2017 period over the central Himalayan region. The determination coefficient in the absorption coefficient and EC for each month and the whole year along with the counts used in each of the regressions is also mentioned. 71

Table 4.2 Statistics for correlation between eBC (corrected and uncorrected) and EC in four seasons during the 2014-2017 period. 81

Table 5.1 Summary of the methods used for SOC segregation. 92

Table 5.2 Monthly values of [OC/EC]pri as obtained from REG, TEN, CAB and MRS methods. 93

Table 5.3 Monthly and annual averaged values for observed POC and SOC using four methods. 95

Table 5.4 The table provides the monthly average values of observed eBC, eBC_{ff}, eBC_{bb} and the percentage contribution of eBC_{ff} and eBC_{bb}. 100

Table 6.1 Results of multiple linear regression ($[CO]_{bgd}$,, r_{ff},, r_{bb}, r_{bgd}, their respective errors and determination coefficient r^2) that are applied for the estimation of CO_{ff} and CO_{bb} for 2014-2017.....122

Table 6.2 Summary of interannual statistics for total CO, CO_{ff}, CO_{bb} and CO_{bgd} for 2014-17.....133

Table 6.3 Monthly percentage difference between WRF and MLR for CO_{bgd}, CO_{ff} and CO_{bb}. 136

Table 7.1 Mann-Kendall trend test results for BC for different periods. The trend is tested for a 95% significance level i.e., p value of 0.05. The slope is in units of ng m^{-3} year $^{-1}$. 145

Table 7.2 Mann-Kendall trend test results for fossil fuel and biomass burning BC for different periods. The slope is in units of ng m^{-3} $year^{-1}$. The trend is tested for a 95% significance level i.e., p value of 0.05.....147

Notations and Abbreviations

The most commonly used notations and abbreviations in the thesis are given below. If a symbol has been used in a different connection than listed here, it has been explained at the appropriate place.

Notations

α	Ångström Exponent
λ	Wavelength
$[OC/EC]_{pri}$	Primary OC to EC ratio
b_{abs}	Absorption coefficient
ΔATN	Change in attenuation
ΔT	Time duration
A	Spot area
Q	Flow rate
C_{ij}	Average weighted concentration in the ij^{th} cell.
C_l	Concentration observed on the arrival of trajectory l
τ_{ijl}	Time spent in the ij^{th} cell by trajectory l
r^2	Determination Coefficient

Abbreviations

AN	Afternoon
AOD	Aerosol Optical Depth
AR	Assessment report
ARIES	Aryabhatta Research Institute of Observational Sciences
ARFI	Aerosol Radiative Forcing over India
ATM	Atmosphere
AVD	Atmospheric volume description
BB	Biomass burning
BC	Black Carbon
BGD	Background
CAD	Cloud-Aerosol Discrimination
CA	Carbonaceous aerosols

CALIOP	Cloud-Aerosol Lidar with Orthogonal Polarisation
CALIPSO	Cloud-Aerosol Lidar and Infrared Pathfinder Satellite Observations
CRDS	Cavity ring down spectroscopy
CO	Carbon Monoxide
COALESCE	Carbonaceous Aerosol Emissions, Source Apportionment and Climate Impacts
CO_ANTH	CO anthropogenic emissions
CO_BB	CO biomass burning emissions
CO_CHEM	CO photochemical production from non-methane hydrocarbon emissions
CO_BDRY	Inflow of CO from lateral boundaries
CWT	Concentration Weighted Trajectory
DIU	Diurnal
EBC	Equivalent Black Carbon
EC	Elemental Carbon
EDGAR	Emissions Database for Global Atmospheric Research
FF	Fossil fuel combustion
FN	Forenoon
GDAS	Global Data Assimilation System
GEOS	Goddard Earth Observing System Model
GES DISC	Goddard Earth Sciences Data Information Services Center
GODARD	Goddard Chemistry Aerosol Radiation and Transport
GWP	Global Warming Potential
HULIS	Humic Like Substances
HYSPLIT	Hybrid Single-Particle Lagrangian Integrated Trajectory Model
IGP	Indo-Gangetic Plain
INCAA	Indian network of Climate Change Assessment
IPCC	Intergovernmental Panel for Climate Change
IR	Infrared
ISRO	Indian Space Research Organization
MAC	Mass Absorption Cross-section
MERRA	Modern-Era Retrospective analysis for Research and Applications
MLR	Multiple Linear Regression model
MODIS	Moderate Resolution Imaging Spectroradiometer
MOPITT	Measurement of Pollution in the Troposphere
MOZART	Model for Ozone and Related Chemical Tracers

NCAP	National Carbonaceous Aerosols Programme
NIOSH	National Institute for Occupational Safety and Health
NTL	Nainital
NE1	Region 0.1^{o} North East of NTL,
NE2	Region 0.2^{o} North East of NTL
OA	Organic Aerosol
OBS	Observed
OM	Organic Matter
OPAC	Optical Properties of Aerosols and Clouds
PM	Particulate Matter
POC	Primary Organic Carbon
POA	Primary Organic Aerosol
RF	Radiative Forcing
ARF	Atmospheric Radiative Forcing
RH	Relative Humidity
SAR	Second Assessment Report
SBDART	Santa Barbara Discrete Ordinate Radiative Transfer model
SOC	Secondary Organic Carbon
SOA	Secondary Organic Aerosol
SSA	Single Scattering Albedo
SURF	Surface
TAR	Third Assessment Report
TSPM	Total Suspended Particulate Matter
TOA	Top of the Atmosphere
TOT	Thermal Optical Transmittance
VOC	Volatile Organic Compounds
WRF-Chem	Weather Research and Forecasting model coupled with Chemistry

Table of Contents

Declaration ..... *iii*

Certificate of Originality ..... *v*

Student Approval Form ..... *vii*

Acknowledgements ..... *xi*

List of Publications ..... *xiii*

Abstract ..... *xv*

List of Figures ..... *xix*

List of Tables ..... *xxvi*

Notations and Abbreviations ..... *xxvii*

1. Introduction *1*

1.1 Aerosols **1**

1.1.1. Shape, Size, and Mixing state 2

1.1.2. Aerosols Size Distribution 3

1.1.3. Aerosol Transformation 4

1.1.4. Aerosol Sources and Sinks 4

1.1.5. Aerosol Residence Time and Transport 6

1.2. Effects on Climate, Health, and Environment **6**

1.2.1. Aerosol Cloud Interaction and Impact on Precipitation 7

1.2.2. Impact on Cryosphere 9

1.2.3. Non-Climatic Effects - Health, Agriculture, Visibility Impairment and Damage to Materials and Buildings 9

1.3. Why Carbonaceous Aerosols? **10**

1.4. Why Carbonaceous Aerosols Over the Central Himalayas? **15**

1.5. Objectives and Organization of the Thesis **19**

2. Measurements and Data Analysis *24*

2.1. Site Description and Meteorology **24**

2.2. Ground-Based Measurements **27**

2.2.1. Aethalometer 27

2.2.2. EC-OC Analyzer 28

2.2.3. CRDS Trace Gas Analyzer 30

2.3 Satellite Data **32**

2.3.1. CALIPSO 32

2.3.2. Measurement of Pollution in the Troposphere (MOPITT) 33

2.3.3 Moderate Resolution Imaging Spectroradiometer (MODIS) 34

2.4 Models **36**

2.4.1. HYSPLIT Back Air Trajectories 36

2.4.1.1 Concentration Weighted Trajectories 37

2.4.2 OPAC and SBDART Simulations for Radiative Forcing Estimation 37
2.4.3. MERRA- 2 39
2.4.4. WRF-Chem 39

3. Characteristics of OC and EC in PM 2.5: Radiative Forcing Estimates and Role of Meteorology and Biomass Burning 41

3.1. Introduction 41

3.2. Results and Discussions 43
3.2.1. Diurnal Variations 43
3.2.2 Annual Variations 48
3.2.3 A Comparison with Other Studies 51
3.2.4 Influence of the Boundary-Layer Height and Meteorological Parameters 52
3.2.5. Influence of Slow-Moving Air Masses and Biomass Burning 56
3.2.6 Ratio and Correlation Between OC and EC 60
3.2.7 Effect of Diurnal Variation on Radiative Forcing 61

3.3. Conclusions 62

4. Implications of Site-specific Mass Absorption Cross-section (MAC) to Black Carbon Observations 64

4.1. Introduction 64

4.2. Derivation of the Expression for MAC 66

4.3. Results and Discussion 67
4.3.1. Relationship Between the Absorption Coefficient (b_{abs}) and EC 67
4.3.2. Spectral and Temporal Variation in MAC 68
4.3.3. Role of Temporal Variations of EC and Absorption Coefficient in Variations of MAC .. 73
4.3.4. Role of Meteorology in Variations of MAC 75
4.3.5. Comparison with Other Studies 77
4.3.6. Impact of MAC on eBC Estimates 79
4.3.7. Impact on Aerosol Radiative Forcing (ARF) Estimation 81

4.4. Conclusions 83

5. Probing the Sources, Diurnal Variations and Radiative Forcing of Carbonaceous Aerosols Using High-resolution Ground-based Measurements 85

5.1. Introduction 85

5.2. Results and Discussions 87
5.2.1. Source Identification Using Variations in Angstrom Exponent and OC/EC Ratio 87
5.2.2. Source Wise Quantification of Aerosols 90
5.2.2.1. Determination of Primary and Secondary Organic Carbon (POC and SOC) 90
5.2.2.2. Fossil Fuel and Biomass Burning 99
5.2.2.3. Impact of eBC and its Fossil Fuel and Biomass Components on Aerosol Radiative Forcing (ARF) 105
5.2.3. Correlation of Carbonaceous Aerosols 107
5.2.4. Source Region Identification 108
5.2.5. Influence of Biomass Burning on eBC, EC, OC, eBC_{bb}, POC and SOC 110

5.3. Conclusions 113

6. Application of Black Carbon Measurements to Quantify Contribution of Sources of Carbon Monoxide 114

6.1. Introduction 114

6.2. Results and Discussions 117

6.2.1. Comparison of CO From MOPITT, WRF-Chem and MERRA-2 Against Ground-Based Observations 117

6.2.2. Evaluation of the Applicability of Multiple Regression Method CO Estimates 119

6.2.3. Comparison of the Estimated and Observed CO 122

6.2.4. Comparison of the Predicted CO from eBC for the Year 2018 with the Observed CO 124

6.2.5. Segregation of the Fossil Fuel and Biomass Burning Fractions of CO and their Temporal Variations 126

6.2.5.1 Diurnal Variations 126

6.2.5.2 Annual Variations 130

6.2.6 Comparison of BC Based Source Apportionment Against those from WRF-Chem 134

6.3. Conclusions 136

7. Trend in Black Carbon Concentrations and its Sources: 17 Years of Ground-Based Observations 138

7.1. Introduction 138

7.2. Results and Discussions 140

7.2.1 Seasonal Variations and Trends in Observed BC and MERRA-2 141

7.2.2 Trend in Total BC and Fractions of Fossil Fuel Combustion and Biomass Burning BC 146

7.2.3 The Contrasting Trends in AOD 148

7.3. Conclusions 151

8. Summary and Future Perspectives 152

8.1. Characteristics of OC and EC in PM 2.5: Radiative Forcing Estimates and Role of Meteorology and Biomass Burning 152

8.2. Implications of Site-specific Mass Absorption Cross-section (MAC) to Black Carbon Observations 154

8.3. Probing the Sources, Diurnal Variations and Radiative Forcing of Carbonaceous Aerosols Using High-resolution Ground-based Measurements . 155

8.4. Application of Black Carbon Measurements to Quantify Contribution of Sources in Carbon Monoxide 157

8.5. Trend in Black Carbon concentration and its Sources: 17 Years of Ground-Based Observations 159

8.6. Future Perspectives 160

Bibliography 163

Chapter 1

Introduction

Even the flutter of a butterfly's wings may have an impact on the atmosphere. This chapter describes the importance of the particulate fractions of the atmosphere - the aerosols, which hugely impact the atmosphere despite being its minor constituents. It starts with a brief yet vivid description of aerosols and later moves on to describing their carbonaceous fraction in more depth, explaining why they take centre stage in this thesis. The chapter subsequently lands in the serene lap of the Himalayas and understands how these aerosols impact them and why studying this region is of utmost importance. Finally, it lays down the objectives and describes the organization of the thesis.

1.1 Aerosols

Tiny particles in the solid, liquid, or mixed phases and suspended in air are known as atmospheric aerosols (Junge, 1963). Despite being minor constituents of the atmosphere, these particles have a profound influence and play a variegated role on the air quality (Hansen et al., 2000), radiation budget (Jacobson, 2001; Lau et al., 2006), cloud properties (Ackerman et al., 2000), atmospheric chemistry (Jacobson, 2001), precipitation patterns (Rosenfeld et al., 2008) and health (Olson et al., 2015). Whilst greenhouse gasses remain the main culprits in global warming, particles in the atmosphere also play a multi-hued role in climate change. Quantifying the influence of aerosols on the climate remains an enigma and they are the greatest lingering sources of uncertainty even in the sixth report of the Intergovernmental Panel on Climate Change (IPCC) which came recently in 2021 after more than 30 years from the advent of the first report in 1990.

Aerosols represent a plethora of particles that can be produced by both natural and anthropogenic sources through a variety of complex processes (Junge, 1963; Seinfeld and Pandis, 1998). Considering the large spatial and temporal variabilities, shorter lifetime and wide range of sources and sinks of aerosols, their budgets have large uncertainties. Therefore, quantifying aerosol impacts becomes more difficult, even with the state of art atmospheric regional and global chemistry models as they themselves utilize these aerosol budgets and some aerosol physical and chemical properties as an input.

1.1.1. Shape, Size, and Mixing state

Aerosols have a variety of shapes usually classified as isometric, platelets, or fibers (Reist, 1984, 1993). Particles formed via gas to particle conversion are generally spherical while those formed from grinding/breaking are non-spherical (Reist et al., 1993). Aerosol sizes for non-spherical shapes can be measured via Martin's diameter - which measures the length of line that separates particles into two equal portions (Rhodes et al., 2008) or via ferret's diameter - that measures the maximum distance from edge to edge (Rhodes et al., 2008). For practical applications two more common definitions for determining the aerosol size are used: aerodynamic diameter - which denotes the diameter of a unit density sphere having the same settling velocity as that of the particle and, stoke's diameter - which corresponds to the diameter of the same density sphere having the same settling velocity as that of the particle.

Aerosols can also have varied mixing states depending upon the distribution of chemical constituents among the particles. They can mainly be either 'externally mixed', (whereby the particles from different sources remain separated thus depicting a non-homogeneity in the chemical composition) or they can be 'internally mixed', (where different chemical components mix within a particle). The possibility of internally mixed particles increases with the aging of the air masses. A core-shell type mixing may also exist when one of the components forms a coating over the other. The nature of mixing state, shape and size affects the microphysical properties of aerosols and hence their impact on the environment.

1.1.2. Aerosols Size Distribution

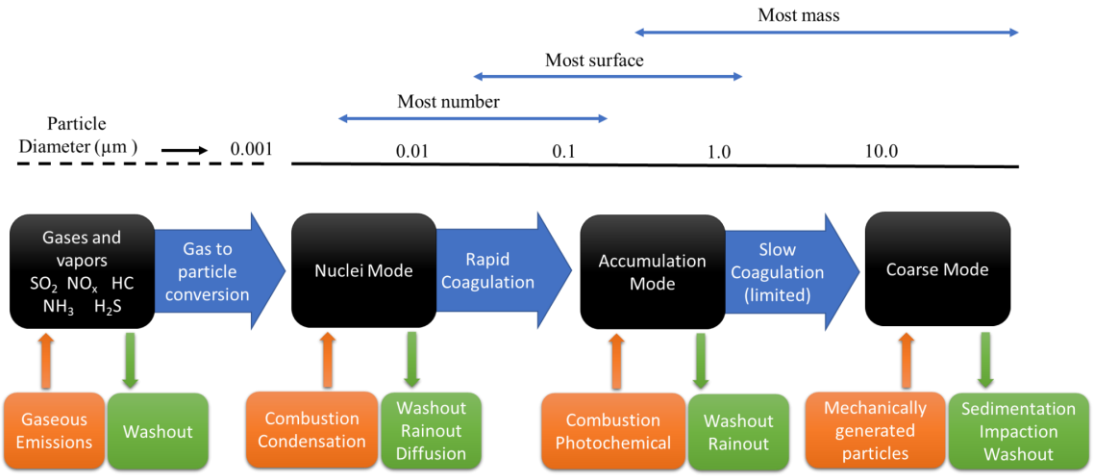

Figure 1.1 *Schematic showing aerosol processes-source, sinks, transformation and size range (Compiled from: Hinds,1999).*

Aerosol characteristics are crucially governed by their size distribution (Figure 1.1) which has a wide range from ~0.001 to 100 µm, depending upon their production mechanism. The smaller particles in the range of ~0.001 to 0.1 µm are called Nuclei or Aitken mode particles. These are generally produced in the atmosphere by gas to particle conversion through nucleation of volatile gasses and are important in atmospheric electricity. The formation of such particles involves three main processes – (i). homogenous homomolecular nucleation which implies particle formation from a single gas species only, (ii). Homogeneous heteromolecular nucleation which requires two or more gaseous species for new particle formation and, (iii). Heterogeneous heteromolecular nucleation in which new particles are formed by the condensation of gaseous species on pre-existing particles.

Particles in the size range of ~0.1 to 1.0 µm are called accumulation mode aerosols. These include single larger particles produced by an accumulation of two or more aerosols and particles from the nucleation mode which have grown by condensation of water vapours. Such particles are known to influence solar radiation budget in the visible range significantly. Particles with size > 1.0 µm fall under the category of coarse mode aerosols and mostly constitute particles directly generated by mechanical disintegration processes (bulk to particle conversion) such as dust.

1.1.3. Aerosol Transformation

Aerosols may also transform from one size range to another thus changing their particle number and size distribution while keeping their mass in the atmosphere intact. This changeover is achieved by two main processes – (i). Coagulation which shifts the particles in the lower size range to the higher by collision and coalescence, the rate of which is governed by particle diffusion (McCartney, 1976; Pruppacher and Klett, 1978) and (ii). Condensation which involves growth in size due to condensation of vapours on the surface of aerosols and its rate is described by Fuchs-Stugin equation (Hegg, 1990).

1.1.4. Aerosol Sources and Sinks

Aerosols have wide range of natural and anthropogenic sources. Sea salt spray, volcanic emissions, windborne dust, natural wildfires, and biogenic emissions constitute the natural sources. Emissions from industries, transportation, crop-residue burning, residential cooking, waste burning and resuspended dust due to construction or mining activities form the anthropogenic fraction of aerosols. Specific details on sources of carbonaceous aerosols are discussed in section 1.3. As shown by the aerosol optical depth and estimated contributions from different aerosol types (Figure 1.2), it is evident that the aerosol distribution is highly inhomogeneous (Myhre et al., 2013). Studies show that the natural aerosols comprise the majority fraction (90%) while anthropogenic aerosols globally form about 10% of the total aerosols (Textor et al., 2006). However, the information on aerosol budget is subjected to several uncertainties which are in part related to the large uncertainties in individual source estimates due to a huge spatial and temporal heterogeneity and are in part associated with the heterogeneous aerosol chemistry, aerosol mixing states and other atmospheric processes relating their genesis, sinks and transformation.

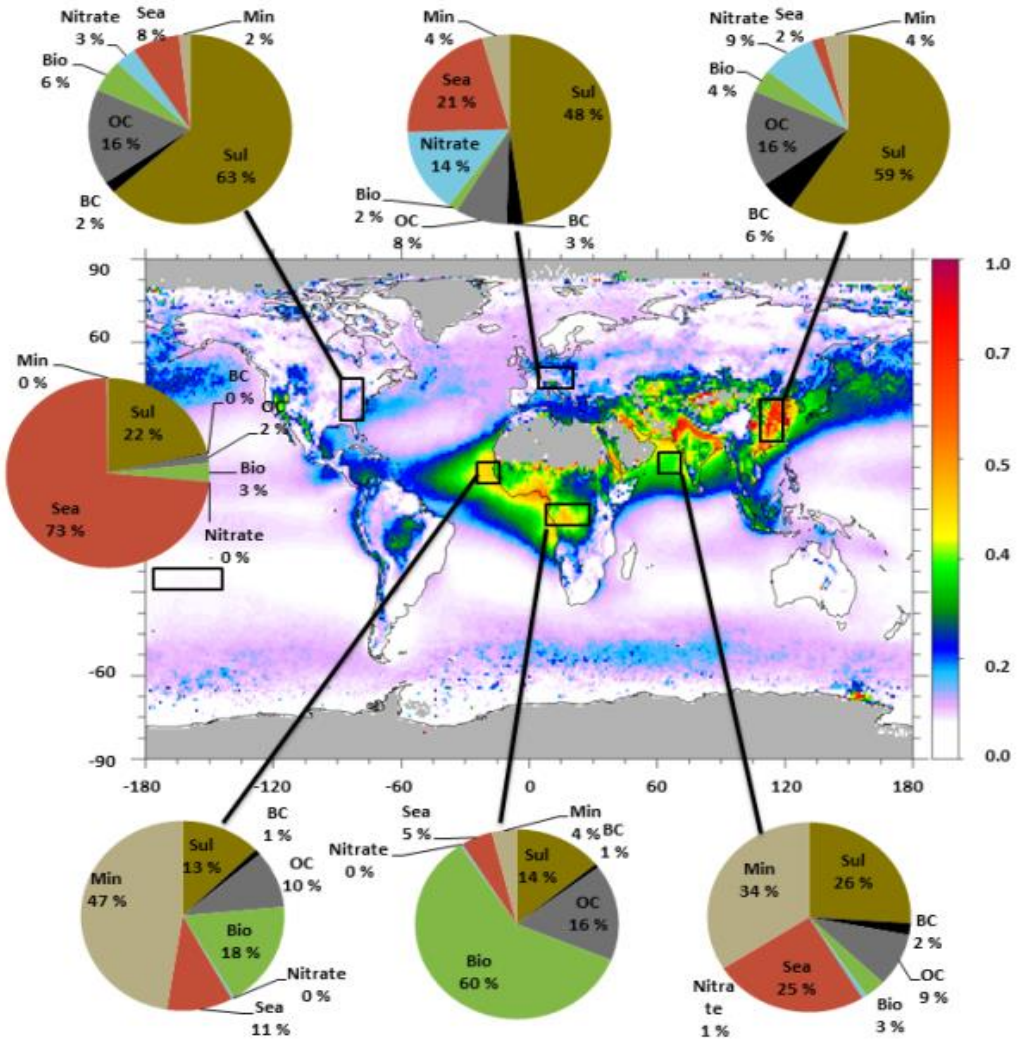

Figure 1.2 *(a) MODIS Aerosol Optical Depth at 0.55 µm averaged over 2001–2010 period (b) Pie charts showing the contribution of sulphate, BC, OC, Bio (OC and BC from biomass burning), sea salt, nitrate and Min(mineral dust) aerosol in building AOD over different regions of the globe (Extracted from:https://www.nature.com/scitable/knowledge/library/aerosols-and-their-relation-to-global-climate-102215345/; Data from Myhre et al., 2013).*

There are two major sinks for aerosols, namely, (i) dry deposition/sedimentation which primarily involves the transfer of aerosols to the surface due to turbulent diffusion or impaction or gravitational sedimentation in the absence of precipitation (Pruppacher and Klett, 1978) and, (ii) wet removal which limits the residence time of particles in 0.05 to 0.3 µm size range (Radke et al., 1980) and in turn involves: 'wash out/below-cloud or precipitation scavenging'. This mechanism implies the removal of aerosols that are in the air stream of the falling raindrops, and 'rain out/in-cloud or nucleation scavenging'. This also includes the incorporation of particles as a precipitation nucleus in the presence of water vapour during cloud formation (Hoppel et al., 1990).

1.1.5. Aerosol Residence Time and Transport

The time upto which the particles remain airborne is known as the aerosol residence time or simply lifetime and is primarily governed by the aerosol properties and their removal and transformation mechanisms. Generally, aerosols in the lower troposphere have a lifetime of less than a week. In the accumulation mode, it could be longer (7 to 10 days) as compared to smaller particles which are removed by Brownian diffusion and also compared to larger particles which are easily removed by sedimentation and wet deposition. In the case of the free troposphere, this time is longer. In the stratosphere, it extends to as long as a few to several years due to the absence of precipitation. A semi-empirical relation, given by Jaenicke, (1984) can be utilized for estimation of residence time. Depending upon their residence time, particles can easily be transported to distances far from their place of origin. Long-range transport of Saharan dust to Caribbean islands (Prospero et al., 1981), aerosols from Africa to Indian oceans (Tyson et al., 1996) and many such instances of aerosol transport are already reported in the literature. Aerosols may also be transported vertically upwards mainly via convective eddies and turbulent motion. Once they reach higher altitudes, aerosols are spread over large horizontal distances by the prevailing winds. In general, the aerosol number concentration is found to decrease with altitude. More discussion on transport, at local and regional scales, will be made in the subsequent chapters.

1.2. Effects on Climate, Health, and Environment

Aerosols alter the climate system through two main kinds of interactions i.e., aerosol-radiation interaction and aerosol-cloud interaction. All aerosols either absorb or scatter the incident radiation. Scattering of radiation by aerosols increases the reflectivity (albedo) of the earth thus reducing the amount of radiation reaching the surface and hence having a cooling effect. Conversely absorbing aerosols, capture the shortwave radiation and re-radiate it in the longer wavelength which has a warming effect on the atmosphere and hence contributes to global warming. This aerosol-radiation interaction is known as the ‘direct aerosol effect’ and it fundamentally changes the radiative balance of the earth, and this change is quantified as ‘aerosol radiative forcing’. Radiative forcing (RF) is a metric used to estimate the changes in the net balance of the outgoing and the incoming solar radiation caused due to the presence of a given atmospheric constituent. IPCC in its

reports since 1990 provides a global mean of the RF for chief atmospheric species (e.g., CO_2, CH_4, BC, sulphates, etc.), expressed as the difference between the present day and the beginning of the industrial era in units of Wm^{-2}. A positive forcing implies warming while a negative one means a cooling effect. Since aerosols can both scatter and absorb radiation, they exhibit both positive and negative RF.

1.2.1. Aerosol Cloud Interaction and Impact on Precipitation

Aerosols that are hydrophilic (e.g., sulphates, salts, nitrates) or those with hydrophilic coating act as cloud condensation nuclei (CCN) on which the water vapours condense and form cloud droplets under the condition of supersaturation. Under the condition of fixed liquid water content, increasing the number of CCN increases the number of smaller sized cloud droplets (Twomey, 1977). Such clouds are brighter and reflect more shortwave radiation, preventing it from reaching the surface and thereby causing surface dimming. This effect of aerosols in enhancing the cloud albedo is termed as the 'first indirect effect' and is known to cause a net cooling effect. Further, clouds with droplets of such small size are less likely to precipitate thus increasing the cloud lifetime (Albrecht, 1989) estimated to cause net cooling and the effect is called the 'second indirect effect'.

Smaller droplets may also result in delayed freezing of droplets in the case of mixed-phase clouds, thus altering the cloud characteristics. This effect is called the 'thermodynamic effect' (Denman et al., 2007). In particular, absorbing aerosols such as BC heat the atmosphere thereby affecting atmospheric stability and hence affecting cloud formation and its lifetime. This effect is referred to as the 'semi-direct effect' (Ackerman et al. 2000) and can cause both warming and cooling depending upon the relative positions of aerosols with respect to the cloud. Earlier, only the decrease in the cloud formation due to the presence of BC was considered as the semi-direct effect or the cloud burn off. Currently, however, it is not clear as to whether the semi-direct and thermodynamic effects cause net cooling or heating. Absorbing aerosols especially those which are hydrophobic such as BC and mineral dust also cause the 'glaciation indirect effect' which has a warming effect and implies increased precipitation rather than delay because such aerosols act as ice nuclei in supercooled mixed-phase clouds.

IPCC's third and fourth reports distinctively characterized these indirect effects into radiative forcing. However, they admitted to a low level of their understanding. Later, the fifth and sixth IPCC reports stated that these different indirect effects are difficult to delineate and only provide effective radiative forcing estimates. This issue is also reflected in the higher uncertainties and a low level of confidence in the aerosol effective radiative forcing estimates (IPCC, 2013). Figure 1.3 shows a range of effects due to aerosol-cloud interactions. It also shows the new terminology used for aerosol–radiation and aerosol-cloud interactions in the fifth assessment report of IPCC (AR5) compared to the ones used in the fourth assessment report (AR4).

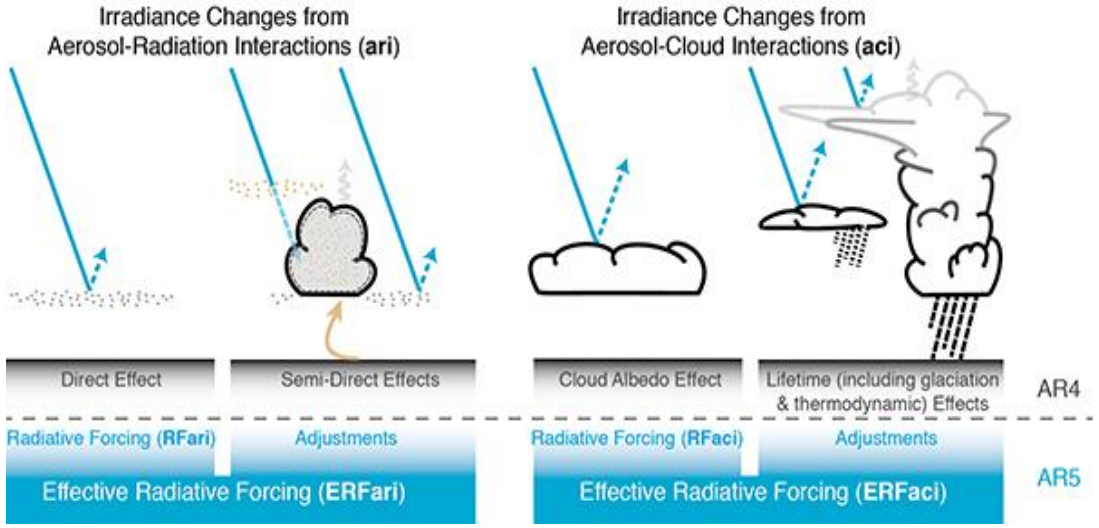

Figure 1.3 *Schematic shows the new terminologies used for the 'aerosol–radiation and cloud interactions' in AR5 and AR4.The solar and terrestrial radiation along with the couplings between the surface and the cloud layer for rapid adjustments is denoted by blue, grey and brown arrows. (Extracted from IPCC, 2013).*

Aerosol cloud and radiation interactions alter the cloud microphysics as well as the atmospheric stability thereby leading to changes in precipitation. Such changes are suggested to operate at two-time scales: short and long. The short time scale changes refer to the rapid response of clouds and atmosphere while the longer time scale is associated with the changes in evaporation induced because of the changes in the surface temperature (Samset et al., 2016). Using precipitation trend from 1950 to 2002 and other observations, Chung and Ramanathan, (2006), showed that the Sahelian droughts, weakening of the Indian monsoons and the North-South shift in rainfall also called as 'northern-drought/southern flooding' in China were a result of the natural variability along with the aerosol forcing effects. In a particular reference to biomass burning,

Kawase et al., (2011) showed that BC induced a decrease in evaporation and enhanced subsidence resulted in a decreased precipitation trend in Africa. Despite being a subject of numerous studies (e.g., Chung and Ramanathan, 2006; Lau et al., 2006; Bollasina et al., 2011), a clear picture attributing changes in Indian monsoon to the regional aerosol effects remains elusive. Even in the IPCC AR6 report, effective radiative forcing due to aerosol-cloud interactions still has a low confidence label.

1.2.2. Impact on Cryosphere

Aerosols when deposited on snow and ice darken them, reducing the surface albedo and thus exaggerating snow melting (Wiscombe and Warren, 1980). This effect results in significant positive warming due to aerosols and is particularly important in snow-covered regions of the Arctic and the Himalayas which have a substantial influence of the transported aerosols. Aerosols once deposited continue to have these positive radiative effects till they remain exposed or are covered by fresh snow. Moreover, the melting snow further exposes the dark surface thus leading to positive feedback (Flanner et al., 2007).

1.2.3. Non-Climatic Effects - Health, Agriculture, Visibility Impairment and Damage to Materials and Buildings

Aerosols, especially in the size range of less than 2.5 microns (PM 2.5) are known to cause significant adverse impacts on human health upon inhalation (Brunekreef and Forsberg, 2005). These particles are not only detrimental to the respiratory system and associated with many respiratory diseases but are also linked to an increasing number of cancer and heart diseases. Moreover, they are known to cause about 3.4 million premature deaths per year globally (Ghude et al., 2016).

Aerosols also affect agricultural yield in several ways. The scattering and absorption by aerosols reduce the solar radiation in the photo-synthetically active visible region reaching the earth's surface, thus decreasing the productivity and extending the growth period. The deposition of aerosols on plants prevents them from receiving sufficient solar radiation subsequently increasing their acidity and ultimately damaging the plants.

Furthermore, the aerosol induced changes in precipitation patterns and surface evaporation significantly impacts agricultural yields (Ramanathan et al., 2005).

Light scattering and absorption by suspended particulates in the atmosphere also make aerosols the major culprits when it comes to visibility. They lead to haze and fog events and to a reduction in the quality and quantity of light reaching a human eye. Thereby making it difficult to recognize the various forms, contrast, and colour of objects in front of them. In low humidity conditions, carbonaceous aerosols have the greatest effect on visibility while sulphates have the largest impact during high humidity conditions (U.S. EPA, 2012). Carbonaceous aerosols have been found to play a larger role in the regional haze events in the eastern United States (DeBell et al., 2006). The vital role of both scattering and absorbing aerosols in the formation of fog droplets was observed during the Winter Fog Experiment in Delhi (Safai et al., 2019). Deposition of particles also damages materials and buildings, including those of historical importance (Kulshrestha et al., 1995). In this context, the discoloration of the Taj Mahal, a universally acclaimed site of world heritage, was reported by Bergin et al., (2015) due to the deposition of carbonaceous aerosols and dust particles.

1.3. Why Carbonaceous Aerosols?

'Carbonaceous aerosols' (CA) is an umbrella term used for a large, highly variable and complex mixture of carbon-containing particles mixed with organic matter (Bond et al., 2013) and may include elements such as hydrogen, oxygen and nitrogen. Sources such as pollens, inorganic carbonates and dust which contains carbon are usually omitted from the definition of carbonaceous aerosols (IPCC, 2013). Despite these exclusions, the term still encompasses aerosols with a spectrum of characteristics such as the level of carbon contained, thermal and optical properties. These aerosols are most commonly classified further as back carbon (BC) and organic carbon (OC).

BC refers to the fraction of CA which is entirely composed of carbon atoms. It is formed only from the incomplete combustion of carbon-based fuels (petroleum, coal, crop residue, wood, etc). BC is known to be the most absorbing aerosol because it strongly absorbs light in the visible and IR range, which is also responsible for its black colour.

Being highly inert, refractive, and insoluble in most solvents, it is one of the most stable aerosols with very high resistance to chemical degradation and transformation. Depending upon the properties exploited for the measurement of BC, different operational definitions also exist in the literature such as elemental carbon (high temperature of volatilization), refractory black carbon (incandescence at a given temperature) and equivalent black carbon (light absorption property). However, all of these mostly refer to the same aerosol species. A more detailed discussion on the terminologies regarding BC could be seen in Petzold et al., (2013).

OC in itself is a collective term used for several individual compounds containing carbon and other organic molecules. Like those of poly aromatic hydrocarbons, alkanes, humic-like substances, etc. OC is found to be more susceptible to thermal degradation as they usually have a lower temperature of volatilization. This high volatility makes OC sampling particularly difficult. OC is further classified as primary organic carbon (POC), which is directly released from its source, and secondary organic carbon (SOC), which is formed from the condensation/nucleation of volatile organic compounds. The term organic aerosols/organic matter (OA/OM) is also used in the literature to signify the full mass of organic aerosols and is subsequently split into the primary and secondary components as primary organic aerosols (POA) and secondary organic aerosols (SOA). In terms of absorption properties, OC can be split as brown carbon (known for absorption of wavelengths lower than 880nm) and non-absorbing OC (Lack et al., 2010). BC and brown carbon are together also known as light-absorbing aerosols. Usually, non-absorbing OC fraction is found to have a refractive index similar to that of sulphates and both are considered as significant light scatterers in the atmosphere (Hegg et al., 1997). Further, OC aerosols also act as cloud condensation nuclei because of the existence of polar groups such as carboxylic and dicarboxylic acids (Saxena and Hildemann, 1996).

Carbonaceous aerosols are of critical importance because they affect several atmospheric processes (Ramanathan and Carmichael., 2008) due to the direct impact on radiation budget (Gogoi et a., 2017), their significant role in glacier retreat (Kaspari et al., 2011) and their role in altering cloud properties by aerosol cloud interactions (Ackerman et al., 2000). In addition to their role in perturbing the radiation budget and hence climate changes, the increased emissions of carbonaceous aerosols pose a major threat in our life

as these aerosols are carcinogenic and can thus cause negative health effects (Kennedy, 2007).

Table 1.1 *Comparison of global mean radiative forcing in SAR, TAR, AR4 and AR5 for seven components - sulphate, nitrate, SOA, mineral dust, BC and OA from biomass burning combined and BC and OC separately in fossil fuel and biofuel due to differences in their ratios from these emissions (Compiled from: IPCC, 2013).*

Global Mean Radiative Forcing (Wm^{-2})				
	SAR	**TAR**	**AR4**	**AR5**
Sulphate aerosols	-0.4 (-0.8 to -0.2)	-0.4 (-0.8 to -0.2)	-0.4 (-0.6 to -0.2)	-0.4 (-0.6 to -0.2)
Black carbon from fossil fuel and biofuel	+0.1 (+0.03 to +0.3)	+0.2 (+0.1 to +0.4)	+0.2 (+0.05 to +0.35)	+0.4 (+0.05 to +0.8)
Primary organic aerosols from fossil fuel and biofuel	Not estimated	-0.1 (-0.3 to -0.03)	-0.05 (0.0 to -0.1)	-0.09 (-0.16 to -0.03)
Biomass burning	-0.2 (-0.6 to -0.07)	-0.2 (-0.6 to -0.07)	+0.03 (-0.09 to +0.15)	-0.0 (-0.2 to +0.2)
Secondary organic aerosols	Not estimated	Not estimated	Not estimated	-0.03 (-0.27 to +0.2)
Nitrate	Not estimated	Not estimated	-0.1 (-0.2 to 0.0)	-0.11 (-0.3 to -0.03)
Dust	Not estimated	-0.6 to +0.4	-0.1 (-0.3 to +0.1)	-0.1 (-0.3 to +0.1)
Total	Not estimated	Not estimated	-0.5 (-0.9 to -0.1)	-0.35 (-0.85 to +0.15)

A comparison of radiative forcing estimates for seven components of aerosols provided by IPCC for the aerosol-radiation interactions over the different years in the subsequent reports is listed in Table 1.1. It is clear from the RF estimates that even amongst aerosols, the positive forcing magnitude is highest for BC from fossil and biofuel. Interestingly, despite considering four separate components for carbonaceous aerosols (including SOA which is included only recently in the AR5), the uncertainty remains high even in the fifth assessment report. A major reason for this is the large spatio-temporal heterogeneity of these aerosols and varied mixing states and atmospheric processes. While most models consider OC scattering equivalent to that of sulphates, studies have shown that OC contains species that absorb in the low visible range (Kirchstetter et al., 2004; Andreae and Geleneser, 2006). This will decrease the overall negative impact attributed to total

OC. The indirect forcing effects of these aerosols are also an important source of this uncertainty.

Effective radiative forcing (RF due to reflecting type aerosols and with indirect effects) estimates show that aerosols in general have an overall cooling effect and are shown to counteract about half of the positive radiative forcing caused by the greenhouse gasses (GHG) since the 1880s (Figure 1.4). While CA (particularly reflecting OC fraction and indirect effects) plays their role in offsetting the warming caused by the GHGs, the picture is far more complex in their case. Greenhouse gasses contribute the most to RF abundantly by absorbing the radiation emitted by the earth's surface while being transparent to the incoming solar radiation.

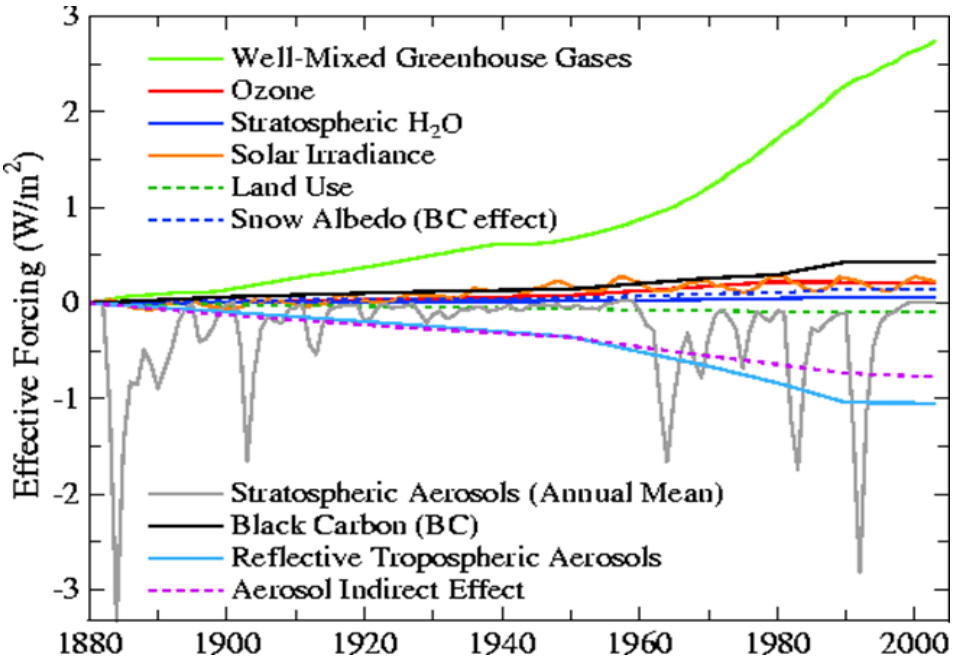

Figure 1.4 *Forcings from 1880-2011 taken from Hansen et al., 2011 (Updated version extracted from- https://data.giss.nasa.gov/modelforce/).*

This radiation is then remitted, thus warming the lower atmosphere and earth's surface. Contrary to this, aerosols and in the current context, BC, absorbs both the incoming and the outgoing solar radiation, thus causing a positive forcing. Further, if BC particles have a coating of chemical components that are transparent or translucent, their probability to absorb solar radiation increases (Jacobson et al., 2007). These properties make BC a far more effective absorber compared to CO_2 implying that a given quantity of BC by weight is capable of absorbing a million times more radiant energy compared to an equal

quantity of CO_2 (Jacobson and Streets, 2009). However, CO_2 usually is known to persist in the atmosphere for about a century which entails sustained radiative forcing before natural processes can remove them. This also means that given the shorter lifespan of BC and/or OC, the benefits of their reduction will be more quickly realized as opposed to long-lived GHGs.

Radiative forcing estimates are inadequate for comparing this magnitude and timing of benefits in BC and/or OC reductions as compared to those for CO_2 like species. This is largely because radiative forcing does not capture changes over time. To address this disparity in the atmospheric lifetime of various pollutants, another metric called Global Warming Potential (GWP), defined as the cumulative forcing over a specified period (typically 100 years) due to a unit mass of a pollutant in reference to the same mass of CO_2, is employed (Bachmann, 2009). Table 1.2 provides the estimates of GWP made in different studies for BC and OC in 20- and 100-years periods. The relative impact of BC and OC is larger over shorter periods (20 years) because of their shorter life span and rapid response to their impacts. More interestingly, the warming potential of BC is 6-10 times greater than the negative/cooling potential of OC of equal mass, thus showing that although OC is emitted in larger quantities, BC warming can be relatively more significant. Yet, even though GWP is a useful metric for understanding the relative cost-effectiveness of mitigation policies targeting a specific pollutant, like forcing, it does not include the complete range of all climatic effects such as negative forcing due to enhanced cloud reflectivity or the positive effects due to darkening of snow which are particularly important for Himalayan and Arctic regions.

Table 1.2 *Global Warming Potential for BC and OC over 20 and 100 years (Compiled from: Bachmann, 2009).*

Black Carbon		**Organic Carbon**		**References**
20 years	**100 years**	**20 years**	**100 years**	
2200	680	-250	-75	Bond and Sun, 2005
2530	840-2240	N/A	N/A	Jacobson, 2005
2900	830	-100 to 290	-28 to -82	Rypdahl et al., 2009
~2000	~500	N/A	N/A	Hansen et al., 2007
1600	460	-240	-69	Fuglestvedt et al., 2009

Additionally, it is worth keeping in mind that, unlike the greenhouse gases which are more uniformly distributed, aerosols are much more unevenly distributed (Figure 1.2) and therefore the impact of aerosols also strongly varies regionally. Globally, BC emissions are estimated to be about 7600 Gg and that of OC are about 35700 Gg for the year 2000 (Lamarque et al., 2010). The sector-wise distribution (Figure 1.5) shows that biomass emissions are the single most important source of emissions for both BC (~35%) and OC (~67%) followed by residential/domestic emissions (BC:25% and OC:22%). Transportation is the next important source for BC and such emissions usually have a low OC/BC ratio. However, these sources also vary regionally. Developed countries such as Japan, United Kingdom, Europe, etc. usually have very low BC emissions and most of them come from anthropogenic sources. India, Africa and China put together, account for the largest BC emitting regions in the world (>500Gg each). About two-thirds of these BC emissions come from anthropogenic sources such as residential/domestic emissions in these three countries. Moreover, while biomass emissions are the dominant contributors to BC in the case of Africa, contributions from anthropogenic sources are the major culprit for BC emissions in India and China. Notably, emission estimates from carbonaceous aerosols are more uncertain compared to GHGs and other pollutants such as SO_2 as they have a shorter lifetime and are emitted from a large number of small and dispersed sources with irregular and heterogeneous combustion conditions.

1.4. Why Carbonaceous Aerosols Over the Central Himalayas?

The paramount importance of studying carbonaceous aerosols have already been discussed in the previous section. These species have an even greater and critical impact in the pristine environment such as the Himalayas. The Himalayan range stretches across eight South Asian countries, is home to the largest ice mass outside the polar region, the source of ten major Asian river systems and contributes to four biodiversity hotspots (Wester et al., 2019). About 240 million people directly depend on the region for their livelihood, about 1.9 billion depend on the region for food security, water and energy and more than 35% of the world's population benefits from its ecosystem services (Wester et al., 2019). The developing countries in Asia - Afghanistan, Pakistan, India, China,

Nepal, Bhutan, Bangladesh and Myanmar fall along the perimeters of the mountain ranges defining the Himalayan region.

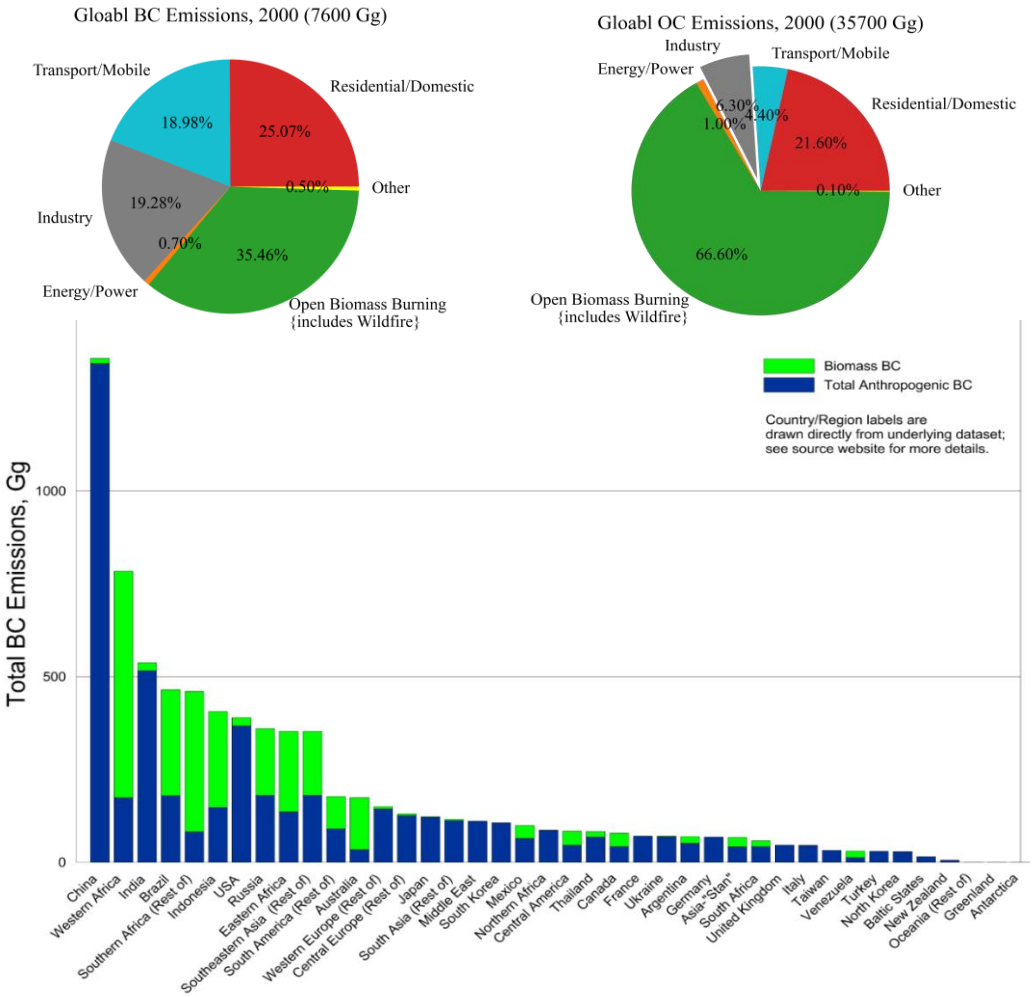

Figure 1.5 *Pie chart showing global distribution of BC and OC emissions by major source category and bar chart showing BC emissions (Gg) by World Region, 2000 (Compiled from: US EPA, 2012; Data from Lamarque et al., 2010).*

While pollution levels are declining in Europe and North America (Bell and Davis, 2001), developing countries in Asia with rapid urbanization and industrialization have become a prime hotspot of aerosol emissions (Ramanathan and Carmichael, 2008). In particular, China in North and Indo-Gangetic Plain (IGP) which bound the Himalayas from South and West serve as an unprecedented huge source of pollution reaching the high mountains. Covering a fertile land area of around 700000 $km^{2,}$ IGP is the world's most densely populated region with over 900 million inhabitants (Wester et al., 2019) and has experienced a dramatic increase in the atmospheric carbonaceous aerosols as shown by modeling works (e.g., Adhikary et al., 2007) and data from ground-based

networks (e.g., Krishna Moorthy et al., 2013). The annual average PM 2.5 concentration in 12 cities of the IGP (including those in Pakistan and Bangladesh) are shown to exceed the WHO 2005 guideline of 10 µg m^{-3} by a factor of ten (Wester et al., 2019). Although Himalayan regions do not have significant sources of pollution of their own, they receive substantial pollution from the outflows of Asia and the Middle East. Pollution episodes at South-central Tibet (Xia et al., 2011; Wang et al., 2015), Western and Central Himalayas (Kumar et al., 2011; Dumka et al., 2015; Kant et al., 2020; Srivastava and Naja, 2021), South-eastern Tibet (Zhao et al., 2013) have been traced back with sources at the IGP. Central and western Himalayas are reported to receive dust from the Thar desert (Hegde et al., 2007; Ram et al., 2010). Dust from the Taklimakan desert is found to have been transported to the Northern Tibetan plateau (Wang et al., 2015). Pollution from Central Asia and the Middle East is shown to be received in the North-east Himalayas (Gul et al., 2018). Such high aerosol emissions, especially carbonaceous aerosols - transported or localized, can lead to extremely deleterious impacts to the Himalayan climate, precipitation and cryosphere, caused primarily as a result of reduced snow albedo by surface deposition, dimming, increased warming and induced changes in precipitation.

Model simulations have suggested that carbonaceous aerosols lead to an increased surface temperature of upto 0.5^{o}C over the Himalayan-Tibetan plateau (Ji et al., 2015), while BC alone on snow is associated with an enhanced temperature of ~1^{o}C (Qian et al., 2011). Average air temperature since the mid-1970s in the central Himalayas is shown to have risen by 1^{o}C i.e., twice as high as the mid-latitude sites over the same period (Shrestha et al., 1999). Such elevated warming with BC, in particular, is expected to play a role comparable to GHGs in this region (Ramanathan and Carmichael, 2008).

Carbonaceous aerosols are also linked with changes in the precipitation patterns over the Himalayas via two mechanisms. One of the mechanisms focuses on aerosols transported from South Asia to the Indian Ocean during the dry seasons of winter and early spring which results in solar insulation of the oceanic surface thus suppressing convection and hence leading to a reduced moisture transport in the peak monsoon season (Satheesh et al., 1999). This tends to weaken the monsoonal rainfall. Another mechanism proposed by Lau et al., (2006), known as the ‘elevated heat pump hypothesis’ focuses on the build-up of absorbing aerosols such as BC in the IGP during the pre-monsoon season which

elevate along Southern Himalayan slopes warming the mid-upper troposphere. This warming creates a temperature anomaly that enhances the moisture influx from the Indian ocean thereby leading to an intensification of the early monsoon. Only a few observations based studies (Gautam et al., 2009; Manoj et al., 2010; Bollasina et al., 2011) have also considered the impact of aerosol warming on the monsoons. Yet the impact of the indirect effect of aerosols on the monsoons remains largely uncertain (IPCC, 2013).

The Himalayan cryosphere is also impacted by carbonaceous aerosols in multiple ways. Simulations predict that warming due to these aerosols will produce a 10-20% reduction in spring-time snow depth over the region (Meehl et al., 2008). However, they do not account for cooling by organic particles, indirect cloud effects and warming due to soot deposition on glaciers. Studies including soot darkening estimate that the Himalayan region has the highest soot related warming (annual-3.8 Wm^{-2}, spring-20 Wm^{-2}) across the world (Flanner et al., 2007). Atmospheric heating due to BC and dust is also found to cause widespread accelerated snowmelt in this region (Lau et al., 2010, Qian et al., 2015). Considering the decadal trend (1990-2001) in snow cover due to aerosol emissions over the region, Menon et al., (2010) have shown a large decrease in snow cover area. BC/soot is shown to be a significant contributor to the observed glacier retreat such as the Gangotri glacier (Figure 1.6) at an average rate of 19 ma^{-1} (Bachmann, 2009) in the Himalayan Tibetan region (Ramanathan and Carmichael 2008; Xu et al., 2009). Satopanth and Bhagirath Kharak glaciers in Chamoli have been reported to retreat at an annual rate of 9.7 meters and 7 meters, respectively (Nainwal et al., 2016). Chhota Shigri glacier in Himachal is shown to retreat at 7.5 meters per year (Dobhal et al., 1995). Similarly, a rapid darkening trend of aerosols was shown over the period of 2000-11 by Ming et al., (2015) using MODIS snow albedo data. The study also estimated the mass-loss equivalent of the Himalayan glacial area to be 10.4 Gt $year^{-1}$ for the years 2003-09 contributing about 1.2% to the sea level global rise annually.

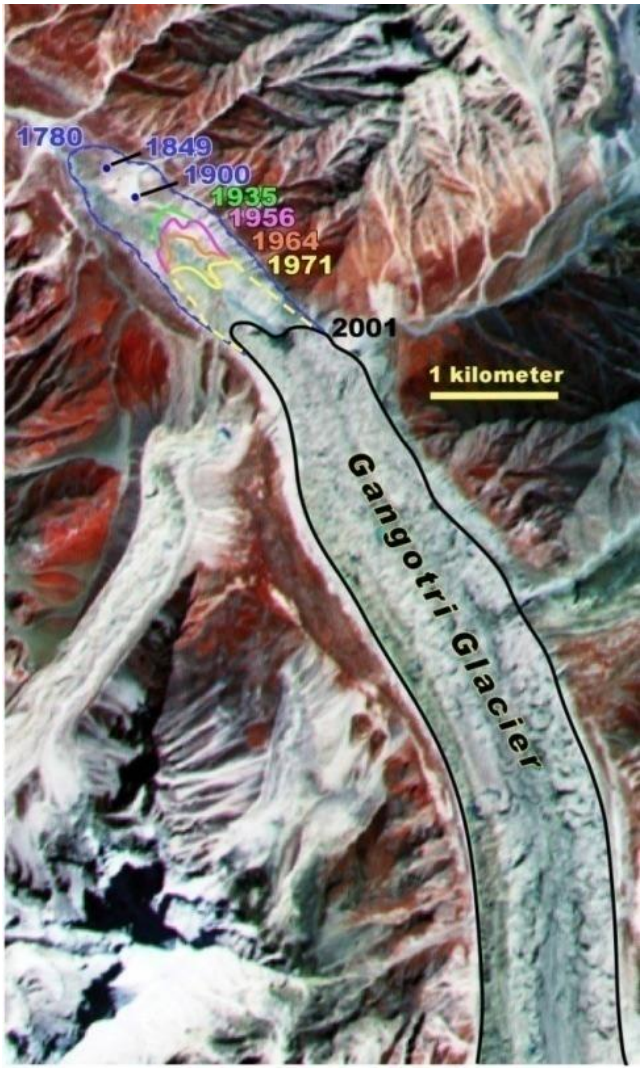

Figure 1.6 *The retreat of the Gangotri glacier retreat which is the source of the river Ganges. (Extracted from: Bachmann, 2009).*

1.5. Objectives and Organization of the Thesis

Considering the aforementioned sensitivity of Himalayas with rest to carbonaceous aerosols, their study over this region forms the focal point of this thesis. It is to be noted that the current model-based estimates in this region for the transport, radiative forcing and deposition of these aerosols have large uncertainties (IPCC, 2013; Qian et al., 2015). These biases are partly a result of the acute deficit in the accurate ground-based data on the optical and physical properties of the carbonaceous aerosols in the region (Wester et al., 2019). Previously reported datasets on carbonaceous aerosols are also found to be associated with large uncertainties (Li et al., 2021). For example, BC and OC concentrations in the total suspended particulates at NamCO and Everest were reported

to be overestimated by ~52% and ~22% respectively due to the contribution of inorganic carbon in mineral dust (Li et al., 2017). Important sample-based offline measurements of OC, EC, SOC and POC (Rastogi et al., 2009; Ram et al., 2010; Satsangi et al., 2012) conducted over the region are mostly campaign-based and vary in terms of the sampling interval. Offline measurements are also known to suffer from positive and negative artifacts because of the presence of volatile species. Further, the very nature of offline measurements integrates whole diurnal variation of the concentrations, which are important to incorporate the swift variations in the assessment of the transportation of pollutants, variations of aerosols with meteorological parameters and their effect on radiative forcing. This is particularly crucial in high-altitude sites (Reddy et al., 2015). Emission estimates of BC over the region have significant uncertainties (a standard deviation of 0.5 x 10^{-9} kg m^{-2} s^{-1}) which is about 47% of the mean (1.1 x 10^{-9} kg m^{-2} s^{-1}) (Gertler et al., 2016). Further, policy decisions regarding mitigation require information on the dominant emission sources contributing to the carbonaceous aerosols but these are currently extremely limited in the region.

Additionally, very few studies have incorporated mass absorption cross-section (MAC) in reporting carbonaceous aerosols, which is used to measure the light absorption properties of BC and OC (Petzold et al., 2013). MAC is found to have large spatiotemporal variation with values ranging anywhere between 2.3-18 m^2g^{-1}, depending on its source, particle size, morphology, and mixing state (Bond and Bergstrom, 2006; Bond et al., 2013). Despite this large variation in MAC, most studies estimating BC from optical absorption have uniformly used the same value for it such as 16.6 m^2g^{-1} at 880 nm in Aethalometer (Dumka et al., 2010; Gogoi et al., 2014; Joshi et al., 2016). This may lead to an underestimation of BC values and its associated radiative forcing. Therefore, *in-situ* measured MAC values are essential for accurately evaluating the radiative forcing of carbonaceous aerosols in the Himalayan region.

Overall, there is a dearth of systematic and high-resolution online and continuous observations of carbonaceous aerosols in the Himalayan region at present owing to its complex topography and strong spatio-temporal heterogeneity of these aerosols. Due to the limited continuous observations in the Himalayas, it is presently difficult to construct trends necessary to evaluate the performance of mitigation policies, validate and compare models, emission inventories and satellite retrievals over the long term. Therefore,

improved, higher time resolution and long-term ground-based measurements of carbonaceous aerosols are urgently needed to improve the estimates of their impact in the Himalayan region (Rana et al., 2019; Wester et al., 2019). To improve our understanding of these aerosols, particularly to quantify the radiative impact of these aerosols, ISRO established a network (Aerosol Radiative Forcing over India; ARFI) of observatories to monitor these species. This research work is a part of this network and is structured with the objective of unravelling the variation, sources and radiative effects of carbonaceous aerosols with a focus on the Central Himalayas. It also broadly caters to the objectives of the National Carbonaceous Aerosols Programme (NCAP) and Carbonaceous Aerosol Emissions, Source Apportionment and Climate Impacts (COALESCE) initiatives devised under the auspices of the Indian Network of Climate Change Assessment (INCCA), Ministry of Environment and Forest.

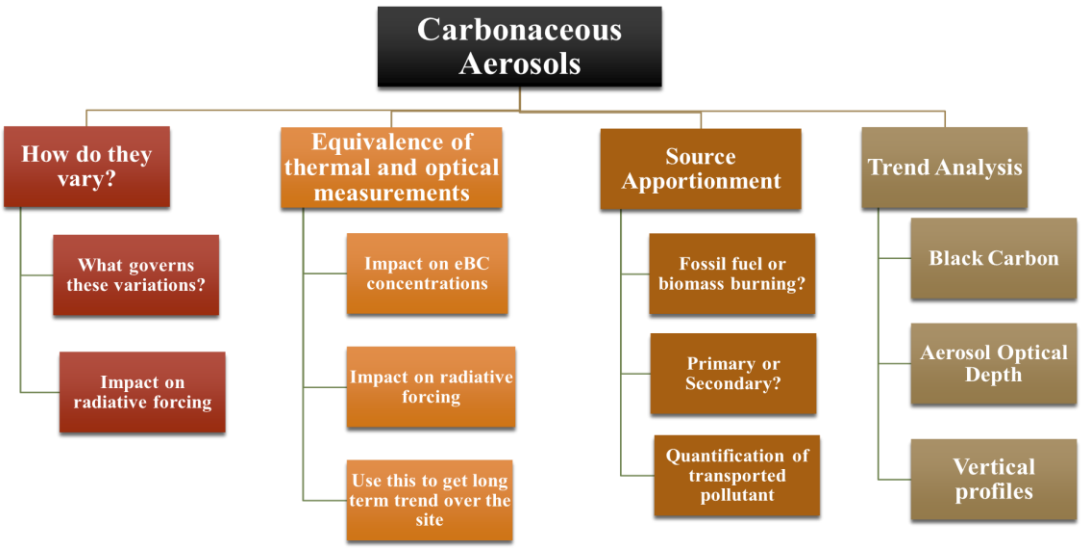

Figure 1.7 *Schematic showing the breakup problems undertaken as part of this thesis.*

Figure 1.7 shows the breakup of scientific problems undertaken during the course of the thesis work to achieve the objectives laid forth. The thesis lays its claims on dedicated high-resolution measurements of carbonaceous aerosols and CO. These measurements are supplemented with satellite measurements, Lagrangian trajectory model, radiative transfer and regional chemistry models. The thesis contains eight chapters which are structured as follows:

Chapter 2 explains the *in-situ* instruments, satellites and models used in this work for the aerosol characterisation. The post-processing involved in data crunching is also discussed here.

The first-ever results of the diurnal variation of OC and EC over the Central Himalayas are presented **in Chapter 3**. Four years of high-resolution continuous observations were made, and these are reported and used to answer the key questions, namely, (1) what the temporal variation of OC and EC at the site is, both at diurnal and seasonal scales, and, (2) what factors govern these variations. The importance of radiative forcing estimates at the diurnal scale are highlighted and the calculations of EC afternoon and forenoon forcing are also presented and discussed.

Till now the BC concentrations from the site were estimated with a constant value of mass absorption cross-section present in the Aethalometer instrument. In **Chapter 4** year-round spectral values of mass absorption cross-section for this site are calculated for the first time using extensive observations of absorption coefficient, b_{abs} and EC concentration. The implications of using a uniform value for MAC instead of its site-specific values are presented. The temporal variations of MAC and their impact on BC measurements and radiative forcing are discussed.

In **Chapter 5,** the BC measurements along with EC-OC measurements have been used to quantitatively characterize the sources of these aerosols over this region employing novel methods. Results from the first year-round segregation of primary and secondary organic carbon are presented and their concentrations using different methods are compared. Further, the impact of emissions due from fossil fuel and biomass on radiative forcing and the contribution of the source regions in transporting pollutants at the site is also quantified.

Chapter 6 begins by showing that the regional chemical model-based CO and satellite-based CO retrievals are significantly biased when compared against observed CO. Therefore, BC and its sources characterized formerly are used in a novel approach employing a multiple linear regression model (MLR) to quantify CO and its sources. The results of the CO estimated using this model is compared with the observations. Given the better performance of the estimated CO, the model parameters are used to predict CO

for the year 2018 and the results are tested against the CO observed from the ground-based measurements. Finally, the regional chemical model-based source segregation is compared against the MLR based CO and its temporal variations and implications are discussed.

The underlying trends in the BC concentrations and their sources are presented in **Chapter 7**. The results are compared with BC obtained from MERRA-2 at the site, together with a discussion on the biases in the reanalysis model. The trend in the columnar and vertical profile of aerosols is also estimated and discussed in the backdrop of the trends obtained in surface BC and those in the emissions.

Chapter 8 summarizes the key results from each chapter in the present work and puts together the conclusions drawn from this study. Finally, the gap areas in which the future scope of research is presented.

Chapter 2

Measurements and Data Analysis

This chapter describes the characteristics of the site, ground and satellite-based instruments used for aerosol and trace gas measurements conducted at the site. It also sheds light on the models used in this work. Additionally, it narrates the methodology employed for data processing and gives an account of the statistical methods utilised in the study.

2.1. Site Description and Meteorology

The observations for the present study were made at ARIES, Manora Peak (29.4°N, 79.5°E, 1950 m a.m.s.l.), situated at the top of a mountain in the Central Himalayas, shown in Figure 2.1. This is a low population density (200 persons per square km) region and is surrounded by low altitude mountains in the Southwest and sharply peaking mountains in the Northeast). It is at an aerial distance of about 2 km from the town of Nainital (a famous tourist spot) and has no potential major pollutant source in proximity. However, Haldwani and Rudrapur, 20-40 km in the south, host small scale industries. The national capital, Delhi, 225 km southwest, is the nearest densely populated megacity. The observing site is considered to be more or less a pristine site, particularly at night time when the boundary layer is below the observational site.

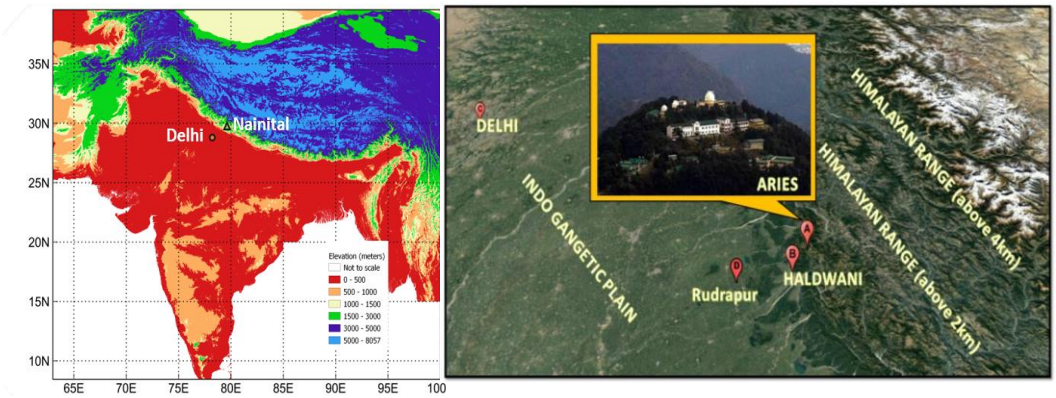

Figure 2.1 *Location of the observation site (Nainital) in the elevation map.*

Observed daily and monthly mean variations in solar radiation, temperature, relative humidity, wind speed and monthly mean rainfall at the ARIES site during 2014-2017 are shown in Figure 2.2 a, b, and c. Monthly variations in the height of the mixing layer depth are also shown. The site receives maximum solar radiation (about 473 Wm^{-2}) and has a maximum temperature of 20.3±2.0^{o}C in May. The Lowest monthly mean temperature of 8.5±2.4^{o}C is observed in January. The lowest solar flux of 197.4±93.3 Wm^{-2} is in July i.e., during the summer monsoon period. This low is mainly due to the high cloud coverage in the monsoon season when the site receives its maximum rainfall (total of about 680 mm in July). On average, relative humidity remains below 65%, except in monsoon (JJAS) when the average relative humidity RH reaches its peak ~88%. The wind speed at the site gradually rises after winter to its maximum in April/May (about 3.6 m/s) and reaches its lowest value (about 1.9 m/s) in September. The mixing layer depth has been obtained from the Global Data Assimilation System (GDAS) 0.5^{o} x 0.5^{o} with the output taken at an hourly interval from 10:30 hour IST to 17:30 hour IST (IST is UTC + 5.5 hours). Monthly averaged mixing layer depth ranged from 583.80±324.25 to 2055.57±57 m a.g.l and closely followed the variation in solar radiation, reaching its maximum in May.

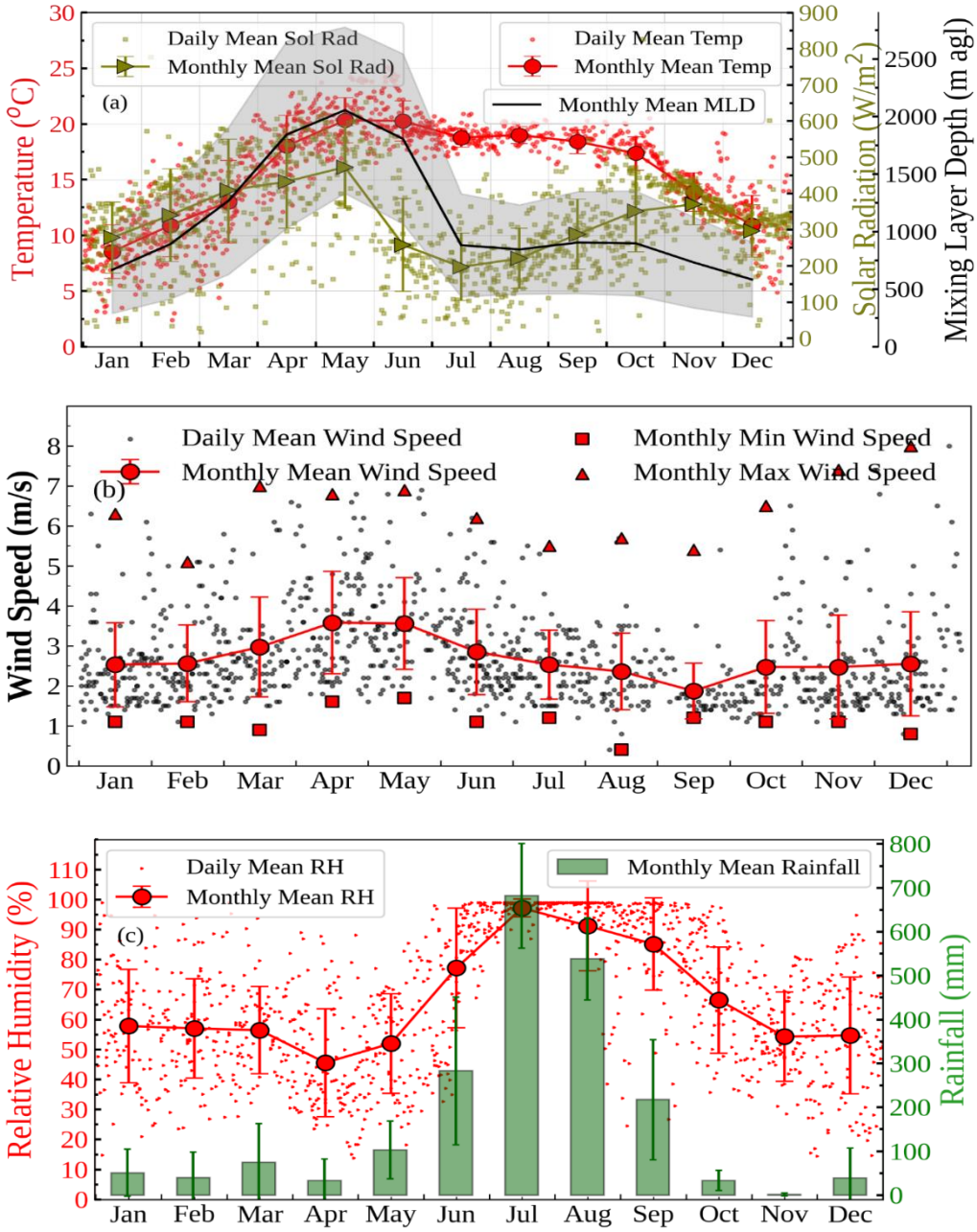

Figure 2.2 *Monthly variation of (a) solar radiation, temperature and mixing-layer depth (b) wind speed and (c) relative humidity and rainfall observed at ARIES, Nainital during 2014-2017. Error bars and shaded portions in the grey show one standard deviation from the average value (Srivastava et al., 2021).*

2.2. Ground-Based Measurements

2.2.1. Aethalometer

Continuous and near real-time measurements of absorption coefficient (b_{abs}) were made using an Aethalometer (AE-42, Magee Sci. Inc.). The estimation of b_{abs} is based on the optical attenuation of light beams at seven wavelengths as shown in Figure 2.3. These measurements were made over a specified duration (2-5 min) at a constant flow rate (3.5 litres per minute). The b_{abs} at a particular wavelength can be given in terms of the change in attenuation (ΔATN) during time ΔT (in minutes) for BC deposition in a spot area (A in cm^2), normalised by the flow rate (Q in litres per minute) (https://www.arm.gov/-publications/tech_reports/handbooks/aeth_handbook.pdf).

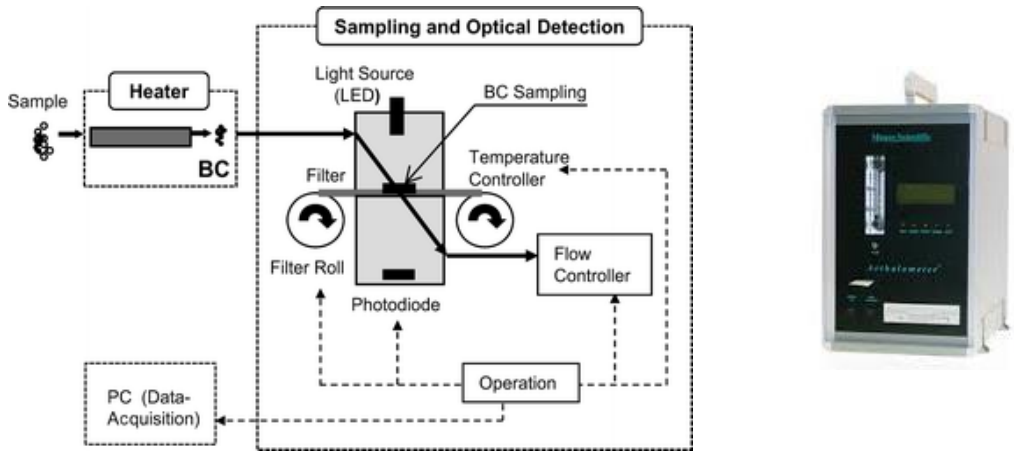

Figure 2.3 *A flow diagram showing the working of an aethalometer, extracted from the Aethalometer manual- (https://www.arm.gov/publications/tech_reports/handbooks/aeth_-handbook.pdf). A picture of the aethalometer AE42 is shown on the right.*

Thus, the expression for absorption coefficient (excluding the terms for multiple scattering and loading effect) is,

$$b_{abs}(\lambda) = (\Delta ATN / \Delta T) * (A/Q) \qquad (2.1)$$

Here, b_{abs} is measured in units of $Mm^{-1}=10^{-6}\ m^{-1}$ and λ is in nm.

This absorption coefficient is multiplied by the wavelength-specific mass absorption cross-section to give equivalent Black Carbon concentrations (eBC). This derivation of

eBC from b_{abs} is our main topic of discussion in Chapter 4 and is excluded here for the sake of brevity and to avoid repetition). Several biases creep into the analysis due to the filter-based optical measurement technique to derive $b_{abs}(\lambda)$ or eBC. Multiple scattering of light in the filter media, loading effect due to successive deposition of aerosol samples and variability of pressure and temperature at the high-altitude site are the major causes of uncertainty in the eBC estimates using Aethalometer (Bond et al., 1999; Arnott et al., 2005; Li et al., 2020). In the present study, we have minimised these biases following the correction schemes as proposed by Weingartner et al., (2003); Drinovec et al., (2015); and have thus taken multiple scattering correction factor C=2.14 and loading correction factor R=1 similar to those incorporated by Moorthy et al., (2004); Dumka et al., (2010); Gogoi et al., (2017); Joshi et al., (2020). Additionally, the data were subjected to rigorous three-sigma outlier removal every ten minutes and then every hour, followed by pressure-temperature correction considering the high altitude of the site (Moorthy et al., 2004). It is reported that with the application of these empirical corrections to overcome artefacts, the uncertainty in the BC measurement ranges between 20-30% (Moorthy et al., 2007; Müller et al., 2011; Joshi et al., 2020).

2.2.2. EC-OC Analyzer

Continuous observation of OC and EC is made using an OC-EC analyzer (Figure 2.4) from Sunset Laboratory, USA (Model 4G) following the National Institute for Occupational Safety and Health (NIOSH) 5040 protocol based on thermal optical transmittance (TOT) (Birch and Cary, 1996). The analysis is performed on a quartz filter punch of 16 mm, which is mounted on the instrument every week or when the laser correction went below 0.90 (to keep up with charring correction). The sample is collected for a time period of 47 min, after which the oven is purged with helium. This sample is then stepwise heated in an oven at a temperature up to 850^{o}C. Evolved carbon fragments are oxidized to CO_2 by flowing them through the MnO_2 oven. This CO_2 is then moved out of this oxidizing oven along with a hydrogen stream and is detected by a non-dispersive infrared (NDIR) detector. In the second ramp, the oven is cooled to 550^{o}C and then the filter is again stepwise heated in an oxidizing atmosphere (98% He and 2% O_2), thus oxidizing off any EC. This EC is then detected like above using the NDIR detector. Correction for the pyrolytic conversion of OC to EC is accomplished by monitoring the transmittance of light from a laser diode (660 nm) through the sample filter. In the second

phase of the oxidizing ramp, the point at which the laser absorbance equals the initial laser absorbance is termed as EC/OC split line. Any EC detected, before this point, is considered to be formed pyrolytically by charring of OC and is subtracted from the EC area observed during the oxidizing phase of the analysis and is designated as OC.

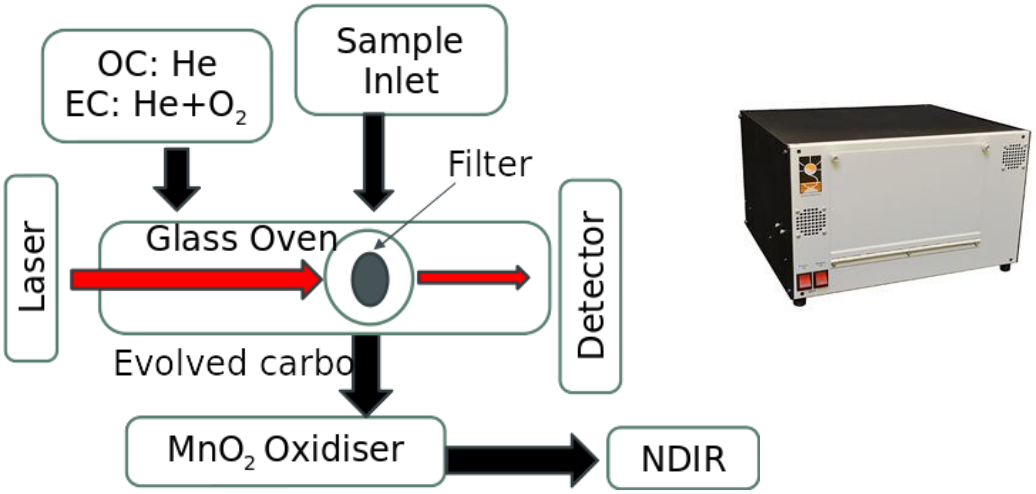

Figure 2.4 *A schematic showing the working of EC-OC analyzer. A picture of the OC-EC analyser is shown on the right (Picture from: https://www.sunlab.com).*

At the end of each analysis, a calibration is performed by introducing a known amount of methane gas into the oven and calculating the results analytically. Standardisation of the instrument is carried out by using a known amount of sucrose solution and confirming that the instrument detected within an error of 5% of the expected sucrose concentration. The lower limit of detection is ~0.2 µg cm^{-3} for both OC and EC in this method. Since the used filter punch area was 2.011 cm^2, the minimum detectable limit came out to be 0.402 µg cm^{-3}. However, considering other possible instrumental noise, the minimum quantifiable limit is taken to be 0.5 µg cm^{-3}. This limit matches the value prescribed by the manufacturer. The number of valid samples is 10,984, excluding some losses due to technical issues and adverse weather.

2.2.3. CRDS Trace Gas Analyzer

CO observations are made using an instrument (Picarro G2401) based on the cavity ring-down spectroscopy (CRDS) technique. The operation of the instrument is as follows. The laser beam enters a three-mirror cavity filled with gas molecules under test (Figure 2.5) and fills it with circulating laser light. The leakage of this light through one of the mirrors is measured using a photodetector. The laser is turned off once the photodetector signal reaches a threshold level. The light already within the cavity steadily leaks out and decays to zero exponentially and the amount of time it takes for the decay or ring down to happen is determined solely by the reflectivity of the mirrors (for an empty cavity). The

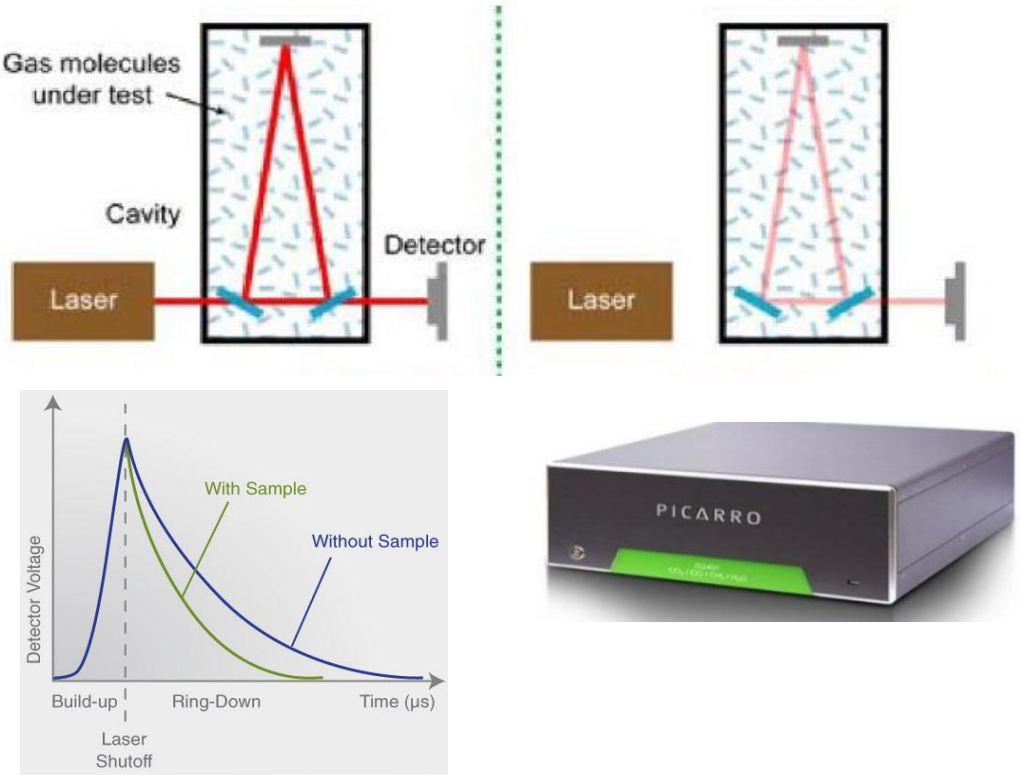

Figure 2.5 *A schematic showing the working of Picarro trace gas analyzer. A picture of the Picarro trace gas analyser is also shown (Extracted from: https://www.picarro-.com/products/g2401_gas_concentration_analyzer).*

introduction of an absorbing gas accelerates the ring down time compared to a cavity alone. The ring down time of the cavity with and without absorption due to the gas species is then measured and compared to provide the final concentration data which is particularly robust being independent of intra-cavity losses and laser intensity fluctuations. This scheme of comparing the ring down times is achieved not by introducing or removing the gas from the cavity but by tuning the laser to several

wavelengths across the gas's spectra and a mathematical fit to the shape of that absorption line is then used to calculate the gas concentration.

Since the effective path length inside the cavity becomes very large (many kilometres), the sensitivity of this system is higher than the conventional non-dispersive infrared or Fourier transform infrared spectroscopy techniques (Bitter et al., 2005). It can measure gases in parts per billion with high accuracy and with very fast response (over a time scale of seconds). More details about the calibration and instrument can be found in Chandra et al., (2016). Horiba APMA 370 trace gas analyzer (Kato, 2006) also operated at the site during 2014-2015. So, a regression between Picarro and Horiba was used to get CO from Horiba wherever CO from Picarro was not available. For consistency and noise reduction, the data collected at every second interval was averaged first to 1 minute after 3 sigma filtrations. It was then averaged over to ten minutes and finally, the hourly averaged concentrations were used in the final analysis.

Figure 2.6 schematically shows the working of a python-based pipeline developed to analyse the raw data from the instruments as mentioned earlier

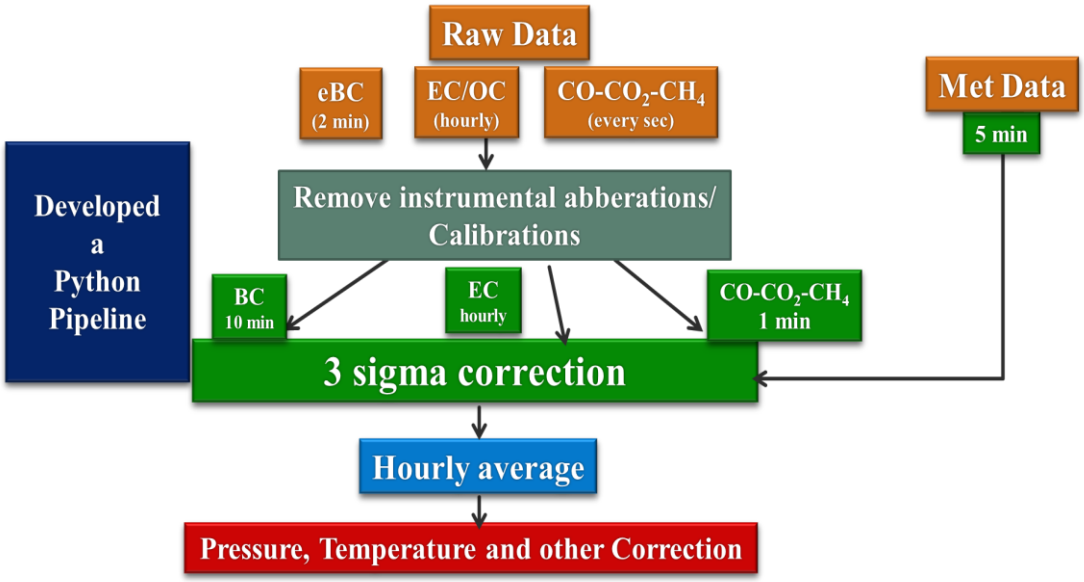

Figure 2.6 *Schematic showing the working of a python pipeline developed to analyse the raw data from various instruments.*

2.3 Satellite Data

2.3.1. CALIPSO

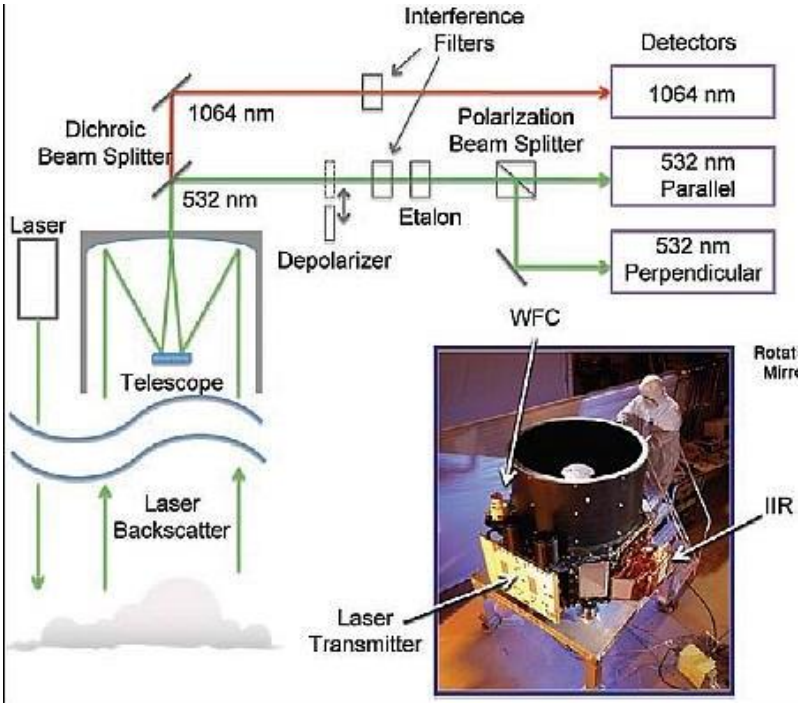

Figure 2.7 *Block diagram and image of CALIPSO payload that consists of CALIOP lidar and two passive sensors (Extracted from: https://earth.esa.int/web/eoportal/satellite-missions/c-missions/calipso).*

In this study, we have utilised the aerosol vertical profile obtained for a period from 2006 to 2017 over the $1^{o}x1^{o}$ region around the site from the level 2 version 4 profile products (5 km horizontal resolution) of "Cloud-Aerosol Lidar with Orthogonal Polarisation" or CALIOP which is aboard the "Cloud-Aerosol Lidar and Infrared Pathfinder Satellite Observations" or (CALIPSO) (Winker et al., 2009). CALIOP (Figure 2.7) transmits two linearly polarised laser pulses at 532 nm and 1,064 nm and measures the backscattered energy through a receiver for the backscattered signal at 1,064 nm and orthogonal polarizations of the backscattered signal at 532 nm. To analyse this data, first, the atmospheric features are detected by a selective, iterated boundary location algorithm. Second, the atmospheric features are identified by a Scene Classifying Algorithm, then backscatter and extinction coefficient of those features are retrieved using a Hybrid Extinction Retrieval Algorithm (Winker et al., 2009). This data is further screened by a rigorous screening technique described by Winker et al. (2013) and the range of various quality flags used currently is described as under. Atmospheric volume description

(AVD) flag is used to identify and filter the aerosol pixels. AVD range bins of 'clean air' - 1 and 'aerosol' - 3 are included. Cloud-Aerosol Discrimination (CAD) values as provided by Liu et al., (2009) are used to screen out cloudy profiles. CAD score ranging between 70 to 101 is used to filter the cloud-free pixels as they signify high confidence (Liu et al., 2009). Only the extinction quality control flag of values 0 and 1 signifying extinction retrievals of high confidence are included. Uncertainty flags with values > 99.9 are excluded in the study. Additionally, data, where laser energy is < 0.08, is rejected. Further details of the uncertainty and its propagation in various aerosol parameters can be found in Young et al., (2013). The aerosol optical depth of the integrated profile around the $1^{o}x1^{o}$ region of the site is also used for analysing the trend over the period from 2006 to 2017.

2.3.2. Measurement of Pollution in the Troposphere (MOPITT)

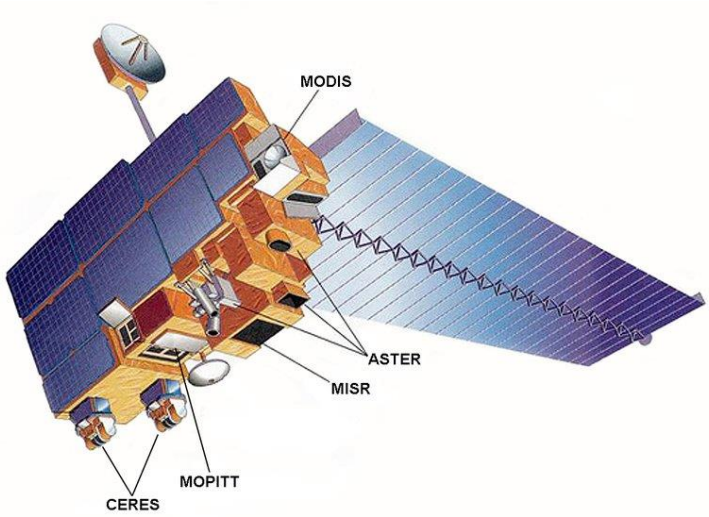

Figure 2.8 *MOPITT and other instruments on board Terra are shown (Extracted from: https://mopitt.physics.utoronto.ca/).*

MOPITT is an eight-channel radiometer onboard the Terra spacecraft (Figure 2.8) which uses gas correlation spectroscopy to provide vertical distribution of CO. It achieves global coverage in about 3 days with a swath width of 600 km (Drummond, 1992). In the present study, we have utilised MOPITT version 9 Level 2 retrieval products from 2014

to 2017 having both thermal and near-infrared spectral band information (MOP02J) as it provides more accurate information in the lower troposphere (Deeter et al., 2014). Further, only the daytime retrievals are used as they provide better thermal contrast conditions compared to night time (Deeter et al., 2017). Version 9 includes revisions to the cloud detection algorithm and an improved calibration strategy for the Near-Infrared channels compared to its predecessors (Deeter et al. 2021). MOPITT CO data thus filtered is then compared against the observed CO which is first smoothed with a priori profiles and averaging kernel matrix following Deeter et al., 2014 to ensure direct comparability between the satellite retrievals and observations.

2.3.3 Moderate Resolution Imaging Spectroradiometer (MODIS)

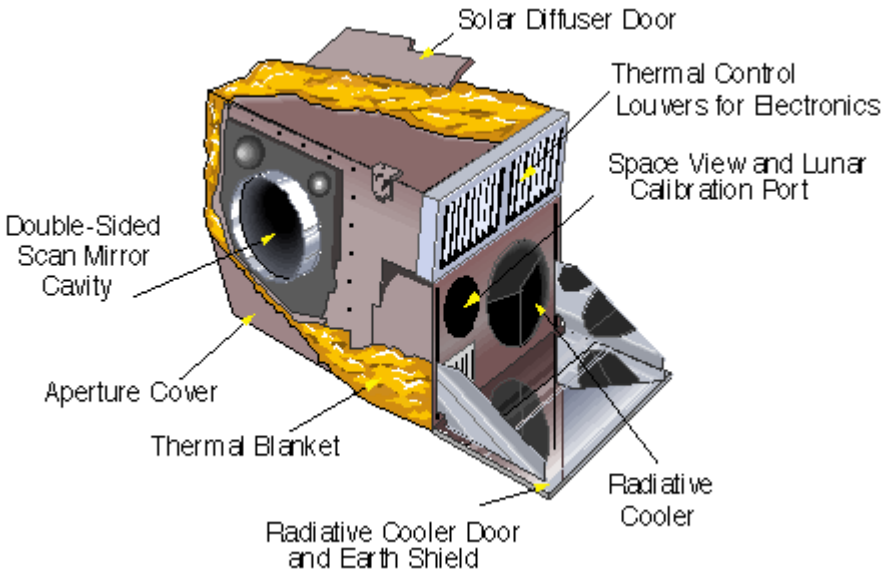

Figure 2.9 *External view of MODIS along with its sub-systems. (Extracted from: https://commons.wikimedia.org/wiki/File:MODIS_sensor.png).*

Fire Counts: MODIS is an instrument (Figure 2.9) onboard two satellites of the earth observing system i.e., Terra and Aqua. The MODIS collection 6 versions 6.2 (combined Aqua and Terra) fire product is used in the study to gain information about the geographic location of fire. Collection 6 uses an updated algorithm that addresses the former limitations such as the occurrence of false alarms due to small forest clearings and the omission of large fires obscured by thick smoke (Giglio et al., 2016). The MODIS fire

detection algorithm uses the 4, 11, and 12-μm brightness temperatures derived from the corresponding 1-km MODIS channel and more details about the algorithm and its validation are available in Giglio et al., 2016. In the study, we have used fires in the Northern Indian region i.e., for the latitude range of 24 - 35^{o} N and longitude range of 70 - 89^{o} E. Additionally only the night time data with confidence levels greater than 80% were preferred because of the greater sensitivity of the satellite sensors as compared to that of daytime.

Aerosol Optical Depth (AOD): We have assessed the trend in aerosol optical depth over the region using daily level 3 MODIS Collection 6.1 data over a 1° × 1° region around the site from 2007 to 2017. A combined dark target (for dark surfaces) and deep blue (for bright surfaces) product is used in the analysis as it is recommended for long-term studies over land (Wei et al., 2019). The combined product benefits from the strengths of individual dark target and deep blue algorithms (Levy et al., 2013) and remains unchanged in collection 6. While AOD from MODIS aboard both AQUA and TERRA show similar performances in terms of trend, Aqua AOD is found to be more accurate hence trends from both AQUA and TERRA are shown (Wei et al., 2019). 2.4. Models Used in the Study

2.4 Models

2.4.1. HYSPLIT Back Air Trajectories

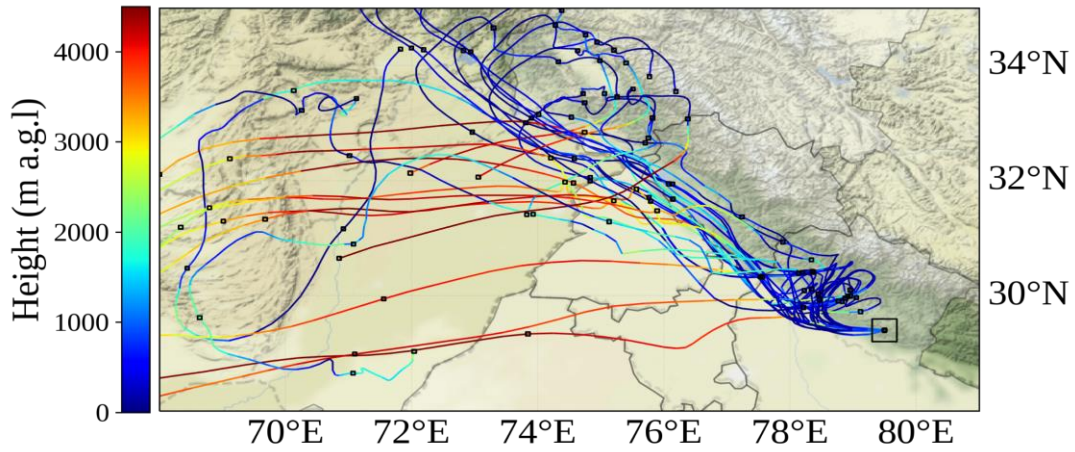

Figure 2.10 *5-day backward, 27-member ensemble, trajectories reaching the observation site (square box) on 22 April. The black squares within trajectories are marked at interval of 24 hours. The colour bar on the left shows the height of the trajectory.*

The influences of air masses reaching a particular observation site mainly depend on the origin and path of the air masses. To assess the influences of the different air masses, 5-particle, and 5 days backwards isentropic air trajectories from HYSPLIT (Hybrid Single-Particle Lagrangian Integrated Trajectory model) (Draxler and Rolph, 2003) have been calculated. Five particle backward air trajectories (four corners and one centre) were calculated around a 1^o x 1^o grid box centred at the observation site (29.4^o N, 79.5^o E). It has been shown that the accuracy of the determined trajectories is generally ascertained from the spatial and temporal resolution of the meteorological data used in the simulation (Naja et al., 2003). We have used 6-hourly archived GDAS meteorology data at a resolution of 0.5^o x 0.5^o in the present backward air trajectory simulations. Here, backward air trajectories were simulated to study the influence of air masses during the biomass-burning period. Extensive analysis of backward air trajectories has shown that most air masses arrive at Nainital from the northwest in winter (January) and are of distant origin. On the other hand, the air masses move faster and come mainly from northern India in spring. Influences of southwest air masses are seen in the summer monsoon period. After the withdrawal of the southwest monsoon, contributions of air masses from the northwest again dominate in October and November.

2.4.1.1 Concentration Weighted Trajectories

To determine the relative contribution of possible source regions of OC and EC at the observation site, concentration weighted trajectory (CWT) analysis (Wang et al., 2009) is performed. For this analysis, the whole area is divided into grid cells of 0.5^o x 0.5^o and each of these cells is assigned a residence time (based on endpoints) weighted observed concentration. We have used 5-particles and 5 days backward trajectories (as mentioned in the previous section 2.3) in this analysis. This analysis is performed for the concentrations of OC, EC, and OC/EC ratio. The method provides the concentration field as a function of the measured OC, EC or OC/EC and the residence time of a trajectory arriving at our site. This can be expressed as -

$$C_{ij} = \frac{1}{\sum_{l=1}^{M} \tau_{ijl}} \sum_{l=1}^{M} c_l \tau_{ijl} \qquad (2.2)$$

where C_{ij} is the average weighted concentration in the ij^{th} cell. l is the index of the trajectory, c_l is the concentration observed on the arrival of trajectory l and τ_{ijl} is the time spent in the ij^{th} cell by trajectory l. M is the total number of trajectories.

2.4.2 OPAC and SBDART Simulations for Radiative Forcing Estimation

In the present study, annually-averaged direct aerosol radiative forcing was estimated using a plane-parallel radiative transfer model known as the Santa Barbara Discrete Ordinate Radiative Transfer model (SBDART; Ricchiazzi et al., 1998). The steps in estimating the radiative forcing are shown in Figure 2.11 and the same is described here. Some aerosol optical properties i.e., the aerosol optical depth (AOD), the single scattering albedo, the asymmetry parameter and the Ångström exponent due to a mixture of aerosols were used as input to SBDART. These spectral optical properties were derived using the OPAC (Hess et al., 1998). About the composition of aerosols at the site, the aerosol mixture in OPAC was selected to be composed of soot, water-soluble, insoluble, mineral (nuclei and coarse mode) at an RH of 50%. Annual EC concentration

measured using an OC-EC analyzer was fixed and used as a representation of soot. The number density of all other aerosol components in OPAC was adjusted to match the climatological (2005-2012) mean of AOD and Ångström exponent at the site within 3% of the OPAC estimated values of both parameters. The model is constrained with EC and AOD measurements to ensure that the initial assumption of the model do not significantly impact the ARF estimation (Srivastava et al., 2012a). This methodology has been validated and widely incorporated in former studies (Kumar et al., 2011, Shaik et al., 2017). It is known to have an accuracy of ±2 Wm^{-2} (Satheesh and Srinivasan, 2006).

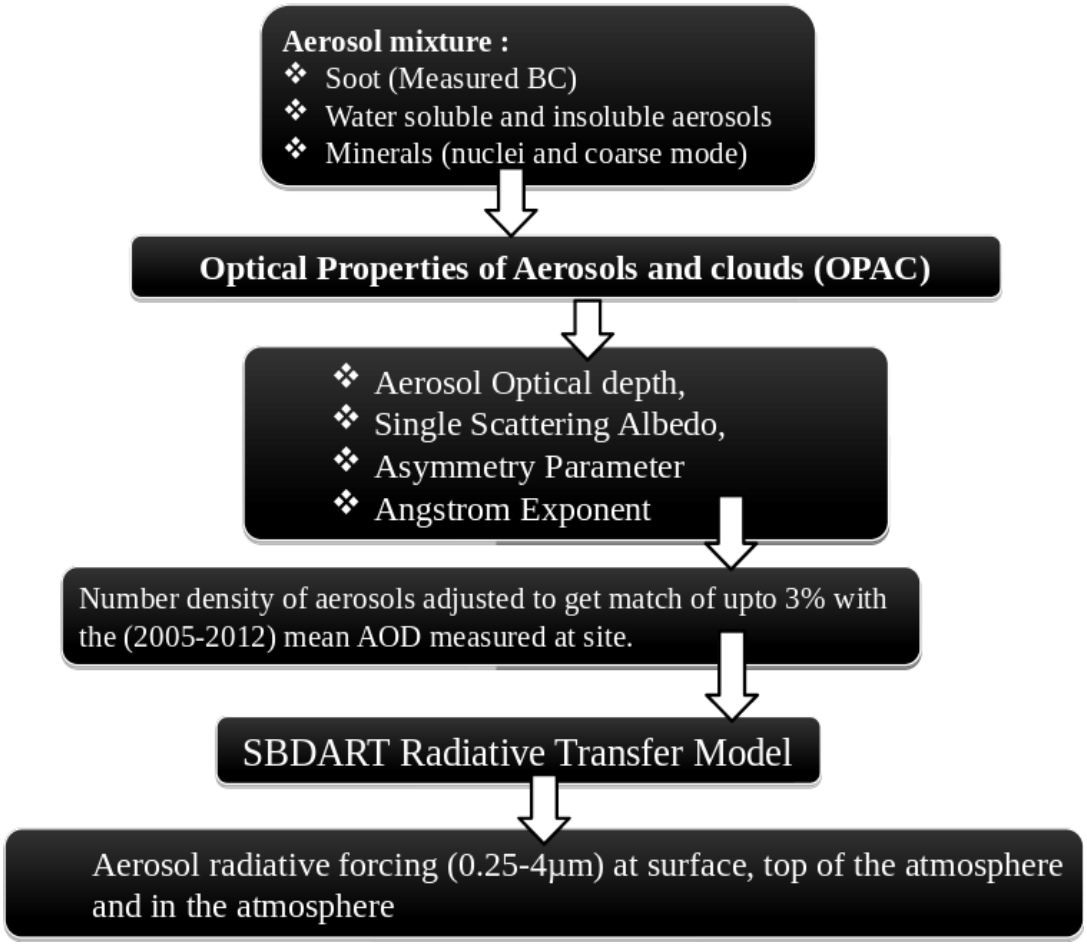

Figure 2.11 *A flow chart showing the steps in retrieving the radiative forcing due to carbonaceous aerosols.*

SBDART was run with the former inputs of spectral optical properties from OPAC, a tropical atmospheric profile and spectral surface albedo set as a mixture of sand (20%) and vegetation (80%) following Kumar et al., (2011). The output of SBDART was obtained for fluxes in the shortwave region (0.25-4µm) with and without aerosols. The

ARF at any level was then described as the difference in the net change in flux (down-up) at any level with and without aerosols. These runs were made at hourly intervals every day for a whole year to result in two cases: (1) forenoon (06 - 09 hour) averaged ARF and (2) afternoon (14 - 17 hours) averaged ARF.

2.4.3. MERRA- 2

The "Modern-Era Retrospective analysis for Research and Applications", Version 2 (MERRA-2) is an improved version of the original reanalysis product MERRA (Gelaro et al., 2017). MERRA-2 incorporates data from various satellite-based observations and emission datasets. It provides reanalysis data from 1980 to the present at a resolution of $0.5° \times 0.625°$. It contains 72 hybrid-eta levels starting from the surface to 0.01 hPa using version 5.12.4 of the "Goddard Earth Observing System Model" (GEOS5) atmospheric data assimilation system (Rienecker et al., 2008). In this work, we have utilised MERRA-2 reanalysis surface CO data from Jan 2014–Dec 2017 accessed through the NASA "Goddard Earth Sciences Data Information Services Center" (GES DISC).

2.4.4. WRF-Chem

To simulate the temporal and spatial distribution of carbon monoxide (CO) and black carbon (BC), a regional chemistry transport model "Weather Research and Forecasting model coupled with Chemistry" (WRF-Chem) version 3.9.1 is used. The model domain spans the entire India with 350 grid points in the east-west and 380 grid points in a north-south direction at 10 km spatial resolution. The model has 51 vertical levels from the surface up to 10 hPa with 7 levels located within 1 km from the surface. The different parameterization schemes used to represent physical and chemical processes in the model are listed in Table 2.1. The gas-phase chemistry used for the model setup is Model for Ozone and Related Chemical Tracers, version 4 (MOZART-4). The aerosol processes are represented by a simple aerosol scheme called Goddard Chemistry Aerosol Radiation and Transport (GOCART), which include five different aerosol species, viz., black carbon (BC), organic carbon (OC), and sulphate aerosols in bulk mode and size-resolved dust and sea salt particles. These aerosols are internally mixed and BC particles are present in hydrophilic and hydrophobic modes. Total BC mass is defined as the sum of

BC in the above two modes. The input BC emissions are assumed to occur in hydrophobic mode and with an e-folding lifetime of 2.5 days, it could be converted to hydrophilic mode. These BC particles are removed from the atmosphere through wet and dry deposition. Further details of the model setup are described in Bhardwaj et al., (2021).

Table 2.1 *List of parameterization schemes used in the WRF-Chem setup.*

Atmospheric Process	**Parameterization**
Cloud Microphysics	Thompson Microphysics
Long-wave Radiation	Rapid Radiative Transfer Model-G
Short-wave Radiation	Rapid Radiative Transfer Model-G
Surface Layer	Monin-Obukhov (Janjic Eta) scheme
Land Surface Model	Unified Noah Land-surface model
Planetary Boundary Layer	MYNN2
Cumulus	Grell-Freitas Ensemble Scheme
Photolysis	TUV – revised
Dry Deposition	Wesely Scheme

To track the contribution of different sources of tropospheric CO, four artificial species "tracers" are added to the model configuration. These tracers undergo the same atmospheric processes as standard CO molecules. The four tracers represent contributions from anthropogenic emissions (CO_ANTH), biomass burning emissions (CO_BB), photochemical production from non-methane hydrocarbon emissions within the domain (CO_CHEM) and inflow of CO from lateral boundaries (CO_BDRY) which include contributions from all other CO sources outside of the domain. The model simulations started on 1st Dec 2014 UTC and ended on Jan 1st, 2016. The first month (Dec 2014) of model output is not used in this analysis and it is discarded as model spin up. The model output is archived at every hour and time series of one year is extracted over desired spatial and vertical regions for detailed analysis.

Chapter 3

Characteristics of OC and EC in PM 2.5: Radiative Forcing Estimates and Role of Meteorology and Biomass Burning

---

This chapter presents the results from the first-ever four-year continuous online observations of OC and EC in the Himalayan region. It begins by describing the advantages of such online observations as opposed to offline observations especially in revealing the diurnal variations. It then sequentially unravels the temporal variation of these aerosols while comparing these with other sites and studies. Then it evaluates the role of meteorology, transport and biomass burning in the observed variations. Finally, it shows the importance of including the radiative forcing at the diurnal scale in such sites.

3.1. Introduction

In the desire of economic growth, large dependence on carbon-based fuel has led to a substantial increase in atmospheric carbonaceous aerosols on a regional scale, particularly in the developing world, as shown by modelling works (e.g., Adhikary et al., 2007) and data from ground-based networks (e.g., Krishna Moorthy et al., 2013). The presence of these carbonaceous aerosols critically affects several atmospheric processes and has deteriorating impacts on human health (Ramanathan and Carmichael., 2008; Kennedy, 2007). The study of carbonaceous aerosols is particularly important due to their direct impact on radiation budget (Satheesh, 2002), their influence on glacier retreat (Lau et al., 2010) and their indirect effect in altering cloud properties (Ackerman et al., 2000; Tao et al., 2007), and thus acting as short-term climate forcers. However, assessment of the overall impact of these aerosols is a challenging task because of the large spatial and temporal variations (Beegum et al., 2009; Kaskaoutis et al., 2009; Babu et al., 2011; Qin and Xie, 2012), types of mixing states (Chandra et al., 2004; Shiraiwa et al., 2007; Kaskaoutis et al., 2010) and dynamic atmospheric processes (Satheesh et al., 2008; Kaskaoutis et al., 2017).

Carbonaceous aerosols are mainly composed of organic carbon (OC) and elemental carbon (EC). Though in general emitted together, OC and EC, differ greatly in their optical and chemical properties and, hence, have different impacts on the earth's atmosphere. OC comprises organic compounds (aliphatic, aromatic compounds and acids) and is hygroscopic thereby acting as cloud condensation nuclei (Safai et al., 2014 and references therein). EC is hydrophobic (Petzold et al., 2013). OC scatters solar radiation, while EC is an efficient absorber. Both are generally generated from combustion at low temperatures with low-oxygen availability. OC, however, can also be formed by secondary origin. Despite these important properties and impacts, there are limited observations of carbonaceous aerosols in South Asia. Over India, few sample-based offline measurements of OC and EC are available (Rastogi et al., 2009; Ram et al., 2010; Satsangi et al., 2012). These observations are mostly campaign-based and vary in terms of the sampling interval. Offline analyses of samples have a risk of contamination due to delayed analyses. Offline measurements are also known to suffer from positive and negative artefacts because of the presence of volatile species. These volatile species may change during collection, transportation, storage and analysis that follows in offline measurements (Chow, 1995; Cheng et al., 2010). The datasets generated during offline sampling are not large enough to enable source/receptor modelling or human exposure studies for shorter periods of time i.e., in days or weeks (Wexler and Johnston, 2008; Morishita et al., 2011). Also, the very nature of offline measurements integrates the whole diurnal variation of the concentrations. This slow response and low time resolution of offline measurements bars the assessment of connections between variations of aerosols and meteorological parameters during a given day (Witting et al., 2004; Timonen et al., 2010). This further also limit assessing diurnal variations of important parameters such as radiative forcing, which is crucial in high-altitude sites (Reddy et al., 2015). Therefore, the online measurements of OC and EC which provide higher time resolution, are relatively cheaper, require lesser interventions, suffer lesser contamination and have lower artefacts because of faster analysis (Malaguti et al., 2015) are more suitable for high-altitude locations.

Despite the scientific attention on carbonaceous aerosols, systematic and high-resolution online observations are still very limited in South Asia. Such observations are non-existent in the Himalayan region, which has a complex topography and lies close to

polluted regions like the Indo-Gangetic Plain (IGP) (Joshi et al., 2016). In this work, we present the first long term online observations of OC and EC from a high-altitude location in the Central Himalayas (ARIES, Nainital) during the period of 2014-2017. Observational techniques for observations of OC and EC along with the description of the site and meteorology are already discussed in Chapter 2. Here, firstly the temporal variations of OC and EC on diurnal and seasonal scales are presented and compared with those from other sites and offline measurements. The influence of long-range transport and the boundary layer dynamics on these species are further analysed. Later, the role of biomass-burning, the effect of meteorological variations, the diurnal nature of radiative forcing and the formation of secondary organics is discussed. This work thus fills the large gap in our current understanding of carbonaceous aerosols, particularly organic carbon in the high-altitude sites of the Himalayas.

3.2. Results and Discussions

3.2.1. Diurnal Variations

Average diurnal variations in OC and EC during the study period (2014-2017) with segregation in four seasons namely winter (Dec, Jan, Feb), spring (Mar, Apr, May), summer-monsoon (Jun, Jul, Aug) and autumn (Sep, Oct, Nov) are shown in Figures 3.1 and 3.2, respectively. Table 3.1 summarizes the monthly and seasonal variations in OC, EC and OC/EC ratios. The monthly average OC concentration varies from 2.9 μg m^{-3} to 12.4 μg m^{-3} and the EC concentration varies from 1.1 μg m^{-3} to 3.2 μg m^{-3}. Generally, higher daytime concentrations are observed in almost all months except the ones affected by the monsoon. The diurnal variations in OC and EC are most prominent during winter with a maximum diurnal amplitude of 5.5 μg m^{-3} and 1.8 μg m^{-3}, respectively (Table 3.1). Slightly lower diurnal amplitude is observed in spring. The diurnal amplitude has been at its lowest in the summer monsoon period.

Table 3.1 *Statistical summary of monthly and seasonal variations in EC, OC and OC/EC ratio for the period of 2014-2017 Nainital.*

Month	Count	OC (μg m^{-3})					EC (μg m^{-3})					OC/EC
		avg±std	Diu Amp*	min	max	%var$	avg±std	Diu Amp*	Min	max	%var$	avg
Jan	831	9.7±6.0	5.7	1.2	39.5	62	2.2±1.3	2.2	0.5	8.6	59	4.4
Feb	1006	9.2±5.3	6.1	1	26.4	58	3.2±1.9	2.1	0.8	11.3	59	2.9
Mar	970	8.4±5.6	7.5	0.9	32.7	67	3.1±1.9	2.2	0.5	9.6	61	2.7
Apr	982	12.4±9.7	8.3	1	56.7	78	3.0±1.7	1.6	0.7	11.3	57	4.1
May	1392	10.4±7.0	4.8	1.5	65.8	67	2.7±1.5	0.7	0.5	12	56	3.9
Jun	1834	8.2±3.8	2.4	1	40.3	46	2.3±1.1	0.5	0.5	6.7	48	3.6
Jul	495	2.9±1.3	1.3	0.7	11.1	45	1.1±0.4	0.5	0.5	3.2	36	2.6
Aug	1103	3.3±1.6	1.4	0.7	10.5	48	1.2±0.5	0.4	0.5	3.7	42	2.8
Sep	724	4.9±1.9	1.4	1	11.3	39	1.8±0.6	0.4	0.6	4.1	33	2.7
Oct	540	6.1±4.1	6.5	0.9	23.2	67	2.0±1.0	1.6	0.5	5.1	50	3.1
Nov	558	9.4±5.3	6.6	1.8	45.5	56	2.6±1.3	1.6	0.5	8.1	50	3.6
Dec	549	9.2±4.8	4.8	1.4	26	52	2.6±1.3	1.4	0.5	6.2	50	3.5
DJF	2386	9.4±5.5	5.5	1	39.5	59	2.7±1.7	1.8	0.5	11.3	63	3.5
MAM	3344	10.4±7.7	5.4	0.9	65.8	74	2.9±1.7	1.4	0.5	12	59	3.6
JJA	3432	5.9±3.9	1.2	0.7	40.3	66	1.8±1.1	0.3	0.5	6.7	61	3.3
SON	1822	6.6±4.3	4.3	0.9	45.5	65	2.1±1.0	0.9	0.5	8.1	48	3.1
Annual	10984	8.1±6	3.1	0.7	65.8	74	2.4±1.5	1.0	0.5	12.0	63	3.4

* *Diu Amp is the diurnal amplitude, which has been calculated as the difference of the maximum and minimum values of the diurnal means in each month for 2014-2017.*

$ *%Var is the %Variability, which is (standard deviation × 100)/ average.*

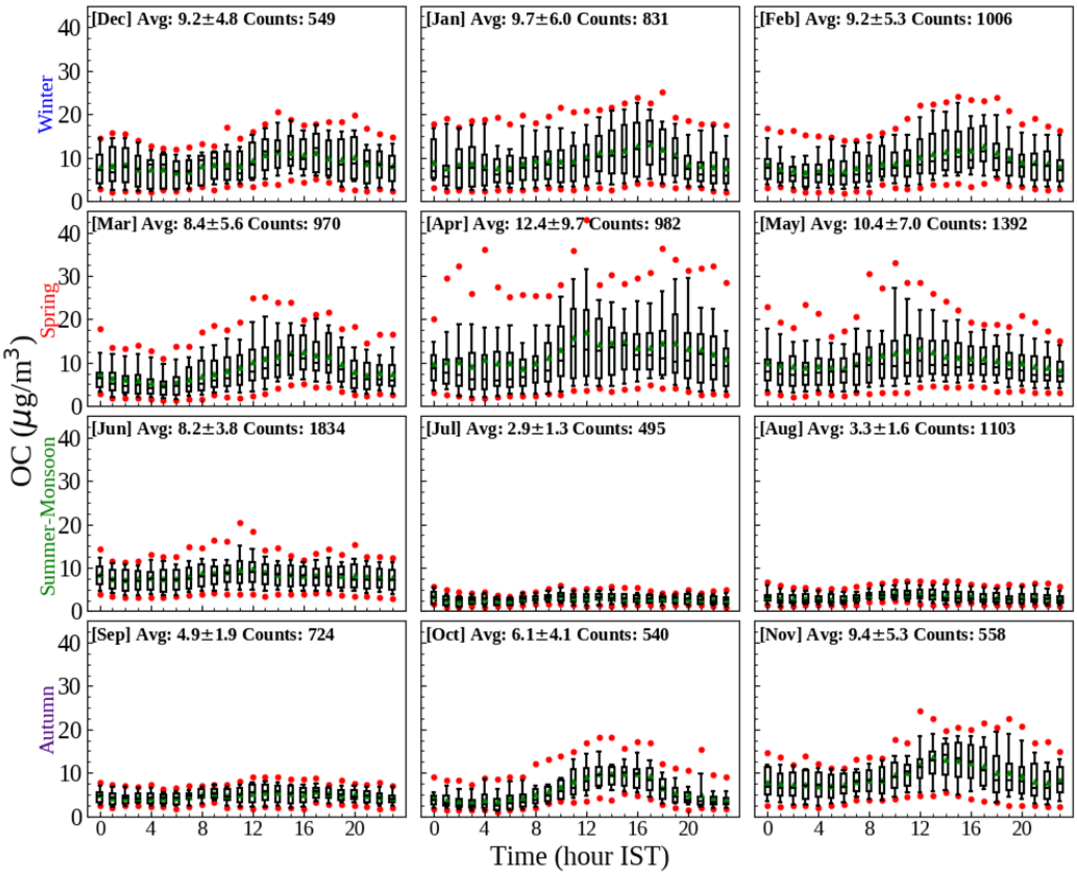

Figure 3.1 *Boxplot showing diurnal variations in hourly averaged OC concentration during 2014-2017. In boxplots, the lower and upper edges of the boxes represent the 25th and 75th percentiles, respectively. The whiskers below and above are the 10th and 90th percentiles and the outliers in the boxplot show the 5th and 95th percentiles. The green triangle inside the box represents the mean and the solid lines inside the box represent the median. The monthly mean, standard deviation and number of observation counts are also mentioned for each month.*

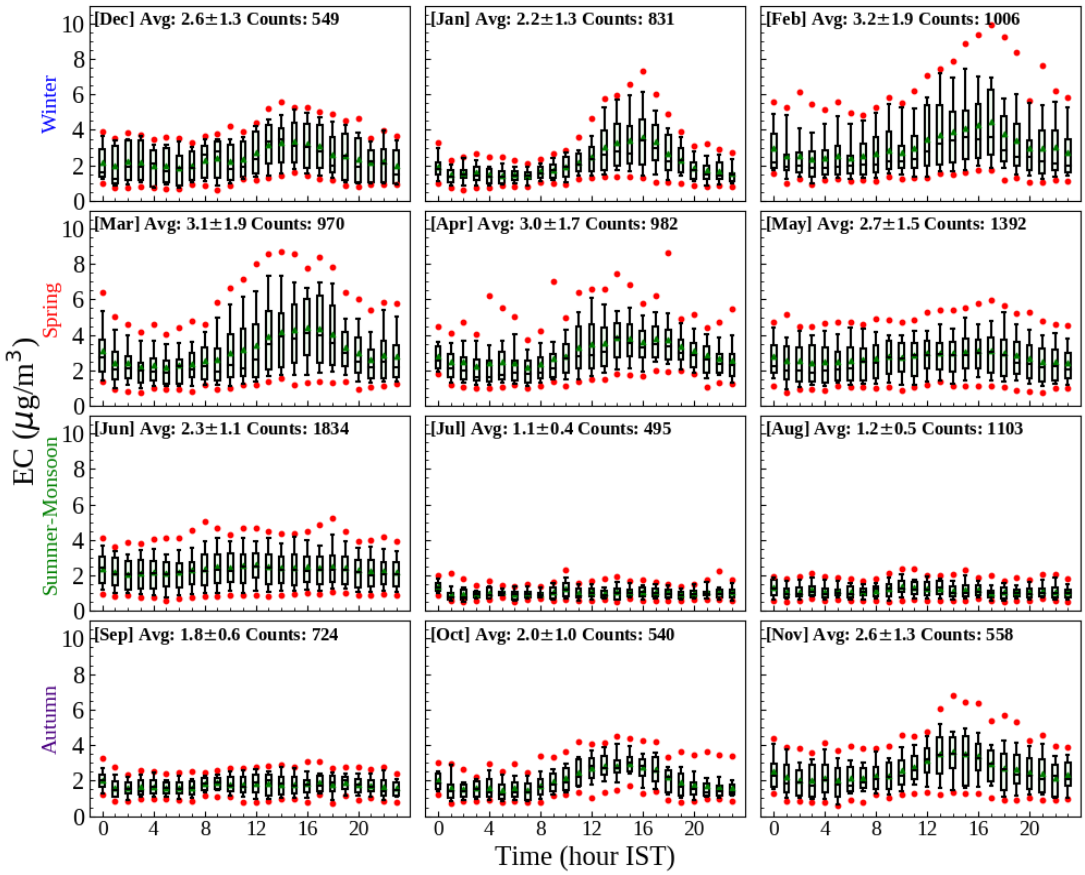

Figure 3.2 *Same as figure 3.1 but for EC.*

The higher daytime concentrations of OC and EC are mainly attributed to convective heating and the boundary-layer dynamics which bring the polluted air from the lower valley region to the observational site during daytime (Naja et al., 2014). This process is intense and occurs for a longer duration in spring when solar heating is highest (Figure 2.2). There is no industry in Nainital; automobiles are the only possible source of emissions. Major sources of pollutant emissions are at lower altitude regions. The absence of a significant diurnal variation in the OC and EC concentrations during July, August and September are due to monsoon rainfall and consequent wet scavenging. In India, available published works about observations of OC and EC exist only at two urban sites in central India i.e., at Delhi (Tiwari et al., 2013; Srivastava et al., 2014) and in west India i.e., at Pune (Safai et al., 2014). Unlike the unimodal distribution in Nainital, both these sites show a bimodal diurnal variation having higher concentrations during the morning period (0800-1000 hours) and late evening period (2000-2300 hours). Both these cities are highly industrialized and dominated by a high traffic density of

automobiles. These morning and night periods coincide with local peak traffic and lower mixing-layer depth. To our knowledge, no published results are showing diurnal variations in OC and EC from a high-altitude site during a year. Therefore, the current work is the first with continuous aerosol observations at a mountain site.

Figure 3.3 shows the average diurnal variations in OC and EC during winter, spring, summer-monsoon and autumn seasons. Seasonal amplitudes are more-or-less similar during spring and winter, but daytime values are somewhat higher during spring. A clear daytime enhancement in OC and EC is also seen during autumn with amplitudes of about 4.3 µg m^{-3} and 0.9 µg m^{-3}, respectively. The summer-monsoon period shows a very small enhancement in OC and EC during the morning with amplitudes of about 1.2 µg m^{-3} and 0.3 µg m^{-3}, respectively. Also, the diurnal peak in spring is broader than the observed during winter, which is mainly due to the longer duration of the day in spring as compared to that in winter. This longer daytime in spring increases the period of higher boundary-layer heights at the site, responsible for bringing the valley pollutants to the site for a longer period on a day.

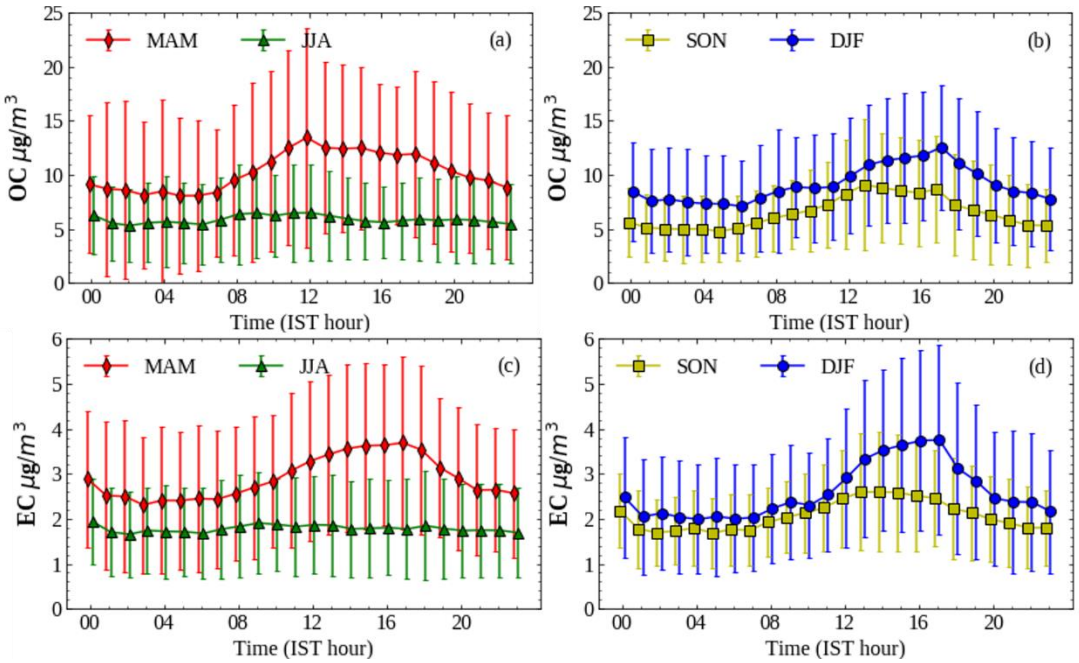

Figure 3.3 *Average diurnal variations in OC and EC concentrations during winter (DJF), spring (MAM), autumn (SON) and summer-monsoon (JJA) at Nainital in 2014-2017 period. The vertical bars denote one standard deviation from the mean.*

3.2.2 Annual Variations

Frequency distributions of OC and EC during winter, spring, summer-monsoon and autumn are shown in Figure 3.4. Broadly, OC shows maximum contribution in the range of 2.5-7.5 µg m^{-3} during all four seasons. EC shows a broad maximum contribution in the range of 0.5-2.5 µg m^{-3}. The highest percentages of low concentrations for both OC (0-5 µg m^{-3}) and EC (0.5-1.5 µg m^{-3}) are from summer-monsoon as expected. This supports the conclusions drawn earlier about the settlement of pollutants during the monsoon resulting in the greatest percentage of decreased concentrations. Greater contribution to a higher range of concentrations in both species (OC: 7-45 µg m^{-3}; EC: 2.5-8 µg m^{-3}) is mainly from the winter and spring seasons. Further, % distributions are significantly skewed towards lower concentrations; this observation leads to the compulsion that the present site remains normally a remote one, with low OC and EC concentrations, while higher ones occur mostly as perturbations caused by the boundary-layer dynamics and transport especially during spring. Possible reasons for the winter high concentrations could be due to local burning for heating; this issue will be discussed in the subsequent Sections.

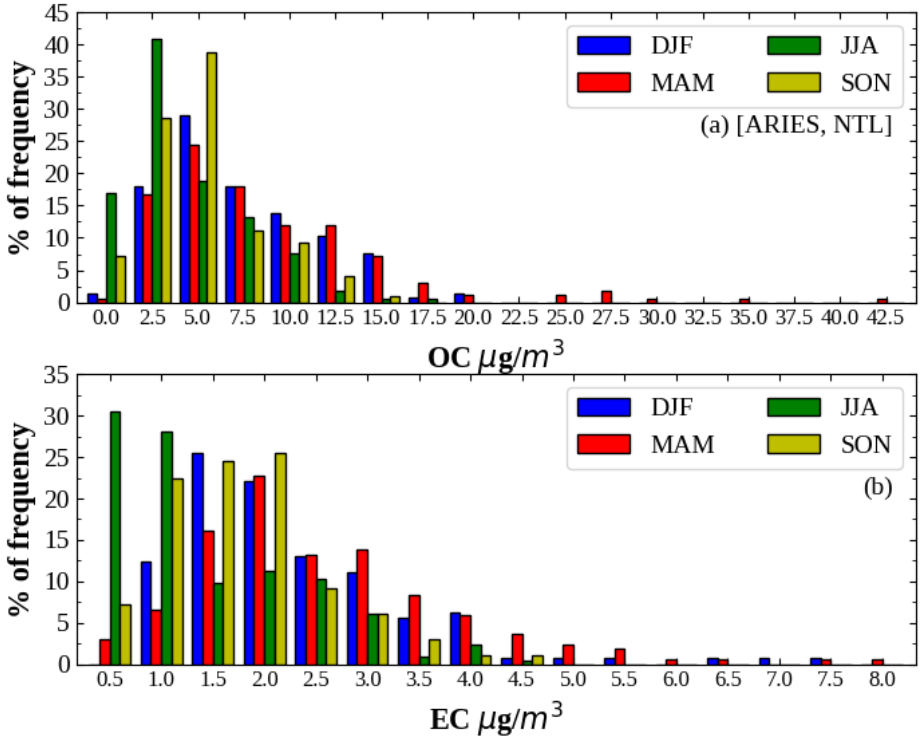

Figure 3.4 *Percentage frequency distribution of OC and EC during winter, spring, summer-monsoon and autumn. The x-axis label of 0.0 represents the OC range 0.0-2.5 µg m^{-3}, 2.5 represents the OC range of 2.5-5.0 µg m^{-3} and so on. In the case of EC, the label of 0 represents a range of 0-0.5 µg m^{-3}, 0.5 represents a range of 0.5-1.0 µg m^{-3} and so on.*

Daily and monthly mean variations in OC and EC are shown in Figure 3.5. The monthly mean OC and EC concentrations are maximum in April-May (10-12 μg m^{-3}) and February-April (about 3 μg m^{-3}), respectively. There is a drastic decrease in OC and EC concentrations in July to average values of 2.9±1.3 μg m^{-3} and 1.1±0.4 μg m^{-3}, respectively, which is almost less than half the values that prevail in other seasons. The percentage variability for each month is also given in Table 3.1. Largest variability in OC and EC is observed during April (78%) and March (61%) respectively, and minimum variability in September for both OC (39%) and EC (33%). Seasonally, OC shows the most variability of 74% in spring followed by summer-monsoon and autumn (66%) while the least variation was observed in winter (59%). On the other hand, EC did not show such prominent seasonal distribution of variability. Although the least variability of 48% was observed in autumn, for the other seasons, variability remained close to 60%. This variability indicates that OC might be dominated by different and variable sources of emissions or chemistry, particularly in the spring season.

EC concentrations remain high from winter to spring while such persistent higher concentrations are not observed in OC. Relatively higher concentrations of OC and EC during spring are possibly a result of greater dilution due to a deeper boundary layer because of higher temperature, solar radiation and wind speed in this season as is evident from Figure 2.2. The role of the boundary layer and biomass burning in this context will be described in Section 3.2.5. The peak in OC value is in April and May could also be an indication of the increased formation of secondary organic carbon, which is favoured by the greater solar flux in these months. This will be discussed further in Section 3.2.6.

OC and EC both show higher concentrations during daytime in their diurnal variations; therefore, their monthly variations in noontime and night time concentrations of OC and EC are also studied to quantify the amount of enhancements. Figure 3.5 shows the noontime (1300-1600 hours) and night time (0100-0400 hours) mean variations in OC and EC. Both noontime and the night time average of OC and EC are lower. Similar values are observed during monsoon affected months i.e., June, July, August and September, leading to show about a unit ratio between them (Table 3.2). Otherwise, the noontime values are prominently higher before and after monsoon periods. Noon to night ratio is more than double for OC during post-monsoon (October and November), while

they are about 1.5 during winter and spring. Similarly, the noon to night ratios of the EC is about 1.7 during post-monsoon, winter and spring. Such a different variation in their noontime to night time ratios suggests a varying process that governs their variability.

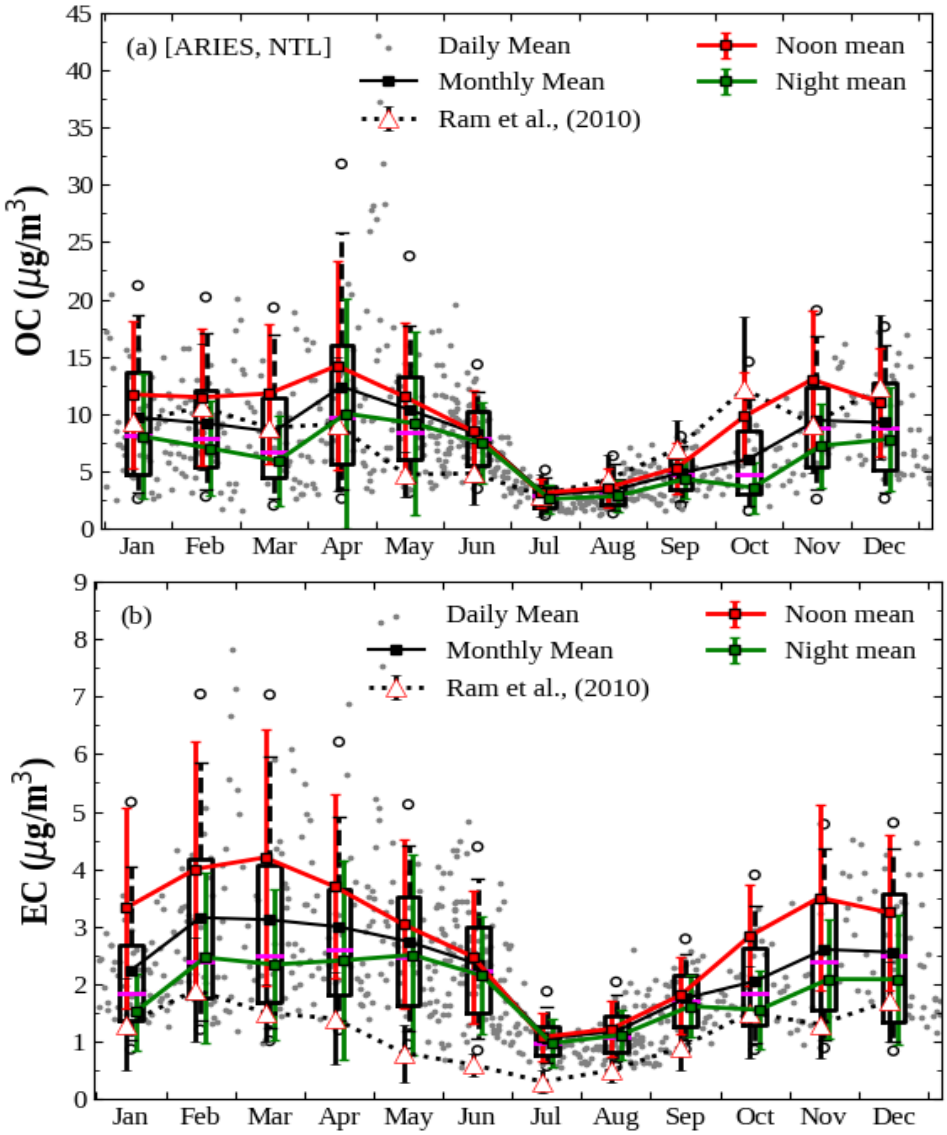

Figure 3.5 *Boxplot showing annual variations in monthly averaged OC and EC concentration during 2014-2017. In boxplots, the lower and upper edges of the boxes represent the 25th and 75th percentiles, respectively. The whiskers below and above are the 10th and 90th percentiles and the blue-circles outliers depict the 5th and 95th percentiles. The black square inside the box represents the mean and the pink solid lines inside the box represent the median. The daily mean data points are shown as grey points. Noon (1300 - 1600 hr IST) and night (0100 - 0400 hr IST) time monthly averages are also shown. The error bars represent one standard deviation from the mean.*

Table 3.2 *Average noontime (1300 - 1600 hours) and night time (0100 - 0400 hours) concentration of OC and EC during winter, spring, monsoon (June, July, August and September) and post-monsoon (October and November) periods. The ratio of noontime to night time is also shown.*

	OC (μg m^{-3})		EC (μg m^{-3})		OC ratio (Noon/Night)	EC ratio (Noon/Night)
	Noon	**Night**	**Noon**	**Night**		
Winter	11.4±5.8	7.5±4.8	3.6±1.9	2.0±1.2	1.52	1.74
Spring	12.4±7.4	8.5±8.0	3.6±1.8	2.4±1.6	1.46	1.46
Monsoon	5.8±3.5	5.3±3.4	1.8±1.0	1.7±0.9	1.08	1.07
Post monsoon	11.4±5.4	5.5±3.6	3.2±1.3	1.8±0.9	2.08	1.73

3.2.3 A Comparison with Other Studies

Offline sample analyses were made for OC and EC using sample collections of total suspended particulate matter (TSPM) at Nainital from February 2005 to July 2008 (Ram et al., 2010) and are also shown in Figure 3.5. The seasonal variations in OC and EC, reported by Ram et al., (2010), are similar to those of the present study but their average concentrations are somewhat at a lower range of standard deviations of present observations, particularly for EC. At first instance, the higher concentrations during 2014-2017 than those of 2005-2008 could indicate the increased emissions levels in the region. But on the other hand, the OC concentrations are found to be somewhat higher at times during 2005-2008 than the mean value during 2014-2017. This could be due to the limitation of the offline analysis that used fewer samples and could not be well representative of the month and region. Additionally, differences in the methods of sampling (online in this work and offline in the previous study), size of the particulates analysed (PM 2.5 in this work and TSPM in Ram et al., 2010), number of samples collected (10,984 in this work and 86 in Ram et al., 2010) and different observational period could also add to the causes of deviation between the two works.

Sample collections of TSPM from another high-altitude site in western India (Mt Abu) and their offline analysis of OC and EC showed average concentrations of 3.7 μg m^{-3} and 0.5 μg m^{-3}, respectively, during March 2005 – February 2006 period (Ram et al., 2008). These values are about half of those observed at Nainital during February 2005 - July

2008 (Ram et al., 2010) and about four times less than the current measurements. It is to be noted that observations are reported to be only from two high-altitude observation sites (Nainital and Mt Abu) in India. Online analysis of EC (10.4 µg m^{-3}) and OC (54.1 µg m^{-3}) during November 2010 - February 2011 showed 4-6 times higher concentrations at Delhi (Tiwari et al., 2013) than that at Nainital. Similarly, OC and EC concentrations are observed to be significantly higher at Pune (Safai et al., 2014) and Kanpur (Ram et al., 2012) than at Nainital in all months. Another highly urbanized city in western India, Ahmedabad (Rastogi et al., 2009) do not show much higher concentrations, which are somewhat comparable in July and August. A high-altitude site (~1300 m a.m.s.l), Bode, Kathmandu in Nepal showed significantly higher concentrations of OC (13-105 µg m^{-3}) and EC (4.8-17 µg m^{-3}) during April 2013 - April 2014 (Wan et al., 2019) than those at Nainital.

3.2.4 Influence of the Boundary-Layer Height and Meteorological Parameters

Figure 3.6 shows the variation of OC, EC with the boundary-layer height during 1130-1630 hours in all seasons. EC and the boundary layer height shows a positive covariation during spring and summer-monsoon, particularly until EC reaches a value of about 4 µg m^{-3}, OC shows a positive covariation until OC obtains a value of about 15 µg m^{-3}. The present site is a cleaner high-altitude site that remains above the boundary layer especially in the nighttime (Shukla et al., 2014; Naja et al., 2016). The upslope winds carry the pollutants from low altitude polluted regions to the site in the daytime. In the night time, the cleaner-upper air flushes down with the reduction in the boundary layer. Therefore, unlike the low-altitude urban sites which show a bimodal variation (Safai et al., 2014) in EC and OC which is inversely related to the boundary-layer height, a high-altitude clean site experiences unimodal pollutant concentrations (Figure 3.3) directly related to PBL. A similar unimodal diurnal variation has also been observed in black carbon in another study (Dumka et al., 2010). For concentrations of EC higher than 4 µg m^{-3}, and OC higher than 15 µg m^{-3}, this variation tends to stabilise but still lies in the higher boundary-layer side. This indicates that very high values of OC and EC might have been due to horizontal transport of air masses once the boundary layer reached a sufficient height. This behaviour is most prominent in spring and declines thereafter. The

boundary layer height remains substantially low after the monsoon season (refer to Figure 2.1) and OC-EC does not show an increase with the boundary-layer height during autumn and winter. Therefore, the boundary-layer process has the least contribution to showing secondary maximum in OC and EC during autumn and winter. This indicates that the higher concentration during this period is not a direct result of the pollutant lift due to the evolution of the boundary layer. This implies that the greater concentrations in autumn and winter are most likely due to local activities like household burning for heating during the cold period when the temperature drops sharply after October and remains low until February over this site.

Figure 3.7 shows the diurnal variation in OC, EC, RH, wind speed, temperature and solar radiation averaged for 2014-2017. OC, temperature, solar radiation and RH have been scaled down by factors of 3, 5, 150, 15, respectively, to fit plots in the same graph. The observation site experiences a dry period from October to May when the average RH is less than 56% and the average rainfall is less than 47 mm. During these months, the diurnal variation in temperature, solar radiation and wind speed tends to have a greater influence on the diurnal variation of OC and EC. Greater temperature and solar radiation during the daytime along with low wind speed lead to increased OC-EC concentrations. On the other hand, lower temperature and no solar radiation during the night time along with high wind speed led to greater ventilation, which consequently results in a reduced concentration of OC and EC. It is also interesting to note that both OC and EC have a near-simultaneous variation in all months, especially in the night time. This co-variation, however, tends to break in the daytime during April and May, when a higher OC concentration precedes the peak in EC concentration. High temperature and moderate humidity as observed in pre-monsoon are known to support secondary organic carbon (SOC) formation through the gas to particle conversion (Sandeep et al., 2020 and references therein). Since EC is only formed by primary sources, this precedence and the higher concentration of OC in April and May is a result of increased SOC formation during this period.

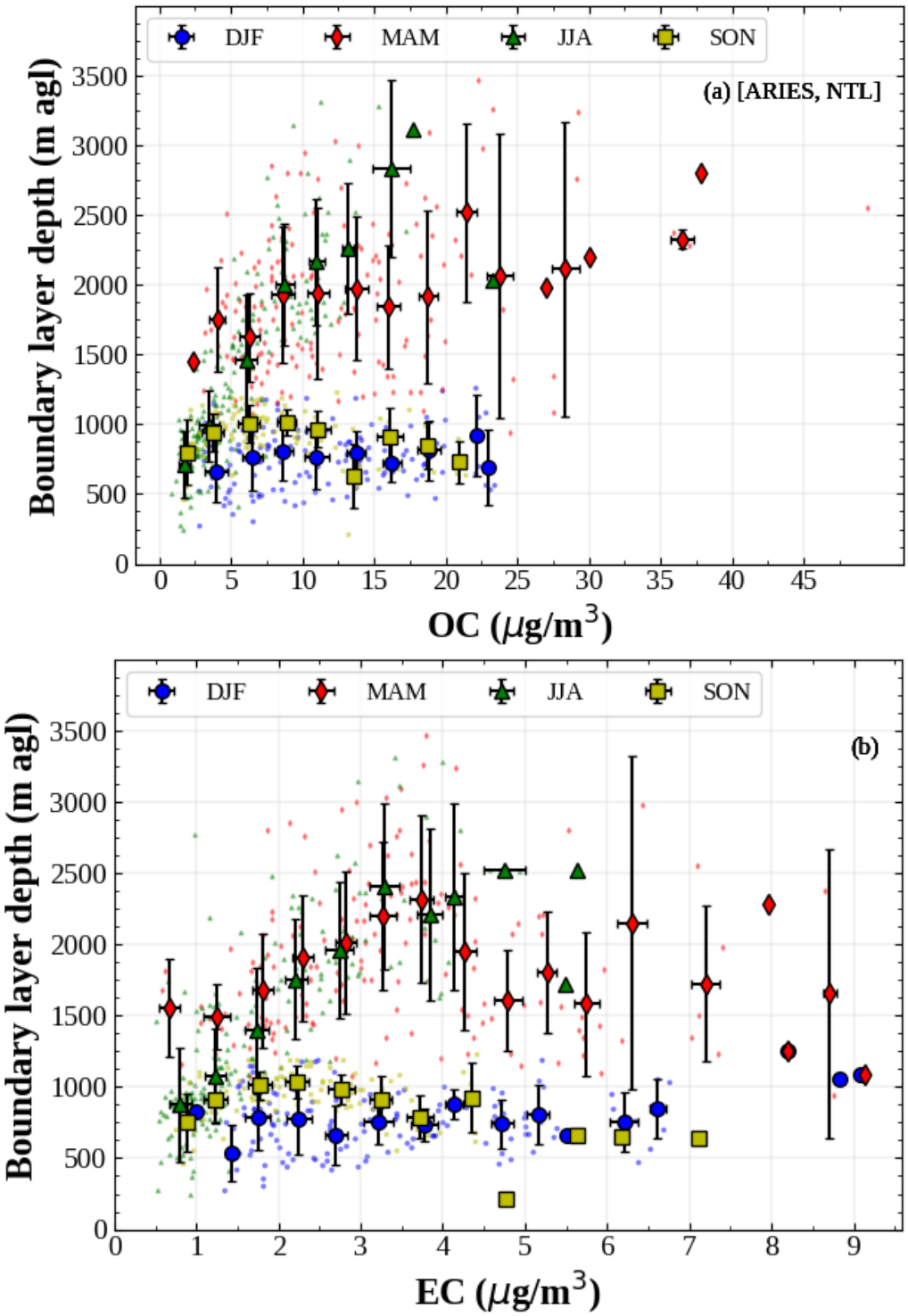

Figure 3.6 *Variation of (a) OC and (b) EC with the boundary-layer height for 1130-1630 hours IST for winter, spring, summer-monsoon, and autumn. Smaller symbols show daily means and binned data are shown in the same colour scheme with a larger size. Spread in x and y axes in the binned data are one standard deviation from the mean.*

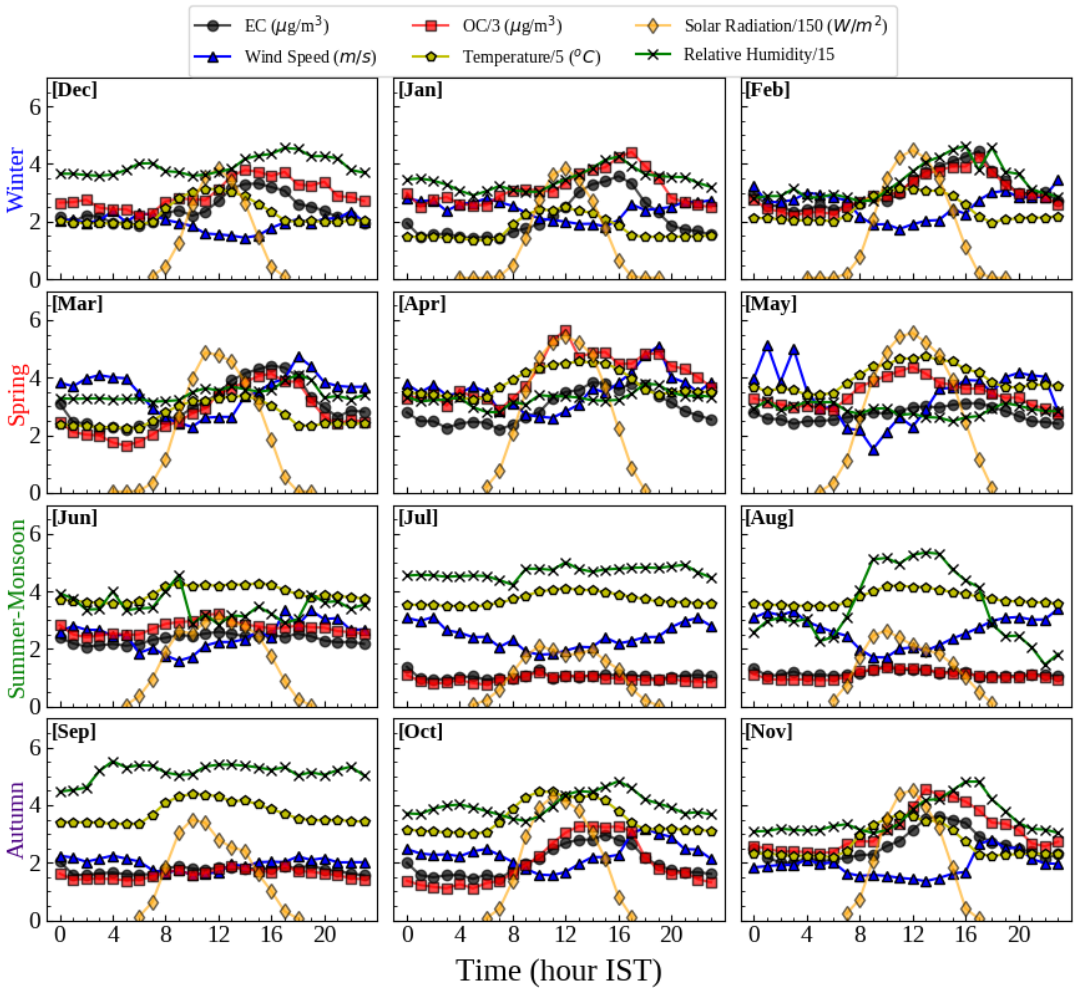

Figure 3.7 *Diurnal variation of OC, EC, RH, wind speed, temperature and solar radiation averaged for all 2014-2017. OC, temperature, solar radiation, and RH have been scaled down by factors of 3, 5, 150, 15, respectively, to fit all plots in the same graph.*

The months from June to September are affected by the summer monsoon and have an average RH of 87% and an average rainfall of 430 mm, which is the highest in the whole year. Thus, although the temperature is high during this period, the concentrations of OC and EC are low due to the removal of OC by cloud scavenging below (Pruppacher and Klett, 1978; Kulshrestha et al., 2009). Additionally, both the negative slope and determination coefficient of OC with RH is relatively greater (Table 3.3) than that of EC, thus showing the hygroscopic nature of OC compared to the hydrophobic nature of EC.

The determination coefficient between temperature and OC-EC is not as strong as expected. This is mainly due to the contribution of monsoon-affected months when the temperature is high, but the OC-EC concentrations remain low. Further, the positive slope of wind speed with OC-EC indicates that an increase in wind speed is probably increasing the OC-EC concentration, except in the dry months when an increase in wind

speed is indeed negatively related to the OC-EC concentrations. Thus, the overall correlation of temperature and wind speed with OC-EC is strongly influenced by the weather in the wet months and fails to show the actual processes. It could also be seen that the analysis of diurnal variations (Figure 3.7) in OC-EC could reveal dependence on the meteorological parameters, which is not very clear with their daily average analysis (Table 3.3) as in offline measurements; however, it highlights the importance of continuous online observations.

Table 3.3 *Correlation of OC and EC with meteorological parameters observed at Nainital during 2014-2017.*

		OC		EC	
Meteorological parameter	**Period**	**slope**	**r^2**	**slope**	**r^2**
Solar Radiation (W/m^2)	Daily	0.01	0.75	0.003	0.67
Temperature (^oC)	Daily	-0.05	0.001	0.01	0.02
Relative Humidity (%)	Daily	-0.15	0.48	-0.01	0.38
Rainfall (mm)	Daily	0.01	0.28	-0.01	0.32
Wind Speed (m/s)	Daily	0.89	0.52	0.16	0.38
	Day	0.04	0.91	0.01	0.95
Residence Time	Night	0.03	0.90	0.01	0.87

3.2.5. Influence of Slow-Moving Air Masses and Biomass Burning

We have assessed the influence of slow-moving winds on OC and EC concentrations. Thus, to assess this effect, we have estimated the residence time of air masses in the region of a 1^ox1^o square around the observation site, utilising 5-particle and 5-day backward air trajectories. The residence time of a trajectory arriving at the site is defined as the number of points associated with that trajectory in the 1^ox1^o square around the site. The residence time is estimated using backward air trajectories for their arrival during daytime (1530 hours) and night time (0130 hours), which are associated with the OC and EC concentrations during daytime (1400 – 1700 hours) and night time (0000 - 0300 hours), respectively. It is observed that the concentration of both OC and EC increases with an increase in the residence time of the air masses (Figure 3.8). As expected, both OC and EC show consistent higher values for all residence times during daytime, when compared with this night time. Besides, OC shows a higher slope (0.03 and 0.04) during daytime and night time (Table 3.3) than that in EC. This is again confirming that the

ageing process is dominating OC in the case of aged air masses and could result in higher SOC.

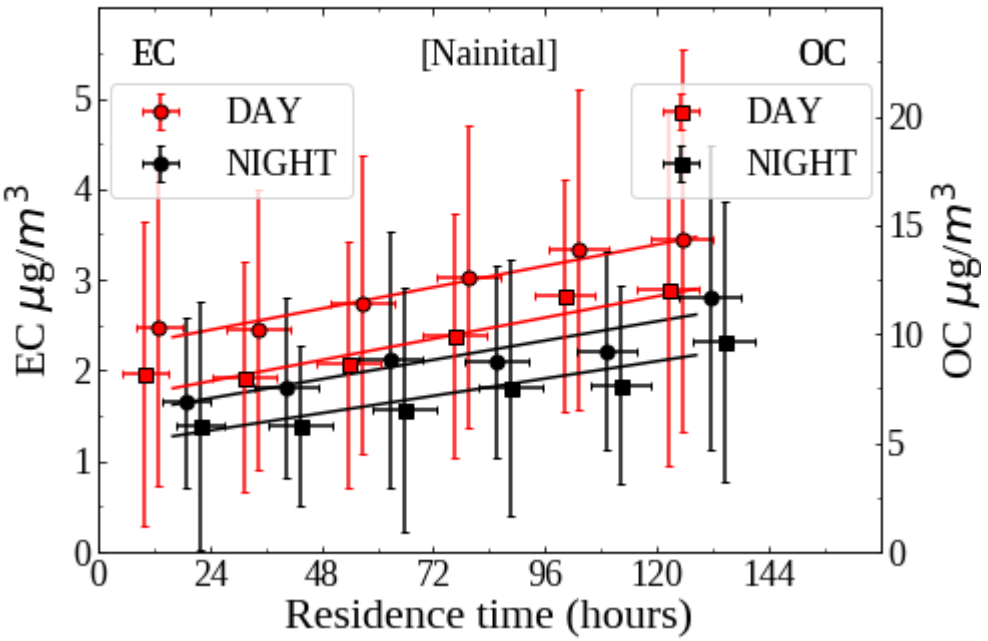

Figure 3.8 *Correlation of OC and EC concentration with the residence time of air masses in daytime and night time during 2014-2017. Backward air trajectories at 1530 and 0130 hours are correlated with the daytime (1400-1700 hours) and night time (0000-0300 hours) average OC-EC concentrations for 2014-2017.*

Figure 3.9 shows the monthly fire events from Moderate Resolution Imaging Spectro-radiometer (MODIS) (night time) over northern India. The MODIS data were downloaded from the NASA Fire Archive (https://firms.modaps.eosdis.nasa.gov/-data/download/). The MODIS collection 6 versions 6.2 for the latitude range of 24 - 35^{o} N and longitude range of 70 - 89^{o} E was used here. Night time data were preferred because of the greater sensitivity of the satellite sensors as compared to that of daytime. Also, we have considered fire events that had confidence levels greater than 80%. The higher fire events are seen in spring, particularly in April and May, hence confirming the period of extensive biomass burning in northern India. Air trajectories arriving from the fire-affected region during these months coincide with the enhanced OC and EC concentrations observed at the site. Few such events are shown in Figure 3.10. Monsoon arrives in mid-June that leads to reductions in fire events. This occurs with a simultaneous southwestern shift of air masses; this scenario prevails until the retreat of the monsoon in September. During this period, concentrations of OC and EC remain at their annual

lows showing the impact of cleaner marine southwestern air masses and contributing to lower fire events in this period. A slight increase in fire events could be seen in October, November and December, but their number remains significantly lower than that observed in spring. Therefore, we feel that enhancement in OC and EC during spring will have a significant contribution from northern India biomass burning; however, a secondary maximum in OC and EC during autumn/winter has a lesser contribution from these fires.

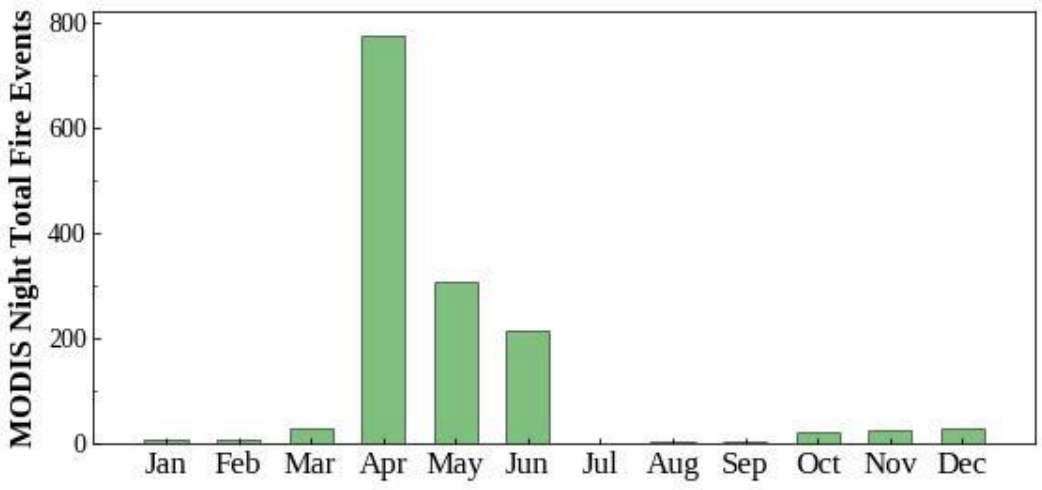

Figure 3.9 *Seasonal variations in MODIS fire events over northern India (24° - 35°N and 70°-89°E) during 2014-2017.*

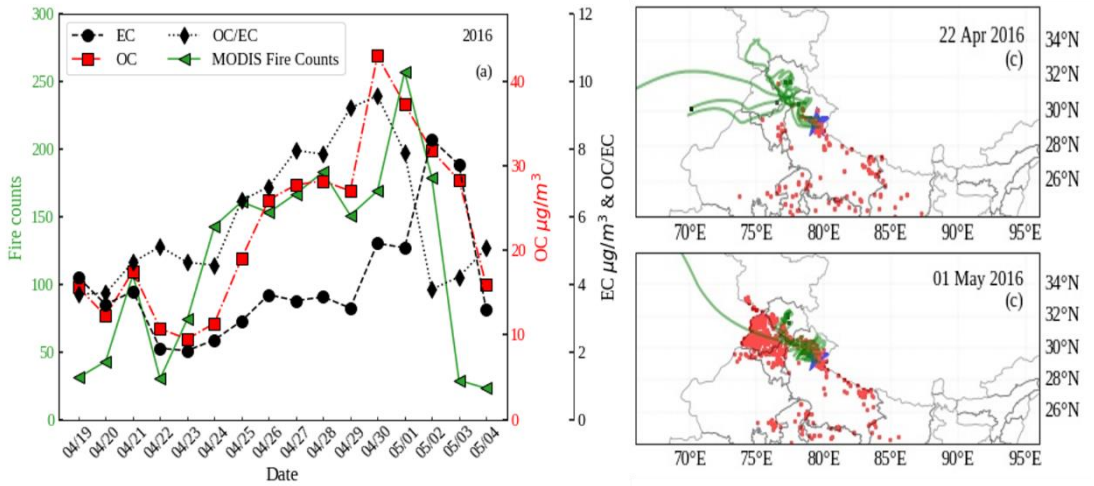

Figure 3.10 *(a) OC, EC, OC/EC and total fire events over northern India from 19 April to 5 May 2016. (b) and (c) show locations of fires observed from MODIS in red and 5-day backward trajectories of 5-particles in green with a square marker at every 24 hours on 22 22 April and 01 May, respectively.*

Figure 3.10 shows a typical event of enhancement in OC during biomass burning in northern India. A systematic enhancement in fire events is seen from 22 April to 1 May 2016. A simultaneous enhancement in OC could also be seen during this period. However, EC shows a somewhat lesser significant increase (Figure 3.10a). Following the decrease in the fire events, after 1 May, the OC concentrations also decreased. This is confirmed by backward air-trajectory analysis. It was observed that trajectories were

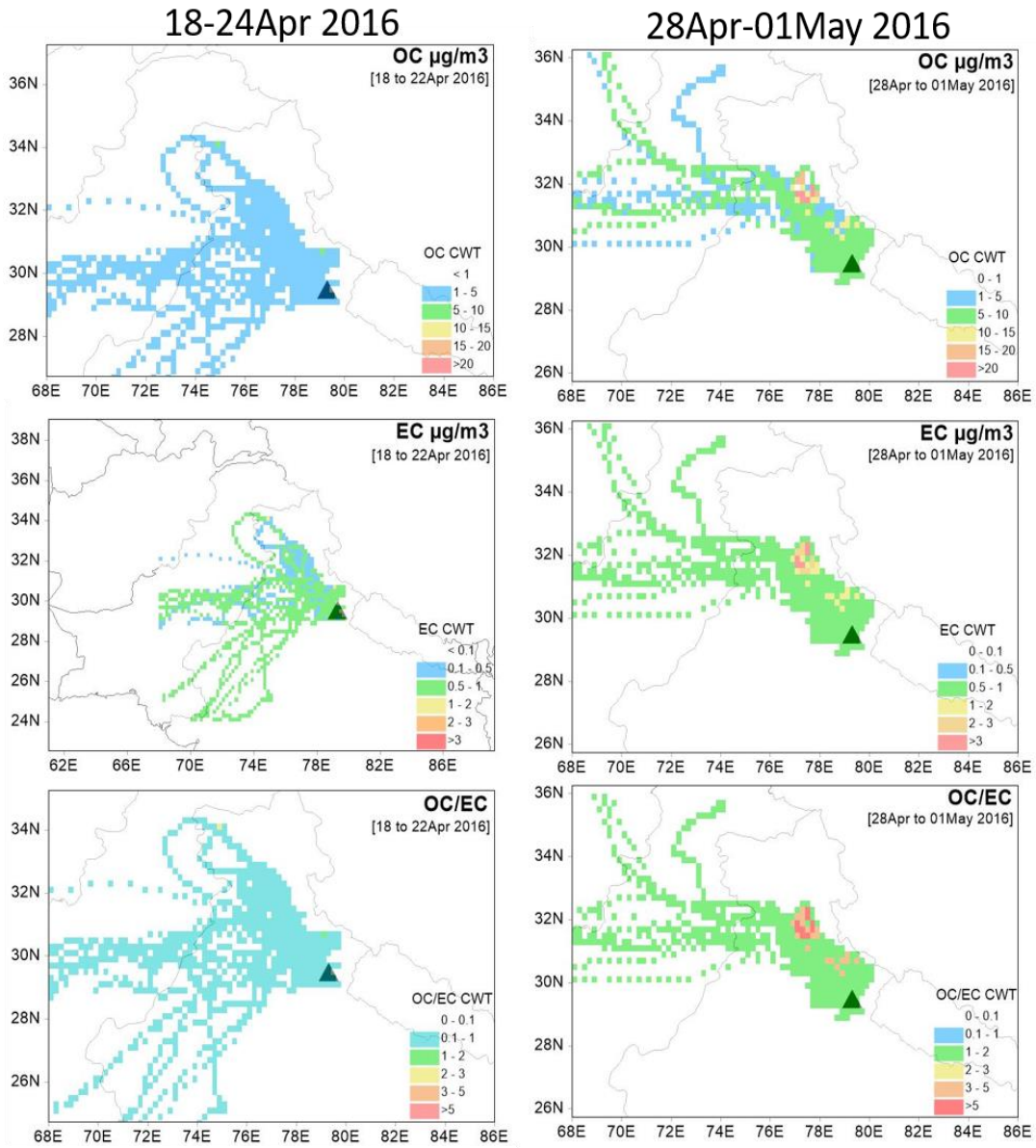

Figure 3.11 *Concentration Weighted Trajectories for OC, EC and OC/EC during low (18 - 24 Apr 2016) and high (28 Apr - 01 May 2016) fire events.*

indeed, arriving at the observation site from the fire-affected regions of northern India on 1 May (Figure 3.10c) when the fire episodes were significantly higher (257). It could also be seen that fire events were much lesser (30) on 22 April; hence, the OC levels were not much higher, despite the arrival of air masses from the same region (Figure 3.10b). The air masses were seen to move faster and contributed to the almost simultaneous rise in the OC/EC concentrations and increased fire events. Additionally, the coinciding rise in the OC/EC ratio from 4.6 to 7.9 further convinced that the enhancement in the concentrations is due to biomass burning (as discussed in Section 3.2.6).

To assess the relative contribution of the regions to these elevated aerosol concentrations along with fire events, we have performed CWT analysis during low fire events (18 - 24 Apr 2016) and high fire events (24 Apr - 01 May 2016) (Figure 3.11). The higher concentrations (shown in yellow, orange and red) of OC and EC and ratio OC/EC are mainly from regions of Himachal, Haryana and Uttarakhand during the high fire events. These regions coincide with the high fire events shown in Figure 11c. Since the OC/EC ratio for these events is >2 hence, it is most likely associated with fires corresponding to biomass burning events. Thus, it further confides that even at this high altitude, the site is considerably affected by the northern India biomass-burning events during spring.

3.2.6 Ratio and Correlation Between OC and EC

Seasonal correlations of OC and EC are shown in Figure 3.12. A greater positive correlation (r^2>0.9) in all seasons suggests their common origins. The maximum slope between OC and EC has been observed in autumn and the minimum slope in monsoon and winter. Generally, the OC to EC ratio of greater than 2 suggests different removal rates of OC and EC and the existence of secondary organic aerosols (Chow et al., 1996). During the present study, it is seen that the OC concentrations throughout the period are much higher than those of EC thus resulting in a high OC/EC ratio with an overall average of 3.4 (Table 3.1). This ratio ranges from 2.7 in March to 4.4 in January. Additionally, the OC-EC slopes lower than 4 and greater than 2 indicate high secondary aerosol formation in the region throughout the period. This is consistent with the previous offline measurements from the site (Ram et al., 2010) although our values are much lower than the ones quoted by them.

The OC/EC ratios have also been used to assess the dominance of biomass burning and vehicular emissions. This is based on studies about the OC/EC ratios from different emission sources. Relatively higher ratios (>4) are reported for biomass burning and lower ratios are attributed to fossil fuel burning (Schauer et al., 2002; Saarikoski et al., 2008, Safai et al., 2014). During the present study period, ratios of 4.4 and 4.1 are observed in January and April and they are between 3.5 and 3.9 in May, June, November and December. It has been shown that April, May, early June, November, December and January are the periods for the large-scale biomass burning in northern India, either as a result of crop-residue burning, forest fires or heating purposes. The impact of these biomass emissions is reflected in these higher OC/EC ratios at the site, while slopes much lower than 4 indicate the dominance of vehicular emissions in the other months.

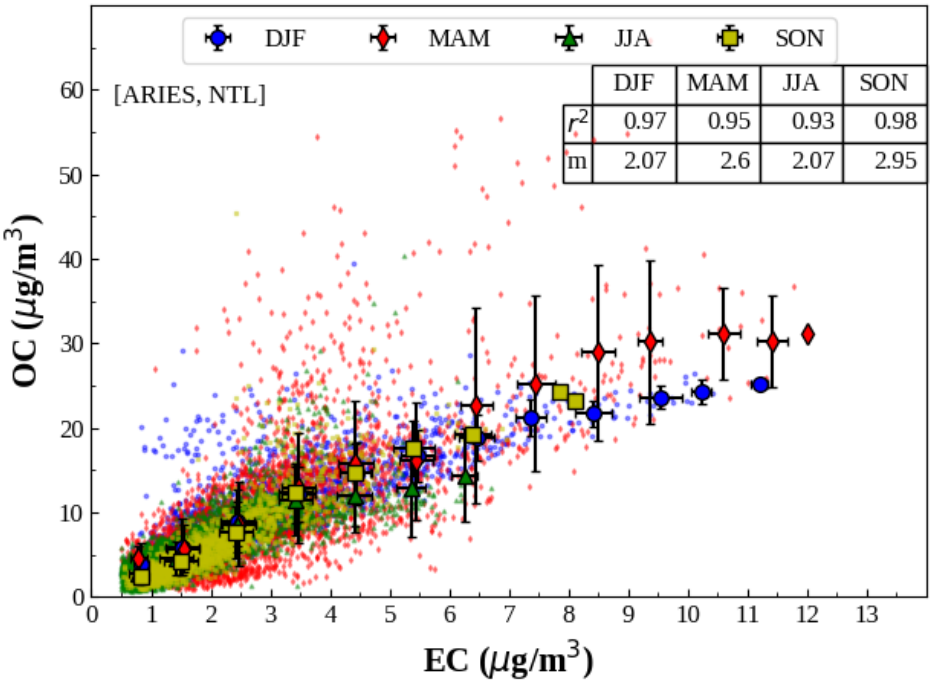

Figure 3.12 *Correlation between the OC and EC concentrations in winter, spring, summer-monsoon and autumn during 2014-2017. Smaller points show daily means and binned data are shown in the same colour scheme with a larger size. Spread in x and y axes in the binned data is one standard deviation from the mean.*

3.2.7 Effect of Diurnal Variation on Radiative Forcing

Figure 3.13 shows the clear-sky shortwave (0.25 – 4.0 µm) averaged direct ARF (Wm^{-2}) at the surface (SUR), in the atmosphere (ATM) and at the top of the atmosphere (TOA)

for forenoon (0600 - 0900 hours) and afternoon (1400 - 1700 hours) averaged EC. The procedure for estimating the radiative forcing is discussed in Section 2.3.2. It could be seen that the afternoon radiative forcing is significantly higher at SUR (51.14%), TOA (361.20%) and ATM (70.44%) when compared to the forenoon radiative forcing. Therefore, considering the diurnal variations in EC, the radiative forcing could be higher by about 20.77 Wm^{-2} in ATM in the afternoon, when compared with the forenoon values. Hence, these online observations help in providing realistic information about the radiative forcing with differences between forenoon and afternoon for this region of the central Himalayas. It has been shown that considering the diurnal effect on AOD and BC, the ARF could be higher by 10-16% (Reddy et al., 2015). These results show that including high-resolution measurements is crucial for better studying the aerosols' influence on radiation.

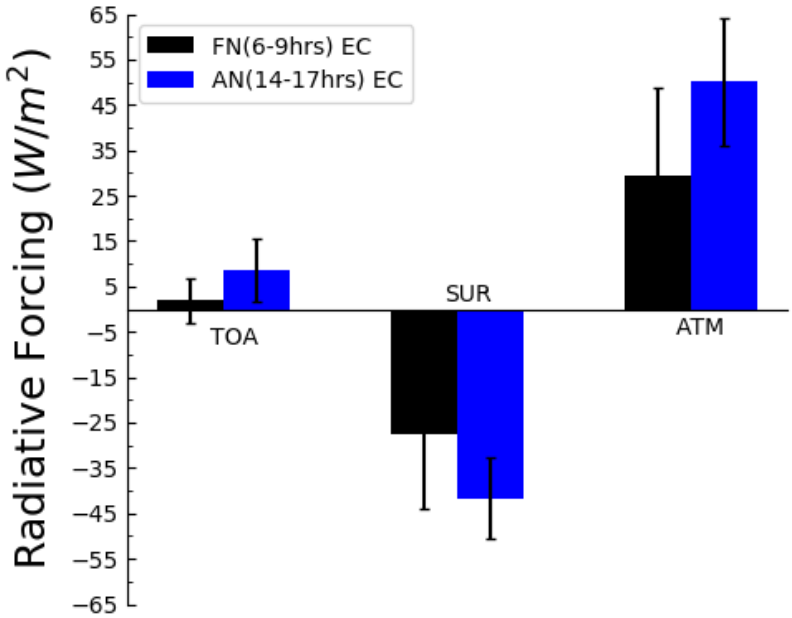

Figure 3.13 *Clear-sky shortwave (0.25–4.0 µm) direct ARF (Wm^{-2}) at the surface (SUR), in the atmosphere (ATM) and at the top of the atmosphere (TOA) for averaged EC during forenoon (0600 - 0900 hours), and afternoon (1400 - 1700 hours).*

3.3. Conclusions

Simultaneous observations (2014-2017) of organic carbon (OC) and elemental carbon (EC) are made over a high-altitude site (Nainital, 29.4°N, 79.5°E, 1958 m a.m.s.l) in the central Himalayas and the role of long-range transport, meteorology and biomass burning

are studied. There are only a few online and simultaneous observations of OC and EC over South Asia and none in the high-altitude Himalayan region. This work presents the first diurnal variations with a unimodal pattern in both OC and EC at the Himalayan site. Such a diurnal pattern is in contrast to the bimodal pattern observed at any continental polluted site. Clear seasonal variations in OC and EC were seen with a primary maximum during spring and a secondary maximum in autumn/winter. OC and EC concentrations are observed to be as high as 65.8 μg m^{-3} and 12 μg m^{-3}, in May respectively. Concentration weighted trajectory (CWT) assisted analysis shows that the biomass burning in northern India is one of the major sources for the springtime maximum even at this high-altitude site. The coinciding rise in OC/EC ratio from 4.6 to 7.9, along with fire events, further convinced that the enhancement in the concentrations is due to the biomass burning at distant regions and long-range transport of air masses influencing this high-altitude site. A poor correlation between OC-EC and the boundary-layer height during autumn and winter suggest that secondary maxima in OC and EC are most likely due to local sources, e.g., household burning for heating during this cold period when the temperature drops sharply after October and remains low until February. The higher temporal resolution of online measurements reveals that swiftly varying meteorological parameters change the OC-EC concentrations at diurnal scales. Back-air trajectory assisted analysis of residence time and its relationship with OC and EC confirms the increase in their concentration in slow-moving air masses. The observed diurnal variations of EC are utilised to estimate the radiative forcing and show that the atmospheric radiative forcing during the afternoon is about 70% higher than the forenoon one. It is envisaged that this dataset with diurnal observations of OC and EC would be an important input for studying the radiation budget and source apportionment over this high-altitude region.

Chapter 4

Implications of Site-specific Mass Absorption Cross-section (MAC) to Black Carbon Observations

For long, optical instruments such as Aethalometer have provided crucial BC observations. However, as a major shortcoming, these instruments utilize a constant mass absorption cross-section value (MAC) for estimating BC. This chapter addresses this issue by estimating the site-specific MAC values for this region. It also shows that these MAC values are not constant and discusses the reasons behind their variations. It concludes with a description of the impacts of not using site-specific MAC in BC estimates and radiative forcing calculations.

4.1. Introduction

Atmospheric Black Carbon (BC), which is characterized by its strong light absorption properties and resistance to chemical transformations (Goldberg, 1985), has drawn global scientific attention due to its strong climate forcing capability next only to carbon-di-oxide (CO_2) (Ramanathan and Carmichael, 2008). BC also contributes to the degradation of both visibility and health (Deng et al., 2012; Jansen et al., 2005). Yet, there exists large uncertainty (2000 to 29000 Gg $year^{-1}$ for the year 2000) in the estimates of total global emissions of BC (Bond et al., 2013). Similarly, the estimation of global mean radiative forcing due to BC (~0.64 Wm^{-2}) has been associated with large uncertainty of about 0.5 Wm^{-2} (Myhre et al., 2013). Thus, accurate estimates of BC mass concentration are crucial for better evaluation of its impact on the radiation budget, climate and health.

Optical methods are widely used to determine equivalent BC mass concentration (eBC) because of their rapid measurability and relative convenience of use (Malaguti et al., 2015). In this method, eBC is estimated by measuring the changes in attenuation of light of a given wavelength while passing through a particle-laden filter. The correspondence of this change in attenuation to mass concentration requires the knowledge of a parameter

called the mass absorption cross-section (MAC), which is also referred to as mass absorption efficiency (MAE) or specific attenuation cross-section (Hansen et al., 1984). The estimates of eBC via optical methods generally assume that MAC remains constant at the observational site (Snyder and Schauer, 2007). Therefore, it is a common practice in optical methods to use a constant value of MAC at a given wavelength. However, a wide range of MAC values (2 to 25 $m^2 g^{-1}$ at 550 nm and 5.9 to 54.8 $m^2 g^{-1}$ at 880 nm) have been reported in different environments (Liousse et al.,1993; Bond and Bergstrom, 2006; Nordmann et al., 2013), including urban (Snyder and Schauer, 2007; Schwarz et al., 2008), urban to remote areas (Sharma et al., 2002) and dominant biomass burning regions (Schwarz et al., 2008). The wide range of MAC values have been attributed to the variety of mixing state (Liousse et al., 1993; Nordmann et al., 2013), sources (Olson et al., 2015) chemical composition (Ram and Sarin, 2009), morphology (Cao et al., 2015) and ageing (Liousse et al., 1993) of the BC particles modulated by moisture content in the atmosphere.

For example, the areas of Savannah, dominated by biomass burning, possess a high MAC of 20 $m^2 g^{-1}$, while the MAC values are as low as 5 $m^2 g^{-1}$ over remote areas (Liousse et al., 1993; Cho et al., 2019). Their study suggested that BC particles acquire a coating of organic particles during biomass burning, which results in its enhanced absorptive capacity. On the other side, BC in the remote areas is aged in nature and due to this aging of aerosols during long-range transport, the individual BC spheres agglomerate into a big spherical aggregate. Particle radius increases as a consequence of this aging and this leads to decreased MAC observed in the remote areas (Liousse et al., 1993). Higher MAC values have also been attributed to asymmetric and cluster like particles, while spheroidal particles have been reported to have low MAC values (Cao et al., 2015 and references therein). Considering this variety and inconsistency in the values of MAC, several authors have suggested the use of its site-specific value (Liousse et al., 1993, Ram and Sarin, 2009; Wang et al., 2013; Cao et al., 2015). Further, MAC is an important parameter for climate forcing calculation (Nordmann et al., 2013); thus, any bias in MAC would imply that aerosol radiative forcing estimates are equivalently biased.

In the above backdrop, the present study aims at defining MAC for accurate eBC estimates at a remote mountainous site in the central part of the Himalayas. The spectral and temporal variability of MAC spanned over four years (2014-2017) period is also

discussed. This is a first of its kind study where both the real-time and spectral values of MAC are estimated for a high-altitude site in the central Himalayas using extensive online observations of four years. In the course of this paper, first, the results of the relationship between light absorption and EC as well as spectral and temporal variations in MAC have been discussed. Corrected eBC values have been provided along with the suggested MAC values for future use. Later, a comparison of various sites and the role of meteorological parameters, EC and OC in these variations is discussed. Finally, the impact of these MAC variations on eBC and subsequently radiative forcing has been highlighted. It is to be noted that all the terminologies referring to BC, eBC and EC used in the current paper are based on the recommendations detailed in Petzold et al., (2013).

4.2. Derivation of the Expression for MAC

Concurrent observations of absorption coefficient and EC enable the calculation of site-specific MAC. Thus, the current study used simultaneous observations from Aethalometer and EC-OC analyzer and a total of 8,227 hourly average data are analyzed here. High-resolution continuous multi-wavelength measurements are an additional advantage in the present study as they allow for the assessment of diurnal and spectral variation in MAC. The expression for MAC has been derived through a linear regression fit of the absorption coefficient (b_{abs}) obtained at seven different wavelengths and thermally obtained EC measurements, as given by,

$$b_{abs}(\lambda) = MAC(1/\lambda) * [EC] + c(\lambda) \qquad (4.1)$$

Here, $b_{abs}(\lambda)$ (Mm^{-1}) is the absorption coefficient as determined from Eq (2.1) and EC is the mass concentration of elemental carbon measured in units of $\mu g\ m^{-3}$ as obtained from the EC-OC analyzer. The equation has been motivated by equations in Knox et al., (2009); Ram and Sarin, (2009) and plots of Wang et al., (2013); Paige et al., (2017). We have modified the equation given in Knox et al., (2009) and Ram and Sarin, (2009) by adding a y-intercept 'c' on the right-hand side in Eq (4.1).

A few points regarding the way we have calculated MAC is in order here. Since we have a large data set over time, we have been able to make a linear least-square fit. Equation 4.1 represents such a fit where the slope gives the value of MAC at a given wavelength. The y-intercept - 'c' indicates the presence of components other than EC, if high and

positive (Wang et al., 2013). The intercept can also be caused by the difference in measurement methods between the two instruments, i.e., thermal in OC-EC analyzer and optical in Aethalometer. The negative intercepts could occur as a result of this difference. The advantage of using Eq 4.1 which includes c (as against merely calculating the ratio of b_{abs} to EC) is that it does not make any assumption on the presence or absence of non-EC components in absorption by taking c=0. Additionally, the MAC obtained from the slope is a better representative of the long-term variation than a simple mean which can be biased by high or low values at times.

4.3. Results and Discussion

4.3.1. Relationship Between the Absorption Coefficient (b_{abs}) and EC

Figure 4.1 shows the correlations between the EC concentrations and the b_{abs} for the seven wavelengths. This figure highlights the long-term variation in MAC with wavelength. Overall, the correlation (r^2>0.7) is reasonably good and has a positive value of the slope. The scatter of hourly points in the lower wavelength (370 nm) is relatively higher and consequently, r^2 is relatively lower compared to other wavelengths. This indicates that there might also be an influence (albeit subdominant) of absorbing factors other than EC at this wavelength (Paige et al., 2017). This low influence of absorbing species other than EC is further consolidated by the near-zero or negative intercept in all the wavelengths. This is also observed in other studies (Wang et al., 2013). The slope of the fit gives the mass absorption cross-section (MAC) offered by the EC particles to the incoming photons for absorption. The annual MAC values for the entire data set range from 12.64 to 4.43 $m^2 g^{-1}$ for wavelengths from 370 nm to 950 nm, respectively. Thus, a systematic decrease in the MAC values along with the wavelengths is observed and this can be used to derive a general wavelength dependence for MAC as done in the next section. A similar regression technique is used to derive MAC by Ram and Sarin, (2009); Wang et al., (2013); Cao et al., (2015); Paige et al., (2017) and others. However multi-wavelength MAC is derived in very limited studies such as Olson et al., 2015 where the values of MAC at different wavelengths were used to demonstrate the variability of

emission source absorption properties and the importance of relative abundance of Brown Carbon.

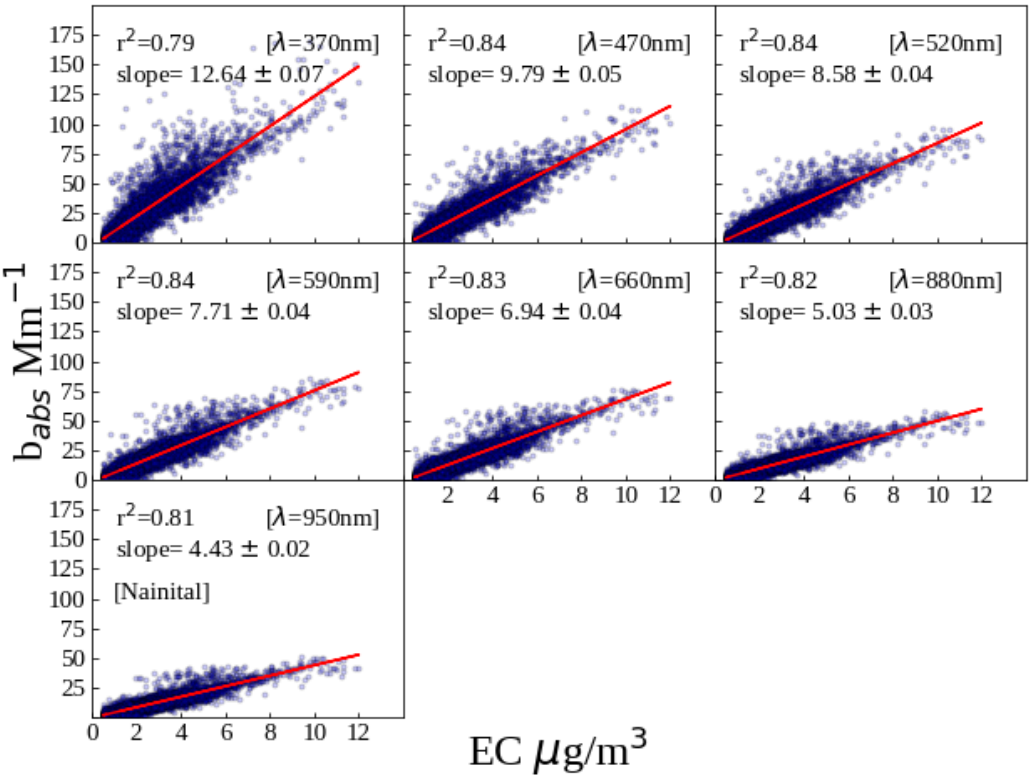

Figure 4.1 *Correlation between the absorption coefficient (b_{abs}) and EC concentrations at each of the wavelengths of Aethalometer observed at Nainital. Smaller points in blue show hourly mean points. The line in red shows the linear regression fit to these data points.*

4.3.2. Spectral and Temporal Variation in MAC

Figure 4.2 (a) shows variations in MAC at seven wavelengths. The plot characterizes the spectral variation of the BC aggregate absorption cross-section. In the Rayleigh limit, the absorption cross-section of a BC particle is inversely proportional to λ (Liu et al., 2020). In the log-log plot, this inverse proportionality is reflected as a straight line with a negative slope. The presence of coating may change this behaviour and the slope, in that case, will be deviated from unity (Liu et al., 2020). The observed slope in our case is very close to 1 (1.08 ± 0.001). In this view, we have fitted the straight line (log MAC = log c- log λ) to the data points to get the intercept (log c). The observed value of the inverse proportionality factor 'c' is 4499.6 ± 55.9. This observed value is less than one third the value of 14625 that is being currently used in the Aethalometer (AE-42). The wavelength

dependence of MAC thus turns out to be ~ 4499/ λ and is used to get an average value of MAC at the site in the wavelength range of 370-950 nm.

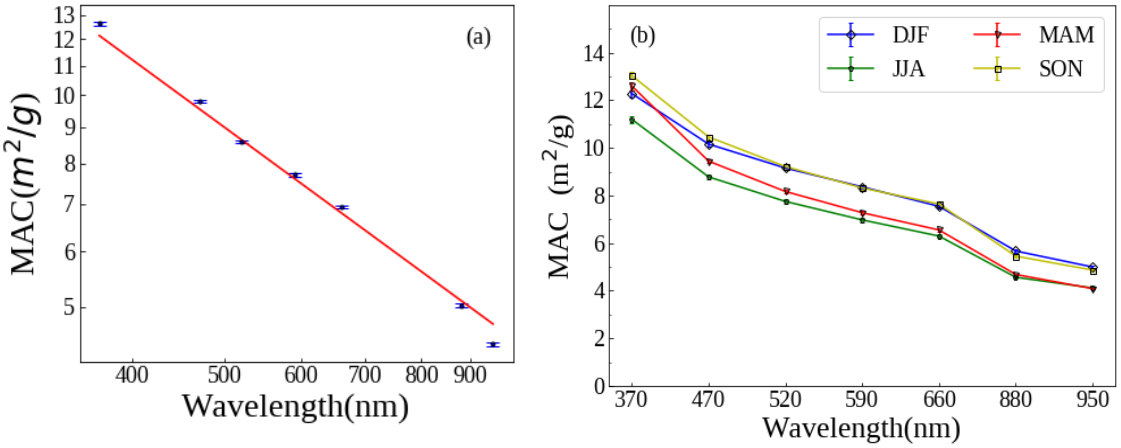

Figure 4.2 *(a) The points in blue show the observed variation of MAC at seven wavelengths on a log-log scale. The red is a linear best fit. (b) Seasonal variations in MAC with wavelengths ranging from 370 – 950 nm. Error bars for each point in the plot represent errors in the slope of the regression fit made for the absorption coefficient and EC at a particular wavelength.*

To assess the seasonal variability in MAC, its values for all seven wavelengths were obtained for four seasons during the 2014 - 2017 period (Figure 4.2b). Each point in the plot is obtained from the slope of the linear regression of b_{abs} and EC for a given season and wavelength. The corresponding error in the slope is also shown as an error bar. MAC values at 370 nm are almost 2.5 times more than their values at 950 nm. At 370 and 470 nm, there is a marked jump in MAC values especially in spring (MAM). A possible reason for this jump in the lower wavelengths could be due to absorption by dust in this period. However, as dust particles are coarser in size, our analysis which used PM 2.5 size cut inlet samples are expected to have very less influence on coarse mode dust. Even with a smaller quantity of fine mode dust, the MAC of dust is reported to be very small i.e., 0.03 $m^2 g^{-1}$ (Ram and Sarin, 2009; and references therein). Another possible reason for this higher MAC in 370 nm during spring could be due to the dominance of organic components in these wavelengths. We use organic carbon (OC) concentrations and OC/EC ratio as a proxy to assess this influence of organic content in spring (MAM) at shorter wavelengths. We observed that the seasonal averaged OC values at this site are 9.4±5.5, 10.4±7.7, 5.9±3.9 and 6.6±4.3 μg m^{-3}, and OC/EC values are 3.5, 3.6, 3.3 and 3.1 during DJF, MAM, JJA and SON respectively (Srivastava and Naja, 2021). Thus, it is found that the maximum of OC concentrations (10.4±7.7 μg m^{-3}) and OC/EC ratio i.e.,

3.6 occurs during spring (MAM). Hence, we suspect that the higher values in MAC in 370 and 470 nm during spring are thus most likely linked to higher organic content during the same period which absorbs in the shorter wavelengths.

The decreasing tendency in MAC values with wavelengths is observed in all the seasons. Winter (DJF) and autumn (SON) have similar MAC values and almost overlap with each other. A similar overlap is seen in the variations of MAC for the spring (MAM) and summer (JJA) seasons. One of the possible reasons for this overlapping variation is suggested to be due to the change in the direction of the air mass flow at the site during different seasons. The air masses at the site are north westerly in the winter and autumn season while they become more south westerly during summer when the monsoon prevails over the Indian subcontinent. The north westerly air masses are of continental origin and are more probable to carry pollutants at the site. On the other hand, the south westerly air masses during JJA are of oceanic origin and relatively cleaner. Thus, possibly the resultant changes in the amount and type of pollutant sources with these air masses could have caused the observed clustering of MAC for the different seasons. A detailed description of the year-round changes in the air masses at the site is provided in Kumar et al., (2010).

Monthly variations in MAC for all seven wavelengths is shown in Figure 4.3. The monthly MAC values are obtained from the linear regression slope of the hourly observations of absorption coefficient and EC for each month at corresponding wavelengths. Table 4.1 provides a statistical summary of the monthly variation at 880 nm, a wavelength that is usually used to obtain BC (Bodhaine 1995) using the Aethalometer. MAC shows significant monthly variations throughout the year for all the wavelengths. The highest value of MAC is observed in September. The values of MAC and r^2 (between EC and b_{abs}) are the lowest in peak monsoon months (July and August). This high determination coefficient with $r^2>0.7$, for all months except July and August, shows that EC is the only dominant absorbing species except in these months.

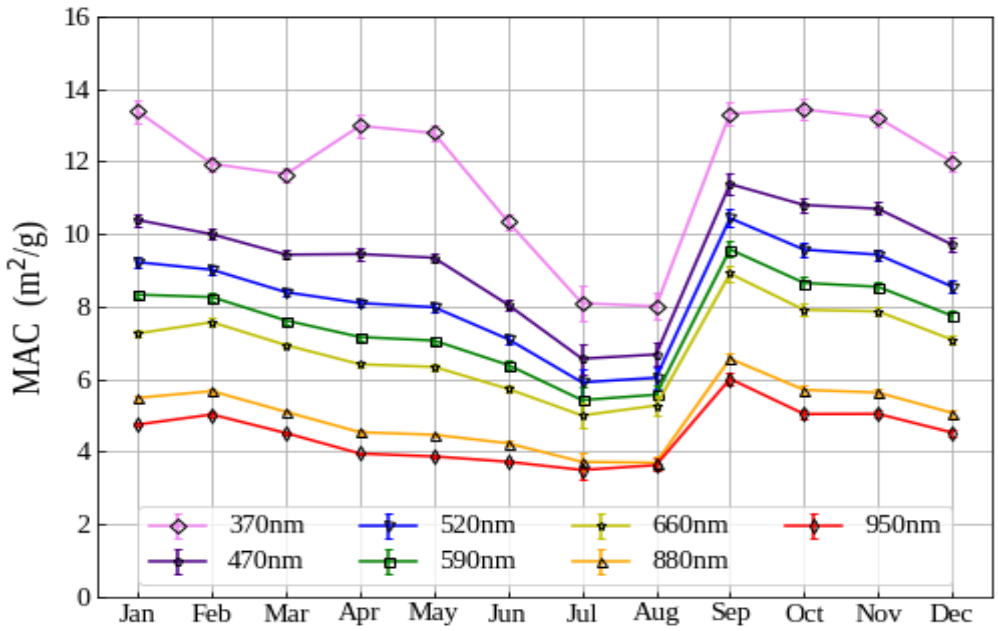

Figure 4.3 *The monthly average variations (2014-2017) in MAC at seven wavelengths ranging from 370 to 950nm. Error bars for each point in the plot represent errors in the slope of the regression fit made for the absorption coefficient and EC for that month at a particular wavelength.*

Table 4.1 *Monthly and annual MAC values at 880 nm for the 2014-2017 period over the central Himalayan region. The determination coefficient in the absorption coefficient and EC for each month and the whole year along with the counts used in each of the regressions is also mentioned.*

Month	**MAC**	**r^2**	**Count**
Jan	5.49±0.07	0.9	792
Feb	5.67±0.09	0.82	949
Mar	5.10±0.07	0.95	326
Apr	4.54±0.05	0.90	787
May	4.47±0.06	0.89	652
Jun	4.23±0.08	0.72	1235
Jul	3.72±0.25	0.36	394
Aug	3.70±0.19	0.27	992
Sep	6.56±0.16	0.72	675
Oct	5.71±0.13	0.79	501
Nov	5.63±0.10	0.86	489
Dec	5.07±0.10	0.84	435
Annual	**5.03±0.03**	**0.82**	**8227**

Figure 4.4. shows the average diurnal variations in MAC during four seasons for all seven wavelengths. These MAC values are obtained by making a linear fit for each hour of four seasons. This method is preferred over taking the simple average from each month's hourly MAC value since it would reduce the propagated error that might be induced otherwise. MAC does not show any significant diurnal variation. It, however, does show some random variability, which is similar to that observed in Riverside (California) during the weekend (Snyder and Schauer, 2007). Nevertheless, MAC values show a tendency of somewhat higher daytime values during spring, particularly at a wavelength of 370 nm. It is also worth noting that the variations are relatively more pronounced at lower wavelengths (e.g., 370 nm) and suppressed at the higher wavelengths. Organic carbon and humic-like substances (HULIS) are known to absorb in the lower wavelengths (Kirchstetter et al., 2004; Hoffer et al., 2006).

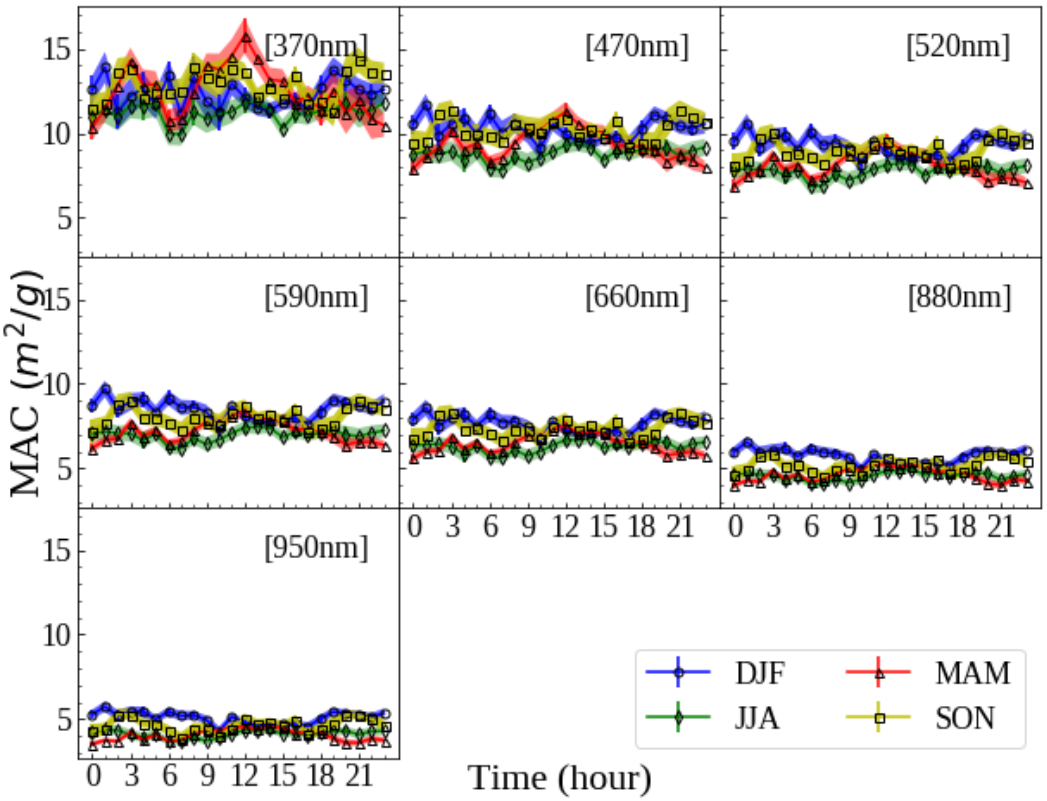

Figure 4.4 *The average diurnal variations in MAC during four seasons in 2014-2017 for all the seven wavelengths. Error bar and shaded area represent the corresponding error in the slope of the line fit for each hour data.*

These fluctuations could be because the lower wavelengths are more sensitive to absorption by other components or mixing states, etc. Thus, indicating the possible role of absorption of such substances at the site as described previously. Higher values in the

daytime during spring might have also resulted due to the meteorological conditions in this period. Therefore, we investigate the role of meteorology and variations in the relative abundance of b_{abs} and EC and their causes in the temporal variability of MAC in sections 4.3.3 and 4.3.4.

4.3.3. Role of Temporal Variations of EC and Absorption Coefficient in Variations of MAC

Here, we discuss the temporal variations of EC and (b_{abs}) and their role in observed variation in MAC. Figure 4.5 shows the average diurnal and monthly variations in b_{abs} and EC for the period 2014-2017. The EC and b_{abs} both exhibit more-or-less similar diurnal and monthly variations. Both these parameters show a unimodal diurnal distribution with daytime higher values, except in the monsoons when such a diurnal feature is suppressed. This daytime rising unimodal distribution at this mountain site is in stark contrast to the bimodal distribution observed at urban and rural sites (Dumka et al., 2010; Joshi et al., 2016; Gogoi et al., 2017). The bimodal distribution is attributed to the trapping of pollutants in the boundary layer during the morning and evening hours. While at high altitude sites, a rise in the boundary layer height along with upslope winds results in a rise of pollutant concentrations during daytime (Naja et al., 2014). Unlike EC and absorption coefficient, MAC does not show any significant diurnal variation (Figure 4.4). This is due to the similar temporal variations in EC and absorption coefficient that will normalize out the diurnal variation in MAC unless absorption coefficient and EC vary in different proportions which are not the case in diurnal scales over this central Himalayan region.

The interannual monthly variation of the absorption coefficient and EC show a steep reduction during the summer monsoon to almost half the earlier values. There is a gradual increase in the post-monsoon period. However, the concentrations are relatively constant during the winter months of November to January, when the boundary layer height is at its annual low (e.g., Shukla et al., 2014). Subsequently, there is again an enhancement in the magnitudes in spring. The maximum absorption coefficient and EC is observed in the spring season (MAM). Similarly, the maximum in the diurnal peak magnitudes also occurs during this season. This behaviour of absorption coefficient and EC is due to the

biomass burning activity, enhanced depth of the mixing layer and higher wind speed which transports the pollutants to the site (Bhardwaj et al., 2016). Higher MAC values in the 370 nm in this season could be due to this biomass burning activity. Higher MAC due to biomass burning has also been reported by Liousse et al., (1993); Schwarz et al., (2008); Ram and Sarin, (2009) and references therein. Absorption of organic components from biomass burning is more in the lower wavelengths like 370 nm (Sandradewi et al., 2008). Therefore, the MAC values are particularly higher in this wavelength during spring.

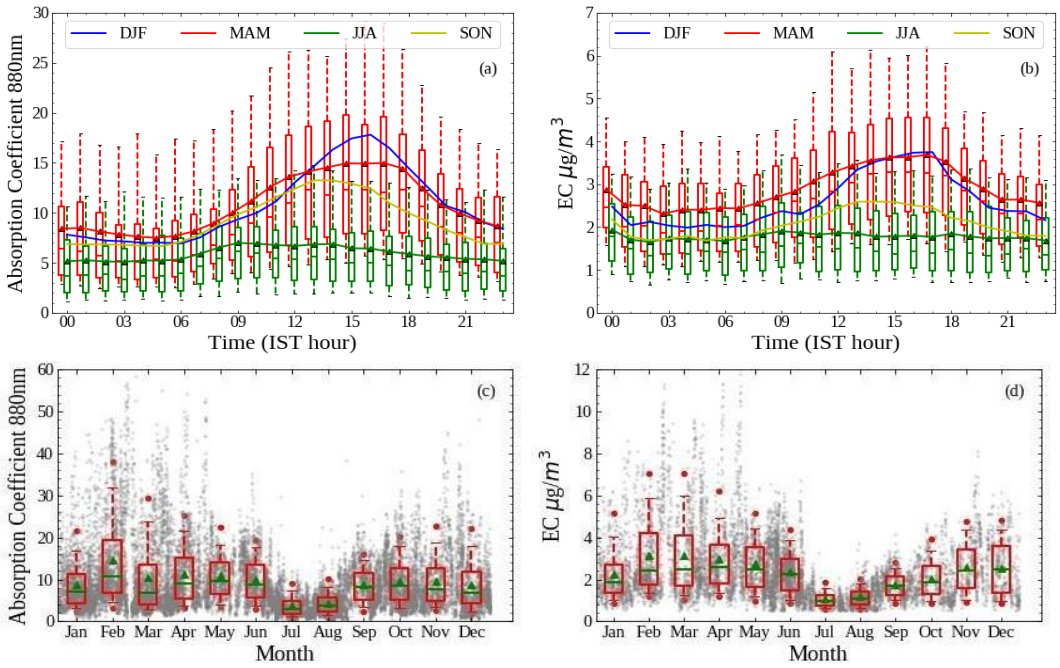

Figure 4.5 *Averaged diurnal variations in (a) absorption coefficient (Mm-1) at 880 nm and (b) EC (μg m^{-3}) in four seasons during 2014-2017. Average monthly variations in (c) absorption coefficient at 880 nm and (d) EC concentrations during 2014-2017. Boxplots for spring (MAM) have been shifted and line plots for winter (DJF) and autumn (SON) are plotted instead of boxplots, for clarity. In boxplots, the triangle inside the box represents the mean and the solid lines represent the median. The lower and upper edges of the boxes represent the 25th and 75th percentiles, respectively. The lower and upper range in whiskers is 10th and 90th percentiles, respectively. Hourly data points are shown in grey in (c) and (d).*

The reduction in absorption coefficient and EC in monsoon is due to the high amount of rainfall (more than 70% of the whole year) during this period which, in turn, results in strong wet scavenging of aerosols. Increased rain and relative humidity (RH) in the monsoon, resulting in lower EC values which could have in turn resulted in the observed decrease in MAC during this period. Diurnal peaks in winter are narrower as compared to those during the spring. This is due to the shorter duration of the day and a smaller

amount of solar radiation during winters (Sarangi et al., 2014). The temporal variations in both absorption coefficient and EC have a similarity in behaviour, although there are visible differences too. The peak of the absorption coefficient in diurnal variations during autumn (SON) is closer to that in summer as compared to that in the case of EC concentrations. Further, the variability of the absorption coefficient is greater in February as compared to that of EC during the same period. Thus, while there are broad similarities, the differences in both these quantities lead to the temporal variability in MAC observed in Figure 4.3. and 4.4. Hence, the changes in the relative proportions of EC concentrations could be inducing the observed variations in MAC. In light of the above observations describing the seasonal nature of the aerosol properties over the central Himalayan region, it is clear that a constant value of MAC over this region may not suffice the accurate estimate of eBC from Aethalometer measurements in different seasons.

4.3.4. Role of Meteorology in Variations of MAC

In this section, we discuss the possible role of meteorology on the variations in MAC (for 880nm). For understanding the role of meteorology, correlations of MAC are studied with wind speed, RH, rain, temperature and solar radiation. It was found that the correlation wasn't very significant in all the cases except in temperature. A higher correlation (r^2 =0.73 and p~0.001) with a negative slope of 0.14±0.03 shows that MAC is somewhat inversely related to the temperature at the site (Figure 4.6a). Thus, the higher temperature seems to reduce the absorption efficiency, possibly due to the evaporation of coating material. Although the determination coefficient is 0.386 and p is slightly greater than 0.01, it is interesting to note that MAC is somewhat positively correlated (r^2=0.39) with solar radiation (Figure 4.6b) but this correlation is highly positive (r^2 = 0.96) till solar radiation is ~450 Wm^{-2}. Thus, it seems that MAC shows a non-linear behaviour and increases linearly only till a threshold solar radiation. Temperature and solar radiation thus show contrasting impacts on MAC. Higher temperature conditions that decrease in the MAC coincide with higher solar flux during spring. This might be responsible for the observed disconnection between the linear rise in solar radiation and MAC till a certain threshold value of ~450 Wm^{-2}, after which the impact of temperature becomes dominant, and this results in a somewhat decreased MAC value.

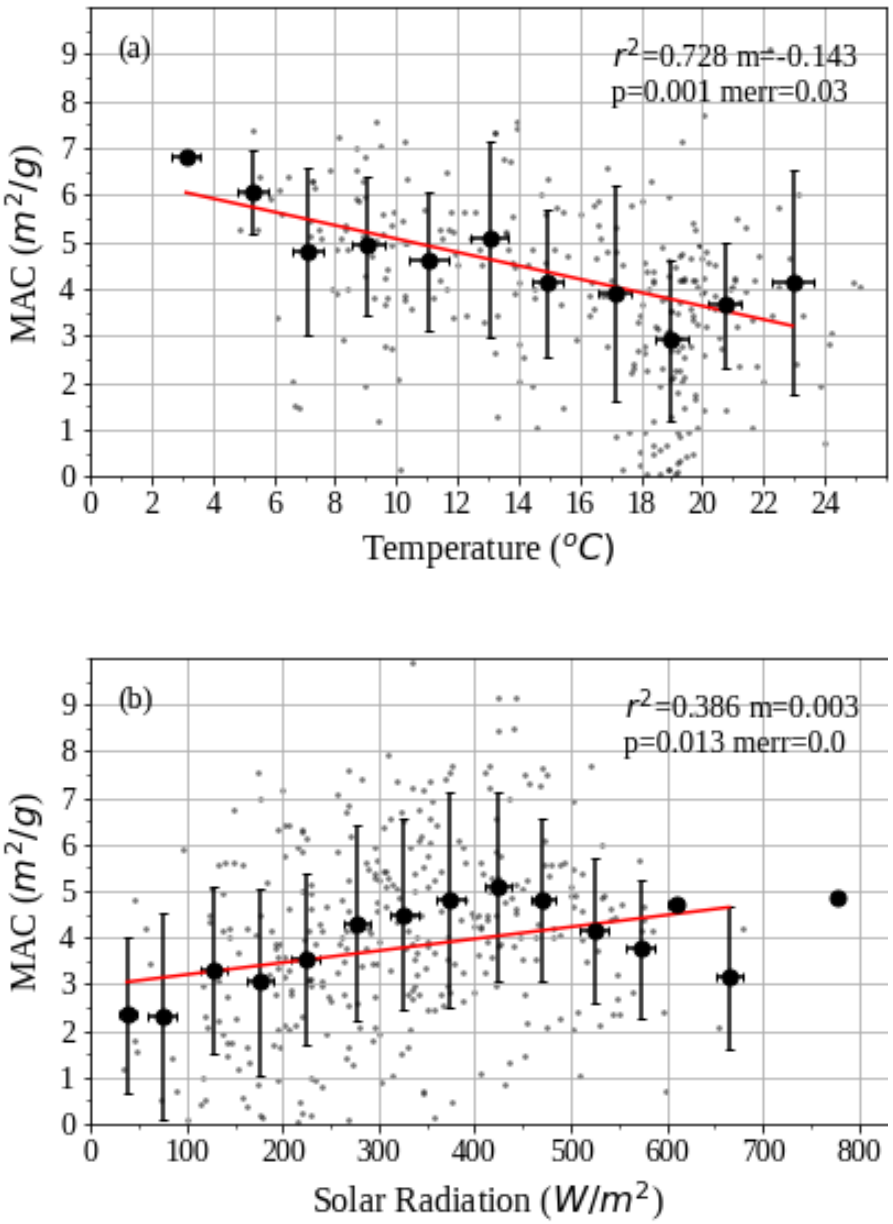

Figure 4.6 *The correlation between MAC (for 880 nm) with Temperature and Solar Radiation for 2014-2017. The determination coefficient, slope, slope error and significance level (p) are also mentioned. Hourly data points are in small grey markers and binned data points are in black markers with error bars in the one sigma level. Red line shows the straight fit line to the binned data points.*

Further during spring, the temperature and solar radiation are maximum in the spring (MAM) with a peak in monthly mean during May (20.3ºC and 473 Wm^{-2}). The wind speed also peaks around the same time and reaches its maximum of about 3.6 ms^{-1} in May. The mixing layer height is also greater during spring and conditions are supportive for photo-oxidation. The higher MAC values in spring could be due to these

meteorological effects, especially higher solar radiation, in addition to the role of biomass burning as discussed in the previous section 4.3.3. Monsoon (JJA), in contrast to the dry pre-monsoon, brings heavy precipitation (total of about 680 mm in July alone) and very high humidity (>70%). Prominent cloud cover in monsoon results in a reduced solar flux and low mixing layer depth. Thus, lower MAC in monsoon can be linked to lowered solar flux along with enhanced RH in the period.

Winter (DJF) is a cold and dry period with the temperature reaching its lowest monthly average in January of 8.5^{o}C. Lower solar flux and temperature in winters result in a lower mixing layer height. Hence, we expect the influence of relatively fresher and local emissions in MAC in this period. Relatively higher values of MAC are seen in the post-monsoon (SON) when wind speed is also lowest (1.9 m/s in September). Lower wind speed along with lower mixing layer depth would lead to a reduction in aged, transported aerosols and their subsequent ventilation. These conditions would result in a relatively higher influence of local emission sources at the site which would be relatively fresh and externally mixed. Hence, it is plausible that such fresher emissions would have a higher MAC against the usual aged emissions in the remote areas which have a lower MAC due to larger particle radius as described in Liousse et al., (1993).

4.3.5. Comparison with Other Studies

Here we compare and discuss the MAC values estimated for other sites. A previous study utilising offline sample analysis has shown that MAC at this site ranges from 6.1 to 19.1 $m^2 g^{-1}$ for 678 nm wavelength (Ram and Sarin, 2009). The MAC value from the present analysis, utilizing wavelength dependence i.e., $4499/\lambda$ is 6.63 $m^2 g^{-1}$ at 678 nm wavelength. This lies at the lower end of the previous study. The earlier study used 67 (December 2004 - June 2007) samples (offline) of total suspended particulates while the present study uses 8,227 samples (online with 2.5 μm cut) spanned over four years. Further, unlike in the present analysis, in earlier studies, 24-hour variability of the species were integrated into the offline samplings and such samplings are also subjected to greater positive artefacts that follow due to delay in the analysis.

Using offline measurements for TSP, Ram and Sarin, 2009 have compared the wintertime (December 2004) variation in MAC of the current site (Manora Peak - 14.5 $m^2 g^{-1}$) with another high-altitude site (Mt. Abu - 10.4 $m^2 g^{-1}$), a rural site (Jaduguda - 6.1 $m^2 g^{-1}$) and two urban sites (Allahabad - 11.1 $m^2 g^{-1}$ and Hisar - 11.3 $m^2 g^{-1}$) in South Asia. This study attributed the large spatial variation in MAC to the variety of emission sources (coal and biomass burning). Therefore, to avoid uncertainty in the estimation of radiative forcing due to BC, the use of site-specific MAC rather than a constant value was advocated in the present work.

In the present study, MAC values at 880 nm are about three times lower than the currently used value of 16.6 $m^2 g^{-1}$ in the Aethalometer. Using similar filter-based optical instruments, Cho et al., (2019) found that the BC MAC values at a continental site in Korea range from 4.6 to 6.5 $m^2 g^{-1}$ at 565 nm. The lower MAC values were attributed to the less active coagulation processes and the partial evaporation of the coating materials during long-range transport. MAC values as low as 5 $m^2 g^{-1}$ were observed over remote areas by Liousse et al., (1993) and it was attributed to the fact that BC in the remote areas is aged in nature, which subsequently leads to a reduction in MAC values. Spheroidal particles have been reported to have low MAC values (Cao et al., 2015 and references therein). Since our site is not surrounded by any major pollutant sources, we suspect that the lower values are due to the receipt of aged emissions mainly during long-range transport.

Paige et al., (2017) have evaluated the relationship between b_{abs} and EC over 10 sites across the USA during 2010-11 to determine MAC using a similar approach as in section 4.2. Their estimated MAC at 880nm is in the range of 6.9 to 9.4 $m^2 g^{-1}$ and varied by region and season. Thus, similar to our analysis it is emphasized in the aforementioned study that a region and season-specific value shall be used and that using a default value may lead to biased BC concentrations. Further, it was also shown that the lower EC content and non-EC species lead to a highly variable MAC and a lower r^2. We have discussed the variation of EC concentration on MAC in section 4.3.3 and have found a similar result, especially in JJA when EC is particularly low.

Extensive field measurements at seven sites of the German Ultrafine Aerosol Network (GUAN) with Raman spectroscopy using a different methodology, concluded that although the average MAC values varied between 3.9 and 7.4 $m^2 g^{-1}$, a value of 5.3 $m^2 g^{-}$

^{1} can be considered suitable for Central European troposphere (Nordmann et al., 2013). Liousse et al., 1993 have shown spatial variation in the MAC values and reported a value of 5 $m^2 g^{-1}$ for remote sites. Therefore, the reported values (5.03±0.03 $m^2 g^{-1}$) at 880 nm for ARIES, Nainital is also in agreement with these studies. However, it can be seen that albeit a good approximation, the use of a constant MAC can significantly bias BC estimates. This is especially important in remote mountainous sites where the difference in the operational and site-specific value of MAC can be large, as shown here and emphasized by Liousse et al., (1993).

MAC values at visible wavelengths in ambient conditions range from 4.6 to 11.3$m^2 g^{-1}$ in East and South Asia. (Cho et al., 2019). An urban site (Xi'an) in China shows a prominent seasonal variation in MAC with values being 20, 33.7, 29.1 and 27.6 $m^2 g^{-1}$ in spring (MAM), summer (JJA), autumn (SO) and winter (NDJF), respectively (Cao et al., 2015). The variations in Xi'an were explained to be due to the changes in the EC loadings and the contribution of the secondary sulphate-/nitrate rich particles. We find that similar to Xi'an, the variation in EC loading is responsible for changes in the MAC values (section 4.3.3). The MAC values do not show much variability over a high alpine station of Jungfraujoch and their values range between 8.9 and 10.9 $m^2 g^{-1}$ at 637 nm during four seasons (Lavanchy et al., 1999). Jungfraujoch's weak seasonality was attributed to the physical transformation of particles due to aged air received at the remote site. Relatively weaker seasonality in MAC over the central Himalayas is like the weak seasonality in Jungfraujoch. This is again suggested to be due to the absence of major emission sources in the surroundings and a receipt of aged emissions over this region (Bhardwaj et al., 2018).

4.3.6. Impact of MAC on eBC Estimates

Monthly variations in corrected (using the site and month specific MAC value) equivalent black carbon (eBC) and uncorrected (MAC value of 16.6 $m^2 g^{-1}$) eBC concentration is shown in Figure 4.7. The corrected eBC values were obtained by multiplying the absorption coefficient with the estimated MAC values given in Table 4.1 for 880 nm. Though the monthly variations between the two are more-or-less similar, the uncorrected eBC is significantly lower than the corrected one. Further, the difference is not constant during all the months. Corrected eBC is about 154% higher in September,

while it is as high as 358% in August. Therefore, it is important to use monthly varying site-specific MAC values that change with emission sources, mixing states and meteorological conditions including wind regime and humidity. Thus, the use of a constant MAC value for different months can give misleading results.

To assess the validity of the obtained eBC, a seasonal correlation of EC is made with the corrected eBC and also with uncorrected eBC (Figure 4.8). The determination coefficient for both ranges from 0.94 to 0.99 during four seasons however, the difference in slopes are quite large (Table 4.2). The slope of EC and uncorrected eBC ranges from 0.2 to 0.35 on average while the slope with corrected eBC showed a significant improvement and slope ranges from 0.78 to 1.05. This improvement in slopes lends credibility to the fact that the use of site-specific MAC leads to a generous improvement in the equivalence of carbon mass quantified from thermal and optical methods.

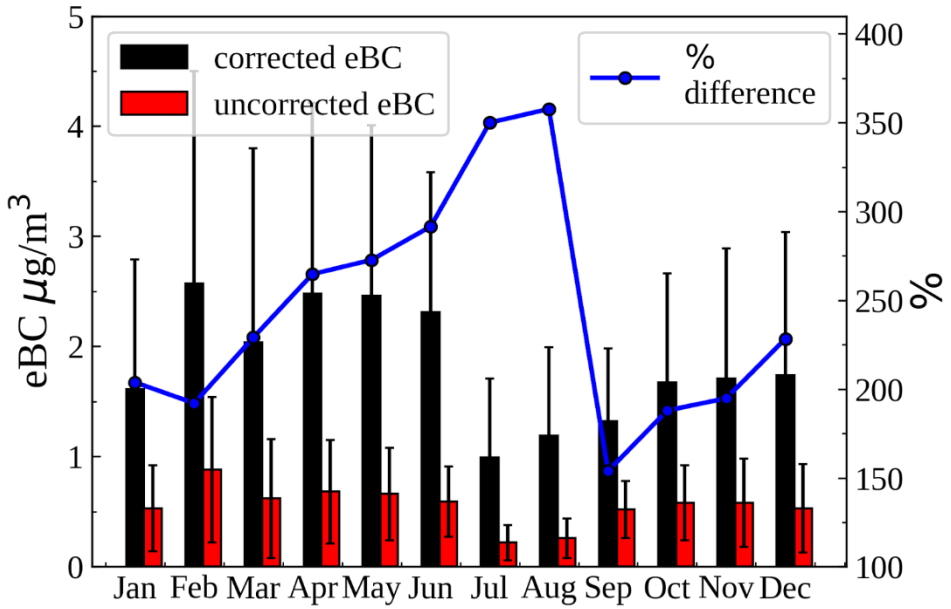

Figure 4.7 *Variations in monthly average equivalent black carbon (eBC) concentrations during the 2014-2017 period using the presently derived site and month specific MAC (corrected eBC) and standard MAC of 16.6m^2 g^{-1} (uncorrected eBC). Error bars in the plot represent one sigma standard variation. Monthly variations in the percentage difference between both are also shown.*

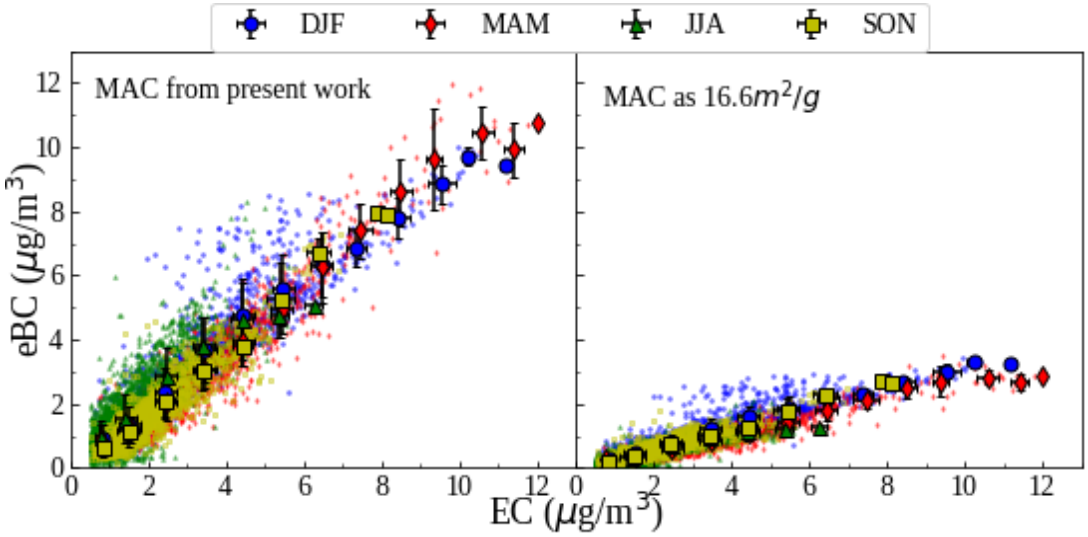

Figure 4.8 *The seasonal correlation between eBC and EC for 2014-2017. Left-hand side correlation is with corrected eBC (using site and month specific MAC values) and right-hand side correlation is with uncorrected eBC (MAC value of 16.6 m^2 g^{-1}).*

Table 4.2 *Statistics for correlation between eBC (corrected and uncorrected) and EC in four seasons during the 2014-2017 period.*

	Corrected eBC		Uncorrected eBC	
Season	**Slope**	**r^2**	**Slope**	**r^2**
DJF	0.87±0.03	0.99	0.3±0.01	0.99
MAM	0.96±0.04	0.98	0.26±0.01	0.97
JJA	0.78±0.09	0.94	0.2±0.02	0.94
SON	1.05±0.03	0.99	0.35±0.01	0.99

4.3.7. Impact on Aerosol Radiative Forcing (ARF) Estimation

An assessment of the impact of site and month specific MAC, derived in the present study, is also made on the estimation of aerosol radiative forcing. Aerosol radiative forcing is estimated for the corrected and uncorrected eBC, using an aerosol optical model known as Optical Properties of Aerosols and Clouds (OPAC, Hess et al., 1998) and SBDART model (Ricchiazzi et al., 1998). Optical properties such as aerosol optical depth (AOD), single scattering albedo (SSA), asymmetry function and angstrom exponent are required for ARF estimation in SBDART and have been derived using OPAC. This method of radiative forcing estimation is extensively used in many studies (Moorthy et al., 2009; Kumar et al., 2011; Gogoi et al., 2017) and has an ARF estimation accuracy of ±2 Wm^{-2} (Satheesh and Srinivasan, 2006).

The main aerosol components of the model are set as soot and other water-soluble and insoluble components as well as mineral (nuclei and coarse mode) for 50% RH. The measured annual EC concentration is used to represent soot in the model. The number densities of the other components are adjusted until the model estimated AOD, angstrom exponent and beta matches within 3% of the measured values obtained from the climatological (2005-2012) mean of both the parameters (Dumka et al., 2009; Joshi, 2015). The number densities of all these other components were then fixed for this model configuration and the optical properties were then derived for annual averaged corrected and uncorrected eBC. These number densities may not be unique but have been seen to successfully represent columnar aerosol properties (Moorthy et al., 2009).

These optical properties are used as an input in SBDART with a tropical model atmosphere and spectral surface albedo as a mixture of vegetation (80%) and sand (20%) following Kumar et al., (2011) and Pant et al., (2006). Radiative transfer calculations were performed daily for the whole year at hourly intervals from 6-18 hours with and without aerosols in the shortwave region (0.25-4μm). Diurnally averaged aerosol radiative forcing (net flux = down - up) at top of the atmosphere (TOA), surface (SUR) and atmosphere (ATM = TOA - SUR) obtained for the corrected and uncorrected eBC are shown in Figure 4.9. The magnitude of diurnally averaged TOA, surface and atmospheric forcing are 6.5±7.4 (3.9±6.5) Wm^{-2}, -32.9±13.1 (-27.7±10.8) Wm^{-2} and 39.5±18.2 (31.7±14.7) Wm^{-2} for corrected (uncorrected eBC), respectively. It could be seen that the use of corrected eBC for the site and month specific MAC, derived in the present study, leads to about 24.6 % higher atmospheric radiative forcing and it is about 66.7% and 18.8% higher for TOA and surface, respectively. This further indicates the need for proper MAC values while making radiation budget estimates utilizing eBC observations from optical attenuation techniques.

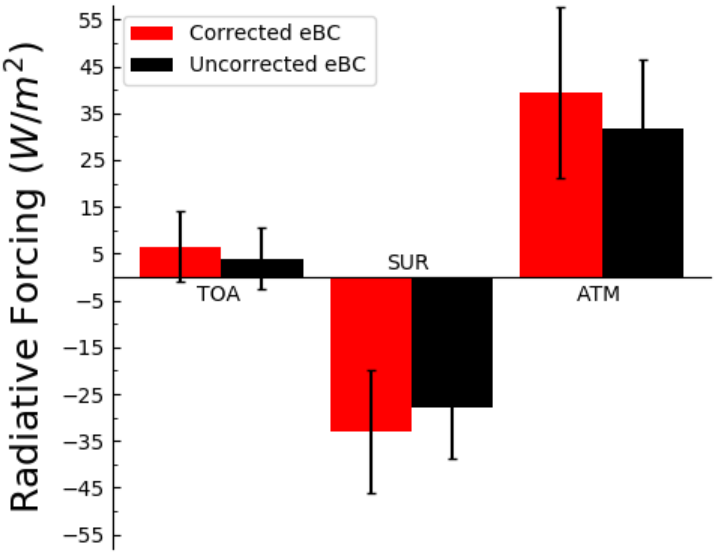

Figure 4.9 *Diurnally averaged clear-sky shortwave (0.25–4.0 µm) direct aerosol radiative forcing (Wm^{-2}) at the surface (SUR), in the atmosphere (ATM) and at the top of the atmosphere (TOA) for corrected eBC and uncorrected eBC.*

4.4. Conclusions

Accurate estimation of black carbon (BC) from the widely used optical attenuation technique is important for the accurate assessment of their climatic impact. The optical instruments use Mass Absorption Cross-section (MAC) for converting light attenuation records to BC mass concentrations and Aethalometer is a largely used optical instrument for BC estimation. Several studies have shown large variability in MAC values. It is thus necessary to examine the accuracy and consistency of MAC in Aethalometer over distinct geographic locations and seasons. In the present study, MAC values are derived using simultaneous observations (2014-2017) from an EC-OC analyzer and an Aethalometer (AE42) over a high-altitude central Himalayan site Nainital (29.4^{o}N, 79.5^{o}E, 1958 a.m.s.l.). The observations reveal that the annual mean value of MAC (5.03 ± 0.03 m^2 g^{-1} at 880 nm) is significantly lower than the constant value used by the manufacturer (16.6 m^2 g^{-1} at 880 nm). The estimated MAC values also showed significant seasonal variation, spanning over a magnitude from 3.7 to 6.6 m^2 g^{-1}. It is found that the seasonal variability of elemental carbon (EC), air mass variation and meteorology play an important role in the variability of MAC over this region. Multi-wavelength determination of MAC shows the contribution of absorption by species other than EC at shorter wavelengths. MAC does not show a clear diurnal variation, unlike EC and

absorption coefficient. The slope between EC and corrected equivalent black carbon (eBC) showed a significant improvement during all seasons when compared with uncorrected eBC. This lends credibility to the fact that the use of site-specific MAC leads to an improvement in the estimates of eBC over the central Himalayan region. It is found that the use of the MAC value supplied with the instrument, instead of using the site-specific MAC, leads to an estimate of lower (upto ~24%) radiative forcing (about 7.8 Wm^{-2}).

Chapter 5

Probing the Sources, Diurnal Variations and Radiative Forcing of Carbonaceous Aerosols Using High-resolution Ground-based Measurements

Now that the former chapters have answered the questions such as how the carbonaceous aerosols vary and have also corrected the BC estimates with site-specific MAC values. This chapter traces back the origins of the carbon-based aerosols and addresses the absolute scarcity in source apportionment studies with the capability of elucidating the diurnal scale phenomena in this respect. It reports the first high-resolution delineation of primary organic and secondary organic carbon and the foremost quantification of fossil fuel combustion and biomass burning fractions of BC over this region. It subsequently examines their temporal variations, underlines the need of forming a standard protocol for their segregation and finally quantifies the portions of transported pollutants, the influence of biomass burning and segregated impact on radiative forcing.

5.1. Introduction

Carbonaceous aerosols - Black carbon (BC) and Organic carbon (OC) have a substantial impact on health (e.g., Ostro et al., 2015) and climate (e.g., Zanatta et al., 2016) and constitute a major fraction of particulate matter (PM 2.5) (Malm et al., 2004). BC absorbs light and is known to be a significant contributor to radiative forcing (~1.1 Wm^{-2}), especially due to its direct as well as indirect effects on radiation and clouds, in addition to its potential to accelerate snow melting (Andreae and Gelencsér, 2006; Bond et al., 2013). Model simulations (1971–2010) suggested that absorbing aerosols, including black carbon, induced a significant increase in surface air temperature (0.2 – 2 °C), with higher warming in parts of the Western and Central Himalayas during spring (Sharma et al., 2022). This also led to an increase in atmospheric radiative forcing thereby resulting in a higher rate of snowmelt.

Globally, 7.6 Tg of BC is emitted, with 25% contribution coming from diesel combustion, 27% from domestic solid fuel emissions and 40% contribution from biomass burning (Bond et al., 2013). These fractions significantly vary between urban, remote, and rural environments (Venkataraman et al., 2005). One of the important reasons for uncertainties in the BC emissions and uncertainty in radiative forcing estimates is our inadequate knowledge about the contribution of fossil fuel combustion and biomass burning to the total BC (Rajesh and Ramchandran, 2017; Kant et al., 2020). Therefore, apportionment of the contribution of fossil fuel combustion and biomass burning to the ambient BC is crucial for better characterization of its impact on health, climate and the ecosystem. However, such source apportionment studies of BC, using long-term observational data, are not available over the central Himalayas, despite India being the second largest BC emitter in the world (Bond et al., 2013).

On the other hand, OC mainly scatters light, is hygroscopic and consists of organic compounds. It thereby acts as nuclei for cloud condensation (Safai et al., 2014 and references therein). Further, BC has only primary sources of emission while OC can have both primary as well as secondary sources of emission (Cabada et al., 2004). Vehicular emissions, coal burning, and biomass burning are the most common sources of both BC and primary organic carbon (POC). Secondary organic carbon (SOC) can be formed through volatile organic compounds (VOC), such as monoterpenes, isoprene, **β**-caryophyllene, and toluene (Tadeusz et al., 2010). Differentiating between the POC and SOC is essential for understanding atmospheric ageing of organic aerosols, radiation budget and formulating control policies (Wu and Yu., 2016). However, due to a lack of knowledge of the chemical composition of these aerosols at a molecular level, direct measurement of SOC is not feasible (Wu and Yu., 2016). Additionally, the determination of POC and SOC is very limited in the high-altitude Himalayan sites. Limited studies available from the region are either for a short period (Sharma et al., 2020, Kumar et al., 2021) or are offline (Ram et al., 2008, Sheoran et al., 2021). Although extremely informative, offline measurements hide the swift variation of aerosols at the diurnal scale and are subject to biases because of delay between sampling and analysis which increases the risk of contamination and artefacts due to the presence of volatile organic compounds. In fact, the only long term online POC-SOC concentrations available in the Indian region are from highly polluted urban sites like Delhi (Tiwari et al., 2013) and Pune (Safai et al., 2014).

To bridge this gap, long term, online and simultaneous measurements of equivalent black carbon (eBC), OC, EC and CO were conducted for four years during 2014-2017 at a high-altitude background site in the Central Himalayas. This paper presents the results of source characterization from these extensive observations which for the first time are able to reveal the diurnal scale phenomenon and is arranged in the following format. In Sections 2 and 3 we describe the characteristic features of the observational site, observed meteorology, instruments and other techniques utilised in this work. Results and their corresponding discussions are presented in section 4. Firstly, we use angstrom exponents in three different wavelength ranges and OC/EC ratio as an identifier of the various sources at the site. Then to quantify the contribution of various sources- we use four versions of the EC tracer method which delineate POC and SOC fractions in the total OC and present the foremost results with their diurnal variations in the Himalayas. These SOC and POC abundances from different methods are later inter compared to identify the differences and similarities amongst them. The relative abundances of biomass sources and fossil fuel components in eBC are also delineated for the first time in this region. Furthermore, we deduce the impact of radiative forcing due to these segregated fossil fuel combustion and biomass burning fractions of eBC segregated for forenoon, afternoon, and daily averaged periods. Then, we utilise concentration weighted trajectory analysis for all the four years divided into four seasons to identify the region and period contributing to the most emission at this site. Finally, we show the influence of biomass burning at this site by a specific event while demonstrating the successful working of the segregating methods. The main highlights from the study are subsequently listed in the conclusions section.

5.2. Results and Discussions

5.2.1. Source Identification Using Variations in Angstrom Exponent and OC/EC Ratio

In this procedure, we first qualitatively identify the dominant sources of emission during different months using the Ångström Exponent and OC/EC ratio. The Ångström Exponent (α) describes the strength of light absorption in each wavelength range and provides information about the predominant aerosol type or source (e.g., Sandradewi et

al., 2008, and references therein). Therefore, to identify the sources of black carbon, we derived α in three different wavelength ranges - short: (370 - 520 nm), long: (660 - 950 nm) and total: (370 - 950 nm), using slope in the power-law ($\lambda^{-\alpha}$) relations of absorption coefficient with wavelengths taken in the log scale. It has been shown by Sandradewi et al., (2008) that the wavelength dependence of the light absorption can be better approximated by these separate exponential fits where greater absorption in the lower wavelength range (370 – 520 nm) indicates biomass burning as the source and that in the higher wavelength range (660 – 950 nm) indicates an abundance of fossil fuel as the source. The seasonal variation of the percentage frequency distribution of α derived for the three aforementioned ranges during 2014 - 2017 is shown in Figure 5.1.

The results show that α values lying in the range of 0.75 - 1.25 have the maximum frequency of occurrence. Traffic or diesel emissions have α values between 0.8 and 1.1 (Sandradewi et al., 2008). Thus, the highest occurring α which is close to 1 and which is more pronounced in the longer wavelength range (Figure 5.1b), indicates an overall dominance of fossil fuel burning. The values of $\alpha < 0.75$ are more frequent in monsoon in all the wavelength ranges. These lower values are associated with the heavy rain (Figure 2.2) observed during this period which results in a washout of pollutants. Relatively higher values (α>1) occur during spring and winter (Figure 5.1c), particularly in April, and November (Figure 5.2). The values are even higher in the short wavelength range (370 - 520 nm). Such higher α values are observed in the case of emissions from biomass burning due to absorption by organic compounds in the ultraviolet and lower visible wavelengths (Kirchstetter et al., 2004; Day et al., 2006; Sandradewi et al., 2008). The influence of the crop-residue burning and forest fires in Northern India has been shown over this region during spring, while during winter, the contribution due to the increased emissions is found, most probably for heating purposes (Srivastava and Naja, 2021). Therefore, the relatively higher values of α observed during winter and spring at the site is consistent with this increased biomass emission and reaffirm their influence.

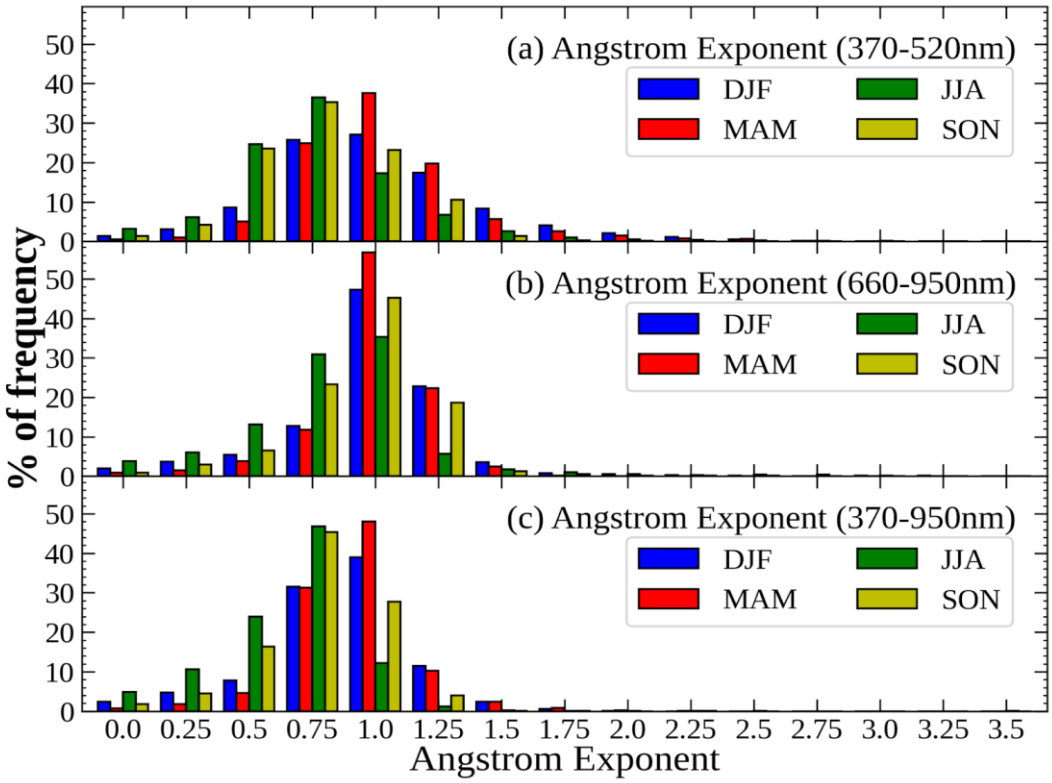

Figure 5.1 *Seasonal variation in the percentage frequency distribution of angstrom exponent for (a) lower (370-520 nm), (b) higher (660-950 nm) and (c) total (370-950 nm) wavelengths.*

In addition to the Ångström Exponent approach, the OC/EC ratios are used to assess the dominance of biomass burning and vehicular emissions and for the identification of relative abundances of SOC and POC. OC/EC ratio ranges from 2.7 to 4.4 over this region. Higher ratios of 3.5 to 4.4 are observed in April, May, early June, November, December, and January (Srivastava and Naja, 2021). Such higher ratios have been found to be usually associated with biomass burning (Saarikoski et al., 2008; Ram et al., 2010; Saud et al., 2013). These months with higher OC to EC ratios at the site are also consistent with the corresponding periods of large-scale biomass burning in northern India, due to crop-residue burning, forest fires as well as burning fuel for heating purposes. The lower ratios (<3) in other months denote a greater association with the burning of fossil fuel (Bernine et al., 2012; Tiwari et al., 2013; Safai et al., 2014). Thus, the impact of these biomass emissions is reflected in these higher OC to EC ratios while lower ratios indicate vehicular emissions which is otherwise the most prominent source of fossil fuel emission at the site. Furthermore, the OC to EC ratios during spring is observed to be greater than 2. Such OC to EC ratios (that is greater than 2) is found to be associated with the existence

of higher secondary organic aerosols (Chow et al., 1996) and hence indicate the presence of secondary aerosol formation in the region particularly in springtime.

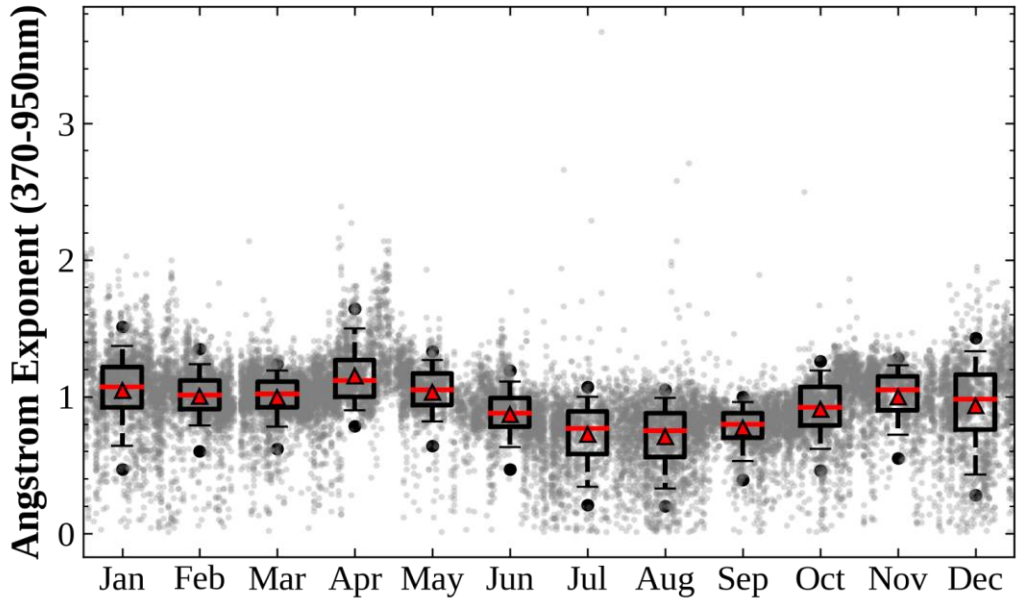

Figure 5.2 *Boxplot showing the monthly variation of angstrom exponent. Daily averages are shown in grey points. Triangles in the box represent the monthly mean and the red line shows the median. Box edges represent the 10 and 90th percentile, whiskers show the 5th and 95th percentiles.*

Both angstrom exponent and OC to EC ratios indicate the influence of SOC, biomass emission and fossil fuel sources thereby suggesting the need to quantify the impact of these sources in carbon aerosols at the site. Therefore, we evaluate the contribution of primary and secondary organic carbon in section 5.2.2.1 and the fractions of fossil fuel and biomass burning to the ambient eBC in sections 5.2.2.2 and 5.2.2.3.

5.2.2. Source Wise Quantification of Aerosols

5.2.2.1. Determination of Primary and Secondary Organic Carbon (POC and SOC)

In this section, we present a detailed account of the POC and SOC content obtained at the site. Since EC has only a primary source of emission and is co-emitted with the OC, it is widely used as a tracer to determine POC (Turpin and Huntzicker 1995; Cabada et

al., 2004; Ram et al., 2008; Safai et al., 2014; Wu and Yu, 2016). The basic principle involved in the EC tracer method can be expressed by the following two equations:

$$POC = [OC/EC]_{pri} \times EC + c \quad (5.1)$$

$$SOC = OC - POC \quad (5.2)$$

where SOC, OC, POC, $[OC/EC]_{pri}$ and c represent secondary organic carbon, total organic carbon, primary organic carbon, the ratio of primary OC to EC and contribution from non-combustion sources/sampling artefacts, respectively (Cabada et al., 2004). Determination of $[OC/EC]_{pri}$ is a key step in this method. This ratio varies vastly with sources and combustion types and different approaches are adopted in literature to determine $[OC/EC]_{pri}$. For example - Cabada et al., (2004) explicitly determined the period of primary and secondary emissions to obtain $[OC/EC]_{pri}$. Ram et al., (2008); Safai et al., (2014) have used seasonal OC/EC minimum ratio as $[OC/EC]_{pri}$ while Lin et al., (2009) have used regression excluding the rain period to get $[OC/EC]_{pri}$. On the other hand, Yao et al., (2020) used the minimum regression square method to find $[OC/EC]_{pri}$ while Yu et al., (2021) have used a bottom-up method.

To understand the temporal variation in POC and SOC at the site and to investigate the impact of using different methods for determining their concentrations, we apply four approaches to determine $[OC/EC]_{pri}$ in the EC tracer method. These four methods are now briefly described below. The first method referred to as 'TEN' implies calculating $[OC/EC]_{pri}$ from the lowest ten percentile of the observed OC/EC ratio. The second method which we refer to as 'REG' uses the regression slope of the OC vs EC plot as the $[OC/EC]_{pri}$. As opposed to 'TEN', this method may also represent the non-combustion sources since it considers the intercept in the above-mentioned regression plot while calculating POC. The third method to be called 'CAB' from now on, determines the regression slope as in the former but from the dataset in which a period of high SOC formation is removed (Cabada et al., 2004).

To ensure that the primary OC to EC ratio is dominated by the most probable period of primary OC-EC emissions and not from the periods of secondary emissions, or rain, we have employed an approach as suggested by (Cabada et al., 2004). In this method, firstly, the dataset with rain affected period was removed, following which, in the remaining set,

only the night-time (1900 to 0500 hours) data was used to avoid daytime periods of high secondary formations. Even in this filtered data set, we further confine our data only to the period of high correlation between eBC and CO (r^2>0.5, p<0.0001). This criterion of correlation is used to confine the dataset to a period of most probable high primary emissions. The slope thus determined from this approach is used in evaluating POC and hence SOC. The fourth method to be called 'MRS' from now on uses the Minimum Regression Square method to get $[OC/EC]_{pri}$ given by Wu and Yu., (2016); Wu et al., (2019). In this method, the OC/EC corresponding to the minimum r^2 (between EC and a range of possible SOC values) represents the actual $[OC/EC]_{pri}$ (Wu and Yu., 2016). In order to account for the diurnal dynamics, the $[OC/EC]_{pri}$ for each hour in a given month is calculated using MRS and then the minimum of these hourly $[OC/EC]_{pri}$ ratios is taken as the actual monthly value of the $[OC/EC]_{pri}$ (Wu et al., 2019). The methods are summarised in Table 5.1 below for a quick reference.

Table 5.1 *Summary of the methods used for SOC segregation.*

Method name	**Methodology**
TEN	10 percentiles
REG	Slope, intercept (all data)
CAB	Slope, intercept (all data – rain – night [19-5hrs] – r^2 < 0.5 [eBC vs CO])
MRS	Diurnal [min {r^2 (EC vs possible SOC) }]

The application of MRS requires the use of a monthly dataset. Hence, to maintain consistency in $[OC/EC]_{pri}$ calculation for various methods and to incorporate monthly variations better, we estimate the monthly $[OC/EC]_{pri}$ for the 2014-2017 period and then estimate SOC and POC from hourly EC-OC data for any given method. The value of $[OC/EC]_{pri}$ thus obtained from these methods are given in the supplementary Table 5.2.

Here, Figure 5.3 shows the averaged seasonal variation in SOC and POC obtained using four methods (MRS, CAB, TEN and REG) and Table 5.3 provides their monthly values. We notice some of the results are consistent in all these methods while they differ in others. First, we discuss the points consistent in all the methods here. Agreeably in all the methods, the annual POC concentration (>4.7 μg m^{-3}) is higher than SOC concentrations (<3.9 μg m^{-3}) in this central Himalayan region, though a few months SOC

is higher. Similarly, the annual POC/OC% (>64%) is also higher than SOC/OC% (<44%). This is consistent with a general prevalence of lower OC/EC ratios (<3), discussed previously and a general dominance of eBC_{ff}, as shown in the next section. Thus, implying the dominance of primary emissions in the region compared to the secondary sources. Seasonally, POC shows maximum values in spring and winter, mainly due to the lower concentrations observed during the rain-affected period of summer-monsoons and early autumn. Further, seasonally all four methods coherently show that the highest SOC concentration occurs during the spring season. Higher solar flux and higher temperature in this season which may induce greater photo-oxidation of VOCs, along with enhanced biomass burning as also shown by higher OC/EC ratio (>3) earlier, is the most likely reason for this enhanced SOC concentration.

Table 5.2 *Monthly values of [OC/EC]pri as obtained from REG, TEN, CAB and MRS methods.*

	REG	**TEN**	**CAB**	**MRS**
Jan	3.43	2.26	4.92	3.12
Feb	2.5	2.01	2.45	2.08
Mar	2.31	1.08	1.44	0.87
Apr	4.07	1.7	3.82	1.96
May	3.45	2.17	2.95	2.51
Jun	2.31	2.23	1.63	1.7
Jul	1.91	1.45	-	0.95
Aug	2.36	1.75	-	1.4
Sep	2.71	1.95	0.96	1.8
Oct	3.86	1.63	2.83	2.44
Nov	3.24	2.68	-	2.39
Dec	3.36	2.8	3.26	2.44

.

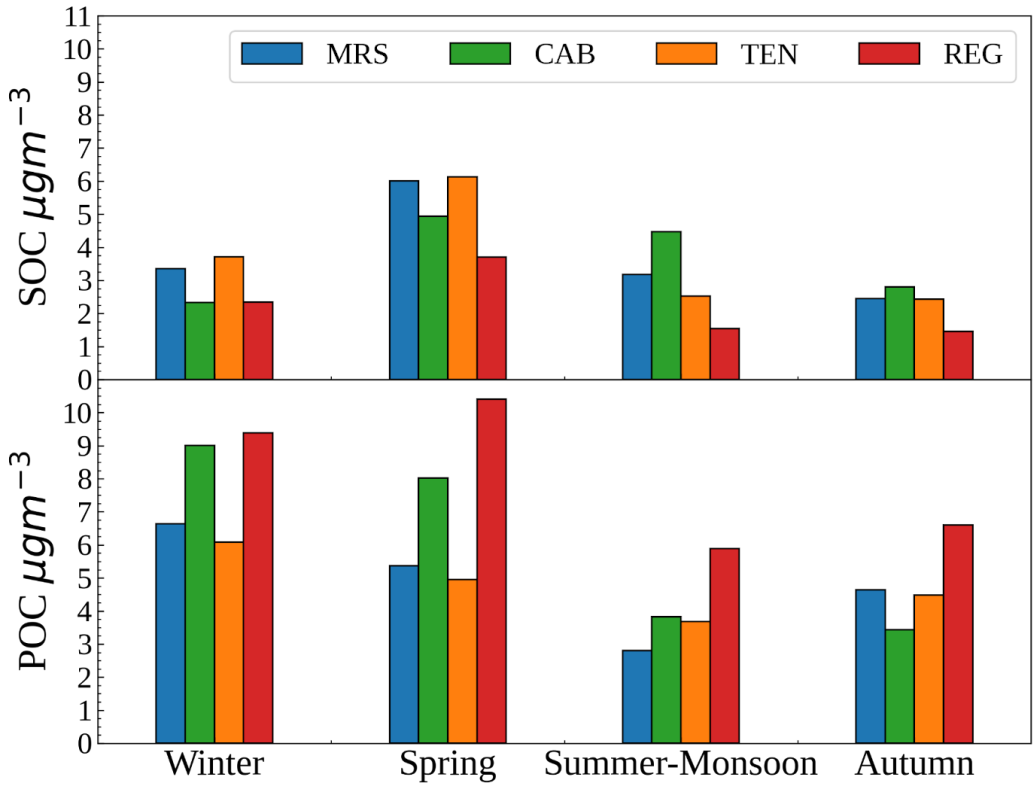

Figure 5.3 *The variation in SOC and POC obtained using MRS, CAB, TEN and REG methods averaged for the four seasons - winter, spring, summer-monsoon and autumn during 2014-2017.*

However, we find that although the four methods agree that this region is dominated by POC annually and a seasonal high value of SOC in spring, they show different variations, both in terms of seasonal changes and in terms of their concentrations. These variations amongst different methods are as follows. The average concentration of SOC is close to ~3.7 µg m^{-3} in MRS, CAB and TEN while it is as low as 2.4 µg m^{-3} in REG. The methods also show a greater variation in POC concentration i.e., ~ 4 µg m^{-3} in MRS and TEN while ~7 µg m^{-3} and 8 µg m^{-3} in CAB and REG, respectively. Additionally, REG and CAB show a similar seasonal variation of POC/OC%, i.e., higher POC/OC% in winter and spring followed by autumn and summer-monsoon. However, MRS and TEN show almost equivalent POC/OC% in all the seasons, with slightly higher percentages in winter and autumn. This higher sensitivity of REG and CAB towards POC is linked to the fact that in the method of CAB, the period of POC and rain is physically segregated while in the REG method, higher POC occurs due to the inclusion of the intercept denoting non-combustion emissions, especially in winter and spring when its seasonal values are the highest (intercept for winter, spring, summer-monsoon and autumn is 2.23, 1.18, 0.7-

0.92, respectively). Moreover, the use of slope leads to a higher OC/EC ratio which will be obtained from already formed secondary aerosols (Ram et al., 2008).

Table 5.3 *Monthly and annual averaged values for observed POC and SOC using four methods.*

	SOC (μg m^{-3})				POC (μg m^{-3})			
	MRS	**REG**	**CAB**	**TEN**	**MRS**	**REG**	**CAB**	**TEN**
Jan	3.9±3.8	3.5±4.0	3.6±4.2	5.2±4.1	7.0±4.1	9.7±4.6	11.0±6.5	5.1±3.0
Feb	3.0±2.2	1.9±2.0	2.3±2.0	3.2±2.2	6.6±4.0	9.2±4.9	7.7±4.8	6.3±3.9
Mar	6.0±4.3	2.3±1.9	5.1±3.2	5.7±3.9	2.7±1.7	8.4±4.4	4.5±2.8	3.4±2.1
Apr	7.8±7.7	6.2±7.0	6.2±7.0	8.2±7.9	5.9±3.3	12.4±6.8	11.4±6.4	5.1±2.9
May	4.6±4.8	3.5±4.6	4.2±4.6	5.0±5.0	6.9±3.8	10.4±5.3	8.1±4.5	6.0±3.3
Jun	4.3±2.8	2.1±2.8	4.5±2.9	3.4±2.6	4.0±1.9	8.2±2.6	3.8±1.8	5.2±2.5
Jul	1.9±1.1	0.8±0.6	--	1.6±0.9	1.0±0.4	2.9±0.8	--	1.5±0.6
Aug	1.8±1.2	1.0±0.8	--	1.5±1.1	1.6±0.7	3.3±1.1	--	2.0±0.8
Sep	1.8±1.1	0.9±0.7	3.2±1.5	1.6±1.1	3.2±1.1	4.8±1.6	1.7±0.6	3.4±1.2
Oct	2.2±2.2	1.4±1.6	1.8±2.0	3.1±2.8	5.0±2.3	6.1±3.7	5.8±2.7	3.3±1.6
Nov	3.4±3.2	2.4±3.7	--	2.8±3.1	6.2±3.2	9.4±4.3	--	7.0±3.4
Dec	3.2±2.2	1.5±1.8	1.7±1.7	2.41±1.9	6.2±3.2	9.3±4.4	8.3±4.3	7.2±3.7
Annual	3.9±4.1	2.4±3.5	3.9±3.7	3.9±4.2	4.7±3.4	8.1±4.9	6.8±5.2	4.7±3.1

After spring, SOC concentration is the highest during winter in MRS, TEN and REG, followed by similar concentrations in summer-monsoon and autumn. In CAB, SOC/OC% is higher in summer-monsoon and autumn followed by spring and winter. The lowest SOC/OC% is observed in the case of REG with negligible seasonal variation. MRS and TEN show the highest SOC/OC% in spring and summer-monsoon followed by winter and autumn. These variations in POC and SOC estimates from different techniques based on the EC-tracer method thus indicate the uncertainty in the organic carbon segregation.

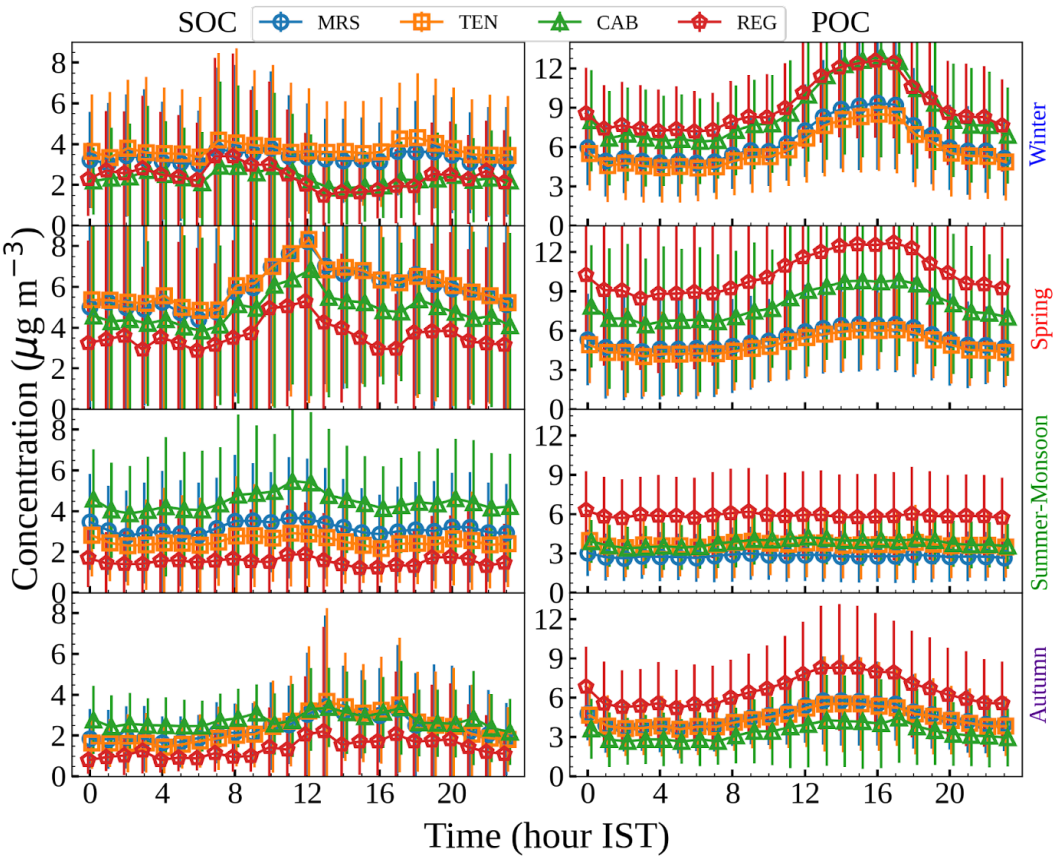

Figure 5.4 *The diurnal variation in SOC and POC obtained using MRS, CAB, TEN, and REG methods averaged for the four seasons winter, spring, summer-monsoon and autumn i.e., DJF, MAM, JJA and SON during 2014-2017. Error bars represent one standard deviation from the mean.*

The diurnal variation of POC and SOC from four methods is shown in Figure 5.4. Diurnally, it is evident that POC follows a unimodal variation during all seasons, except in monsoon, with a noontime maximum and a higher diurnal amplitude in winter and spring. EC and OC are also found to follow this same unimodal variation which occurs due to a rise in boundary layer height in the noon time (Srivastava and Naja, 2021). This covariation of POC with EC and OC suggests that most of the OC observed at the site is primarily emitted from combustion sources common to EC. The diurnal variation of POC and SOC is only reported by one more study in India which is from an urban site in Pune (Safai et al., 2014). However, the diurnal variation observed for both POC and SOC at Pune shows a bimodal variation (morning and evening peak concentration) which is typical of a low-lying urban site. In addition to highlighting the spatial heterogeneity in POC and SOC concentrations at sites with different topography and differences in emission sources, this also reflects on the fact that the primary emissions from the low-

lying sites during the daytime are transported to the cleaner high-altitude sites and enhance the primary concentrations observed at such sites.

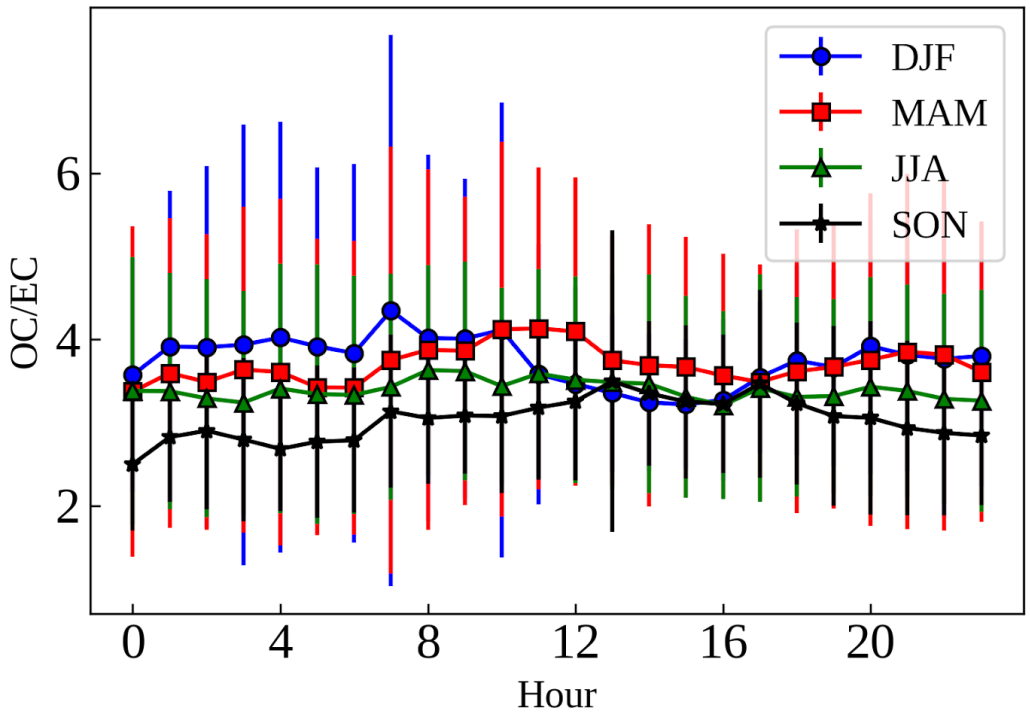

Figure 5.5 *The diurnal variation in OC/EC ratio averaged for seasons winter, spring, summer-monsoon and autumn i.e., DJF, MAM, JJA and SON during 2014-2017. Error bars represent one standard deviation from the mean.*

In comparison to POC, the noon peak in the diurnal variation of SOC is not prominent, except in spring. The highest noon time rise is observed during spring in all the methods. It is also found that the variation of SOC closely follows the diurnal variation in OC/EC (Figure 5.5). Many other studies have reported the covariation of SOC with OC/EC ratio and O_3 (Cabada et al., 2004, Safai et al., 2014). The covariation of SOC with O_3 can be explained by the fact that the oxidation of VOCs by O_3 is one of the important pathways of SOC formation (Lin et al., 2009). Further, O_3 is used as an important indicator of photochemical oxidation. It has been shown earlier (Kumar et al., 2010) that photochemical oxidation is low at the present observation site during the daytime compared to the urban sites, where a photochemical build-up of O_3 during the day is found. Thus, the observed daytime lower concentration of SOC is in accordance with this lower photochemical oxidation here and is in stark contrast to the higher daytime SOC in the low-lying urban sites.

Further, both POC and SOC show a higher diurnal amplitude in spring in all the methods. This rise in their amplitude during spring is linked to the increased solar flux and higher boundary layer height in the daytime during this period which supports both, the upward lift of pollutants from the low-lying polluted regions of the IGP and an increased photo-oxidation. Thus, from our present work, we find that all the methods agree in capturing broad features of the annual averaged variations, diurnal variations and in showing high SOC in spring and an overall low concentration in summer-monsoon. However, the results from the methods are much different when comparing their relative concentrations at monthly scales and while comparing their diurnal amplitudes. These differences are inherently linked to the procedures adopted in the methods, for example - the use of slope and intercept for the whole dataset made REG biased to POC. Further, we also notice that methods like TEN, REG and CAB are used for different study periods in the literature and do not provide a uniform quantifiable way of determining. It is also worth considering that this is a mere coincidence that selecting primary OC/EC ratios, based on different percentiles which themselves can range anywhere from 5-25 percentile, are able to represent the actual primary formation period and thus percentile methods may yield larger errors (Wu and Yu., 2016). Yao et al., (2020) also compared SOC from MRS and regression over 20% dataset and found that MRS gave smaller errors. We also found that MRS captures the major seasonal variations well and includes the diurnal variations too while selecting the primary period. Nevertheless, all this suggests that there is a need to formulate a standard protocol for determining the POC-SOC concentration to avoid the resulting ambiguity while comparing the concentrations from different SOC segregation methods.

In section 5.2.2.5, we explore the correlations of carbonaceous aerosols with other pollutants and meteorological parameters. Later, we also attempt to identify the influence of long-range transport and biomass burning. In all this analysis we continue to use POC and SOC from all the methods. This is done to examine the scenarios under which a generalized result can be obtained irrespective of the method considered and highlight the situations where the use of a given method may impact our interpretation of results.

5.2.2.2. Fossil Fuel and Biomass Burning

The absorption coefficient (b_{abs}) at a given wavelength denotes light absorption by aerosols and is proportional to $\lambda^{-\alpha}$ where α, depends on the emission sources i.e., fossil fuel or biomass. This relation can be employed for quantifying the source apportionment of ambient BC concentrations (Sandradewi et al., 2008) and has been used to study this aspect for a number of sites, like those at Athens (Kalogridis et al., 2018), Los Angeles Basin (Mousavi et al., 2018) as well as Ahmedabad (Rajesh and Ramchandran, 2017), Agartala (Kaur et al., 2020) and a number of other sites in India (Kumar et al., 2020). This method relies on two basic assumptions:

1. The total absorption coefficient (b_{abs}, total) at a given wavelength is simply the sum of the absorption coefficient due to fossil fuel combustion (b_{abs},ff) and biomass burning (b_{abs}, bb).

   b_{abs},total (λ) = b_{abs},ff (λ) + b_{abs},bb (λ). (1)

2. Absorption from burning of fossil fuel and biomass follows different spectral dependencies given by,

   $$\frac{b_{abs}ff(\lambda_1)}{b_{abs}ff(\lambda_2)}=\left(\frac{\lambda_1}{\lambda_2}\right)^{-\alpha_{ff}} \quad (2a)$$

   $$\frac{b_{abs}bb(\lambda_1)}{b_{abs}bb(\lambda_2)}=\left(\frac{\lambda_1}{\lambda_2}\right)^{-\alpha_{bb}} \quad (2b)$$

There are no combustion industries in the Nainital region and therefore the first assumption is valid to a high degree for the current site as the emissions from other sources are not significant. The second assumption is met since the absorption due to biomass burning dominates in the lower (370-520 nm) wavelength range while that due to fossil fuel combustion is the dominant term in the higher (660-950 nm) wavelength (described in section 5.2.1.). To avoid the absorption due to volatile organic compounds or other absorbing non-BC particles in the 370 nm channel, light absorption measurements are instead taken at $\lambda_1 = 470nm$ and $\lambda_2 = 950nm$ for source quantification (Zotter et al., 2017.). Ångström exponents for fossil fuel (α_{ff}) and biomass burning (α_{bb}) are chosen to be 0.9 and 1.68 as recommended by Zotter et al., (2017).

Using equations 1, 2a and 2b, the concentrations eBC_{bb} and eBC_{ff} can be determined as:

$$eBC_{bb}=\frac{b_{abs},bb(\lambda_2)}{MAC(\lambda_2)} \quad (5.3)$$

$$eBC_{ff}=\frac{b_{abs},ff(\lambda_2)}{MAC(\lambda_2)} \quad (5.4)$$

where,

$$b_{abs,bb}(\lambda_2)=\frac{b_{abs}(\lambda_1)-b_{abs}(\lambda_2)\left(\frac{\lambda_1}{\lambda_2}\right)^{-\alpha_{ff}}}{\left(\frac{\lambda_1}{\lambda_2}\right)^{-\alpha_{bb}}-\left(\frac{\lambda_1}{\lambda_2}\right)^{-\alpha_{ff}}} \quad (5.5)$$

$$b_{abs,ff}(\lambda_2)=\frac{b_{abs}(\lambda_1)-b_{abs}(\lambda_2)\left(\frac{\lambda_1}{\lambda_2}\right)^{-\alpha_{bb}}}{\left(\frac{\lambda_1}{\lambda_2}\right)^{-\alpha_{ff}}-\left(\frac{\lambda_1}{\lambda_2}\right)^{-\alpha_{bb}}} \quad (5.6)$$

and the monthly MAC (950 nm) values for the present sites are taken from Srivastava et al., (2021).

Using the method described above, hourly values of eBC_{bb} and eBC_{ff} are estimated and diurnal variations during twelve months are shown in Figure 5.6. Additionally, Table 5.4 gives their monthly and annually averaged values, along with that of eBC.

Table 5.4 *The table provides the monthly average values of observed eBC, eBC_{ff}, eBC_{bb} and the percentage contribution of eBC_{ff} and eBC_{bb}.*

	eBC µg m^{-3}	**eBC_{ff} µg m^{-3}**	**eBC_{bb} µg m^{-3}**	**$\%BC_{ff}$**	**$\%BC_{bb}$**
Jan	1.72 ± 1.26	1.2 ± 1.04	0.52 ± 0.47	69 ± 19	31 ± 19
Feb	2.61 ± 1.93	2.11 ± 1.78	0.5 ± 0.38	77 ± 15	23 ± 15
Mar	2.1 ± 1.79	1.72 ± 1.6	0.38 ± 0.35	79± 12	21 ± 12
Apr	2.53 ± 1.75	1.68 ± 1.31	0.85 ± 0.92	67 ± 21	33 ± 21
May	2.59 ± 1.58	1.9 ± 1.14	0.69 ± 0.74	74 ± 16	26 ± 16
Jun	2.48 ± 1.26	2.09 ± 1.11	0.39 ± 0.43	84 ± 14	16 ± 14
Jul	0.8 ± 0.61	0.72 ± 0.6	0.08 ± 0.07	86 ± 14	14 ± 14
Aug	0.81 ± 0.64	0.72 ± 0.61	0.09 ± 0.13	86 ± 13	14 ± 13
Sep	1.23 ± 0.63	1.12 ± 0.61	0.11 ± 0.14	90 ± 12	10 ± 12
Oct	1.67 ± 1	1.35 ± 0.89	0.31 ± 0.31	80 ± 14	20 ± 14
Nov	1.77 ± 1.19	1.34 ± 1.02	0.43 ± 0.32	74 ± 14	26 ± 14
Dec	1.83 ± 1.32	1.4 ± 1.21	0.43 ± 0.35	72 ± 20	28 ± 20
Annual	1.97±1.54	1.53±1.3	0.44±0.52	77 ± 17	23 ± 17

.

The concentrations of eBC, eBC_{ff} and $eBC_{bb,}$ exhibit a strong unimodal diurnal variation (Figure 5.6). Such unimodal diurnal variation is expected for a cleaner site, where the sources are not in proximity and are largely governed by the changes in the boundary layer height. The maximum eBC concentrations are observed in the afternoon when the boundary layer is fully evolved, and it brings the pollutants from the sources in the low altitude regions. The decrease in observed eBC concentration starts as the sun sets when

the boundary layer height decreases, and the minimum concentrations are thus observed at night.

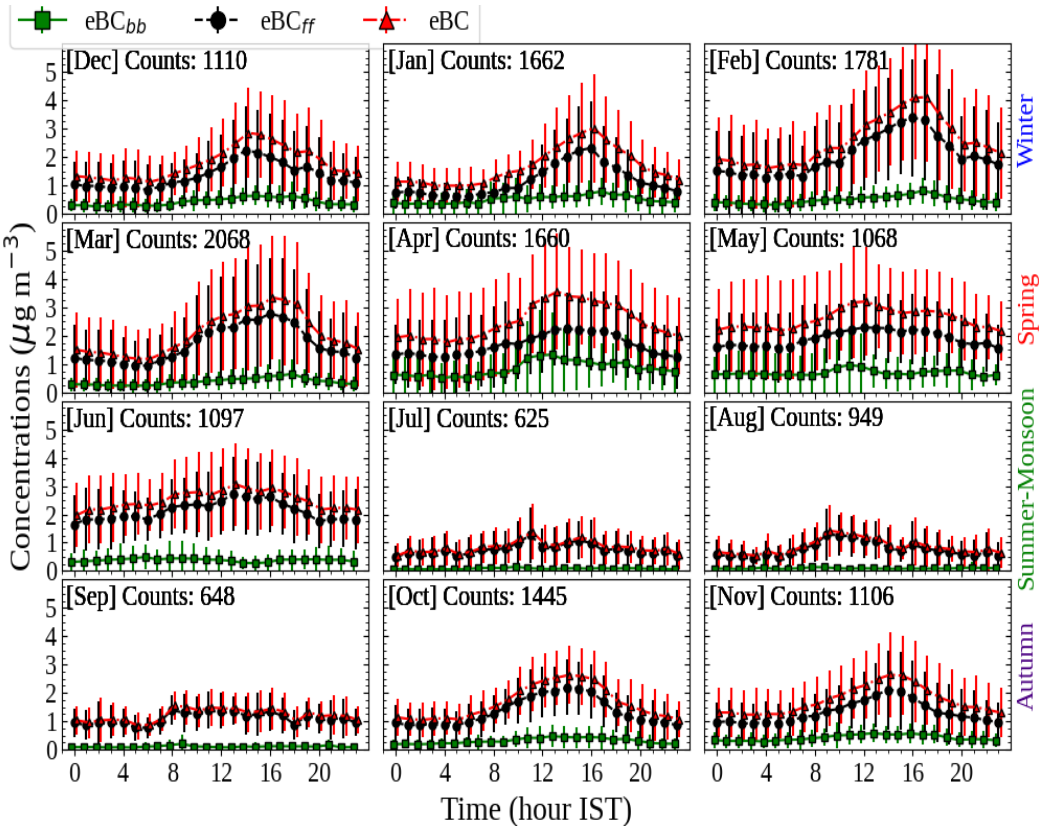

Figure 5.6 *Diurnal variations of eBC and its fossil fuel (eBC$_{ff}$) and biomass burning (eBC$_{bb}$) components. Data counts in each month are also given.*

The diurnal variation in both eBC$_{ff}$ and eBC$_{bb}$ consistently follows the diurnal variation in total eBC and they too have a noontime maximum. Such variations peaking during noontime at this site is in complete contrast with the bimodal diurnal variations observed at low lying urban sites of Pantnagar (Joshi et al., 2016), Delhi (Tiwari et al, 2013) and Ahmedabad (Rajesh and Ramchandran, 2017) which are found to have maximum concentrations during morning and evening. The bimodal variation at these urban sites is attributed to the fumigation effect of the boundary layer and the increase in anthropogenic activities during morning and evening. Furthermore, at these urban sites, eBC$_{ff}$ shows a higher contribution during the night and early morning while the higher contribution from eBC$_{bb}$ is found during morning and evening hours.

Additionally, it is shown that the contribution of fossil fuel (eBC_{ff}) is dominant (67-90%) when compared with the biomass burning (10-33%) in monthly (Table 5.4) and diurnal scale (Figure 5.7). Thus, indicating that the emissions from sources such as automobile and industrial combustion contribute much more than biomass burning, which includes forest fire and crop residue burning.

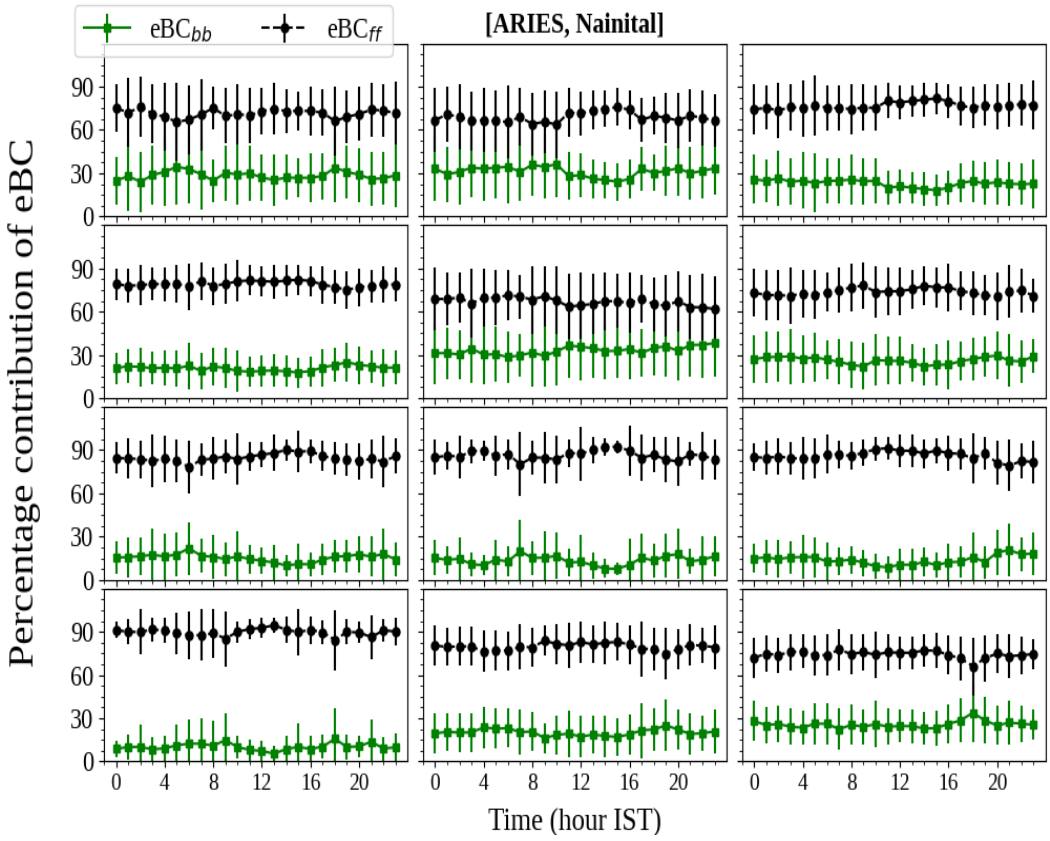

Figure 5.7 *Diurnal variation of the percentage contribution of fossil fuel (eBC_{ff}) and biomass burning (eBC_{bb}) components.*

Figure 5.8. shows monthly variations in the average diurnal amplitude of eBC_{ff} and eBC_{bb}. It is found that the difference between both the diurnal amplitudes reduced very significantly, reaching a minimum (0.17 - 0.33 µg m^{-3}), during April and May. The percentage difference between eBC_{bb} and eBC_{ff} also drops to the lowest value of 9-32% in April-May. This signifies the relative importance of biomass emissions at a diurnal scale during the spring months. This increased influence of biomass emissions also reflects in the monthly scale and is consistent with the increased fire counts in the Northern Indian region (Figure 5.9). The lowest diurnal amplitude of eBC_{ff} and eBC_{bb} is found during summer-monsoon due to the washout because of rain in this period. The

same effect of rain is also visible in the monthly scale. Additionally, the lowest fires in this period result in a much lower contribution from biomass emissions.

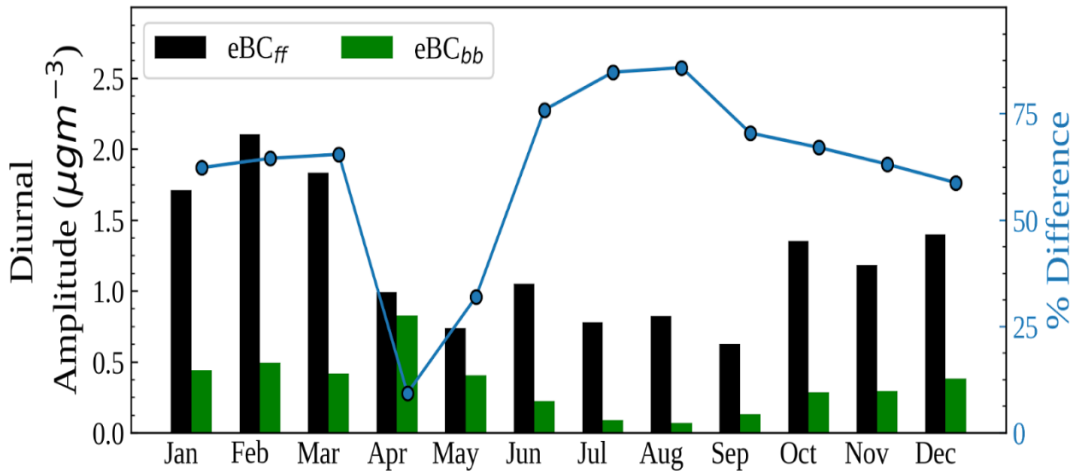

Figure 5.8 *Monthly variations in the diurnal amplitudes of eBC$_{ff}$ and eBC$_{bb}$ observed in the central Himalayas during 2014-2017. The percentage difference between them is also shown.*

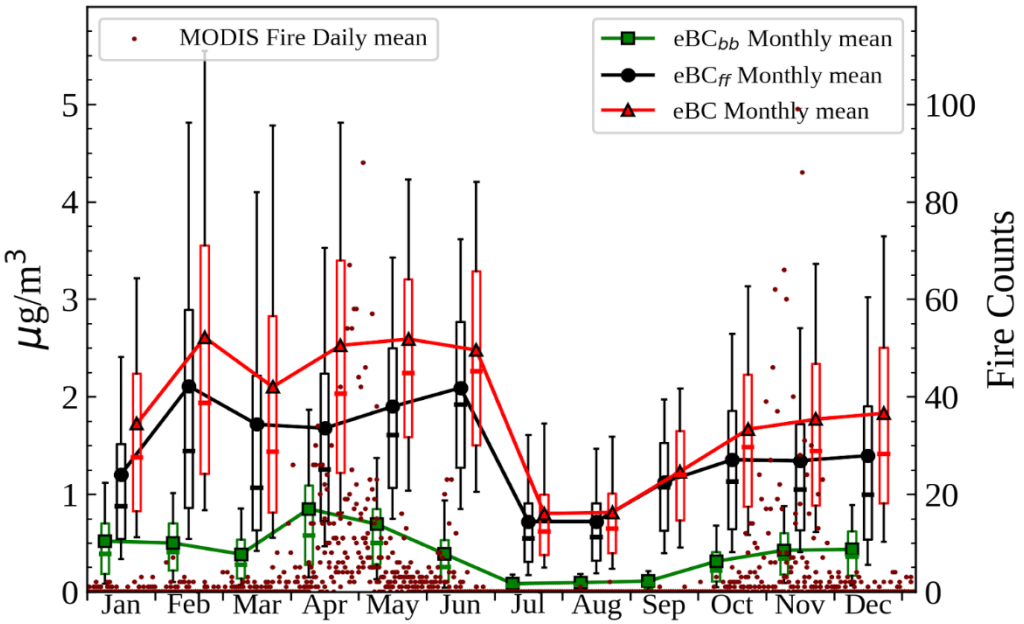

Figure 5.9 *Monthly averages in eBC, eBC$_{ff}$, and eBC$_{bb}$. Fire counts in the region 24-34^{o}N, 70-90^{o}E from MODIS are also shown as a bar plot in the secondary y-axes.*

Fossil fuel fraction (eBC$_{ff}$) closely follows the monthly variation in ambient eBC in general. The annual averaged fossil fuel component is higher than the biomass component with an eBC$_{ff}$ of 1.53±1.3 µg m^{-3} and eBC$_{bb}$ of 0.44±0.52 µg m^{-3}. This implies that the contribution of eBC$_{ff}$ is ~3.5 times higher than that of eBC$_{bb}$ annually. Nainital is a hill station hence a tourist destination, attracting a large flux of tourists. As

a result, influences of vehicular emissions could become the most important source of eBC at the site. In an otherwise clean atmosphere, devoid of any other major emitting sources, these emissions show up significantly and this is the most likely cause for the higher components arising from fossil fuel combustion (eBC_{ff}) in all the months as shown in Figure 5.9. Furthermore, it has been shown that the low-lying sites of the IGP have a higher contribution associated with fossil fuel in general (Kumar et al., 2020). Thus, when the boundary layer height flushes pollutants from these low altitude sites in the daytime to our sites, they are richer in the fossil fuel emissions and hence we find that in all the months, fossil fuel emissions prevail the eBC concentration.

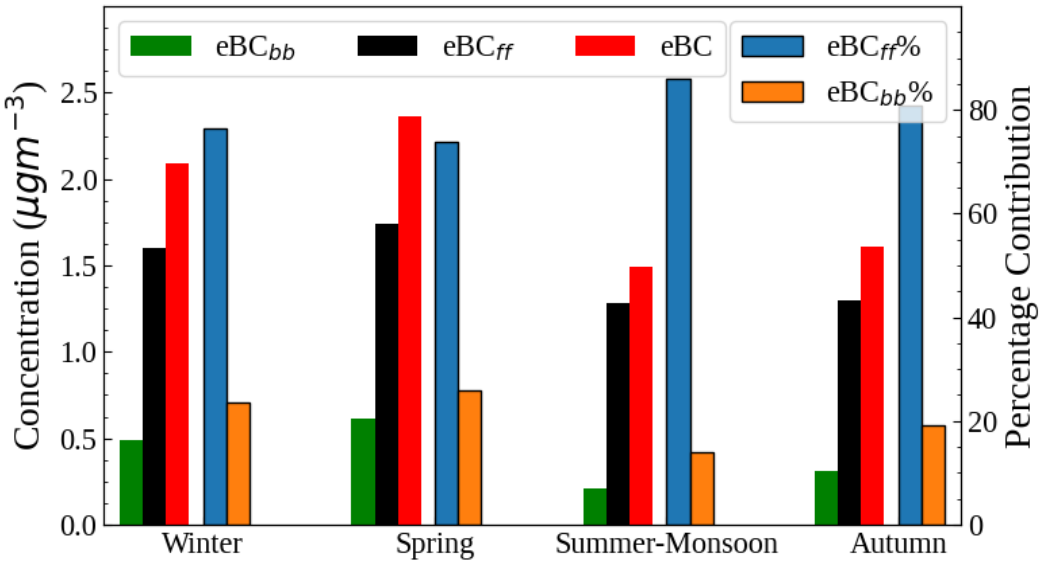

Figure 5.10 *The concentrations of eBC along with fossil fuel (eBC_{ff}) and biomass (eBC_{bb}) components during four seasons over the central Himalayas during 2014-2017. Percentage contributions of eBC_{ff} and eBC_{bb} are also shown.*

The seasonal average concentrations arising from both fossil fuel (1.3±1.1 µg m^{-3}) and biomass (0.2±0.3 µg m^{-3}) components of eBC are minimum during the monsoons (Figure 5.10) consistent with the impact of the heavy precipitation during this period (Figure 2.1). Seasonally, the lowest eBC_{bb} percentage of ~15% is also observed during monsoons resulting as a direct consequence of the least fires in this period, which is also evidenced from Figure 5.9. The biomass burning component peaks during spring with an average concentration of 0.6±0.7 µg m^{-3} due to the rise in the long-range transport of emissions from crop residue burning during this period in the Northern Indian region. We have examined this influence further in sections 4.2.5 and 4.2.6. These results thus hereby

quantify the temporal variation of emissions due to the burning of fossil fuel and biomass at the site. We now utilize these observations to estimate the impacts on radiative forcing and eBC emissions from a top-down approach.

5.2.2.3. Impact of eBC and its Fossil Fuel and Biomass Components on Aerosol Radiative Forcing (ARF)

In this section, we estimate the impact of eBC together with its fossil fuel and biomass fractions, on aerosol radiative forcing. For this, we first utilize an aerosol optical model: Optical Properties of Aerosols and Clouds (OPAC, Hess et al., 1998) to get the optical properties such as AOD, SSA, asymmetry function and angstrom exponent. These optical properties are then fed to the Santa Barbara Discrete Ordinate Atmospheric Radiative Transfer model (SBDART, Ricchiazzi et al., 1998) for ARF estimation. OPAC and SBDART have been widely used for ARF estimation in former studies (Satheesh et al., 2002; Moorthy et al., 2009; Gogoi et al., 2017).

The main aerosol components used in OPAC are - soot, water-soluble, insoluble and mineral (nuclei and coarse mode) at 50% RH. Averaged eBC concentrations for the whole period are used as the representative of soot in OPAC. For other components, the number densities are adjusted so that there is a match of upto 3% between the model estimated and measured climatological (2005-2012) mean values of AOD and angstrom exponent (Dumka et al., 2009; Joshi, 2015). These number densities are then rendered fixed in the model and the optical properties are derived for averaged eBC, eBC_{ff} and eBC_{bb}. It has been shown earlier that although these number densities might not be unique, they successfully represent the columnar aerosol properties (Moorthy et al., 2009). Optical properties are then used as input to SBDART which is run with a 'tropical' atmosphere and spectral surface albedo of - 80% vegetation and 20% sand following Pant et al., (2006) and Kumar et al., (2011). Daily RF calculations are performed in the shortwave region (0.25-4μm) for the whole year at hourly intervals in three categories namely (i) diurnal (6-18 hours) (ii) forenoon (6-9 hours) and (iii) afternoon (14-17 hour), for both with and without aerosols (separately for eBC_{ff} and eBC_{bb}).

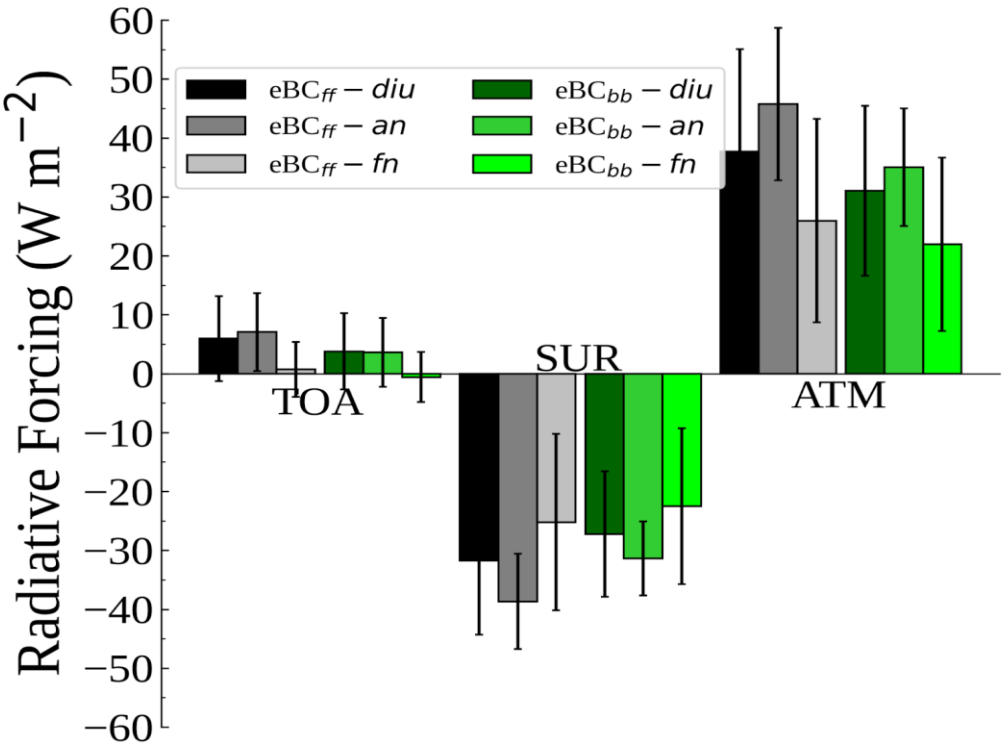

Figure 5.11 *Diurnally averaged, forenoon (fn) (0600 - 0900 hours) and afternoon (an) (1400 - 1700 hours), clear-sky shortwave (0.25–4.0 µm) direct aerosol radiative forcing (Wm^{-2}) at the surface (SUR), in the atmosphere (ATM) and at the top of the atmosphere (TOA)) for eBC$_{ff}$ and eBC$_{bb}$.*

The diurnally averaged aerosol radiative forcing calculated at top of the atmosphere (TOA), surface (SUR) and atmosphere (ATM) obtained for eBC$_{ff}$ and eBC$_{bb}$ are shown in Figure 5.11. The magnitude of diurnally averaged TOA, SURF and ATM forcing are 6.8±7.5, -33.5±13.3, and 40.3±18.6 Wm^{-2} for eBC, respectively. Further analysis reveals that the maximum fraction of RF comes from the fossil fuel fraction for TOA, SURF and ATM forcing (5.9±7.2, -31.7±12.6, and 37.6±17.42 Wm^{-2}) when compared with that from biomass fraction (3.7±6.4, -27.3±10.6 and 31.01±14.4 Wm^{-2}), respectively. These results reveal that the maximum fraction of RF comes from the fossil fraction. Further, it is found that the fossil fuel component leads to about 16.4 %, 13.3% and 32.0% higher radiative forcing than that from biomass fraction at ATM, SURF and TOA, respectively. This implies that reduction in fossil fuel combustion is more effective in mitigating the adverse effect of positive atmospheric radiative forcing over this region.

It is evident that the afternoon RF is significantly higher at TOA (6.3 and 4.2 Wm^{-2}), SURF (-13.4 and -8.8 Wm^{-2}) and ATM (19.8 and 13.0 Wm^{-2}) than the forenoon one in

eBC_{ff} and eBC_{bb} respectively. Thus, the results show less effect of biomass in noon time and further highlight that the emission from fossil fuel is of much greater concern compared to that due to biomass, when doing radiative forcing estimates. Moreover, the results underline the importance of afternoon radiative forcing at the site. Previous studies have shown that atmospheric radiative forcing may increase by 10-16% when aerosol diurnal variations are taken into account (Reddy et al., 2015). This also shows that incorporating high-resolution measurements is particularly essential while studying aerosol-radiation interaction over the high-altitude Himalayan sites.

5.2.3. Correlation of Carbonaceous Aerosols

Figure 5.12 shows the correlation of POC and SOC concentrations with eBC, eBC_{ff}, eBC_{bb} and boundary layer height. It is found that eBC_{ff} exhibits a high correlation ($r^2 \geq 0.5$ and slope ≥ 1.5) with POC derived from all four methods. On the contrary, the correlation between eBC_{ff} and SOC is low ($r^2 < 0.1$ and slope <0.2) in all the methods. This is as expected since both POC and eBC_{ff} are emitted primarily from incomplete combustion as opposed to SOC. Moreover, these results enforce confidence in the segregation schemes employed since we arrive at the expected conclusions using two independent segregation methodologies: optical (eBC_{ff} and eBC_{bb}) and thermal (POC and SOC). These results are also strengthened by a higher correlation of POC found with eBC compared to SOC.

For correlations between eBC_{bb} and POC-SOC, we found that 95 percentiles of eBC_{bb} data lie below 1.5 μg m^{-3} and therefore we show here the eBC_{bb} data between 0-1.5 μg m^{-3} instead of the full range (0-3 μg m^{-3}) to avoid the impact of outliers. Results show that in general, the correlation of eBC_{bb} with POC was lower than that with SOC for all the methods. In fact, for MRS, TEN and REG, the r^2 is greater than 0.9 between eBC_{bb} and SOC while r^2 is lesser than 0.6 for regression between eBC_{bb} and POC from MRS, TEN and CAB, thus, implying that the secondary organic content is better correlated with the biomass burning fraction. This happens because biogenic volatile organic compounds are associated with SOC formation (Tadeusz et al., 2010) unlike fossil fuel emissions. It is also found that the SOC has a higher correlation (r^2~0.7 for three methods) with mixing layer height compared to that with POC (r^2<0.1) implying that the SOC formation is linked more to the rise in mixing layer height compared to POC. This is reasonable

because SOC formation is more likely to be favoured in cases of higher ageing which are associated with greater mixing layer heights. The results, therefore, highlight that the POC emissions at the site are associated with eBC_{ff} emissions while the SOC emissions are associated with eBC_{bb} and higher mixing layer height.

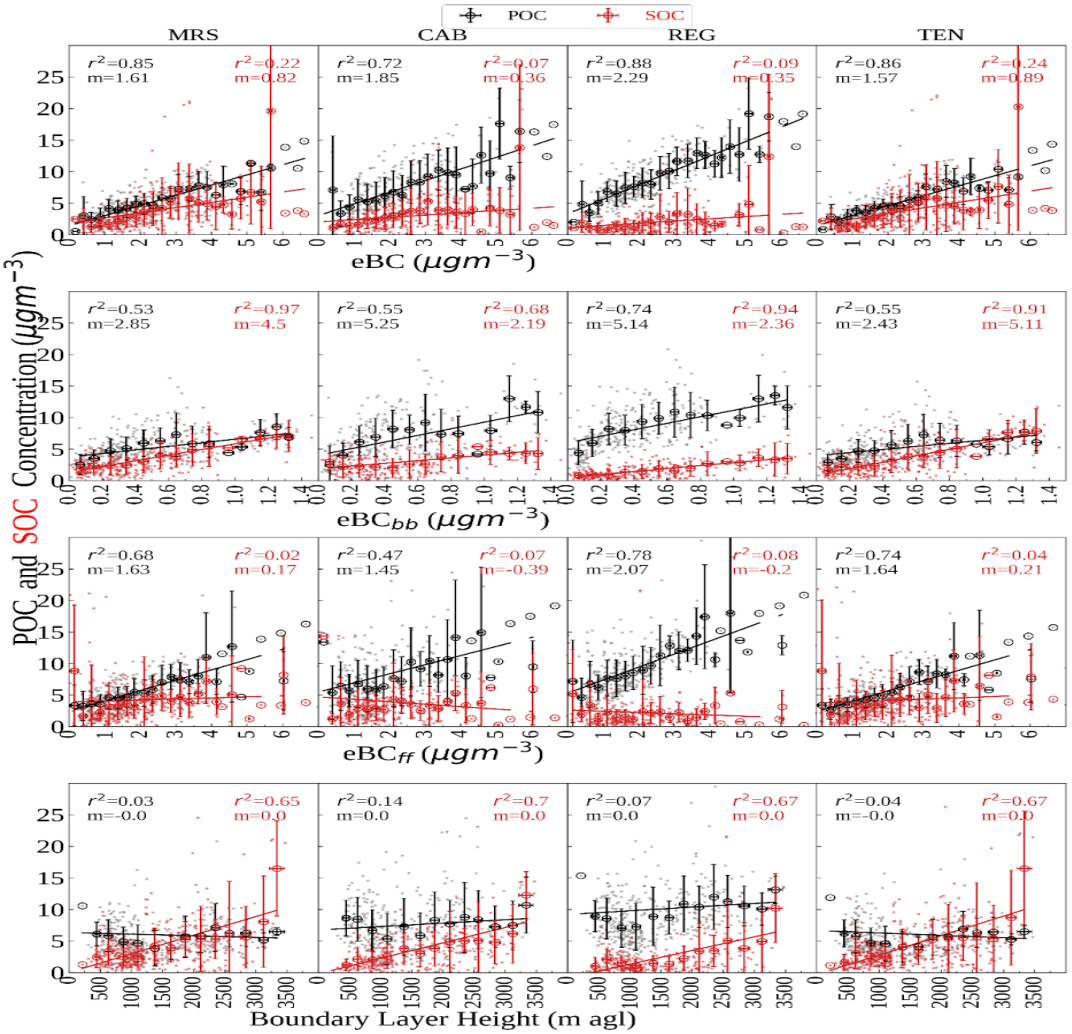

Figure 5.12 *Correlation of POC and SOC concentrations (obtained from four methods) with eBC, eBC_{ff}, eBC_{bb} and the boundary layer height during 2014-2017.*

5.2.4. Source Region Identification

In this section, we quantify the contribution of the eBC transported with the air masses arriving at the site using concentration weighted analysis (CWT). The method and information on the used input data are described in section 2.3.1. Figure 5.13 shows the concentration weighted trajectories of eBC averaged during four seasons of the 2014-2017 period. The weighted concentrations in µg m^{-3} indicate the potential eBC contribution level of each grid. In general, it is evident from the figure that the higher

eBC concentrations observed at the receptor site are mainly associated with the air masses from the north-western regions of the IGP. The greatest contribution of these higher concentrations ($\geq$2μg m^{-3} shown in orange and red) are observed during spring followed by winter. These potential source zones lie coherently with the sources of fossil fuel combustion such as factories, power plants, transportation activities which are located at the densely populated urban core of the IGP. However, these are relatively constant sources of emissions. The higher concentrations are also a result of the high fire events in IGP which are associated with the seasonal stubble burning that mainly occurs twice a year - in spring and with the onset of winter. In addition to this seasonal nature of biomass emissions, the higher wind speed and greater convection during spring support the transport of pollutants even from far off regions of the IGP to the site, despite its high altitude.

It is also evident that since for any other season, the convection and wind speed is relatively lower than that during spring, the pollutants transported to the site also remains lesser. Lower concentrations ($\leq$ 2μg m^{-3}) observed during autumn are a likely result of this pattern. It is important to note that given the dominance of north-westerly trajectories at the site, most of the pollutant transport is from the north-western IGP region. Additionally, the area of pollutant transport is the least during the summer monsoon. This is particularly due to the fact that this period is associated with heavy rain spells brought to the region by the southwest monsoon winds which are of the cleaner oceanic region. Much lesser concentrations (<1.5μg m^{-3}) are associated with the air masses arriving from regions farther from India. The results thus reveal that even at this high altitude, the site is considerably affected by the transported pollutants from the north-western IGP region and biomass-burning events, especially during spring. We now assess the impact of such a biomass burning event on carbonaceous aerosols in the next section.

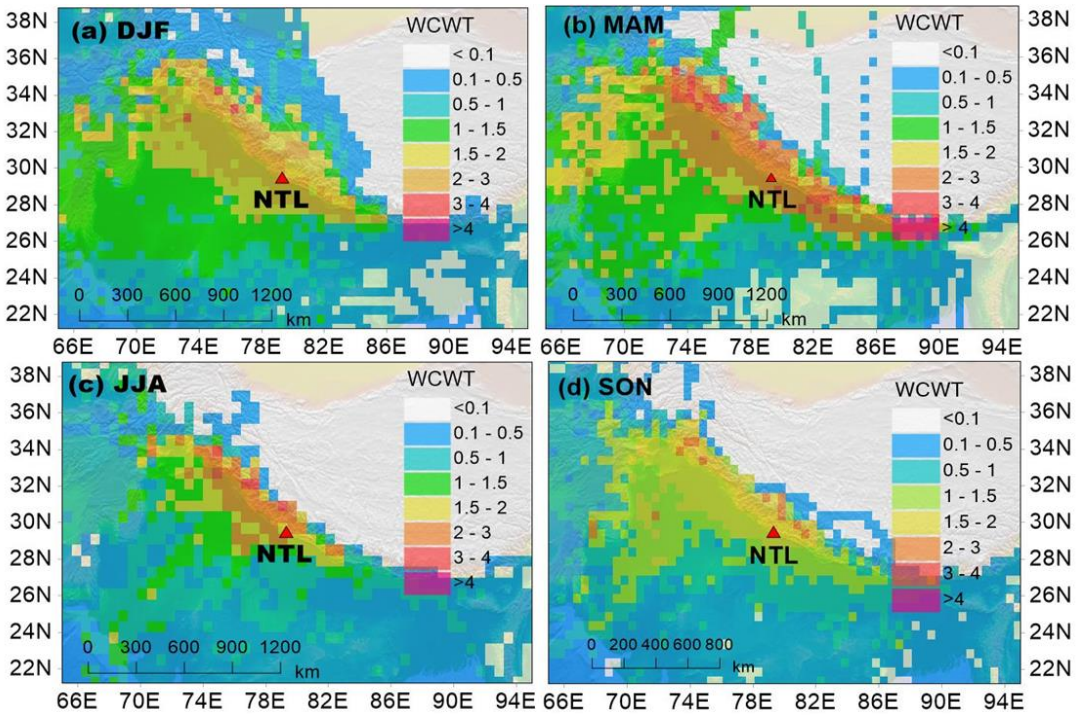

Figure 5.13 *Concentration Weighted Trajectories of eBC for seasons winter, spring, summer-monsoon and autumn i.e., DJF, MAM, JJA and SON during 2014-2017.*

5.2.5. Influence of Biomass Burning on eBC, EC, OC, eBC_{bb}, POC and SOC

To explore the impacts of biomass burning on concentrations of carbonaceous aerosols, we analyse an event of rising fire emissions from 19 Apr 2016 to 04 May 2016 as shown in Figure 5.14. MODISv6.2 fire data (https://firms.modaps.eosdis.nasa.gov/) for the night-time (since it has greater sensitivity, Bhardwaj et al., 2016) with a confidence level greater than 80% is taken for the region 24^{o}N to 35^{o}N and 70^o to 89^{o}E. A systematic rise in the fire events is observed from 22 April to 1 May 2016. The fires in the North-western region are mainly associated with the few cropland regions in the states of Punjab, Haryana, Himachal, and Uttarakhand where fires for crop residue removal are common during this period. The backward trajectories show that the air mass arrives at the site from the north-western region in both the low (22 Apr) and high (1 May) fire days. Thus, the emissions from these fires have a very high probability of being transported to the site with the north-westerly air masses. The impact of this transport is evidenced by the near simultaneous enhancement in the carbonaceous aerosols during this period. The OC concentration on 30 May almost doubled from its concentration on 22 Apr. The OC/EC ratio also rose around the same period from 4.6 to 7.9. When the fire events on 22 Apr

were lower than 30, the SOC concentrations were also less than 10 μg m^{-3} in all the methods. As the fire counts gradually rose to as high as 257 on 01 May, simultaneously, the SOC concentration also crossed over 20 μg m^{-3} in all the methods. These SOC concentrations were much greater than the POC ones which are usually found to

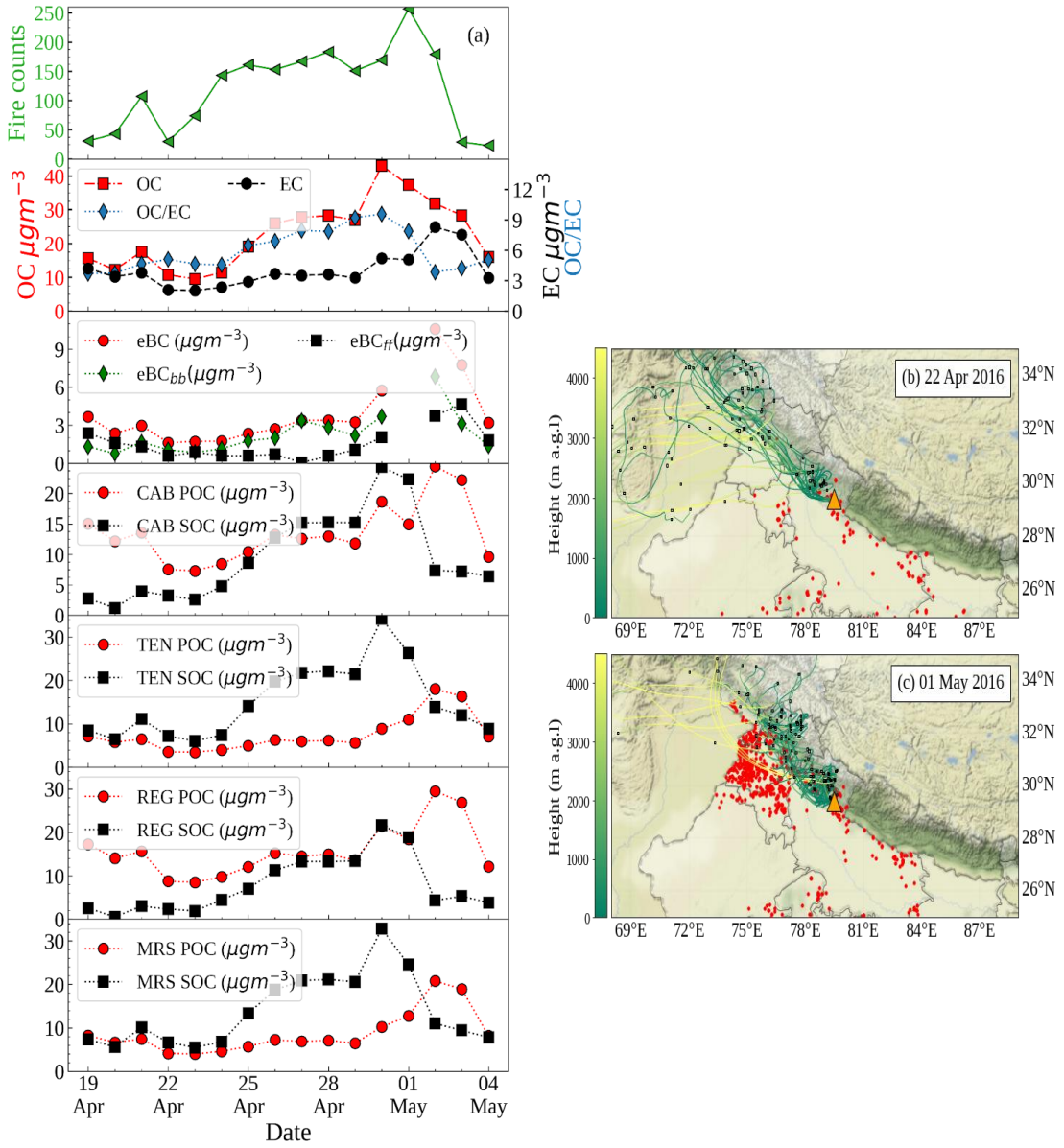

Figure 5.14 *(a) Fire counts, OC, EC, OC/EC, eBC, eBC_{ff}, eBC_{bb}, POC SOC from CAB, TEN, REG and MRS during 19 April - 5 May 2016. Locations of fires (red dots) observed from MODIS and 5-day backward, 27-member ensemble, trajectories reaching the observation site (orange triangle) on (b) 22 April and (c) 01 May 2016. The black squares within trajectories are marked at the interval of 24 hours. The colour bar on the left shows the height of the trajectory.*

dominate the OC fraction at the site. Thus, suggesting that the biomass emissions are associated with higher SOC formations.

Further, the magnitude of this rise in SOC with fire events varied in different methods. It is clear that MRS and TEN showed greater sensitivity and the fraction of OC allotted to SOC is higher compared to POC. However, the difference in POC and SOC concentrations is comparatively lesser in CAB and REG during the fire events. Similarly, the eBC_{bb} concentration which is usually lower than the eBC_{ff} component at the site also enhanced to levels higher than those of eBC_{ff} with the rise in fire events. Cloud-Aerosol Lidar and Infrared Pathfinder Satellite Observation (CALIPSO) aerosol subtype imagery

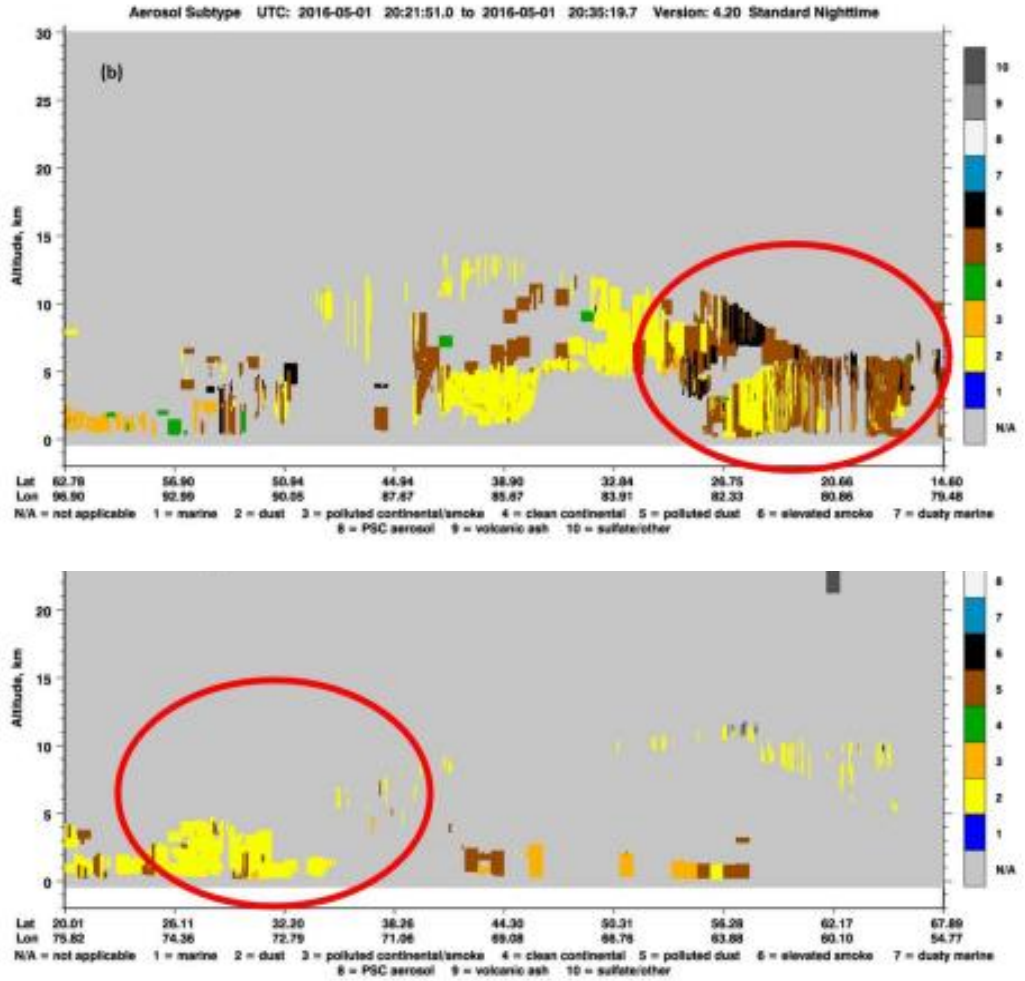

Figure 5.15 *Aerosol subtype with altitude observed by CALIPSO near the study region encircled in red during (a) low fire (22 April) and (b) high fire (1 May) days.*

(Figure 5.15) during this period (01 May) around the site also reveals the presence of elevated smoke and polluted dust. However, such elevated smoke aerosols are not classified (supplementary Figure 5.14a) during the low fire period (22 May). These results clearly emphasize the importance of biomass burning emissions which lead to

significantly higher concentrations of carbonaceous aerosols at otherwise cleaner high-altitude sites.

5.3. Conclusions

Several studies have reported about the transport of carbonaceous aerosols which adversely impact health and climate from the polluted regions of Asia and Europe to the pristine and vulnerable Himalayan region. Yet to date, there remains a dearth of source apportionment studies that can elucidate the diurnal scale phenomena with respect to emission sources, quantification of transported pollutants, the influence of biomass burning and radiative forcing. Therefore, in this work, we report the first high-resolution delineation of primary organic carbon (POC) and secondary organic carbon (SOC) contents in total organic carbon (OC) and the foremost assessment quantifying the relative contributions of fossil fuel combustion and biomass burning to equivalent black carbon (eBC) over the Central Himalayas using four-year (2014-2017) online observations. The deconvolution of OC to POC and SOC is performed using four methods, all of which consistently show that POC (>64%) with a prominent unimodal diurnal variation dominates over SOC (< 44%) at an annual time scale. However, these methods show large intra-annual variations: POC 64-116%; SOC 20-44% and suggest a need for having a standard protocol for POC and SOC determination. Further, it is shown that the contribution of fossil fuel combustion (eBC_{ff}) is 3.5 times greater than that of biomass burning (eBC_{bb}). The impact of transported pollutants and biomass burning on carbonaceous aerosols at the site is evidenced using four-year concentration weighted trajectories analysis and study of a specific high-fire event. Radiative forcing estimates are made at a diurnal scale, and it is shown that eBC_{ff} contributes more (16.4 %) atmospheric forcing than eBC_{bb} and that the noon time atmospheric forcing of both eBC_{ff} and eBC_{bb} is higher (19.8 and 13.0 Wm^{-2}, respectively) than that of the forenoon one. It is shown that incorporating high-resolution measurements is particularly essential while studying aerosol-radiation interaction over the high-altitude Himalayan sites.

Chapter 6

Application of Black Carbon Measurements to Quantify Contribution of Sources of Carbon Monoxide

Black carbon is co-emitted with other key pollutants such as CO during the incomplete combustion of carbon-based fuels. This chapter highlights the discrepancies between the ground-based CO measurements and the CO estimates from both satellites and the regional chemistry model simulations over the complex Himalayan terrain. It then takes leverage from the long term multiwavelength BC measurements made at the site and the source apportionment of BC done to estimate the sources of CO which are otherwise not known from any ground-based measurements currently in India. Later these source apportionment results are compared against the WRF-Chem CO tracer runs.

6.1. Introduction

Black carbon (BC) and Carbon monoxide (CO) are emitted primarily as a by-product of incomplete combustion processes (e.g., forest and agricultural fires, power generation, automobile combustion) and other anthropogenic activities. BC is an absorbing aerosol also known to be the second most important climate change forcer as a result of its direct and indirect effects (Bond et al., 2013). Thus, a number of studies have been conducted in the past investigating BC, its transport and characterising its sources (Satheesh et al., 2002; Moorthy et al., 2004; Ramanathan and Carmichael, 2008; Bond et al., 2013; Bhardwaj et al., 2021). On the other hand, CO also plays a critical role in atmospheric chemistry by removing the hydroxyl radical from the atmosphere (Novelli et al., 1998) and influences the mixing ratios of key greenhouse gases such as methane and ozone (Wigley et al., 2002). It is emitted in the atmosphere by both natural (oxidation of hydrocarbons, oceans and plants) and anthropogenic sources (fossil fuel and biomass burning) (van der Werf et al., 2010). Anthropogenic sources account for more than half of global CO emissions (Granier et al., 2011).

It has also been observed that anthropogenic emissions have rapidly increased in the past decades due to urbanisation and industrialization. During 1950-2011, the anthropogenic CO emissions increased from 57.2 to 323.2 Tg $year^{-1}$ over Asia (Kurokawa and Ohara, 2019). The highly populated region of the Indo Gangetic Plain is a hub of several anthropogenic activities including power plants, transportation, mining, domestic cooking, crop-residue burning, etc and thereby produces enormous amounts of CO (Beig and Ali, 2006; Guttikunda et al., 2014).

Further, while most of these emissions do not vary during the course of the year, the CO emissions from crop residue burning in the Northern Indian region and Northeast India are seasonal and peak during April-May and October-November (Venkataraman et al., 2006; Kumar et al., 2011). These result in spatiotemporal variability in CO emissions. Considering its crucial climatic and health impacts, it is essential to quantify the contribution of these anthropogenic/natural sources to the ambient CO for formulating effective mitigation strategies in the Northern Indian region. However, the information about CO budget and source attribution is associated with several uncertainties and large discrepancies are found between different emission inventories (Park et al., 2015).

Numerous *in-situ* measurements of CO in India have been made in the past over the low altitude rural and urban environments (Lal et al., 2000; Naja et al., 2002; Beig et al., 2007, Ojha et al., 2012; Yarragunta et al., 2020), high-altitudes (Sarangi et al., 2014; Bhardwaj et al., 2018; Kumar et al., 2019) and marine regions using ship-borne observations (Sahu et al., 2006; Srivastava et al., 2012b; Mallik et al., 2013). To capture the vertical profile, aircraft-based measurements have also been used (Allen et al., 2004; Sahu et al., 2016) alongside satellite-based observations (Girach and Nair, 2014; Yarragunta et al., 2019). The above-mentioned observations have provided important insights into the spatial and temporal variation of CO, its vertical structure, and the influence of convection and continental outflows on pristine environments. However, only a limited set of studies have tried to understand the influence of the sources of CO over the Indian region (Kumar et al., 2013; Yarragunta et al., 2019; Nandi et al., 2020; Bhardwaj et al., 2021) and all these are based on regional-chemical models. These model-based studies do provide important information on the atmospheric processes, variability and transport of CO responsible for pollution episodes but show a significant deviation of about 29 to 97% from the ground observations over different urban sites (Nandi et al.,

2020). Furthermore, these models have higher biases (>25%) over the Indian Himalayas, whose pristine environment is vulnerable to the outflows from the IGP region (Bhardwaj et al., 2021). Thus, the uncertainties in the source apportionment over the Himalayan region remain large and this can be mainly ascribed to the paucity of *in-situ* observations, required to test and constrain the model-based simulations.

To this end, the present work aims to demonstrate the use of ground-based observations of BC to segregate and quantify the fossil fuel and biomass burning CO components. In the course of this chapter, we start by showing the results of comparison among the CO mixing ratio from reanalysis product, satellite observations and regional model simulations against the ground-based measurements over this high-altitude Central Himalayan region to establish the need for a ground observation-based method in determining the CO sources. Then we utilise the four years long (2014-17) ground-based ambient BC and CO measurements to delineate and quantify the fossil fuel and biomass burning CO components. Following this, we discuss the nature of this estimated CO against the observed CO and use the model parameters to predict CO for 2018, which is also compared against observed CO for 2018. WRF-Chem CO tracer runs are also utilized to delineate the CO sources over the site and present the comparison between the two segregation methodologies. We finally summarise the main points from this study in the conclusions section.

Measurements of carbon monoxide (CO) are made using Cavity Ring-Down Spectroscopy (CRDS) from Picarro G2401 analyser (Picarro Inc., CA, USA). CO observations from Horiba APMA 370 trace gas analyzer which is based on non-dispersive IR method, are also used during 2014-2015 wherever Picarro data was not available, after a thorough regression between the two. Continuous measurements of the mass concentration of BC are made in real-time using a seven wavelength (0.37-0.95μm) Aethalometer (AE42) from Magee Scientific, USA. Further, MERRA2 reanalysis surface CO data ($0.5° \times 0.625°$) from Jan 2014–Dec 2017 using version 5.12.4 of the Goddard Earth Observing System Model (GEOS-5) are also utilized. Model (WRF-Chem) simulated CO data are used from Jan 01, 2014, to Dec 31, 2015, with a time step of 60 s after discarding the first month of model output as a spin-up period. In the present study, MOPITT version-9, Level-2 retrieval products of CO are utilized from 2014 to 2017. Here, only the daytime retrievals are used as they provide better thermal contrast

conditions compared to night time (Deeter et al., 2017). More details on the ground-based instruments, reanalysis data, model and satellite data are already provided in Chapter 2.

6.2. Results and Discussions

6.2.1. Comparison of CO From MOPITT, WRF-Chem and MERRA-2 Against Ground-Based Observations

The observed surface CO are compared against MOPITT surface CO in Figure 6.1 (top) for 2014-2017 period. Observed CO shows large monthly variation with low mixing ratios in July and August, and higher mixing ratios during April and May. Both show a reasonable agreement, particularly in late autumn and in the months of November, December and January. MOPITT CO is unable to reproduce the higher values in the spring months. Very high mixing ratios are shown by MOPITT in the months of August and September while mixing ratios are shown to be low during April and May, a pattern contrary to the observations. The percentage difference between the observed and the MOPITT CO also has a significant monthly variation and ranges from about -25% in May to about +60% in August.

Surface average CO mixing ratio from MERRA-2 and observations for the 2014-2017 period are shown in Figure 6.1 (bottom). MERRA-2 does not show significant monthly variation with a mixing ratio of about 100 ppbv in almost all the months. MERRA-2 is thus not only unable to capture the monthly variation but also underestimates the actual mixing ratio throughout the period. The percentage difference between the mixing ratios of CO from observed and MERRA-2 is always greater than 25% and even exceeds 50% in the month of May when the site has the highest observed CO mixing ratio.

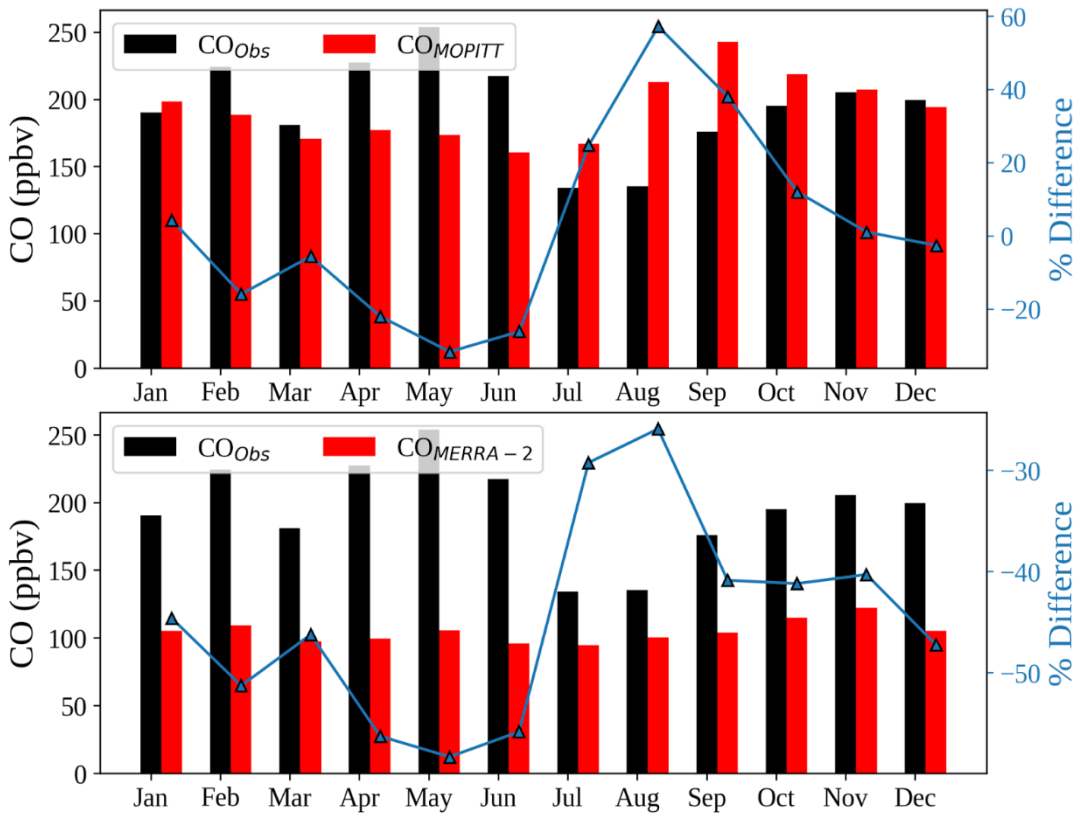

Figure 6.1 *Monthly averaged surface CO mixing ratios from (top) MOPITT and (bottom) MERRA-2 for a 0.5°x0.5° region around the site (Nainital) and those from observations are shown in red and black bars respectively. The % difference between the two is also shown on the secondary axis.*

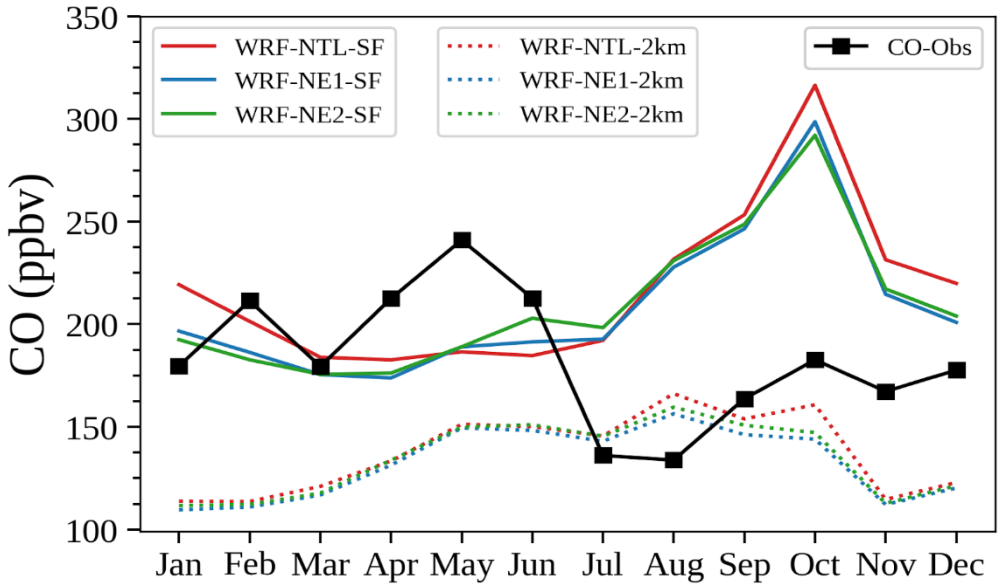

Figure 6.2 *Monthly averaged surface (solid lines) and two km (dashed lines) CO mixing ratios from WRF-Chem for NTL-Nainital, NE1-0.1° North East of NTL, NE2-0.2° North East of NTL and those from in-situ observations (black line with square markers) at the site are shown.*

Figure 6.2. shows the comparison of the seasonal cycle of CO at the site simulated from WRF-Chem at the surface of Nainital (79.45^{o} N, 29.36^{o} E) for the year 2014 with the *in-situ* measurements. It is clear that the model is unable to capture the monthly variation of CO at the site. We observed that the model's altitude (1309 m) of the site does not match the site altitude of 1950 m. Therefore, we made sensitivity tests by comparing the simulated CO mixing ratios with two other locations - NE1 (79.55^{o}, 29.46^{o}, model terrain-1560 m) which is about 0.1^{o} Northeast of NTL and, NE2 (79.65^{o}, 29.56^{o}, model terrain-1696 m) which is about 0.2^{o} Northeast of NTL. We also compared the simulated mixing ratios at 1950 m altitude for the three locations (shown with dashed lines as NTL-2km, NE1-2km and NE2-2km in Figure 6.2). We find that none of the simulations is able to capture the seasonal variation in observed CO. In fact, all the simulations for 1950 m altitude for NTL, NE1 and NE2 are in general always underestimating the observed CO mixing ratios and unable to capture the springtime high and monsoonal low in the observed CO mixing ratios. Further, contrary to the observations, these simulations show a higher mixing ratio in the monsoon and a lower mixing ratio in winter and monsoon. This inability of the model to replicate the CO variations can be attributed to the complex topography of the region which makes it difficult to capture the microscale processes at a coarse resolution, uncertainties and inaccuracies in emission inputs and uncertainties associated with parameterization of physical processes.

The above analysis suggests that the current satellite measurements, reanalysis products and model simulations might not accurately reproduce the temporal variations in CO over this high-altitude site in the Himalayan region. Further, although the surface observations represent the ground truth, they lack in their ability to delineate the markers of different sources which is feasible with the regional chemical models. These results thus underline the importance of methods based on ground observations to deconvolve the fraction of different sources in the ambient CO mixing ratios. We present the results from one such approach in the subsequent sections at this site.

6.2.2. Evaluation of the Applicability of Multiple Regression Method CO Estimates

A method for the source apportionment of CO was described by Kalogridis et al., (2018) using BC and CO in the multiple linear regression model. This Method makes use of the

fact that both CO and BC are produced by similar combustion processes and if both CO and BC have a good correlation, then CO/BC ratios can be regarded as equivalent to their source emission ratios and the total CO mixing ratio may then be expressed as the following:

$$[CO]=[CO]_{bgd} + r_{ff}\times[eBC]_{ff} + r_{bb}\times[eBC]_{bb} \quad (6.1)$$

where eBC_{ff} and eBC_{bb} are estimated using spectral dependence of light absorption by the emissions from fossil fuel and biomass burning from a method developed by Sandradewi et al., (2008) and used successfully in several other studies (Favez et al., 2010; Zotter et al., 2017; Dumka et al., 2018; Kant et al., 2020). During the course of this study, the eBC measurements and their fossil fuel (eBC_{ff}) and biomass burning (eBC_{bb}) fractions are also estimated (Srivastava et al., 2022) for the 2014-2017 period and discussed in section 6.2.5. The mixing ratio of background CO ($[CO]_{bgd}$), r_{ff} and r_{bb} can be calculated by a multiple linear regression model. Finally, using these values CO fractions of fossil fuel (CO_{ff}) and biomass burning (CO_{bb}) can be deduced as:

$$[CO]_{ff}= r_{ff}\times[eBC]_{ff} \quad (6.2)$$

$$[CO]_{bb}= r_{bb}\times[eBC]_{bb.} \quad (6.3)$$

The hypothesis of equivalent emission ratios of CO and eBC is largely true for the present site as a strong correlation between eBC and CO is observed ($r^2>0.9$) in all the seasons (Figure 6.3a). Additionally, for the model to work, it is essential that there is no significant correlation between eBC_{ff} and eBC_{bb}, so that they can be treated as independent of each other. At the same time, the CO mixing ratio should be well correlated with both the independent variables eBC_{ff} and eBC_{bb}. Both these conditions were satisfied in our case as $[eBC]_{ff}$ and $[eBC]_{bb}$ did not show any significant correlation ($r^2<0.5$, $p\geq0.05$) amongst each other while both had a reasonable correlation ($r^2>0.8$, $p<0.0001$) with the measured mixing ratio of CO.

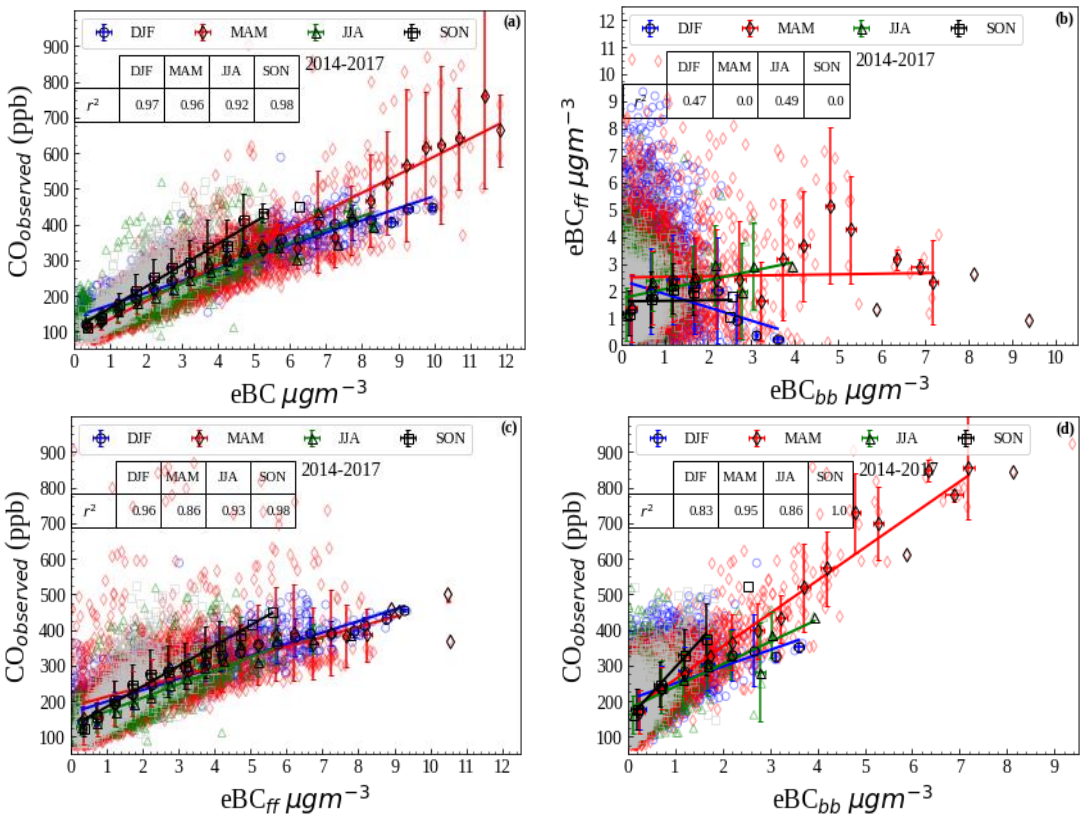

Figure 6.3 *Correlation between (a) CO and eBC (b) eBC_{ff} and eBC_{bb} (c)CO and eBC_{ff} (d) CO and eBC_{bb} mixing ratios in winter, spring, summer-monsoon and autumn during 2014-2017. Smaller points show daily means and binned data are shown in the same colour scheme with a larger size. Spread in x and y axes in the binned data is one standard deviation from the mean. Determination coefficient for each season is also mentioned.*

A key point here is that this multiple linear regression is not applied grossly over the whole dataset. Instead, the complete data was first segregated into different months and then the regression was applied diligently to each month separately. This approach improves the estimated CO results and helps capture the intra-annual variation in the background, fossil fuel, and biomass burning components of CO better, as shall be discussed later. Table 6.1 provides a summary of the parameters obtained from this regression.

Table 6.1 *Results of multiple linear regression ($[CO]_{bgd}$,, r_{ff},, r_{bb}, r_{bgd}, their respective errors and determination coefficient r^2) that are applied for the estimation of CO_{ff} and CO_{bb} for 2014-2017.*

Month	**$[CO]_{bgd}$**	**r_{ff}**	**r_{bb}**	**err-r_{bgd}**	**err-r_{ff}**	**err-r_{bb}**	**r^2**
Jan	98.93	45.8	68.32	0.92	0.54	1.19	0.9
Feb	113.98	34.59	65.08	1.24	0.37	1.76	0.89
Mar	99.7	30.14	73.04	1.01	0.43	1.97	0.85
Apr	90.53	36.92	87.17	1.81	0.8	1.14	0.86
May	126.4	42.43	67.22	2.07	1.01	1.55	0.85
Jun	114.91	40.52	45.65	3.06	1.28	3.32	0.57
Jul	109.2	28.42	46.86	1.54	1.41	11.66	0.45
Aug	124.39	17.98	11.48	1.48	2.07	5.93	0.11
Sep	112.99	52.08	67.43	3.55	2.75	10.65	0.48
Oct	87.71	59.96	84.85	1.98	1.16	3.29	0.76
Nov	83.54	74.1	111.17	2.62	2.46	5.02	0.82
Dec	115.48	41.14	67.47	1.86	0.9	2.97	0.77

We find that the regression determination coefficient r^2 is greater than 0.7 in all the months except those affected by the monsoon (June-September). This shows that the application of multiple regression will yield reasonable results at the site in general. These parameters can now be used for estimating the CO and its components of fossil fuel and biomass burning by utilising the observed eBC concentrations at this site using equations 6.2 and 6.3. We evaluate the comparability of estimated CO for the period 2014-2017 with the predicted CO for the year 2018 using the above parameters with the observed CO in the next section.

6.2.3. Comparison of the Estimated and Observed CO

Figure 6.4 shows monthly variations in the estimated and observed CO. Estimated CO is the sum of $[CO]_{bgd,}$ CO_{ff} and CO_{bb} as obtained from parameters in Table 6.1. The estimated CO captures very well the monthly mean variation of observed CO and the average values of the two have a difference of $<0.25 \times 10^{-3}$ ppbv. The spread in the box

plot however suggests that there could be differences among daily data between the two. Figure 6.5 shows the correlation between the estimated and the observed CO. The determination coefficient (r^2) is greater than 0.9 in all the seasons except monsoon. Even during monsoon, the r^2 is about 0.8. Broadly, these results suggest that the multiple regression (MLR) model can be reliably used to estimate the contribution of different sources to CO at the site for the same period and the parameters can be further used to predict the CO for the future as well. We evaluate this MLR model predicted CO against the observed one in the next section.

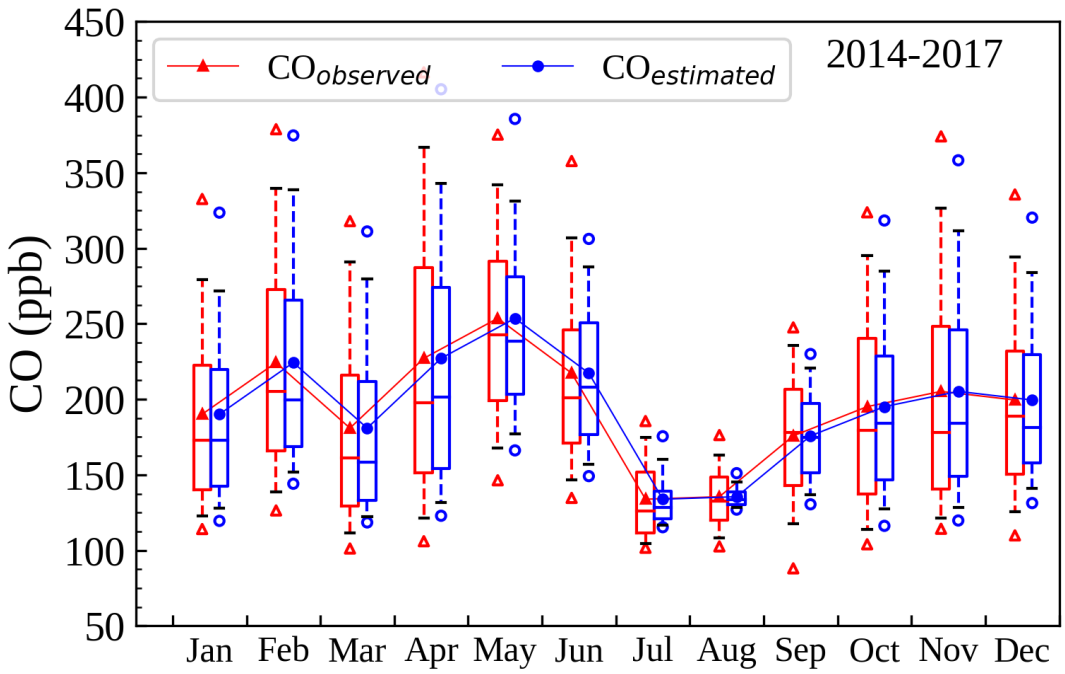

Figure 6.4 *Box plot showing the intra annual monthly mean variation in observed CO and estimated CO and their averaged for the year 2014-2017. In boxplots, the lower and upper edges of the boxes represent the 25th and 75th percentiles, respectively. The whiskers below and above are the 10th and 90th percentiles and the unfilled triangles and circles depict the 5th and 95th percentiles. The solid triangles and circles inside the boxes represent the mean and the solid lines inside the boxes represent the median.*

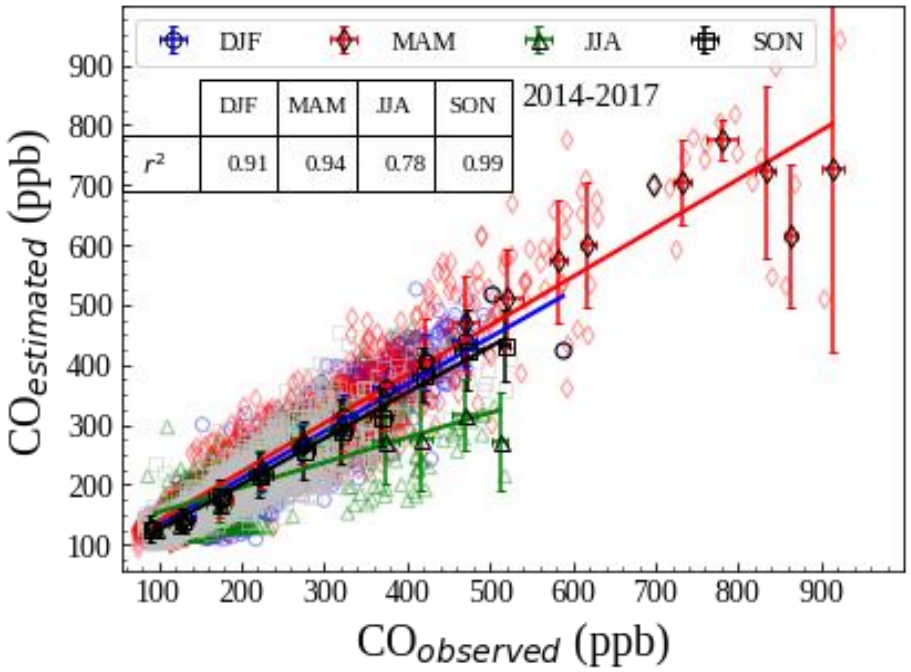

Figure 6.5 *Correlation between estimated and observed CO mixing ratios in winter, spring, summer-monsoon and autumn during 2014-2017. Smaller points show daily means and binned data are shown in the same colour scheme with a larger size. Spread in x and y axes in the binned data is one standard deviation from the mean. The determination coefficient for each season is also mentioned.*

6.2.4. Comparison of the Predicted CO from eBC for the Year 2018 with the Observed CO

Provided the correlation between eBC and CO holds, the parameters obtained from the multiple linear regression calculation, summarised in Table 6.2 for the years 2014-2017 can be utilized for estimating the CO and its components (CO_{bgd}, CO_{ff} and CO_{bb}) for other periods if the corresponding eBC concentrations are available for the site. Here, we evaluate the comparability of the CO thus predicted using the observed eBC and the derived regression parameters (r_{ff} and r_{bb}) with the observed CO at the site for the year 2018.

The seasonal correlation between the predicted and observed CO are shown in Figure 6.6. The coefficient of determination is found to be $\geq$0.8 in any of the seasons with a high significance level of $p < 0.0001$. The monthly mean variation in the observed and the predicted CO, and their percentage difference for the year 2018 is shown in Figure 6.7. The predicted and the observed CO are found to very closely follow each other and the percentage difference between them lies in the range of -16.1% to 16.8%. More

importantly, it is evident that the MLR model is able to reproduce the monthly variation quite well, capturing the high mixing ratios in spring and low mixing ratios during monsoon as opposed to MERRA2, WRF-Chem and MOPITT. Thus, the above analysis lends credibility to this method of estimating CO using multiple regression in eBC for usage to sites with high eBC-CO correlations. Interestingly, this method is particularly useful in the context of India since a network of eBC observations from multiwavelength Aethalometers already exists and a number of studies have already reported results on eBC source apportionment (Dumka et al., 2018, Kant et al., 2020, Kumar et al., 2020 and references therein). Further, these results also imply that the parameters derived in Table 6.1 are statistically significant and may be utilized in future to determine CO and its fossil fuel and biomass burning fractions from eBC observations at this site. We now present the results of this source segregation for CO in the next section.

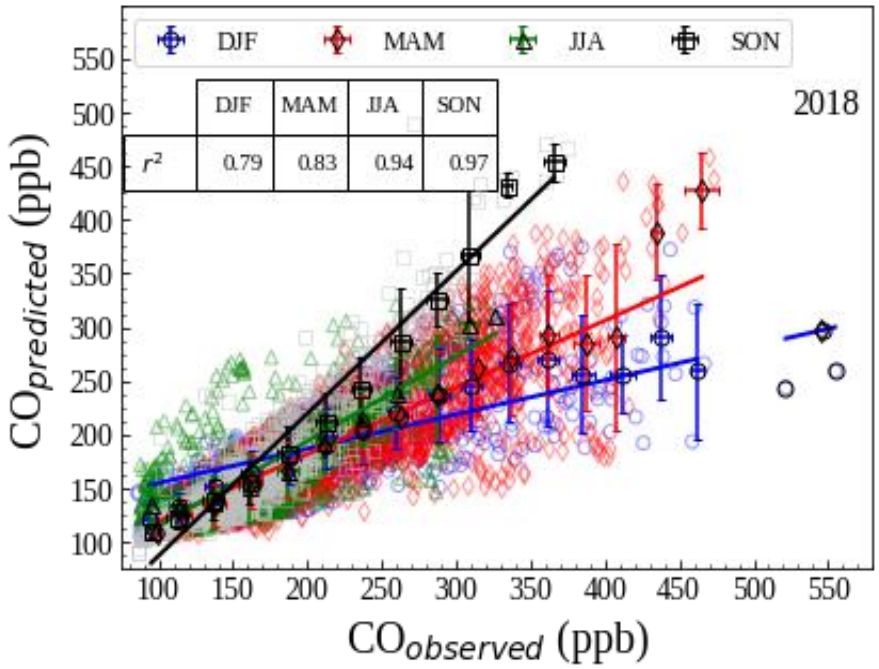

Figure 6.6 *Correlation between predicted and observed CO mixing ratios in winter, spring, summer-monsoon and autumn during 2018. Smaller points show daily means and binned data are shown in the same colour scheme with a larger size. Spread in x and y axes in the binned data is one standard deviation from the mean. The determination coefficient for each season is also mentioned.*

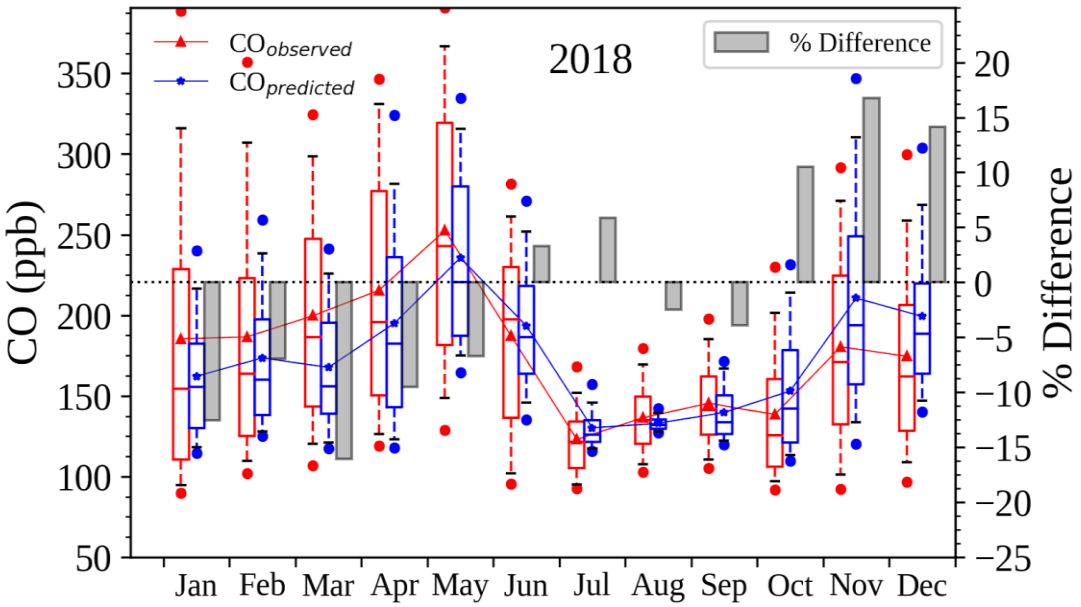

Figure 6.7 *The monthly mean variation in observed CO and predicted CO for the year 2018 are shown. In boxplots, the lower and upper edges of the boxes represent the 25th and 75th percentiles, respectively. The whiskers below and above are the 10th and 90th percentiles and the unfilled triangles and circles depict the 5th and 95th percentiles. The solid triangles and circles inside the boxes represent the mean and the solid lines inside the boxes represent the median. The percentage difference between observed and predicted CO for the year 2018 is also shown on the secondary y-axis in grey bars.*

6.2.5. Segregation of the Fossil Fuel and Biomass Burning Fractions of CO and their Temporal Variations

6.2.5.1 Diurnal Variations

The diurnal variation of the observed CO along with the estimated CO, its fossil fuel and biomass burning components are shown in Figures 6.8, 6.9, and 6.10 respectively. The estimated and observed CO show similar diurnal variations with very low biases (Figure 6.8). CO shows a feature of daytime high during 1100-1700 hours which is typical of this clean high altitude site and is consistent with the CO variation observed by Sarangi et al., (2012) for the year 2009-11. Such diurnal variation is mainly governed by the boundary layer evolution which brings the pollutants from the low-lying region with the upslope winds to this high-altitude site during the daytime. This daytime rise is found to be similar to that observed for eBC (Figure 6.8) showing their covariation. Component wise, diurnally, the mixing ratios of both CO_{ff} and CO_{bb} (Figure 6.9 and 6.10) rise to their peak during the noon and then fall which is very similar to eBC_{ff} and eBC_{bb} (Figure 6.8).

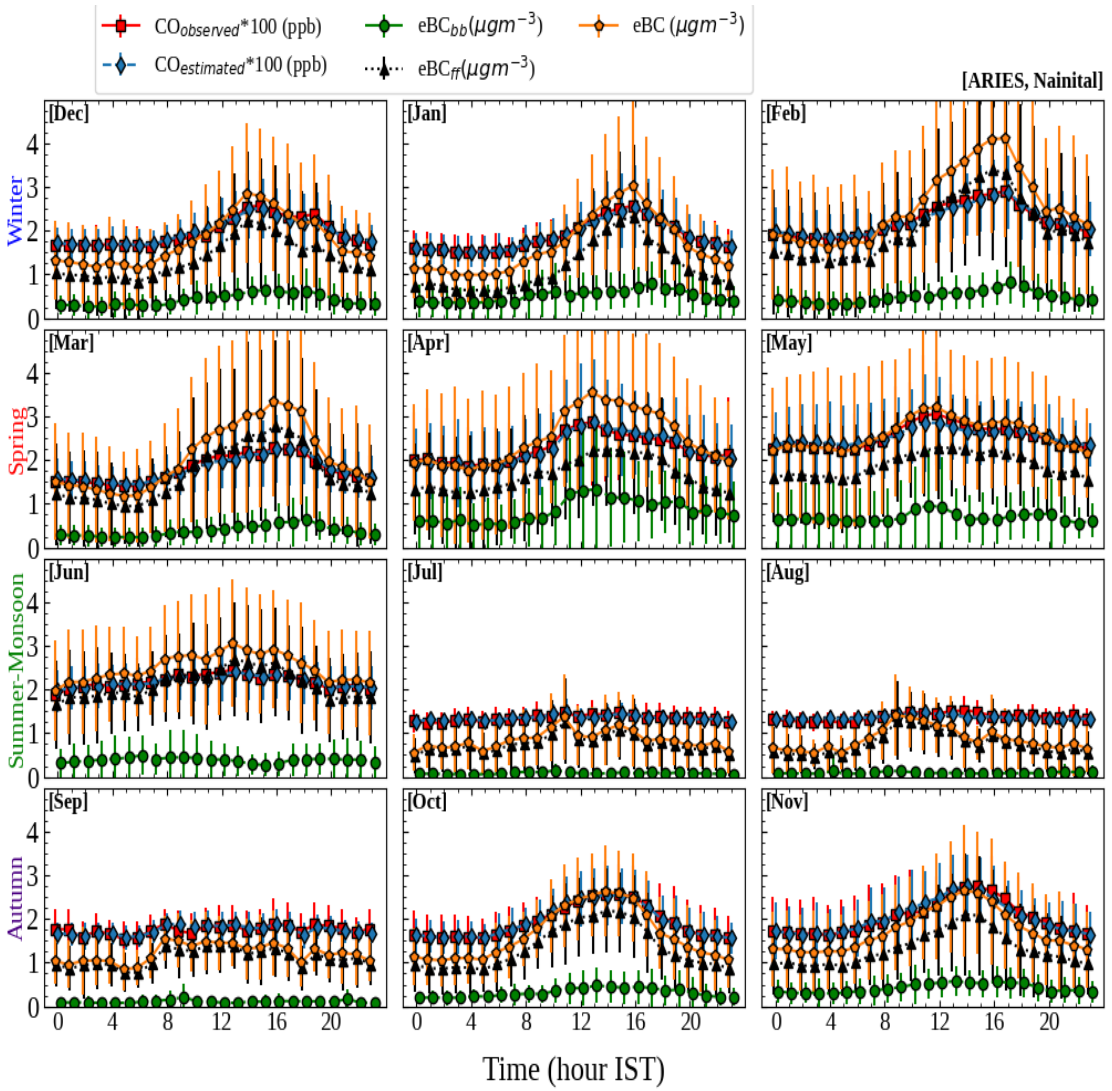

Figure 6.8 *Diurnal variations in hourly averaged $CO_{observed}$, $CO_{estimated}$, eBC_{ff}, and eBC_{bb} concentrations averaged for 2014-2017. $CO_{observed}$, $CO_{estimated}$ have been scaled down by a factor of 100 to fit all plots in the same graph. The vertical bars denote one standard deviation from the mean.*

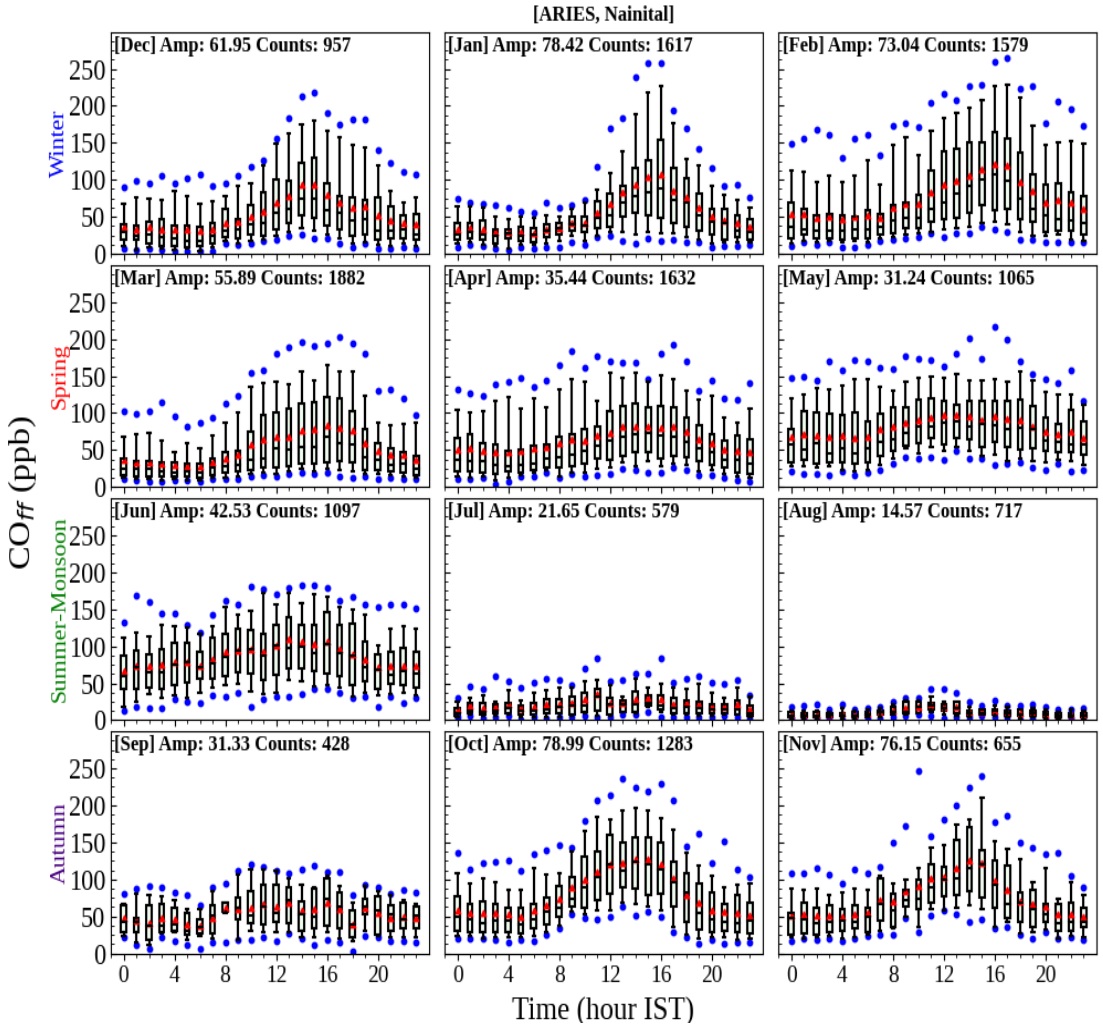

Figure 6.9 *Boxplot showing diurnal variations in hourly averaged CO_{ff} mixing ratio during 2014-2017. In boxplots, the lower and upper edges of the boxes represent the 25th and 75th percentiles, respectively. The whiskers below and above are the 10th and 90th percentiles and the blue circled outliers in the boxplot show the 5th and 95th percentiles. The red triangle inside the box represents the mean and the solid lines inside the box represent the median. The diurnal amplitude and number of observations are also mentioned for each month.*

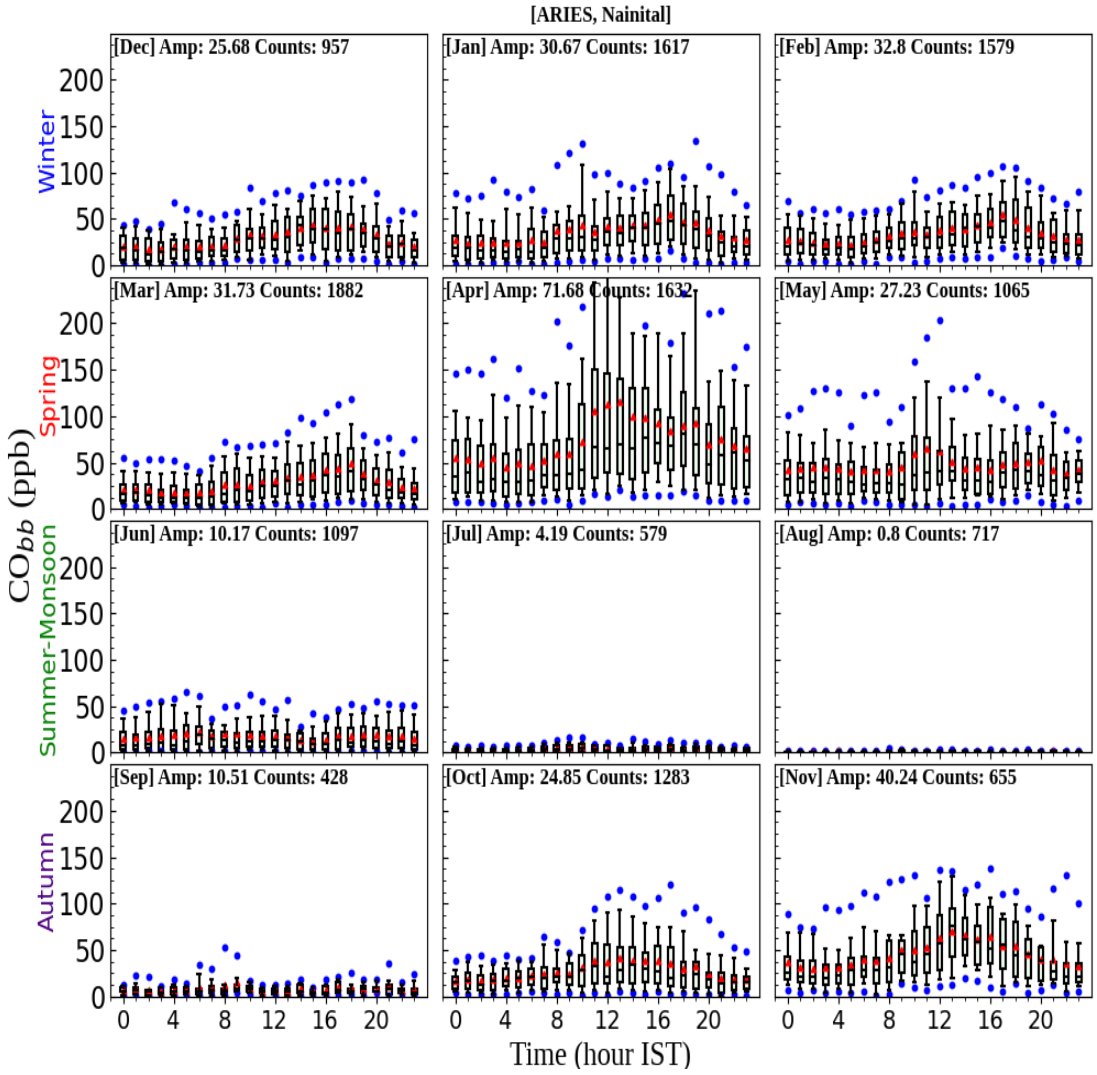

Figure 6.10 *Boxplot showing diurnal variations in hourly averaged CO_{bb} mixing ratio during 2014-2017. In boxplots, the lower and upper edges of the boxes represent the 25th and 75th percentiles, respectively. The whiskers below and above are the 10th and 90th percentiles and the blue circled outliers in the boxplot show the 5th and 95th percentiles. The red triangle inside the box represents the mean and the solid lines inside the box represent the median. The diurnal amplitude and number of observations are also mentioned for each month.*

To evaluate the diurnal variation quantitatively, we calculated the diurnal amplitudes for each month which is defined as the difference of the maximum and minimum hourly averaged CO mixing ratio for that month. The magnitude of this amplitude is mentioned in Figures 6.9 and 6.10 for every month. We find that despite a similar unimodal diurnal profile of both CO_{ff} and CO_{bb}, their diurnal amplitudes are very different. The amplitude of CO_{ff} ranges from 14.56 to 78.99 ppbv while that of CO_{bb} ranges from 0.8 to 71.68 ppbv. Interestingly, the amplitude of CO_{bb} is very high (71.68 ppbv) in April, otherwise, its range is only 0.8 to 40.24 ppbv. This shows that fossil fuel combustion is more closely associated with boundary layer evolution at this site compared to the biomass burning

counterpart. A similar observation is found in eBC where the daytime high feature is more prominent in the fossil fuel component showing that both eBC and CO, most likely have common sources of origin. This is also in line with another study on eBC reporting a dominance of fossil fuel components in most of the low altitude sites in the Indo Gangetic Plain (Kumar et al., 2020). Therefore, it is very likely that the evolving mixing layer height picks up the pollutants rich in fossil fuel fraction from these low altitude sites in the daytime and flushes them to higher altitude sites. The rise in CO mixing ratio (Sarangi et al., 2014) and EC and OC concentrations (Srivastava and Naja, 2021) with the increase of the boundary layer height has been observed at the mountain site, Nainital.

The amplitude of the diurnal peak is lowest in July (CO_{obs}-27.5 ppbv, CO_{ff}-14.6 ppbv, CO_{bb}-0.8 ppbv and CO_{est}-14.3 ppbv) and remains low during July-September, owing to the influence of summer monsoon which brings heavy rain and cleaner oceanic air masses at the site. In April, the amplitude of CO_{bb} is ~72 ppbv, much more than the CO_{ff} which is only ~35 ppbv. The next highest amplitude of CO_{bb} is observed in the month of November which is about 40 ppbv. These results are in good consistency with the previous studies from this site that have reported a significant influence of biomass burning particularly in spring on the mixing ratio of pollutants such as ozone and CO (Kumar et al., 2019), eBC (Joshi et al., 2020) and EC and OC (Srivastava and Naja, 2021). Going a step further, these results are now able to distinctively show that the biomass burning contribution in fact overtakes the usual dominance of fossil fuel fraction during the daytime in these months.

6.2.5.2 Annual Variations

Motivated by this observation of a prominent rise of CO during the daytime, we assessed the differences in this noon time and night time rise in biomass and fossil fuel components of CO and studied their monthly variations.

A clear intra annual variation in CO and its components is shown in Figure 6.11 (a) and (b). The intra annual monthly mean variation during noon (1300 - 1600 hours), night (0000 - 0300 hours) and the ratio of noon-to-night values for CO_{ff} and CO_{bb} is also shown. A summary of these interannual statistics for CO, CO_{ff}, CO_{bb} and CO_{bgd} is given in Table 6.2.

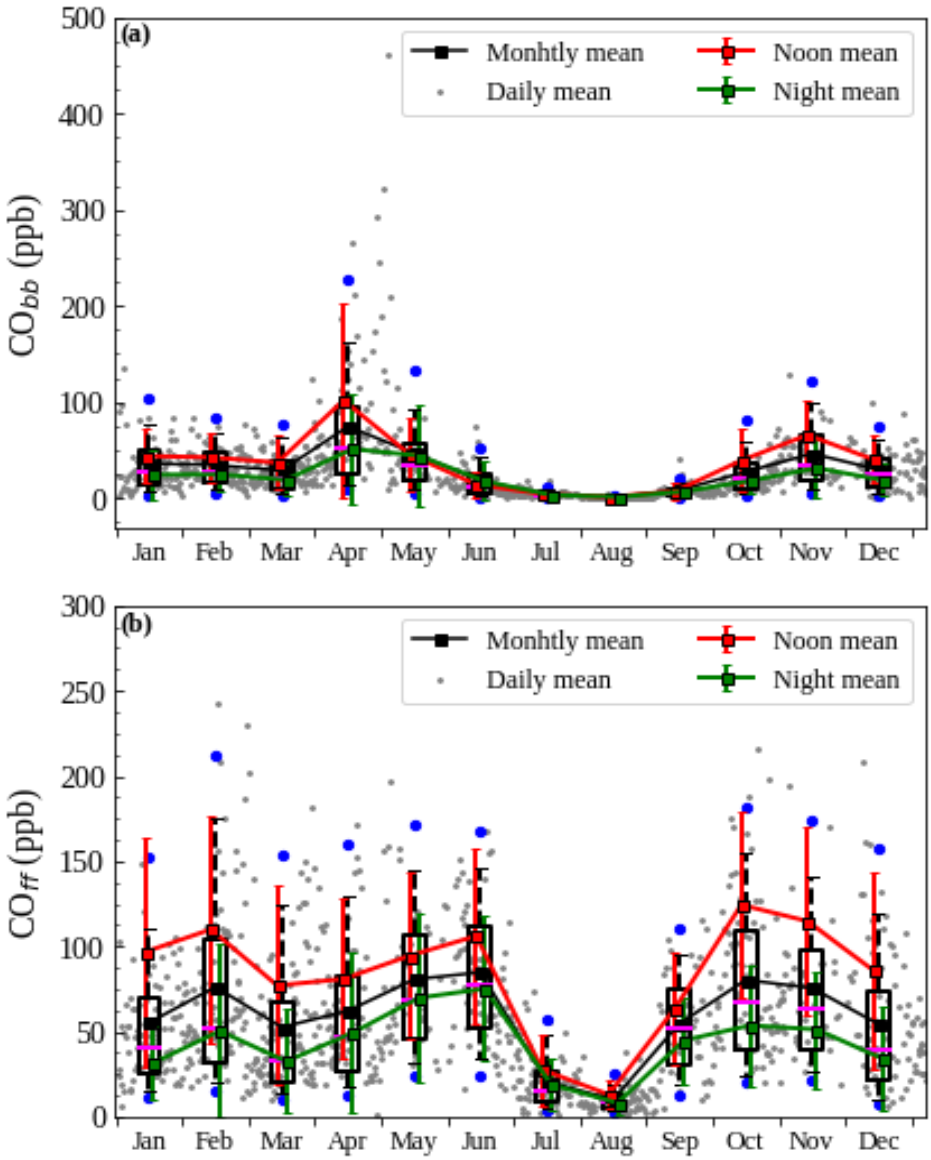

Figure 6.11 *Boxplot showing intra annual monthly and daily mean variation in (a) fossil fuel and (b) biomass burning CO fractions for 2014-2017 are shown in black. In boxplots, the lower and upper edges of the boxes represent the 25th and 75th percentiles, respectively. The whiskers below and above are the 10th and 90th percentiles and the blue-circles outliers depict the 5th and 95th percentiles. The black square inside the box represents the mean and the pink solid lines inside the box represent the median. The daily mean data points are shown as grey points. Noon (1300 - 1600 hours) and night (0100 - 0400 hours) time monthly averages are also shown. The error bars represent one standard deviation from the mean.*

Clearly, the noon time contribution of both CO_{ff} and CO_{bb} is much higher than the night time in all the months. Annually, the noon fraction in both CO_{ff} and CO_{bb} is about 3 times greater than the night time one. This is a direct consequence of the upliftment of pollutants by MLH observed in the diurnal scale as mentioned previously. Even in the monsoon months (June, July, August and September) although the noon/night ratio of

CO fractions reduces, the noon time contributions in both the CO fractions remain higher i.e., ≥1.4 times the night time one. Additionally, the noon time fossil fuel contribution remains higher than the biomass burning one. The results are consistent with the results obtained earlier for eBC.

To quantify the contribution of each of the components to total CO, we also calculated their percentage contributions. In all the months, the percentage of CO_{bb} is less than 28% and that of CO_{ff} remains less than 38%, thus signifying a high percentage of background CO on the site. The intercept value from the MLR model for each month is regarded as the background CO (CO_{bgd}). This CO_{bgd} forms the maximum portion of CO constituting ~58% annually and is followed by CO_{ff} (27%) and at last CO_{bb} (15%). The CO emissions from oceans, plants and hydrocarbon oxidation along with the long atmospheric lifetime of CO are found to form a significant background mixing ratio (Kalogridis et al., 2018). The annual mean mixing ratio of CO_{bgd} is found to be 104.9±13 ppbv which is in the range (95-189 ppbv) of previously estimated CO background levels over the same site using back-air trajectory analysis (Sarangi et al., 2014). This value is also quite close to those reported at other sites (Demokritos i.e., 108.5 and National Observatory of Athens i.e., 146 ppbv) (Kalogridis et al., 2018). The resulting CO_{bgd} is also in agreement with the 1.25th percentile level of the monthly dataset (100.2 ppbv at the site) considered as the background level (Kondo et al., 2006).

Following the background CO, the next major contributor to CO in all the months are fossil fuel emissions. In the absence of any major industries nearby, these emissions are most likely a result of vehicular emissions. The results thus underline that transportation and other fossil fuel emissions remain the major and regular sources of pollutants for the site. Further, biomass burning fraction, although subdominant mostly, peaks during spring (MAM) particularly in the month of April when the monthly value of CO_{bb} 74.4±80.1 ppbv exceeds that of CO_{ff} (62.03±48.5 ppbv). Relatively higher mixing ratios are also observed during November when CO_{bb} reaches its next highest magnitude of 46.1±36.9 ppbv. Thus, the results very well capture the influence of biomass burning emissions at the site during the crop residue burning period of spring (MAM) and November in the Northern Indian region. Moreover, the results not only demonstrate the seasonal nature of biomass emissions particularly crop-residue burning and forest fires but also show that their contribution to the ambient CO is significant. Here, we can thus

see a clear contribution of these biomass emissions at the site delineated from the background and fossil fuel emissions.

Table 6.2 *Summary of interannual statistics for total CO, CO_{ff}, CO_{bb} and CO_{bgd} for 2014-17.*

	Counts	CO_{obs}	CO_{est}	CO_{bgd}	CO_{ff}	CO_{bb}	Noon / Night ratio		
							CO_{est}	CO_{ff}	CO_{bb}
Jan	1617	190.1±68.8	190.1±65.4	98.9±0.0	55.3±47.8	35.9±32.3	1.6±0.5	4.6±5.2	3.9±4.7
Feb	1579	224.3±77.7	224.3±73.3	114±0.0	76.2±62.8	34.1±24.8	1.5±0.4	4.2±6.6	2.6±3.8
Mar	1882	180.9±69.4	180.9±64.0	99.7±0.0	52.6±48.2	28.7±25.7	1.5±0.4	3.4±2.6	3±3.6
Apr	1632	227.1±109.8	227.1±101.6	90.5±0.0	62.2±48.5	74.4±80.1	1.6±0.7	3.2±3.8	3.4±3.7
May	1065	253.6±88.7	253.6±81.8	126.4±0.0	80.7±48.3	46.6±49.6	1.1±0.2	1.7±0.8	1.4±1.1
Jun	1097	217.3±69.5	217.3±52.3	114.9±0.0	84.7±44.8	17.7±19.5	1.1±0.2	1.5±0.9	1.5±1.7
Jul	579	133.8±27.4	133.8±18.3	109.2±0.0	20.7±17.4	3.9±3.5	1.1±0.1	2.6±4.0	9.1±33.3
Aug	717	135.5±23.5	135.5±7.6	124.4±0.0	10±7.3	1.1±1.6	1±0.1	2.1±1.3	2.8±3.8
Sep	428	175.8±44.7	175.8±31.0	113±0.0	54.7±29.6	8.1±9.9	1.1±0.2	1.4±0.7	1.7±1.5
Oct	1283	195.1±72.4	195.1±62.9	87.7±0.0	80.3±52.5	27.1±26.2	1.6±0.5	2.9±2.7	4.1±8.0
Nov	655	205.2±84.8	205.2±76.9	83.5±0.0	75.6±50.3	46.1±36.9	1.7±0.5	2.8±1.6	10.0±36.0
Dec	957	199.5±7	199.5±57.9	115.5±0.0	54.5±47.7	29.6±23.8	1.4±0.3	3.7±2.6	5.8±10.8
DJF	4153	205.3±73.3	205.3±68.7	108.5±7.6	63±54.9	33.8±27.8	1.5±0.4	4.2±5.4	3.8±6.2
MAM	4579	214.3±94.7	214.3±88.3	102.6±13.7	62.5±49.5	49.1±59.4	1.4±0.6	2.9±2.9	2.8±3.3
JJA	2393	172.6±65.2	172.6±55.2	116.4±5.7	46.9±47.3	9.4±15.4	1.1±0.1	1.9±2.0	3.4±14.7
SON	2366	194.4±72.7	194.4±63.6	91.1±10.4	74.3±49.4	29±30.5	1.5±0.5	2.6±2.3	5.2±19.1
Annual	13491	200.6±81.2	200.6±74.6	104.9±13	62±51.5	33.8±42.8	1.4±0.5	3.1±3.7	3.6±11.1

6.2.6 Comparison of BC Based Source Apportionment Against those from WRF-Chem

In this section, we will discuss the comparison of CO-based tracer runs from WRF-Chem, which are used for segregating sources of CO against the source segregation from MLR. For a direct comparison, WRF Chem simulations for anthropogenic emissions are regarded as the fossil fuel CO and the contribution from photochemical production in the domain and inflow of CO from lateral boundaries are together taken as the background CO.

Figure 6.12 shows monthly variations in percentage difference between WRF-Chem and MLR method for fossil fuel, biomass and background component of CO. Percentage difference is calculated with respect to the MLR method. We find that biomass burning fraction of CO from WRF are significantly underestimated compared to those from MLR in all the months and the two vary over a wide range from -38 to -98%. WRF based CO_{bb} shows higher emissions during May, June and October which is contrary to the observations which show higher biomass emissions during April and November.

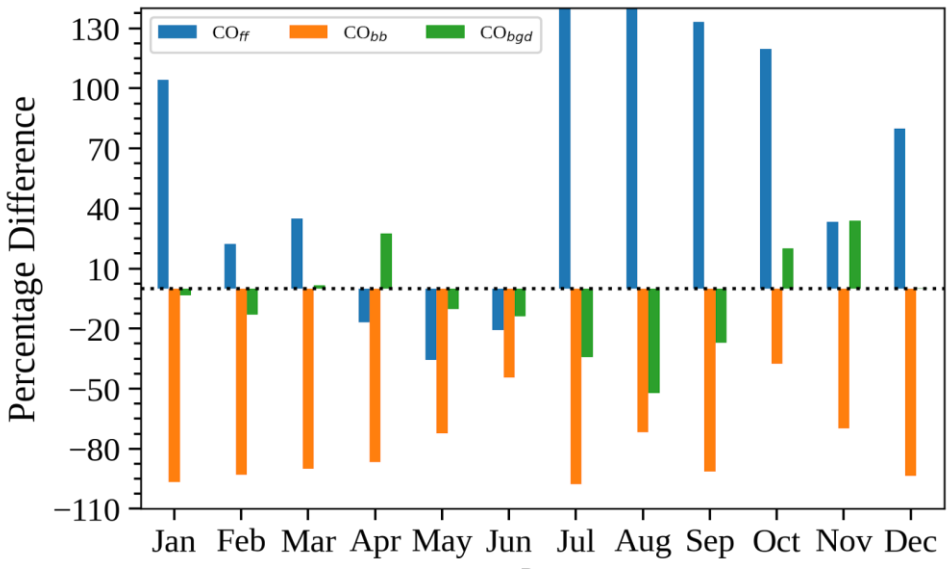

Figure 6.12 *Monthly variations in percentage difference between WRF-Chem and MLR method for fossil fuel, biomass and background component of CO. Percentage difference is calculated with respect to the MLR method. Fossil fuel fraction of CO ranges up to +962%. To clearly illustrate the monthly variation in other fractions of CO, the y-axis scale is not extended till the full range of +962%.*

The percentage difference between the fossil fuel fraction of CO is even higher and ranges from about -17% to +962%. The magnitude of the percentage differences is given in Table 6.3. An important point while comparing the anthropogenic CO fraction in WRF to the fossil fuel fraction in CO from MLR is that the anthropogenic fraction in CO may include anthropogenic CO sources other than fossil fuel as well. Although this might lead to some discrepancies, those are more or less reasonable since most of the anthropogenic emissions come from fossil fuel-based emissions. Further, this would mainly lead to a positive bias since anthropogenic components other than fossil fuel would be added in CO_{ff} from WRF. Interestingly we find that despite this inclusion of additional components to fossil fuel CO in WRF, it still significantly underestimated the MLR based CO_{ff} during April and May, when usually high CO mixing ratios are observed at the site. On the other hand, the fossil fuel emissions during monsoons, especially July and August, in WRF are found to be much higher than MLR (even higher than those in springtime). This significant overestimation by WRF is quite unrealistic as this period is marked by heavy rain and is under the influence of cleaner marine origin air masses.

Table 6.3 *Monthly percentage difference between WRF and MLR for CO_{bgd}, CO_{ff} and CO_{bb}.*

	CO_{ff} (%)	CO_{bb} (%)	CO_{bgd} (%)
Jan	104.3	-96.6	-3.3
Feb	22.4	-93.1	-12.9
Mar	34.9	-90.0	1.6
Apr	-17.0	-86.7	27.7
May	-35.6	-72.2	-10.2
Jun	-20.6	-44.6	-13.9
Jul	293.9	-97.7	-34.2
Aug	962.5	-71.7	-52.2
Sep	133.1	-91.3	-27.1
Oct	119.8	-37.5	20.1
Nov	33.3	-69.8	33.8
Dec	79.9	-93.6	0.2

Background mixing ratio in MLR and WRF seems to be relatively better represented as compared to the other sources. Yet even they have a wide percentage difference ranging from -52% to +34%. We thus find that WRF-Chem is not able to provide representativeness of the monthly variations in the sources at the site. The analysis reveals that the major fraction of this discrepancy comes from the misrepresentation of fossil fuel components followed by biomass burning fractions. Although these results provide important preliminary information, we realise that a more detailed analysis including the comparison of emission inventories, resolution and physical schemes will be needed in future to pinpoint the exact genesis of this discrepancy at the site.

6.3. Conclusions

Given the increasing levels of carbon monoxide (CO) over the South Asian region and its impact over the Himalayas, there is a pressing need to better understand and quantify its emission sources. This will lead to effectively reducing the existing discrepancies in emission estimates of CO. The discrepancies in emissions estimates are furthermore over the South Asian region, particularly in the IGP and the Himalayan region having diverse emission sources in the same region and topography is also complex. In this context, the present work provides crucial *in-situ* information to robustly constrain the relative source fractions of CO. Simultaneous *in-situ* measurements of eBC and CO made at a high-altitude site in the Central Himalayas from 2014 to 2018 are used in a multiple linear

regression based (MLR) framework to serve this purpose and the results are compared against data from MOPITT satellite, MERRA-2 reanalysis data and WRF-Chem simulations.

It is found that the satellite measurements, model results and reanalysis data show a large difference in the temporal variations of CO at this high-altitude site. The evaluation of the MLR model against ground-based observations shows that MLR does quite well in replicating the diurnal and monthly variation and estimates CO with an r^2 of $\geq$ 0.8 for 2014-2017. The comparison of CO predicted using MLR model parameters and eBC for the year 2018 shows that the monthly predicted CO closely follows the observed variations, and the mixing ratios lie in the range of -16.1% to 16.8% of the observed average CO values in any given month. The source segregation results show a clear unimodal variation with a daytime high of fossil fuel (CO_{ff}) and biomass burning (CO_{bb}) fractions of CO, very similar to eBC. We show that the diurnal variation is mostly governed by the boundary layer evolution. Fossil fuel combustion is found to be the major contributor (27%) in CO after background CO (58%). CO_{bb} shows a large increase and reaches up to (28%) during April as a result of increased agricultural and forest fires in the Northern Indian region. WRF-Chem tracer runs for source segregation are found to underestimate the biomass burning emissions (-38% to -98%) while they largely overestimate the fossil fuel CO mixing ratios especially during monsoon. The results thus highlight the successful applicability of MLR in delineating the contribution of fossil fuel and biomass burning from the CO. The parameters for future estimation of CO from eBC at the site are also provided. This work also underlines the dire need to mitigate the fossil fuel and biomass-based incomplete combustion activities to maintain the sanctity of the pristine region of the Himalayas.

Chapter 7

Trend in Black Carbon Concentrations and its Sources: 17 Years of Ground-Based Observations

---

Till now the former chapters have looked at variations, sources and the impacts of carbon aerosols critically but only in parts i.e., about 4 years of their long timelines. Although long, it is not enough to evaluate the climatic impacts over this region. This chapter stitches together the ground-based observations from this region from 2004 onwards forming a dataset of 17 years. In the first half, we discuss the importance of this long time series and then scrutinise the trends in observed BC and its sources. We then contrast and make sense of these results with the simultaneous reanalysis of the model BC, satellite optical depth and fire events observations. Later we also dive deep to analyse the trend of BC emissions in various countries and different sectors and finally investigate the vertical profile of these aerosols over the Himalayan region.

7.1. Introduction

The ongoing climatic changes fueled by rapid industrialization and urbanisation, are projected to have major consequences for the Himalayan region. Temperature over the region is estimated to increase by at least 0.3^{o}C more even if global warming is restricted to 1.5^{o}C (Wester et al., 2019). Extreme warm events are on a rise (1.26 days per decade) in the region for the past 5 to 6 decades while cold events have shown a falling (2.4 days per decade) trend (Wester et al., 2019). Overall, the intensity and frequency of extreme precipitation has increased over the past 5 decades and is in turn likely to increase water-induced hazards if such a scenario persists. The cryosphere in the region is impacted even worse. Snow area and volume are decreasing (Gertler et al., 2016), permafrost is thawing (Zhao et al., 2010) and glaciers in most of the Himalayan region are retreating (Figure 1.6) at an accelerated rate of 0.37 m w.e./year which is higher than the rate of 0.27 m

w.e./year before the year 2000 (Wester et al., 2019), and thereby increasing the risk of glacial lake outburst floods (Hewitt and Liu, 2010).

Anthropogenic greenhouse gases and aerosols are known to be the key drivers behind this climate change. While the effects and emissions of greenhouse gases are known with reasonable confidence, aerosols remain the single largest source of uncertainty (IPCC, 2013). In particular, Black Carbon (BC) aerosols, known for being the highest absorbing aerosol species, are associated with significant regional climatic implications over the Himalayas apart from their health-related hazards. Model simulations have suggested that BC alone on snow has led to an increase in temperature of ~1^{o}C over the Himalayan-Tibetan plateau (Qian et al., 2011). Such elevated warming with BC, in particular, is expected to play a role that is comparable to that due to greenhouse gases in this region (Ramanathan and Carmichael, 2008). The simulated warming due to these aerosols predictively produces a 10 to 20% reduction in spring-time snow depth over the region (Meehl et al., 2008). Studies including soot darkening estimate that the Himalayan region has the highest soot related warming (annual - 3.8 Wm^{-2}, spring - 20 Wm^{-2}) across the world (Flanner et al., 2007). Atmospheric heating due to BC and dust is also found to cause widespread accelerated snowmelt in this region (Lau et al., 2010, Qian et al., 2015). The warming caused by these aerosols is also suggested to cause a temperature anomaly that enhances the moisture influx from the Indian ocean thereby leading to an intensification of the early monsoon (Lau et al., 2006). Therefore, it is essential to accurately quantify the contribution of different sources of BC over the Himalayas. It is particularly important because the Himalayas lie in close proximity to the world's most polluted regions of Indo-Gangetic Plains. While emissions over the USA, Europe and mid-latitudes have been reported to decrease, those over the developing Asian countries are reportedly increasing (Akimoto, 2003; Naja and Akimoto, 2004).

Most of the trend ($\geq$10 years) based studies over Asia, particularly in South Asia, are either from model simulations or are from satellite measurements. Unfortunately, results from both these deviate considerably from ground-based measurements in the Himalayan regions. The deviations could be due to the coarse resolutions in some models and the complex topography of the region, thus necessitating ground observations. Yet only limited datasets from ground-based observations are available over this region and even these are either for a short period (less than a few years) or are non-continuous.

Further, very few studies have incorporated a mass absorption cross-section (MAC) that is corrected for the appropriate parameters/situation in reporting BC aerosols, which is used to measure its light absorption properties (Petzold et al., 2013). MAC is found to have large spatiotemporal variation depending on its source, particle size, morphology and mixing state (Bond and Bergstrom, 2006). Different Himalayan regions are reported to have a wide range of values (at 632 nm) such as 6.85 m^2g^{-1} (at Lulang) and 6.49 m^2g^{-1} (at Everest) (Li et al., 2016b), 7.19 m^2g^{-1} (at Lhasa) (Li et al., 2016a), 12.2 m^2g^{-1} (at NamCo) (Li et al., 2021). Despite this large variation in MAC, most studies estimating BC from optical absorption have used only a constant value such as 16.6m^2g^{-1} at 880nm in the analysis from Aethalometer data (Dumka et al., 2010; Gogoi et al., 2014; Joshi et al., 2016). This is shown to lead to an underestimate of BC values and its associated radiative forcing (Srivastava et al., 2021). Therefore, it is essential to incorporate the *in-situ* MAC values to get accurate estimates of trends in BC in the Himalayan region. This will enable a better assessment of the radiation budget and regional climate change.

To bridge the aforementioned gap, in this work we present the first MAC corrected trend of ambient BC using a comprehensive ground-based 7-channel Aethalometer from 2004 to 2020 conducted over a high-altitude site in the Central Himalayas. We not only analyse the long-term time series for the monotonous trends and seasonal variations but also compare the former against the results from a popular reanalysis model and highlight its discrepancies over the whole period at the site. Later, we delineate the ambient BC to segregate its fossil fuel and biomass fractions. We finally evaluate these BC measurements in the backdrop of trends in fire events over the northern Indian region, aerosol optical depth, vertical aerosol profile and their type and changes in BC emissions over India. Instrument details for the observations of BC, along with incorporations of corrections factors have been described in Chapter 2.

7.2. Results and Discussions

In this work, the trends in BC concentrations during the period 2004-2020 are derived using three different approaches: (i) Linear regression model, (ii) Mann-Kendall test, and (iii) Theil-Sen slope. The linear regression model is based on the least square minimisation method to predict the best fit line between two variables. The slope of this

best fit line then provides the trend in the BC timeline. We have also performed a non-parametric Mann-Kendall test which is used extensively to estimate the monotonic trend in the time series data (Hussain et al., 2019). The Kandell-tau value from this test represents the strength of the trend while the p-value gives the significance of measurement. The Theil-Sen slope-estimator is used to quantify the trend in the slope at a 90% confidence level. As this test is not too sensitive to outliers, it is found suitable for a highly skewed dataset (Sen, 1968).

7.2.1 Seasonal Variations and Trends in Observed BC and MERRA-2

Temporal variations in observed BC and MERRA-2 during 2004-2020 over the observational site are shown in figure 7.1. Bias in the MERRA-2 is also shown. Prominent diurnal and monthly variations are seen in both observed BC and MERRA-2. The features of diurnal and monthly variations in observed BC have already been discussed in chapters 3 and 4. A comparison of daily and monthly mean between observed BC and MEERA-2, along with the percentage difference between them is shown in Figure 7.2. Monthly mean variations in noon and night time are also shown. Higher values in BC during autumn and winter are captured by MERRA-2 but misses out on the higher values in spring. This feature is also reflected in its noon time values, indicating that MERRA-2 is missing the daytime higher values. MERRA-2 underestimates (>60%) the observed concentrations during spring while it overestimates (<-26%) during late autumn and early winter (NDJ). There is an overall bias in the range of -17.6 to 21.22 μg m^{-3} with a mean bias of 0.47 μg m^{-3} between the observed and MERRA-2 BC concentrations.

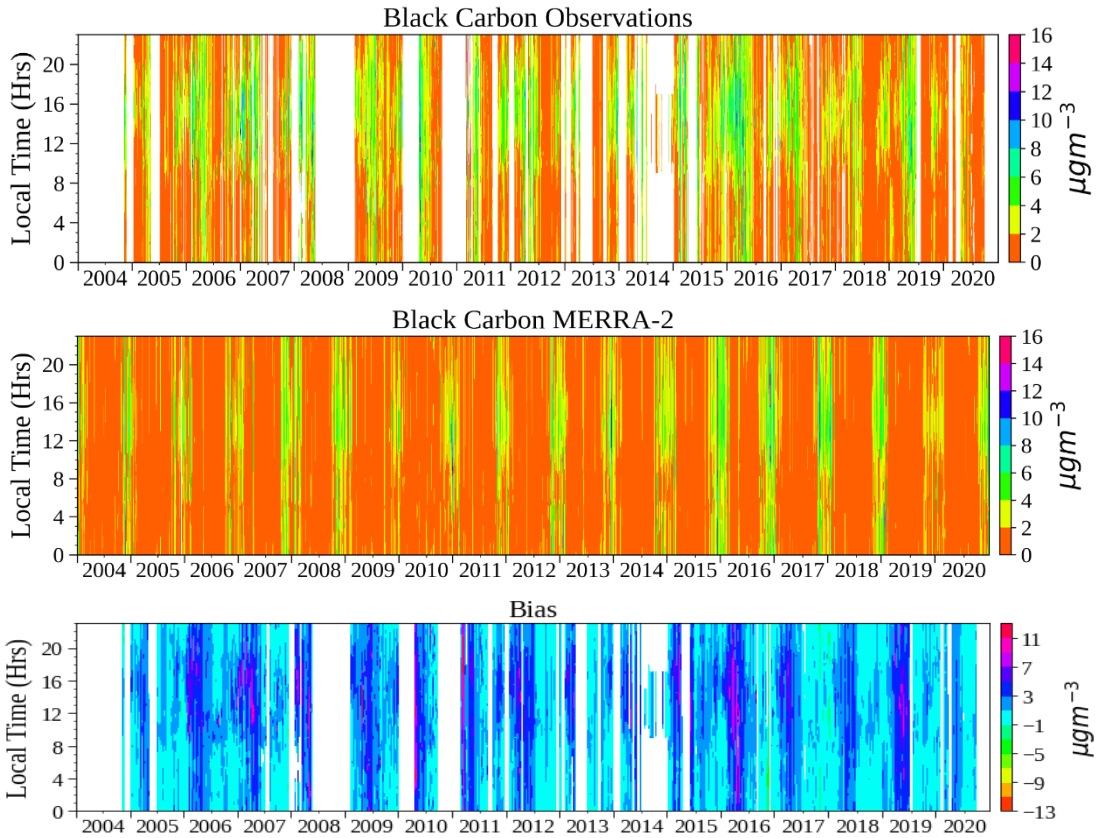

Figure 7.1 *Long-term variations in the observed BC, MERRA-2 and the bias in MERRA-2 during 2004-2020 over the observations site.*

Figure 7.3 shows long-trends in the observed BC and in MERRA-2 from 2004 to 2020. This shows a statistically significant, yet weak, negative trend with a slope of –20.03 ng m^{-3} $year^{-1}$. The value of the slope is estimated from linear regression using 365 days moving average. Unlike the trend in observed BC, the analysis of BC from MERRA-2 shows a positive trend with a slope +12.99 ng m^{-3} $year^{-1}$. The trend for this dataset is also estimated using the Mann-Kendall test. The obtained results are almost similar to those obtained from linear regression of 365 days moving average and are shown in Table 7.1. Mann-Kendall test results are also performed for winter, spring, summer-monsoon and autumn seasons. The negative trends are found to be present in all the seasons with the maximum rate in winter (-37.4 ng m^{-3} $year^{-1}$) and minimum in spring (-11 ng m^{-3} $year^{-1}$). Trend analysis for noontime (1400-1700 hrs) shows a negative value of -26.31 ng m^{-3} $year^{-1}$ while there is no significant trend in the night time (0100-0400 hrs) concentrations (Table 7.1). Since the noon time concentrations are governed by the rise in pollutants transported to the site, this negative trend suggests a decreasing tendency of pollutants in the adjacent regions.

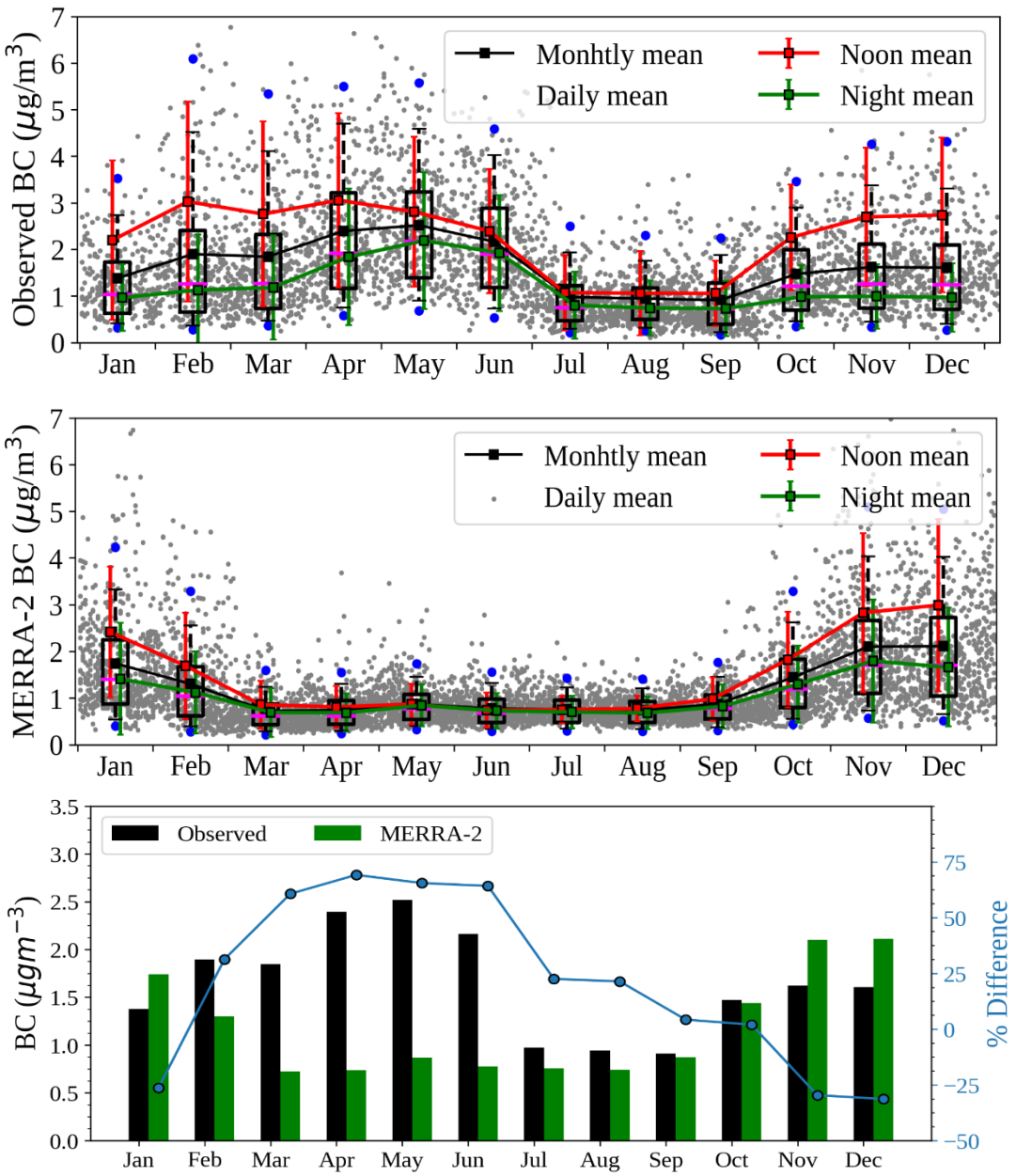

Figure 7.2 *Monthly average variations in observed BC and BC from MERRA-2 during 2004-2020. Daily, noon and night time average values are also shown. The percentage difference between observed BC and BC from MERRA-2 is shown in the bottom panel.*

The trend in extreme events of high and low concentrations was assessed using the trend in daily maximum and minimum concentrations. It is found that the minimum concentrations have a weak negative trend of -3.39 ng m^{-3} year $^{-1}$ while the maximum BC concentrations decrease relatively at a faster rate of -40.69 ng m^{-3} year $^{-1}$, thus, implying a decay in the events of higher BC concentrations. The overall observed trend (-20.55 ng m^{-3} year $^{-1}$) in BC at the present mountain site in the central Himalayas is lesser (-70 ng m^{-3} $year^{-1}$) than the ones reported for an urban site (Trivandrum) in

southern India (Manoj et al., 2019). In addition, the reported trend for the Indian region (-242 ng m^{-3} year $^{-1}$) is highly negative (Manoj et al., 2019). Therefore, there is an overall negative trend over the central Himalayas, but the trend is much lower than the other parts in India. This may help in deciding on the suitable action and strategy in controlling the BC emissions in this and surrounding regions.

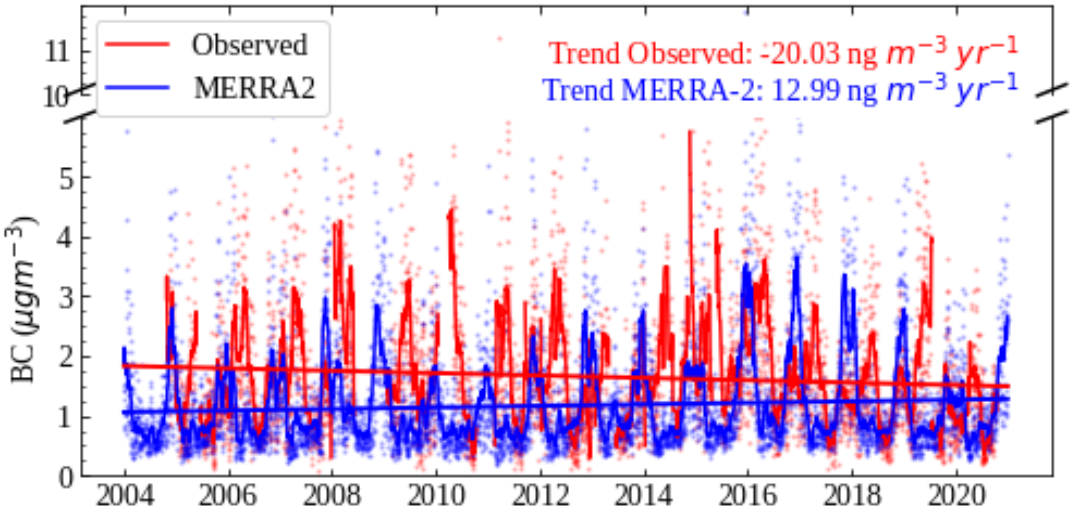

Figure 7.3 *Long-term trends in observed BC and MERRA-2 during 2004-2020 over the observational site. Scattered points in blue and red show the daily average values for observed BC and MERRA-2, respectively. Monthly moving averages in BC are shown in curved lines. Linear regression for the 365 days moving average is also shown for the entire period. Mentioned slope values are from this linear regression of 365 days moving average.*

Table 7.1 *Mann-Kendall trend test results for BC for different periods. The trend is tested for a 95% significance level i.e., p value of 0.05. The slope is in units of ng* m^{-3} *year* $^{-1}$.

	Period	***Slope***	***Trend***	***p value***
Obs BC	*Annual*	*-20.55*	*Decreasing*	*<0.0001*
MERRA-2 BC	*Annual*	*+12.11*	*Increasing*	*<0.0001*
Trends during four seasons				
Obs BC	*Winter*	*-37.4*	*Decreasing*	*<0.0001*
	Spring	*-11*	*Decreasing*	*0.029*
	Summer-monsoon	*-30.50*	*Decreasing*	*<0.0001*
	Autumn	*-25.96*	*Decreasing*	*<0.0001*
MERRA-2 BC	*Winter*	*23.38*	*Increasing*	*<0.0001*
	Spring	*20.62*	*Increasing*	*<0.0001*
	Summer-monsoon	*9.93*	*Increasing*	*0.0004*
	Autumn	*11.33*	*Increasing*	*<0.0001*
Trends during noon time, night time, maximum and minimum values				
Obs BC	*Noon*	*-26.31*	*Decreasing*	*<0.0001*
	Night	*-0.068*	*No trend*	*0.737*
	Max	*-40.69*	*Decreasing*	*<0.0001*
	Min	*-3.39*	*Decreasing*	*0.009*
MERRA-2 BC	*Noon*	*7.53*	*Increasing*	*<0.0001*
	Night	*9.09*	*Increasing*	*<0.0001*
	Max	*1.20*	*Increasing*	*<0.0001*
	Min	*6.54*	*Increasing*	*<0.0001*

7.2.2 Trend in Total BC and Fractions of Fossil Fuel Combustion and Biomass Burning BC

BC concentrations were delineated into fossil fuel and biomass fractions using the methodology described in Chapter 5 (section 5.2.2.2). It has already been shown in Chapter 5 that the fossil fuel fractions have seasonal and diurnal variations that have variability that is closer to the total BC, as compared with the biomass fraction. Nevertheless, biomass BC fraction shows higher concentrations during spring owing to the peak period of stubble burning and forest fires over Northern India (Srivastava et al., 2022). It has been shown that the fossil fuel fraction dominates by about 77% during the analysis period of 2014-2017 (section 5.2.2.2.) and this dominance is found to be about 76% for the period 2004-2020.

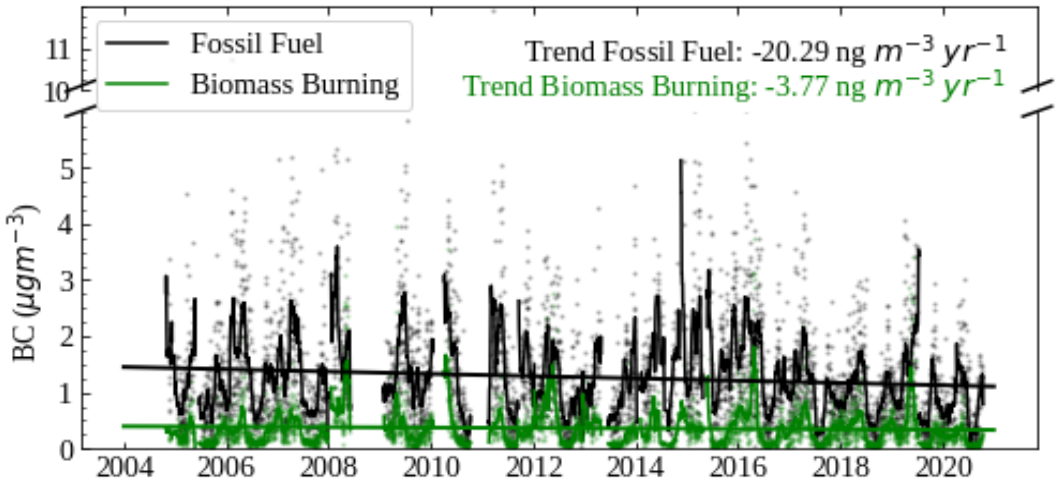

Figure 7.4 *Long-term variations in fossil fuel and biomass burning components of BC during 2004-2020. Scattered points in black and green show the daily average values for fossil fuel and biomass burning BC, respectively. Monthly moving averages in BC are shown in curved lines. Linear regression for the 365 moving average is also shown and the slope for the same is also mentioned.*

Figure 7.4 shows long-term changes in fossil fuel and biomass fraction of BC. The trend analysis with linear regression shows that the decline in the rate of fossil fuel burning (-20.29 ng m^{-3} $year^{-1}$) is greater than that in the biomass burning BC fraction (-3.77 ng m^{-3} $year^{-1}$). Results from the Mann-Kendall test reveal that the decay in biomass burning is not significant (p value of - 0.7) while that of fossil fuel is significant (p value < 0.0001) with a trend of -23.02 ng m^{-3} $year^{-1}$ (Table 7.2). The trend in biomass burning BC fractions over different seasons is either not significant or weak (-3.85 to 5.5 ng m^{-3} $year^{-1}$). On the other hand, the trend during all the seasons in fossil fuel burning BC fraction

is significant at 95% level and large (-37.68 to -18.02 ng m^{-3} $year^{-1}$). This implies that the observed decrease in the ambient BC fraction is largely attributed to the decline in the fossil fuel combustion fraction. As in the case of ambient BC, the fossil fuel BC also shows a stronger noon time decrease (-16.93 ng m^{-3} $year^{-1}$) compared to its night time value (-3.13 ng m^{-3} $year^{-1}$). Such a trend is insignificant in biomass burning fraction thus implying that the reduction in noon time (the uplifted pollutants) fraction of total BC is mainly due to a decline in its fossil fuel component.

Table 7.2 *Mann-Kendall trend test results for fossil fuel and biomass burning BC for different periods. The slope is in units of ng m^{-3} $year^{-1}$. The trend is tested for a 95% significance level i.e., p value of 0.05.*

	Period	***Slope***	***Trend***	***p value***
BB BC	*Annual*	*+0.08*	*No trend*	*0.706*
FF BC	*Annual*	*-23.02*	*Decreasing*	*<0.0001*
Trends during four seasons				
FF BC	*Winter*	*-36.3*	*Decreasing*	*<0.0001*
	Spring	*-18.02*	*Decreasing*	*0.001*
	Summer-monsoon	*-37.68*	*Decreasing*	*<0.0001*
	Autumn	*-26.05*	*Decreasing*	*<0.0001*
BB BC	*Winter*	*-3.85*	*Decreasing*	*0.021*
	Spring	*+0.09*	*No trend*	*0.926*
	Summer-monsoon	*+5.08*	*Increasing*	*<0.0001*
	Autumn	*-1.22*	*No trend*	*0.457*
Trends during noon time, night time, maximum and minimum values				
FF BC	*Noon*	*-16.93*	*Decreasing*	*<0.0001*
	Night	*-3.13*	*Decreasing*	*0.05*
BB BC	*Noon*	*-0.63*	*No trend*	*0.44*
	Night	*+0.61*	*No trend*	*0.16*

7.2.3 The Contrasting Trends in AOD

To comprehend the underlying reasons behind the observed trends in BC, we compare them with the trends in aerosols optical depth (AOD) and data from emission inventories. The daily data of MODIS from both AQUA and TERRA are analysed for the period 2006-2020 and the trend is estimated to be positive (Figure 7.5). The trend is also analysed with the Mann-Kendall test and found to be positive and significant (p value < 0.0001). As we have found a negative trend in surface BC, it is suggested that the overall columnar aerosol content is rising but its surface BC fraction is declining.

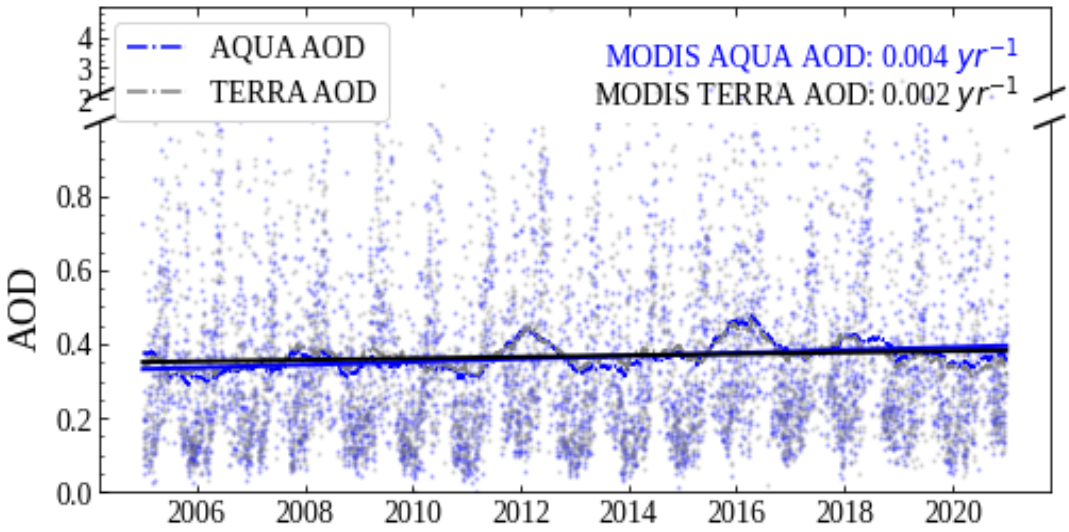

Figure 7.5 *Long-term variations in MODIS AQUA and MODIS TERRA for the period 2006-2020. Scattered points are the daily AOD values and curved lines are monthly moving averages. Linear regression is estimated using 365 days moving average and shown by the linear fit line.*

Trend analysis of ground-based AOD observations from this site during the period 2005-2014 also showed a positive trend of 0.009 per year (Joshi et al., 2022). Using long term data from satellites over a period of 2005-2018, Singh et al., (2020) have shown that AOD over most of the Indian regions is on a rise. Regional AOD using ground-based radiometers over the Indian region was reported earlier to be escalating by 4% per decade (Moorthy et al., 2013). Another AOD trend analysis over different low altitude Indian stations also reported a positive trend in AOD with slopes ranging from 0.0057 to 0.0208 $year^{-1}$ (Babu et al., 2013). This AOD rise was attributed to an increase in anthropogenic emissions. A similar juxtaposition in BC and AOD trends was observed earlier in Trivandrum and other peninsular Indian regions (Manoj et al., 2019). Two possible

hypotheses for these contradictory trends in BC and AOD could be first - a decline in surface BC concentrations with a subsequent rise in the higher altitudes which lends towards the escalation of the AOD and, second - a decline in BC while a rise in other aerosol contents. Therefore, these results suggest a strong need for deeper investigations to test these speculations.

For this purpose, we extracted and analysed the extinction coefficient, particulate depolarisation ratio (PDR) and frequency of occurrences of five aerosol types (dust, polluted dust, clean continental, polluted continental and smoke) using CALIOP observations over 0.5^{o}x0.5^{o} around the site. Details on CALIOP and quality flags used in this extraction can be found in section 2.3.1. The monthly averaged vertical profile of extinction coefficient from 2006 to 2017 reveals that the highest aerosol related extinction occurs in the lowest 2 km region in any given month. A similar analysis for the particulate depolarisation ratio shows that below 1.5 km it usually remains lower than 0.2 which indicates the presence of spherical anthropogenic particles. However, higher values ($0.2<PDR<0.4$) are observed at altitudes greater than 1.5 km especially during the pre-monsoons. This indicates the presence of non-spherical dust particles which are also reported to be transported to the Himalayas from the desert regions of Sahara and Rajasthan (Gautam et al., 2013; Duchi et al., 2014; Sharma et al., 2020). The observed increase in AOD could be a result of these dust aerosols. We also analysed the vertical profile of the averaged normalised frequency of occurrence of different aerosols at the site. The analysis reveals the presence of an elevated layer of aerosols at 2-4 km a.m.s.l. of the site. We further investigated if this aerosol frequency is rising over time using trend analysis. The results of this trend analysis show a negative slope (-0.020 $year^{-1}$) in the lowest 1.5 km of the polluted continental particles while a positive slope (+0.022 $year^{-1}$) in the 1.5-3.5 km layer. Similarly, a positive slope is also observed in the smoke and polluted dust type aerosols till 3.5 km. On the other hand, the trend in the upper altitudes is negative in dust particles after 1.5 km while it is positive in the lower 1.5 km. All this indicates a possibility that anthropogenic aerosols such as black carbon might be reducing in the lower altitudes while they are building in the higher altitudes. However, the observed trends are not significant according to the Mann-Kendall test. Therefore, licensing deeper analysis before any concrete decisions can be drawn.

We also explored the trend in fire events over the northern Indian region (25°-35°N, 70-89°E) to investigate its correlation with BC, especially the biomass fraction. It was found that the trend in fire count is negligible and insignificant. As mentioned previously, the trend in biomass BC fractions was also very small and insignificant. We further investigate the trend in BC emissions from the EDGARv5.0 (Crippa et al., 2019) countries bounding the Himalayas (Figure 7.6). We find that there is a significant positive trend in BC emissions in all six countries. China has the highest BC emissions, followed by India. It may be noticed that BC emissions from China show a tendency of decline since 2013. These emissions data are available till 2015, therefore this decline could not be ascertained thereafter. Further, while the emissions in China are observed to be declining, those in India are still on a rise, though at a slower rate.

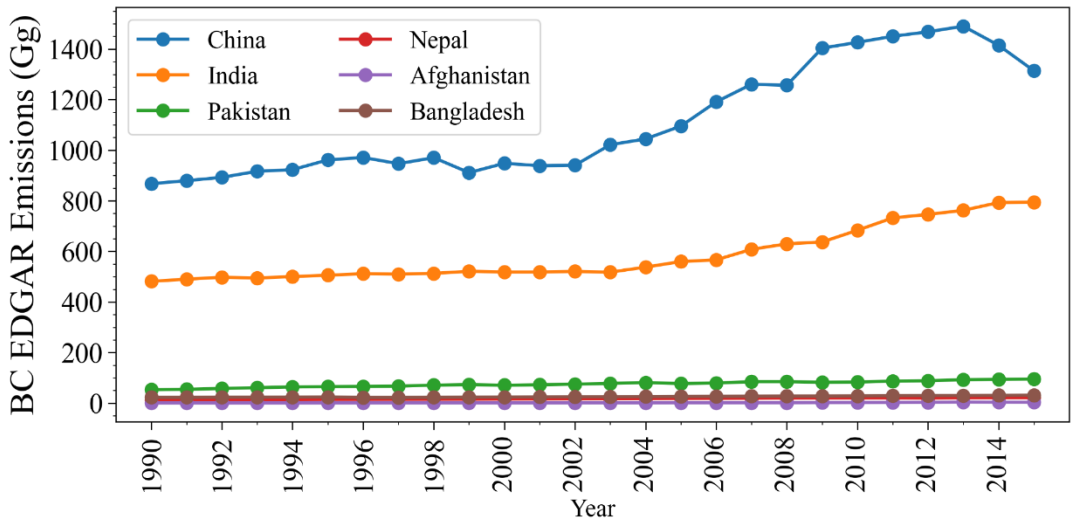

Figure 7.6 *BC emission estimates from EDGARv5.0 during 1990-2015 for China, India, Pakistan, Nepal, Afghanistan and Bangladesh.*

Further, the trend in observed BC is investigated till the year 2016 and it is found that the trend has a significant and positive slope of 27.77 ng m^{-3} $year^{-1}$. The trend declined thereafter with a negative slope of -138 ng m^{-3} $year^{-1}$ from 2017 to 2020. Similar features are observed in the fossil fuel and biomass BC fractions. A significant positive trend is observed in the fossil fuel and biomass BC fractions with a slope of 15.61 ng m^{-3} $year^{-1}$ and 6.05 ng m^{-3} $year^{-1}$ respectively during 2004-2016, while a significant negative trend with a slope of -90.73 ng m^{-3} $year^{-1}$ and -55.86 ng m^{-3} $year^{-1}$ is observed during the period 2017-2020.

This indicates that the trend in BC has reversed from positive to negative since 2017 possibly as a result of stringent control policies imposed in China and India. The results also bring out the importance of continuous ground-based monitoring of these aerosols in ever-changing scenarios. These observations are thus crucial to test and validate the model simulations which incorporate the emission inventories. These inventories are usually prepared for a given base year and model projections made on their basis might be different in a changing world.

7.3. Conclusions

Long-term trends in aerosols are pivotal in understanding the evolution of air quality and its impact on a region. Therefore, we have, in this chapter, presented and discussed the long-term trend in 17 years of ground observations of black carbon (BC) at a high-altitude site in the Central Himalayas. Data from MERRA-2, satellites and emission inventories are also studied. This analysis reveals a statistically significant, yet weak, decreasing trend (Mann-Kendall test) in BC over the Central Himalayas at an average rate of ~18 ng m^{-3} $year^{-1}$ during the period 2004–2020. This trend is in contrast with the trends obtained from MERRA-2 BC data which show a slightly increasing tendency. Further, BC was segregated into fossil fuel and biomass burning fractions and it is found that the fossil fuel fraction dominates (76%) the total BC content. It is also evidenced that the fossil fuel BC fraction declines faster (-20.29 ng m^{-3} $year^{-1}$) than the biomass burning (-3.77 ng m^{-3} $year^{-1}$) fraction. In contrast to the negative trend observed in BC, AOD and emissions over the region are found to show a positive trend. The results unveil a reversal in BC trend from positive to negative after 2017 which leads to an overall negative trend. These observations thus provide a unique long-term characterization of aerosols in an otherwise sparsely studied complex terrain of Central Himalayas and will be very important to test and validate model results, constraint them, assess the regional radiation budget and ascertain the impact of BC in the Himalayas.

Chapter 8

Summary and Future Perspectives

This chapter brings closure to ongoing analysis which explored the effect of carbonaceous aerosols in the serene environment of the Himalayas. It first walks us through the key points in each of the main chapters of this ride. And then in the latter part of this chapter describes the possible mystical paths ahead which unfold as we bring an end to this journey of ours.

8.1. Characteristics of OC and EC in PM 2.5: Radiative Forcing Estimates and Role of Meteorology and Biomass Burning

Online observations of OC and EC were made from a site in the Central Himalayas (ARIES, Nainital; 29.4^{o}N, 79.5^{o}E, 1958 a.m.s.l.) during 2014-2017 and for the first time, the diurnal variations for a complete annual cycle are recorded at a high-altitude site in South Asia. The major points of the study are summarised below:

- The present observations reveal prominent daytime higher concentrations in OC and EC. The noon to night time ratio showed almost double concentrations throughout the period except in monsoons. The diurnal variations at the site are unimodal while such variations in urban sites have been reported to be bimodal.
- Clear seasonal variations in OC and EC were seen with a primary maximum during spring and a secondary one in autumn/winter. The fire events data, the backward air trajectories, CWT analysis and the boundary-layer heights suggest that the spring maximum is predominantly due to large-scale springtime biomass burning in northern India and long-range transport of air masses that influence the central Himalayas. The role of biomass burning is also confirmed by enhancement in the OC/EC ratio from 4.6 to 7.9. On the other hand, higher concentrations in

autumn/winter are suggested to be due to burnings for heating purposes at a local scale.

- The boundary-layer mixing plays an important role in showing OC-EC seasonal variations. A high correlation of OC-EC concentrations with the boundary-layer height indicates the transport of pollutants from the underlying valley region due to the boundary-layer dynamics. The larger heights and the efficient mixing process in spring result in the site coming under the influence of polluted air masses from distant sources. On the other hand, suppressed boundary-layer heights during the rest of the months limit the contribution from other regions and the concentrations are mainly due to local sources.
- Lowest OC/EC concentrations during summer-monsoon are mainly due to the arrival of pristine air masses and could be due to wet scavenging.
- Skewed percentage frequency distributions of OC/EC concentrations show that the site is a relatively cleaner one with perturbations of higher concentrations mainly from transported pollutants.
- Higher OC/EC ratios suggest increased secondary organic aerosols and a mix of biomass burning and fossil fuel combustions, with each dominating during different periods. The higher slope of OC with the residence time confirms that the ageing process dominates OC in the case of aged air masses and leads to higher secondary organic carbon.
- Concentrations of both OC and EC showed a systematic increase with an increase of the residence time of the air masses, confirming the influence of slow-moving winds.
- Comparison of offline with online measurements highlighted positive artefacts and incomplete representation of pollutant variations over time in the offline measurements.
- A real-time variation of OC-EC with meteorological parameters is observed at the diurnal scale. The variation of OC-EC with wind speed and temperature is not captured by averaged observations.
- The impact of diurnal changes in the OC-EC concentrations affects the radiative forcing strongly at the high-altitude site. It was found that the afternoon atmospheric radiative forcing is much higher (about 20.77 Wm^{-2}) than the forenoon one.

The datasets provided here with the online methods could also be useful in performing source characterization of carbon aerosols and epidemiological studies. Both pieces of information hold immense importance for decision-makers to evaluate their current policies on emissions of various species.

8.2. Implications of Site-specific Mass Absorption Cross-section (MAC) to Black Carbon Observations

The simultaneous online observations (2014-2017) of EC and absorption coefficient (b_{abs}) over this high-altitude central Himalayan site of Nainital (29.4^{o}N, 79.5^{o}E, 1958 a.m.s.l) are used to derive the site-specific MAC values. The spectral and temporal (diurnal and monthly) variabilities in MAC are studied and their impacts are also assessed for the central Himalayan region. Important results from this work are:

- Inverse wavelength relation in MAC was established and its proportionality factor was found to be three times lower than the one currently used in Aethalometer.
- A significant seasonal and monthly variation in MAC spanning over a magnitude of 3.7-6.6 $m^2 g^{-1}$ (880 nm) was observed. EC was shown to be the leading absorbing species during all the months except July and August.
- Although MAC does not show any significant diurnal variation, it does show a tendency for greater variability at lower wavelengths. This is attributed to the absorption by species other than EC at the present site, as shown by higher organic content, particularly in spring, when the site is influenced by biomass burning emissions.
- MAC values change with the change of wind regime from north westerly to south-westerly. Low MAC values in monsoons were attributed to the changes in absorptive properties of species along with low EC concentration due to high relative humidity and rainfall in that period.
- It is found that MAC is negatively correlated with temperature, thus showing that the higher temperature seems to reduce the absorption efficiency, possibly due to evaporation of coating material. A positive correlation between MAC and solar radiation shows the role of increased photo-oxidation in increasing organic content and hence MAC.

- The significant improvement in the slope values (with EC) while using corrected eBC, lends credibility to the fact that the use of site-specific MAC leads to an improvement in the estimates of eBC.
- It is shown that uncorrected eBC concentration underestimates the eBC concentration non-linearly during different months. Corrected eBC is higher in September by a factor of 1.54, while this factor is as high as 3.58 in August. Therefore, it is important to use monthly varying MAC values that change with emission sources, mixing states and meteorological conditions including wind regime.
- The use of presently derived site-specific MAC for the eBC leads to higher values (24.6%) of atmospheric radiative forcing when compared with the use of standard MAC value. This difference is about 66.7% and 18.8% higher for TOA and surface, respectively.

This work highlights the necessity of using a site-specific, temporally and spectrally varying MAC, especially for a high-altitude site, which has a far lower MAC value due to aged emissions. It is suggested that a constant MAC value of 16.6 m^2g^{-1} (at 880 nm) should not be used for estimates of eBC when using Aethalometer. The MAC values provided here can be further examined for long term variations over the site and can be considered for future reporting of eBC measurements.

8.3. Probing the Sources, Diurnal Variations and Radiative Forcing of Carbonaceous Aerosols Using High-resolution Ground-based Measurements

There are different offline studies that have performed chemical speciation over the Himalayan region and have qualitatively reported an influence of transported pollutants from the Indo-Gangetic Plain. However, there still remains a knowledge gap in terms of online source apportionment studies which are capable of elucidating the diurnal scale phenomena with respect to the emission sources, quantification of transported pollutants, the influence of biomass burning and radiative forcing. With the aim to fill this gap, the *in-situ* simultaneous online observations of OC, EC, eBC and CO were conducted at a

high-altitude site in the Central Himalayas during the period of 2014–2017. The major conclusions from this study are summarised below:

- The year-round diurnal variations in POC and SOC are estimated for the first time in the Indian Himalayan region. POC is shown to dominate the OC concentration at the site and is shown to have a significant unimodal diurnal variation while SOC does not show such prominent diurnal variation. The highest POC and SOC is observed during spring and is found to be associated with increased pollutant transport, solar flux and photo-oxidation.
- Seasonal variations in both angstrom exponent and OC/EC ratio are found to be influenced by both biomass burning and fossil fuel combustion at the site. The quantitative assessment showed the significant diurnal and monthly variations in fossil fuel (eBC_{ff}) and biomass (eBC_{bb}) components of BC. It is shown that the fossil fuel component of eBC dominates the site throughout the year. Although the biomass burning component peaks during spring, it remains lower than the fossil fuel component.
- Estimated radiative forcing due to fossil fuel component (eBC_{ff}) is shown to be higher than that of biomass burning component (eBC_{bb}). It is also shown that the radiative forcing during the afternoon plays a dominant role with 19.8 and 13.0 Wm^{-2} higher radiative forcing than in the forenoon one for eBC_{ff} and eBC_{bb}, respectively.
- Correlation of carbonaceous aerosols with other pollutants shows the POC concentrations are well correlated with the eBC_{ff} while the SOC concentrations are more influenced by eBC_{bb} and higher mixing layer height.
- CWT analysis and study of biomass burning events reveals that even at this high altitude, the site is significantly affected by the transported pollutants particularly during spring from the north-western IGP region.
- We find that although all the methods indicate that the annual averaged POC is greater than SOC and that the POC/OC% is greater than SOC/OC% at the site in general, they still show different variations, both in terms of seasonal changes and the total concentrations. These variations in the four methods highlight the uncertainty in OC segregation techniques. This clearly emphasises the need of formulating a reference standard for determining SOC to avoid the resulting

ambiguity while comparing POC and SOC obtained from different OC segregation methods.

This study thus provides unique estimates of POC and SOC using long term observations and characterises the carbon-based pollutants at a 'high-resolution' revealing the diurnal scale variations for the first time in an otherwise less-studied region of the Central Himalayas which has significant climatological importance. We envisage that this unique long-term high-resolution assessment of the carbonaceous aerosols and their source characterization can serve as an important piece of dataset and will be resourceful in formulating the mitigation policies, constraining radiation budget and studying their impact on health and climate in the otherwise poorly studied and fragile region of the central Himalayas.

8.4. Application of Black Carbon Measurements to Quantify Contribution of Sources in Carbon Monoxide

The *in-situ* and simultaneous observations of carbon monoxide (CO) and equivalent black carbon (eBC) are utilised to estimate the contribution of the burning of fossil fuel and biomass to ambient CO over the high-altitude region of Central Himalayas. A multiple regression model (MLR) is used to estimate CO during 2014-2017 and the results are compared with the observations. Further, the MLR model is also used to predict CO values for 2018 and are again compared with the observations. Important results from this work are:

- It is found that currently neither the satellite measurements nor the models are able to reproduce well the monthly variations in CO over this region of the central Himalayas. The percentage difference between the observed and the MOPITT CO has a significant monthly variation that ranges from about -25% in May to about +60% in August. WRF-Chem simulated surface CO concentrations underestimate the observed concentrations from February to June while they overestimate CO for other months. MERRA-2 significantly underestimates the observed CO concentration throughout the period.

- The evaluation of the MLR model against ground-based CO observations for the period 2014 to 2017 shows that MLR does quite well in replicating the monthly variation and estimates CO with an r^2 greater than 0.9 for winter, spring and post-monsoon seasons and an r^2 of about 0.8 for monsoon period.
- MLR model setup, which is validated well with the 2014-2017 data was used to predict CO for 2018. It is found that the monthly prediction of CO closely follows the observed variations, and the concentrations lie within 17% of the observed average CO values in any given month during 2018.
- The source segregation analysis shows a clear unimodal diurnal variation in fossil fuel component (CO_{ff}), biomass component (CO_{bb}) and CO, which is largely governed by the boundary layer evolution at the observation site. The diurnal amplitude of CO_{bb} is lesser than CO_{ff} in all the months except for April.
- Fossil fuel combustion is found to be the major contributor (27%) in CO after background CO (58%). CO_{bb} shows a significant rise and reaches up to (28%) during April as a result of increased agricultural and forest fires in the Northern Indian region.
- WRF-Chem tracer runs for source segregation are found to underestimate the biomass burning emissions (-38% to -98%) while they significantly overestimate the fossil fuel CO concentrations especially during monsoon.

We thus find that in comparison to MOPITT, MERRA-2 and WRF-Chem, MLR is successfully able to replicate the CO estimates of the site and is also more reasonable in its source segregation. We envisage that the application of this methodology can be considered more appropriate for regions like India where a network of eBC observations from multiwavelength Aethalometers already exists. This work thus presents an observation-based method to constrain the uncertainties in emission inventories and hence also reduce the uncertainties in the modelling of the climate and radiative impact in this Himalayan region. It also underlines the dire need to mitigate the fossil fuel and biomass-based incomplete combustion activities to maintain the sanctity of the pristine region of the Himalayas.

8.5. Trend in Black Carbon concentration and its Sources: 17 Years of Ground-Based Observations

The Himalayas are facing consequences of the ongoing climate change such as rising temperature, extreme precipitation, glacier retreat, thawing and reduced snow cover. Although much has been speculated about the role of black carbon aerosol in the processes leading to the above effects, there still exist large uncertainties in their detailed understanding and quantification. Ground-based long term BC trends over this region are indispensable in this context to provide the ground truth and help test, constraint and validate the model simulations. With this aforementioned aim, this work presented the results from the first MAC corrected long-term trend in BC and its sources from a high-altitude Central Himalayan site ranging over 17 years from 2004 to 2020 supplemented with satellite measurements and MERRA-2. The key outcome from this work is summarised below:

- The trend of observed BC during the period 2004-2020 shows a statistically significant yet weak negative trend with a slope of –20.03 ng m^{-3} $year^{-1}$. The fall in BC concentrations in this part of the Himalayas is lower than the one reported in other Indian regions.
- Trend analysis from MERRA-2 shows a positive trend with slope +12.99 ng m^{-3} $year^{-1}$, in complete contrast to the negative trend obtained from BC observations. About the BC concentrations, MERRA-2 consistently underestimates (>60%) the observed concentrations during MAM while it overestimates (< -26%) the concentrations during NDJ.
- The fossil fuel fraction dominates (76%) during the entire study period. The trend analysis with linear regression shows that the biomass burning BC fraction declines (-3.77 ng m^{-3} $year^{-1}$) slower than fossil fuel burning (-20.29 ng m^{-3} $year^{-1}$). It was found that the trend in both fire and biomass BC fractions during spring is negligible and insignificant.
- While the linear trend in BC is negative, AOD from the ground, CALIOP and MODIS are all positive. Further, the emissions till 2015 show that BC in China is declining but it is still on a rise in India and other countries.
- The trend in surface BC is significant and positive till 2016 with a slope of 27.77 ng m^{-3} $year^{-1}$ and it started to decline thereafter with a negative slope of -138 ng m^{-3} $year^{-1}$ from 2017 to 2020. Similar features are observed in the fossil fuel and

biomass BC fractions. Thus, indicating a reversal of trend possibly as a result of control policies imposed in China and India.

- The monthly averaged vertical profile of extinction coefficient during 2006-2017 reveals that the highest aerosol related extinction occurs in the lowest 2 km region in any given month. It also shows that below 1.5 km PDR usually remains lower than 0.2 which indicates the presence of spherical anthropogenic particles while higher values (0.2<PDR <0.4) are observed at altitudes greater than 1.5 km especially during the pre-monsoons, suggesting the presence of dust.
- Although insignificant, a negative slope (-0.020 $year^{-1}$) in the lowest 1.5 km of the polluted continental particles while a positive slope (+0.022 $year^{-1}$) in the 1.5-3.5 km layer is observed. This points towards a possibility that anthropogenic aerosols such as black carbon might be reducing in the lower altitudes while they are building in the higher altitudes.

The results thus bring out the importance of continuous ground-based monitoring of these aerosols. These observations are crucial to test and validate the model simulations which incorporate the emission inventories. These inventories are usually prepared for a given base year and model projections made on their basis might deviate from the truth in the ever-changing scenarios of our world. In these cases, such observations can provide a unique long-term characterization of aerosols in an otherwise sparsely studied complex terrain of Central Himalayas and will be very important to assess the regional radiation budget and to ascertain the impact of BC in the Himalayas.

8.6. Future Perspectives

This thesis unveiled several aspects of carbonaceous aerosols ranging from their diurnal and seasonal variations and mass absorption cross-section to their sources, applications, trends and radiative forcing. These results are drawn from rigorous observations made in the complex terrain of the central Himalayan site and were supplemented with data from space-borne sensors and models. The comprehensive analysis not only emphasises the importance of continuous ground-based measurements but also bring to light gaps in our understanding that still need to be addressed. A list of such aspects which can be pursued in future studies are summarized below:

- First and foremost, it is essential to re-emphasize the importance of continuing and further increasing the ground-based observation sites in this Himalayan region. They are invaluable not only to elucidate the current impacts of the carbonaceous aerosols and to develop our understanding of their processes, but they are also indispensable to test and constraint the models and satellites data and evaluate possibilities while formulating the mitigation strategies implicated for these aerosols.
- Many important facets of the carbonaceous aerosols such as their mixing states, size distribution, new particle formation, vertical profile from *in situ* observations and online chemical composition remained largely untouched. The next step should be to initiate a protocol of measurements at the site with an aim to bridge this gap.
- As an important part of this thesis, extensive observations were made to provide the first real-time understanding of secondary and primary organic carbon. It will be extremely important in the near future to continue measurements simultaneously with measurements for volatile organic compounds such as isoprene and monoterpenes. Given the variety of flora around the site, these measurements will surely prove to be invaluable in revealing many possible pathways of new particle formation.
- This work also showed that the performance of current models and satellite-based observations in retrieving the aerosol parameters at this site is not at par with other low altitude sites with higher concentrations. It will be critical in the future to work closely to improve these models and satellite performances. Developing a high-resolution emission inventory for this region will be a crucial step in this direction.
- Another important aspect that can be undertaken immediately could be utilizing the current multi-spectral Aethalometer measurements to evaluate the brown carbon concentrations at the site. New methods developed in the community can be intricately applied for achieving this. The results will be able to provide the first-time long-term characterization of brown carbon over the site.
- Further, peer studies in other parts of the world have shown the potential of geostationary satellites in retrieving carbonaceous aerosols and their optical properties. It will be very useful to evaluate their performance in this Himalayan region having complex topography. Though the Himalayan region is partially covered by an international program (GEMS). Efforts directed towards planning and building suitable payloads for Indian geostationary satellites and developing retrieving methodology will also prove extremely fruitful.

This brings us to the time where we bid farewell to this milestone. This journey unfolded innumerable aspects of carbonaceous aerosols and has simultaneously opened up new mystical paths to be traversed. In our quest for truth and realisation in science, 'older answers give rise to newer questions'. So, we close this door to open up the door of new possibilities with the belief that this will build a chain of incremental improvements in our understanding.

Farewell.

Bibliography

Ackerman, A. S., Toon, O. B., Taylor, J. P., Johnson, D. W., Hobbs, P. V., & Ferek, R. J.: Effects of aerosols on cloud albedo: Evaluation of Twomey's parameterization of cloud susceptibility using measurements of ship tracks. J. Atmos. Sci, 57(16), 2684-2695, 2000.

Adhikary, B., Carmichael, G. R., Tang, Y., Leung, L. R., Qian, Y., Schauer, J. J., Stone EA, Ramanathan V & Ramana, M. V.: Characterization of the seasonal cycle of south Asian aerosols: A regional-scale modelling analysis. J. Geophys. Res. Atmos. 112(D22), 2007.

Akimoto, H.: Global air quality and Pollution, Science, 302, 1716-1719, 2003.

Albrecht, B. A.: Aerosols, cloud microphysics and fractional cloudiness, Science, 245 (4923), 1227-1230, 1989.

Allen, D., Pickering, K., Fox-Rabinovitz, M.: Evaluation of pollutant outfow and CO sources during TRACE-P using model-calculated, aircraft-based, and Measurements of Pollution in the Troposphere (MOPITT)-derived CO concentrations. J. Geophys. Res. Atmos. 109 (D15), 2004.

Andreae, M.O. and Gelencsér, A.: Black carbon or brown carbon? The nature of light-absorbing carbonaceous aerosols. Atmos. Chem. Phys., 6(10), pp.3131-3148, 2006.

Arnott, W.P., Hamasha, K., Moosmüller, H., Sheridan, P.J., Ogren, J.A.: Towards Aerosol Light-Absorption Measurements with a 7-Wavelength Aethalometer: Evaluation with a Photoacoustic Instrument and 3-Wavelength Nephelometer. Aerosol Sci. Technol. 39, 17–29, 2005.

Babu, S. S., Moorthy, K. K., Manchanda, R. K., Sinha, P. R., Satheesh, S. K., Vajja, D. P., Srinivasan S, & Kumar, V. A.: Free tropospheric black carbon aerosol measurements using high altitude balloon: Do BC layers build “their own homes” up in the atmosphere? Geophys. Res. Lett., 38(8), 2011.

Babu, S.S., Manoj, M.R., Moorthy, K.K., Gogoi, M.M., Nair, V.S., Kompalli, S.K., Satheesh, S.K., Niranjan, K., Ramagopal, K., Bhuyan, P.K. and Singh, D.: Trends in aerosol optical depth over Indian region: Potential causes and impact indicators. J. Geophys. Res. Atmos. 118(20), pp.11-794, 2013.

Bachmann, J. Black carbon: A science/policy primer. Pew Center on Global Climate Change, 2009.

Banta, R.M., Mahrt, L., Vickers, D., Sun, J., Balsley, B.B., Pichugina, Y.L., Williams, E.J.: The very stable boundary layer on nights with weak low-level jets. J. Atmos. Sci. 64, 3068–3090, 2007.

Beegum, S. N., Moorthy, K. K., Babu, S. S., Satheesh, S. K., Vinoj, V., Badarinath, K. V, Safai PD, Devara PC, Singh S, Dumka UC, Pant P.: Spatial distribution of aerosol black carbon over India during pre-monsoon season. Atmospheric Environ. 43(5), 1071-1078, 2009.

Beig, G., Ali, K.: Behavior of boundary layer ozone and its precursors over a great alluvial plain of the world: Indo-Gangetic Plains. Geophys. Res. Lett. 33 (24), L24813, 2006.

Beig, G., Gunthe, S., Jadhav, D.B.: Simultaneous measurements of ozone and its precursors on a diurnal scale at a semi urban site in India. J. Atmos. Chem. 57 (3), 239–253, 2007.

Bell, M.L. and Davis, D.L.: Reassessment of the lethal London fog of 1952: novel indicators of acute and chronic consequences of acute exposure to air pollution. Environmental health perspectives, 109(suppl 3), pp.389-394, 2001.

Bernine Khan, Michael D. Hays, Chris Geron & James Jetter: Differences in the OC/EC Ratios that Characterize Ambient and Source Aerosols due to Thermal-Optical Analysis, Aerosol Sci. Technol. 46:2, 127-137, 2012.

Bergin, M.H., Tripathi, S.N., Jai Devi, J., Gupta, T., McKenzie, M., Rana, K.S., Shafer, M.M., Villalobos, A.M. and Schauer, J.J.: The discoloration of the Taj Mahal due to articulate carbon and dust deposition. Environmental science & technology, 49(2), pp.808-812, 2015.

Bhardwaj, P., Manish Naja, R. Kumar, and H. C. Chandola.: Seasonal, interannual, and long-term variabilities in biomass burning activity over South Asia. Environmental Science and Pollution Research 23, no. 5: 4397-4410, 2016.

Bhardwaj, Piyush, Manish Naja, Maheswar Rupakheti, Aurelia Lupascu, Andrea Mues, Arnico Kumar Panday, Rajesh Kumar.: Variations in surface ozone and carbon monoxide in the Kathmandu Valley and surrounding broader regions during SusKat-ABC field campaign: role of local and regional sources. Atmos. Chem. Phys. 18, no. 16, 2018.

Bhardwaj, P., Kumar, R. and Seddon, J.: Interstate transport of carbon monoxide and black carbon over India. Atmospheric Environ. 251, p.118268, 2021.

Birch, M. E., & Cary, R. A.: Elemental carbon-based method for monitoring occupational exposures to particulate diesel exhaust. Aerosol Sci. Technol., 25(3), 221-241, 1996.

Bisht, D.S., Dumka, U.C., Kaskaoutis, D.G., Pipal, A.S., Srivastava, A.K., Soni, V.K., Attri, S.D., Sateesh, M. and Tiwari, S.: Carbonaceous aerosols and pollutants over Delhi urban environment: temporal evolution, source apportionment and radiative forcing. Science of the Total Environment, 521, pp.431-445, 2015.

Bitter, M., Ball, S. M., Povey, I. M., and Jones, R. L.: A broadband cavity ringdown spectrometer for in-situ measurements of atmospheric trace gases, Atmos. Chem. Phys. 5, 2547–2560, 2005.

Bodhaine, B.A., Aerosol absorption measurements at Barrow, Mauna Loa and the south pole. J. Geophys. Res. Atmos. 100(D5), pp.8967-8975, 1995.

Bollasina, M.A., Ming, Y. and Ramaswamy, V.: Anthropogenic aerosols and the weakening of the South Asian summer monsoon. Science, 334(6055), pp.502-505, 2011.

Bond, T.C., Anderson, T.L., Campbell, D.: Calibration and Intercomparison of Filter-Based Measurements of Visible Light Absorption by Aerosols. Aerosol Sci. Technol. 30, 582–600, 1999.

Bond, T. C., & Bergstrom, R. W.: Light absorption by carbonaceous particles: An investigative review. Aerosol Sci. Technol. 40(1), 27-67, 2006.

Bond, T. C., Sarah J. Doherty, David W. Fahey, Piers M. Forster, Terje Berntsen, Benjamin J. DeAngelo, Mark G. Flanner.: Bounding the role of black carbon in the climate system: A scientific assessment. J. Geophys. Res. Atmos. 118, no. 11: 5380-5552, 2013.

Brunekreef, B. and Forsberg, B.: Epidemiological evidence of effects of coarse airborne particles on health. European respiratory journal, 26(2), pp.309-318, 2005.

Cabada, J.C., Pandis, S.N., Subramanian, R., Robinson, A.L., Polidori, A. and Turpin, B.: Estimating the secondary organic aerosol contribution to PM2. 5 using the EC tracer method special issue of aerosol science and technology on findings from the fine particulate matter supersites program. Aerosol Sci. Technol., 38(S1), pp.140-155, 2004.

Cao, J., Zhu, C., Ho, K., Han, Y., Shen, Z., Zhan, C., & Zhang, J.: Light attenuation cross-section of black carbon in an urban atmosphere in northern China. Particuology, 18, 89-95, 2015.

Chandra, S., Satheesh, S. K., & Srinivasan, J.: Can the state of mixing of black carbon aerosols explain the mystery of ‘excess’ atmospheric absorption? Geophys. Res. Lett. 31(19), 2004.

Chandra, N., Lal, S., Venkataramani, S., Patra, P.K. and Sheel, V.: Temporal variations of atmospheric CO 2 and CO at Ahmedabad in western India. Atmos. Chem. Phys. 16(10), pp.6153-6173, 2016.

Cheng, Y., He, K.B., Duan F.K., Zheng, M., Ma Y.L., Tan, J.H., Du Z.Y., Vartiainen E., Kulmala M., Skorokhod A.I., Elansky N.F. and Belikov, I.B.: Improved Measurement of Carbonaceous Aerosol: Evaluation of the Sampling Artifacts and Inter-comparison of the Thermal-optical Analysis Methods. Atmos. Chem. Phys. 10: 8533–8548, 2010.

Cho, Chaeyoon, Sang-Woo Kim, Meehye Lee, Saehee Lim, Wenzheng Fang, Örjan Gustafsson, August Andersson, Rokjin J. Park, and Patrick J. Sheridan.: Observation-based estimates of the mass absorption cross-section of black and brown carbon and their contribution to aerosol light absorption in East Asia. Atmospheric Environ. 212: 65-74, 2019.

Chow, J.C.: Measurement Methods to Determine Compliance with Ambient Air Quality Standards for Suspended Particles. J. Air Waste Manage. Assoc. 45: 320–382, 1995.

Chow, J. C., Watson, J. G., Lu, Z., Lowenthal, D. H., Frazier, C. A., Solomon, P. A., Thuillier RH & Magliano, K.: Descriptive analysis of PM2. 5 and PM10 at regionally representative locations during SJVAQS/AUSPEX. Atmospheric Environ. 30(12), 2079-2112, 1996.

Chung, C.E. and Ramanathan, V.: Weakening of North Indian SST gradients and the monsoon rainfall in India and the Sahel. Journal of Climate, 19(10), pp.2036-2045, 2006.

Crippa, M., Guizzardi, D., Muntean, M., Schaaf, E., Lo Vullo, E., Solazzo, E., Monforti-Ferrario, F., Olivier, J. and Vignati, E.: EDGAR v5. 0 global air pollutant emissions. European Commission, Joint Research Centre (JRC)[Dataset] PID: http://data. europa. eu/89h/377801af-b094-4943-8fdc-f79a7c0c2d19, 2019.

Day, D. E.; Hand, J. L.; Carrico, C. M.; Engling, G.; Malm, W. C.: Humidification factors from laboratory studies of fresh smoke from biomass fuels. J. Geophys. Res., 111, D22202, 2006.

Debell, L.J., Gebhart, K.A., Malm, W.C. and Schichtel, B.A.: December. Spatial trends and urban-rural contrasts in speciated aerosol measurements for the United States. In AGU Fall Meeting Abstracts (Vol. 2006, pp. A43G-04), 2006.

Deng, J., Du, K., Wang, K., Yuan, C. S., & Zhao, J.: Long-term atmospheric visibility trend in Southeast China, 1973–2010. Atmospheric Environ. 59, 11-21, 2012.

Denman, K., Brasseur, G., Chidthaisong, A., Ciais, P., Cox, P., Dickinson, R., Hauglustaine, D., Heinze, C., Holland, E., Jacob, D., Lohmann, U., Ramachandran, S., Silva Dias, P., Wofsy, S., and Zhang, X.: Couplings between changes in the climate system and biogeochemistry, in Climate Change 2007: The Physical Science Basis. Contribution of Working Group I to the Fourth Assessment Report of the Intergovernmental Panel on Climate Change, edited by S. Solomon, D. Qin, M. Manning, Z. Chen, M. Marquis, K. B. Averyt, M. Tignor, and H. L. Miller, pp. 499– 588, Cambridge Univ. Press, Cambridge, United Kingdom and New York, NY, USA, 2007.

Draxler, R.R. and Rolph, G.D.: HYSPLIT (HYbrid Single-Particle Lagrangian Integrated Trajectory) model access via NOAA ARL READY website (http://www. arl. noaa. gov/ready/hysplit4. html). NOAA Air Resources Laboratory, Silver Spring, 2003.

Deeter, M.N., Martínez-Alonso, S., Edwards, D.P., Emmons, L.K., Gille, J.C., Worden, H. M., Sweeney, C., Pittman, J.V., Daube, B.C., Wofsy, S.C.: The MOPITT Version 6 product: algorithm enhancements and validation. Atmos. Meas. Tech. 7 (11), 3623–3632, 2014.

Deeter, M.N., Edwards, D.P., Francis, G.L., Gille, J.C., Martínez-Alonso, S., Worden, H. M., Sweeney, C.: A climate-scale satellite record for carbon monoxide: the MOPITT Version 7 product. Atmos. Meas. Tech. 10 (7), 2533–2555, 2017.

Deeter, M.N., Mao, D., Martínez-Alonso, S., Worden, H.M., Andreae, M.O. and Schlager, H.: Impacts of MOPITT cloud detection revisions on observation frequency and mapping of highly polluted scenes. Remote Sensing of Environment, 262, p.112516, 2021.

Dobhal, D.P., Kumar, S. and Mundepi, A.K.: Morphology and glacier dynamics studies in monsoon–arid transition zone: an example from Chhota Shigri Glacier, Himachal-Himalaya, India. Current science, pp.936-944, 1995.

Drinovec, L., Močnik, G., Zotter, P., Prévôt, A.S.H., Ruckstuhl, C., Coz, E., Rupakheti, M., Sciare, J., Müller, T., Wiedensohler, A. and Hansen, A.D.A.: The" dual-spot" Aethalometer: an improved measurement of aerosol black carbon with real-time loading compensation. Atmos. Meas. Tech. 8(5), pp.1965-1979, 2015.

Drummond, J.R.: Measurements of pollution in the troposphere (MOPITT). In: The Use of EOS for Studies of Atmospheric Physics. North-Holland, New York, pp. 77–101, 1992.

Duchi, R., Cristofanelli, P., Marinoni, A., Bourcier, L., Laj, P., Calzolari, F., Adhikary, B., Verza, G.P., Vuillermoz, E. and Bonasoni, P.: Synoptic-scale dust transport events in the southern Himalaya. Aeolian Research, 13, pp.51-57, 2014.

Dumka, U C, R Sagar, P. Pant.: Retrieval of Columnar Aerosol Size Distributions from Spectral Attenuation Measurements over Central Himalayas, AAQR, 9, 344-351, 2009.

Dumka, U. C., Moorthy, K. K., Kumar, R., Hegde, P., Sagar, R., Pant, P., Singh N & Babu, S. S.: Characteristics of aerosol black carbon mass concentration over a high altitude location in the Central Himalayas from multi-year measurements. Atmospheric Research, 96(4), 510-521, 2010.

Dumka, U. C., Kaskaoutis, D. G., Srivastava, M. K., & Devara, P. C. S.:Scattering and absorption properties of near-surface aerosol over Gangetic-Himalayan region: The role of boundary-layer dynamics and long-range transport. Atmos. Chem. Phys. 15(3), 1555–1572, 2015.

Dumka, U.C., Kaskaoutis, D.G., Tiwari, S., Safai, P.D., Attri, S.D., Soni, V.K., Singh, N. and Mihalopoulos, N.: Assessment of biomass burning and fossil fuel contribution to black carbon concentrations in Delhi during winter. Atmospheric Environ. 194, pp.93-109, 2018.

Favez, O., Haddad, I.E., Piot, C., Boréave, A., Abidi, E., Marchand, N., Jaffrezo, J.L., Besombes, J.L., Personnaz, M.B., Sciare, J. and Wortham, H.: Inter-comparison of source apportionment models for the estimation of wood burning aerosols during wintertime in an Alpine city (Grenoble, France). Atmos. Chem. Phys. 10(12), pp.5295-5314, 2010.

Flanner, M.G., Zender, C.S., Randerson, J.T. and Rasch, P.J.: Present-day climate forcing and response from black carbon in snow. J. Geophys. Res. Atmos. 112(D11), 2007.

Gautam, R., Hsu, N. C., Lau, K.-M., & Kafatos, M.: Aerosol and rainfall variability over the Indian monsoon region: Distribution, trends, and coupling. Annales Geophysicae, 27, 3691–3703, 2009.

Gautam, R., Hsu, N.C., Lau, W.K.M. and Yasunari, T.J.: Satellite observations of desert dust-induced Himalayan snow darkening. Geophys. Res. Lett. 40(5), pp.988-993, 2013.

Gelaro, R., McCarty, W., Suárez, M.J., Todling, R., Molod, A., Takacs, L., Randles, C.A., Darmenov, A., Bosilovich, M.G., Reichle, R. and Wargan, K.: The modern-era retrospective analysis for research and applications, version 2 (MERRA-2). Journal of climate, 30(14), pp.5419-5454, 2017.

Gertler, C.G., Puppala, S.P., Panday, A., Stumm, D. and Shea, J.: Black carbon and the Himalayan cryosphere: A review. Atmospheric Environ. 125, pp.404-417, 2016.

Ghude, S.D., Chate, D.M., Jena, C., Beig, G., Kumar, R., Barth, M.C., Pfister, G.G., Fadnavis, S. and Pithani, P.: Premature mortality in India due to PM2. 5 and ozone exposure. Geophys. Res. Lett. 43(9), pp.4650-4658, 2016.

Giglio, L., Schroeder, W. and Justice, C.O.: The collection 6 MODIS active fire detection algorithm and fire products. Remote sensing of environment, 178, pp.31-41, 2016.

Girach, I.A., Nair, P.R.: Carbon monoxide over Indian region as observed by MOPITT, Atmos. Environ. Times 99, 599–609, 2014.

Granier, C., Bessagnet, B., Bond, T., D'Angiola, A., van der Gon, H.D., Frost, G.J., Heil, A., Kaiser, J.W., Kinne, S., Klimont, Z., Kloster, S., Lamarque, J.F., Liousse, C., Masui, T., Meleux, F., Mieville, A., Ohara, T., Raut, J.C., Riahi, K., Schu, D.P.: Evolution of anthropogenic and biomass burning emissions of air pollutants at global and regional scales during the 1980–2010 period. Climatic Change 109 (1–2), 163–190, 2011.

Goldberg, E. D.: Black carbon in the environment: properties and distribution. New York: J. Wiley, 1985.

Gogoi, M.M., Moorthy, K.K., Kompalli, S.K., Chaubey, J.P., Babu, S.S., Manoj, M.R., Nair, V.S. and Prabhu, T.P.: Physical and optical properties of aerosols in a free tropospheric environment: Results from long-term observations over western trans-Himalayas. Atmospheric Environ. 84, pp.262-274, 2014.

Gogoi, M. M., Babu, S. S., Moorthy, K. K., Bhuyan, P. K., Pathak, B., Subba, T., Chutia L, Kundu SS, Bharali C, Borgohain A, Guha A.: Radiative effects of absorbing aerosols over northeastern India: Observations and model simulations. J. Geophys. Res. Atmos. 122(2), 1132-1157, 2017.

Gul, C., Puppala, S.P., Kang, S., Adhikary, B., Zhang, Y., Ali, S., Li, Y. and Li, X.: Concentrations and source regions of light-absorbing particles in snow/ice in

northern Pakistan and their impact on snow albedo. Atmospheric Chemistry and Physics, 18(7), pp.4981-5000, 2018.

Guttikunda, S.K., Jawahar, P.: Atmospheric emissions and pollution from the coal- fred thermal power plants in India. Atmospheric Environ. 92, 449–460, 2014.

Hansen, A.D.A., Rosen, H. and Novakov, T.: The aethalometer—an instrument for the real-time measurement of optical absorption by aerosol particles. Science of the Total Environment, 36, pp.191-196, 1984.

Hansen, J. E., M. Sato, R. Reudy, A. Lacis, and V. Oinas, Global warming in the 21st century: an alternative scenario, Proc. Nat. Acad. Sci, 97, 9875-9880, 2000.

Hansen, J., Sato, M., Kharecha, P. and Von Schuckmann, K.: Earth's energy imbalance and implications. Atmos. Chem. Phys. 11(24), pp.13421-13449, 2011.

Hinds, W.C.: Aerosol technology: properties, behavior, and measurement of airborne particles. John Wiley & Sons, 1999.

Hegg, D. A.: Heterogeneous production of cloud condensation nuclei in the marine atmosphere, Geophys. Res. Lett., 17, 2165- 2168, 1990.

Hegg, D.A., Livingston, J., Hobbs, P.V., Novakov, T. and Russell, P.: Chemical apportionment of aerosol column optical depth off the mid-Atlantic coast of the United States. J. Geophys. Res. Atmos. 102(D21), pp.25293-25303, 1997.

Hegde, P., Pant, P., Naja, M., Dumka, U. C., & Sagar, R.: South Asian dust episode in June 2006: Aerosol observations in the central Himalayas. Geophys. Res. Lett. 34, L23802, 2007.

Hess, M., P. Koepke, and I. Schult.: Optical properties of aerosols and clouds: The software package OPAC, Bull. Am. Meteorol. Soc., 79, 831–844,1998.

Hewitt, K., & Liu, J.: Ice-Dammed lakes and outburst floods, Karakoram Himalaya: Historical perspectives on emerging threats. Physical Geography, 31(6), 528–551, 2010.

Hoffer, A., Gelencsér, A., Guyon, P., Kiss, G., Schmid, O., Frank, G.P., Artaxo, P. and Andreae, M.O.: Optical properties of humic-like substances (HULIS) in biomass-burning aerosols. Atmos. Chem. Phys. 6(11), pp.3563-3570, 2006.

Hoppel, W.A., J.W. Fitzgerald, G.M. Frick, and R.E. Larson.: Aerosol size distribution and optical properties found in the marine boundary layer over the Atlantic ocean, J. Geophys. Res., 95, 3659-3686, 1990.

Hussain, M.M. and Mahmud, I.: pyMannKendall: a python package for non parametric Mann Kendall family of trend tests. Journal of Open Source Software, 4(39), p.1556, 2019.

IPCC - Boucher, O., D. Randall, P. Artaxo, C. Bretherton, G. Feingold, P. Forster, V.-M. Kerminen, Y. Kondo, H. Liao, U. Lohmann, P. Rasch, S.K. Satheesh, S. Sherwood, B. Stevens and X.Y. Zhang: Clouds and Aerosols. In: Climate Change

2013: The Physical Science Basis. Contribution of Working Group I to the Fifth Assessment Report of the Intergovernmental Panel on Climate Change [Stocker, T.F., D. Qin, G.-K. Plattner, M. Tignor, S.K. Allen, J. Boschung, A. Nauels, Y. Xia, V. Bex and P.M. Midgley (eds.)]. Cambridge University Press, Cambridge, United Kingdom and New York, NY, USA, 2013.

Jansen, K. L., Larson, T. V., Koenig, J. Q., Mar, T. F., Fields, C., Stewart, J., & Lippmann, M.: Associations between health effects and particulate matter and black carbon in subjects with respiratory disease. Environmental health perspectives, 113(12), 1741-1746, 2005.

Jacobson, M. Z.: Strong radiative heating due to the mixing state of black carbon in atmospheric aerosols, Nature, 409, 695–697, 2001.

Jacobson, M.Z., Kaufman, Y.J. and Rudich, Y.: Examining feedbacks of aerosols to urban climate with a model that treats 3-D clouds with aerosol inclusions. J. Geophys. Res. Atmos. 112(D24), 2007.

Jacobson, M.Z. and Streets, D.G.: Influence of future anthropogenic emissions on climate, natural emissions, and air quality. J. Geophys. Res. Atmos. 114(D8), 2009.

Jaenicke, R.: Physical aspects of atmospheric aerosol, in Aerosols and their climatic effects, (Ed. H.E. Gerbard and A. Deepak), A. Deepak Publishing, Hampton, Virginia, pp.7-34, 1984.

Ji, Z., Kang, S., Cong, Z., Zhang, Q., & Yao, T.: Simulation of carbonaceous aerosols over the Third Pole and adjacent regions: Distribution, transportation, deposition, and climatic effects. Climate Dynamics, 45(9–10), 2831–2846, 2015.

Joshi, H.: Study of aerosols characteristics over Central Himalayas, Ph. D. thesis, Kumaun University, Nainital, India, 2015.

Joshi, H., Manish Naja, K.P. Singh, Rajesh Kumar, P. Bhardwaj, S. Suresh Babu, S.K. Satheesh, K. Krishna Moorthy, H.C. Chandola: Investigations of aerosol black carbon from a semi-urban site in the Indo-Gangetic Plain region. Atmospheric Environ. 125, 346-359, 2016.

Joshi, H., Naja, M., David, L.M., Gupta, T., Gogoi, M.M. and Babu, S.S.: Absorption characteristics of aerosols over the central Himalayas and its adjacent foothills. Atmospheric Research, 233, p.104718, 2020.

Joshi, H., Naja, M., Srivastava, P., Gupta, T., Gogoi, M.M. and Babu, S.S.: Long-Term Trends in Aerosol Black Carbon and Aerosol Optical Depth from a HighAltitude Site in the Central Himalayas, under review in Frontiers in Earth Science, 2022.

Junge, C. E.: Air Chemistry and Radioactivity, Academic Press, New York, 1963.

Kalogridis, A.C., Vratolis, S., Liakakou, E., Gerasopoulos, E., Mihalopoulos, N. and Eleftheriadis, K.: Assessment of wood burning versus fossil fuel contribution to wintertime black carbon and carbon monoxide concentrations in Athens, Greece. Atmos. Chem. Phys. 18(14), pp.10219-10236, 2018.

Kant, Y., Shaik, D.S., Mitra, D., Chandola, H.C., Babu, S.S. and Chauhan, P.: Black carbon aerosol quantification over north-west Himalayas: Seasonal heterogeneity, source apportionment and radiative forcing. Environmental Pollution, 257, p.113446, 2020.

Kato, J.: Measurement technique and its application to trace components of atmospheric gas. HORIBA Readout, 10, pp.30-35, 2006.

Kaspari, S. D., Schwikowski, M., Gysel, M., Flanner, M. G., Kang, S., Hou, S., & Mayewski, P. A.: Recent increase in black carbon concentrations from a Mt. Everest ice core spanning 1860–2000 AD. Geophys. Res. Lett. J. 38(4), 2011.

Kaskaoutis, D.G., Badarinath, K.V.S., Kumar Kharol, S., Rani Sharma, A. and Kambezidis, H.D.: Variations in the aerosol optical properties and types over the tropical urban site of Hyderabad, India. J. Geophys. Res. Atmos. 114(D22), 2009.

Kaskaoutis, D.G., Kalapureddy, M.C.R., Krishna Moorthy, K., Devara, P.C.S., Nastos, P.T., Kosmopoulos, P.G. and Kambezidis, H.D.: Heterogeneity in pre-monsoon aerosol types over the Arabian Sea deduced from ship-borne measurements of spectral AODs. Atmos. Chem. Phys. 10(10), pp.4893-4908, 2010.

Kaskaoutis, D.G., Rashki, A., Houssos, E.E., Legrand, M., Francois, P., Bartzokas, A., Kambezidis, H.D., Dumka, U.C., Goto, D. and Takemura, T.: Assessment of changes in atmospheric dynamics and dust activity over southwest Asia using the Caspian Sea–Hindu Kush Index. International Journal of Climatology, 37, pp.1013-1034, 2017.

Kaur, P., Srinivasan, P., Dhar, P., De, B.K. and Guha, A.: Study of spectral characteristics of black carbon from biomass burning and source apportionment over Agartala in the northeastern India. Environmental Science and Pollution Research, 27(14), pp.16584-16598, 2020.

Kawase, H., Takemura, T. and Nozawa, T.: Impact of carbonaceous aerosols on precipitation in tropical Africa during the austral summer in the twentieth century. J. Geophys. Res. Atmos. 116(D18), 2011.

Kennedy, I. M.: The health effects of combustion-generated aerosols. Proceedings of the Combustion Institute, 31(2), 2757-2770, 2007.

Kirchstetter, Thomas W., T. Novakov, and Peter V. Hobbs.: Evidence that the spectral dependence of light absorption by aerosols is affected by organic carbon. J. Geophys. Res. Atmos. 109, no. D21, 2004.

Knox, A., Evans, G.J., Brook, J.R., Yao, X., Jeong, C.H., Godri, K.J., Sabaliauskas, K. and Slowik, J.G.: Mass absorption cross-section of ambient black carbon aerosol in relation to chemical age. Aerosol Sci. Technol. 43(6), pp.522-532, 2009.

Kondo, Y., Komazaki, Y., Miyazaki, Y., Moteki, N., Takegawa, N., Kodama, D., Deguchi, S., Nogami, M., Fukuda, M., Miyakawa, T. and Morino, Y.: Temporal variations of elemental carbon in Tokyo. J. Geophys. Res. Atmos. 111(D12), 2006.

Krishna Moorthy, K., Suresh Babu, S., Manoj, M. R., & Satheesh, S. K.: Buildup of aerosols over the Indian Region. Geophys. Res. Lett. 40(5), 1011-1014, 2013.

Kulshrestha, U.C., Kumar, N., Saxena, A., Kumari, K.M. and Srivastava, S.S.: Identification of the nature and source of atmospheric aerosols near the Taj Mahal (India). Environmental monitoring and assessment, 34(1), pp.1-11, 1995.

Kulshrestha, U.C., Reddy, L.A.K., Satyanarayana, J. and Kulshrestha, M.J.: Real-time wet scavenging of major chemical constituents of aerosols and role of rain intensity in Indian region. Atmospheric Environ. 43(32), pp.5123-5127, 2009.

Kumar, R., Naja, M., Venkataramani, S., & Wild, O.: Variations in surface ozone at Nainital: A high-altitude site in the central Himalayas. J. Geophys. Res. Atmos. 115(D16), 2010.

Kumar, R., M. Naja, S. K. Satheesh, N. Ojha, H. Joshi, T. Sarangi, P. Pant, U. C. Dumka, P. Hegde, and S. Venkataramani: Influences of the springtime northern Indian biomass burning over the central Himalayas, J. Geophys. Res. Atmos. 116, D19302, 2011.

Kumar, R., Naja, M., Pfster, G.G., Barth, M.C., Brasseur, G.P.: Source attribution of carbon monoxide in India and surrounding regions during wintertime. J. Geophys. Res. Atmos. 118 (4), 1981–1995, 2013.

Kumar, A., Bali, K., Singh, S., Naja, M. and Mishra, A.K.: Estimates of reactive trace gases (NMVOCs, CO and NOx) and their ozone forming potentials during forest fire over Southern Himalayan region. Atmospheric research, 227, pp.41-51, 2019.

Kumar, R.R., Soni, V.K. and Jain, M.K.: Evaluation of spatial and temporal heterogeneity of black carbon aerosol mass concentration over India using three year measurements from IMD BC observation network. Science of the Total Environment, 723, p.138060, 2020.

Kumar, A., Singh, S., Kumar, N., Singh, N., Kumar, K., Mishra, A.K., Chourasiya, S. and Kushwaha, H.S.: Seasonal Abundance and Source Attribution of Carbonaceous Aerosols at Different Altitude of Mountainous Locations in Uttarakhand Himalaya. Aerosol Science and Engineering, 5(2), pp.233-246, 2021.

Kurokawa, J., Ohara, T., Morikawa, T., Hanayama, S., Greet, J.-M., Fukui, T., Kawashima, K., Akimoto, H.: Emissions of air pollutants and greenhouse gases over Asian regions during 2000e2008: Regional Emission inventory in ASia (REAS) version 2. Atmos. Chem. Phys. Discuss. 13, 10049e10123, 2013.

Kurokawa, J., Ohara, T.: Long-term historical trends in air pollutant emissions in Asia: regional Emission inventory in ASia (REAS) version 3.1. Atmos. Chem. Phys. Discuss, 2019.

Lack, D.A., Cappa, C.D.: Impact of brown and clear carbon on light absorption enhancement, single scattering albedo and absorption wavelength dependence of black carbon. Atmos. Chem. Phys. 10, 4207–4220, 2010.

Lal, S., Naja, M., Subbaraya, B.H.: Seasonal variations in surface ozone and its precursors over an urban site in India. Atmospheric Environ. 34 (17), 2713–2724, 2000.

Lal, S., Chandra, N. and Venkataramani, S.: A study of CO 2 and related trace gases using a laser-based technique at an urban site in western India. Current Science, pp.2111-2116, 2015.

Lamarque, J.F., Bond, T.C., Eyring, V., Granier, C., Heil, A., Klimont, Z., Lee, D., Liousse, C., Mieville, A., Owen, B. and Schultz, M.G.: Historical (1850–2000) gridded anthropogenic and biomass burning emissions of reactive gases and aerosols: methodology and application. Atmos. Chem. Phys. 10(15), pp.7017-7039, 2010.

Lau, K. M., M. K. Kim and K. M. Kim.: Asian monsoon anomalies induced by aerosol direct forcing: the role of the Tibetan Plateau Clim. Dyn. 26 855–64, 2006.

Lau, W. K., Kim, M. K., Kim, K. M., & Lee, W. S.: Enhanced surface warming and accelerated snow melt in the Himalayas and Tibetan Plateau induced by absorbing aerosols. Environmental Research Letters, 5(2), 025204, 2010.

Lavanchy, V. M. H., H. W. Gäggeler, S. Nyeki, and U. Baltensperger.: Elemental carbon (EC) and black carbon (BC) measurements with a thermal method and an Aethalometer at the high-alpine research station Jungfraujoch. Atmospheric Environ. 33, no. 17: 2759-2769, 1999.

Levy, R.C., Mattoo, S., Munchak, L.A., Remer, L.A., Sayer, A.M., Patadia, F., Hsu, N.C.: The Collection 6 MODIS aerosol products over land and ocean. Atmos. Meas. Tech. 6, 2989–3034, 2013.

Li, C., Chen, P., Kang, S., Yan, F., Hu, Z., Qu, B. and Sillanpää, M.: Concentrations and light absorption characteristics of carbonaceous aerosol in PM2. 5 and PM10 of Lhasa city, the Tibetan Plateau. Atmospheric Environ. 127, pp.340-346, 2016a.

Li, C., Yan, F., Kang, S., Chen, P., Hu, Z., Gao, S., Qu, B. and Sillanpää, M.: Light absorption characteristics of carbonaceous aerosols in two remote stations of the southern fringe of the Tibetan Plateau, China. Atmospheric Environ. 143, pp.79-85, 2016b.

Li, C., Yan, F., Kang, S., Chen, P., Hu, Z., Han, X., Zhang, G., Gao, S., Qu, B. and Sillanpää, M.: Deposition and light absorption characteristics of precipitation dissolved organic carbon (DOC) at three remote stations in the Himalayas and Tibetan Plateau, China. Science of The Total Environment, 605, pp.1039-1046, 2017.

Li, H., McMeeking, G.R., May, A.A.: Development of a new correction algorithm applicable to any filter-based absorption photometer. Atmos. Meas. Tech. 13, 2865– 2886, 2020.

Li, C., Yan, F., Kang, S., Yan, C., Hu, Z., Chen, P., Gao, S., Zhang, C., He, C., Kaspari, S. and Stubbins, A.: Carbonaceous matter in the atmosphere and glaciers of the

Himalayas and the Tibetan plateau: An investigative review. Environment international, 146, p.106281, 2021.

Lim, H.J. and Turpin, B.J.: Origins of primary and secondary organic aerosol in Atlanta: Results of time-resolved measurements during the Atlanta supersite experiment. Environmental Science & Technology, 36(21), pp.4489-4496, 2002.

Lin, P., Hu, M., Deng, Z., Slanina, J., Han, S., Kondo, Y., Takegawa, N., Miyazaki, Y., Zhao, Y. and Sugimoto, N.: Seasonal and diurnal variations of organic carbon in PM2. 5 in Beijing and the estimation of secondary organic carbon. J. Geophys. Res. Atmos. 114(D2), 2009.

Liousse, C., Cachier, H., & Jennings, S. G.: Optical and thermal measurements of black carbon aerosol content in different environments: Variation of the specific attenuation cross-section, sigma (σ). Atmospheric Environment. Part A. General Topics, 27(8), 1203-1211, 1993.

Liu, Z., Vaughan, M., Winker, D., Kittaka, C., Getzewich, B., Kuehn, R., Omar, A., Powell, K., Trepte, C. and Hostetler, C.: The CALIPSO lidar cloud and aerosol discrimination: Version 2 algorithm and initial assessment of performance. Journal of Atmospheric and Oceanic Technology, 26(7), pp.1198-1213, 2009.

Liu, Fengshan, Jérôme Yon, Andrés Fuentes, Prem Lobo, Gregory J. Smallwood, and Joel C. Corbin: "Review of recent literature on the light absorption properties of black carbon: Refractive index, mass absorption cross section, and absorption function." Aerosol Sci. Technol. 54, no. 1: 33-51, 2020.

Malaguti, A., Mircea, M., La Torretta, T. M., Telloli, C., Petralia, E., Stracquadanio, M., & Berico, M.: Comparison of online and offline methods for measuring fine secondary inorganic ions and carbonaceous aerosols in the central Mediterranean area. Aerosol and Air Quality Research, 15(7), 2641-2653, 2015.

Mallik, C., Lal, S., Venkataramani, S., Naja, M., Ojha, N.: Variability in ozone and its precursors over the Bay of Bengal during post monsoon: transport and emission effects. J. Geophys. Res. Atmos. 118 (17), 2013.

Malm, W.C., Schichtel, B.A., Pitchford, M.L., Ashbaugh, L.L. and Eldred, R.A.: Spatial and monthly trends in speciated fine particle concentration in the United States. J. Geophys. Res. Atmos.109(D3), 2004.

Manoj, M. G., Devera, P. C. S., & Safai, P. D.: Absorbing aerosols facilitate transition of Indian monsoon breaks to active spells. Climate Dynamics, 37, 2181–2198, 2010.

Manoj, M.R., Satheesh, S.K., Moorthy, K.K., Gogoi, M.M. and Babu, S.S.: Decreasing trend in black carbon aerosols over the Indian region. Geophys. Res. Lett. 46(5), pp.2903-2910, 2019.

McCartney, E.J.: Optics of the atmosphere, John Wiley, New York, 1976.

Meehl, G. A., Arblaster, J. M., & Collins, W. D.: Effects of black carbon aerosols on the Indian Monsoon. Journal of Climate, 21, 2869–2882, 2008.

Menon, S., Akbari, H., Mahanama, S., Sednev, I. and Levinson, R.: Radiative forcing and temperature response to changes in urban albedos and associated CO2 offsets. Environmental Research Letters, 5(1), p.014005, 2010.

Millet, D.B., Donahue, N.M., Pandis, S.N., Polidori, A., Stanier, C.O., Turpin, B.J. and Goldstein, A.H.: Atmospheric volatile organic compound measurements during the Pittsburgh Air Quality Study: Results, interpretation, and quantification of primary and secondary contributions. J. Geophys. Res. Atmos. 110(D7), 2005.

Ming, J., Wang, Y., Du, Z., Zhang, T., Guo, W., Xiao, C., Xu, X., Ding, M., Zhang, D. and Yang, W.: Widespread albedo decreasing and induced melting of Himalayan snow and ice in the early 21st century. PLoS One, 10(6), p.e0126235, 2015.

Moorthy, K.K., Suresh Babu, S., Sunilkumar, S.V., Gupta, P.K., Gera, B.S.: Altitude profile of aerosol BC, derived from aircraft measurements over an inland urban location in India. Geophys. Res. Lett. 31, 22103, 2004.

Moorthy, K. Krishna, S. Suresh Babu, S. K. Satheesh, J. Srinivasan, and C. B. S. Dutt. "Dust absorption over the “Great Indian Desert” inferred using ground-based and satellite remote sensing." J. Geophys. Res. Atmos. 112, no. D9, 2007.

Moorthy, K.K., Nair, V.S., Babu, S.S. and Satheesh, S.K.: Spatial and vertical heterogeneities in aerosol properties over oceanic regions around India: Implications for radiative forcing. Quarterly Journal of the Royal Meteorological Society: A journal of the atmospheric sciences, applied meteorology and physical oceanography, 135(645), pp.2131-2145, 2009.

Moorthy, K. K., Babu, S. S., Manoj, M. R., Satheesh, S. K.: Buildup of aerosols over the Indian Region. Geophys. Res. Lett. 40, 1011– 1014, 2013.

Morishita, M., Keeler, G.J., Kamal, A.S, Wagner, J.G, Harkema, J.R. and Rohr, A.C.: Identification of Ambient PM2.5 Sources and Analysis Pollution Episodes in Detroit, Michigan Using Highly Time-resolved Measurements. Atmos. Environ. 45: 1627–1637, 2011

Mousavi, A., Sowlat, M.H., Hasheminassab, S., Polidori, A. and Sioutas, C.: Spatio-temporal trends and source apportionment of fossil fuel and biomass burning black carbon (BC) in the Los Angeles Basin. Science of the Total Environment, 640, pp.1231-1240, 2018.

Müller, T., J. S. Henzing, G. de Leeuw, Alfred Wiedensohler, Andrés Alastuey, H. Angelov, M. Bizjak et al.: Characterization and intercomparison of aerosol absorption photometers: result of two intercomparison workshops. Atmos. Meas. Tech. 4, no. 2, 245-268, 2011.

Myhre, G., D. Shindell, F.-M. Bréon, W. Collins, J. Fuglestvedt, J. Huang, D. Koch, J.-F. Lamarque, D. Lee, B. Mendoza, T. Nakajima, A. Robock, G. Stephens, T. Takemura and H. Zhang: Anthropogenic and Natural Radiative Forcing. In: Climate Change 2013: The Physical Science Basis. Contribution of Working Group I to the Fifth Assessment Report of the Intergovernmental Panel on Climate Change [Stocker, T.F., D. Qin, G.-K. Plattner, M. Tignor, S.K. Allen, J. Boschung, A.

Nauels, Y. Xia, V. Bex and P.M. Midgley (eds.)]. Cambridge University Press, Cambridge, United Kingdom and New York, NY, USA, 2013.

Nainwal, H.C., Banerjee, A., Shankar, R., Semwal, P. and Sharma, T.: Shrinkage of Satopanth and Bhagirath Kharak glaciers, India, from 1936 to 2013. Annals of glaciology, 57(71), pp.131-139, 2016.

Naja, M., Lal, S.: Surface ozone and precursor gases at Gadanki (13.5◦N, 79.2◦E), a tropical rural site in India. J. Geophys. Res. Atmos. 107 (D14), 4197, 2002.

Naja, M., Akimoto, H., & Staehelin, J.: Ozone in background and photochemically aged air over central Europe: Analysis of long-term ozonesonde data from Hohenpeissenberg and Payerne. J. Geophys. Res. Atmos. 108(D2), 2003.

Naja, M. and Akimoto, H.: Contribution of regional pollution and long-range transport to the Asia-Pacific region: Analysis of long-term ozonesonde data over Japan, J. Geophys. Res., 109, D21306, 2004.

Naja, M., C Mallik, T. Sarangi, V Sheel, S. Lal: SO2 measurements at a high altitude site in the central Himalayas: Role of regional transport, Atmospheric Environ, 2014.

Naja, M., Piyush Bhardwaj, N. Singh, Phani Kumar, R. Kumar, N. Ojha, Ram Sagar, S. K. Satheesh, K. Krishna Moorthy and V. R. Kotamarthi: High-frequency vertical profiling of meteorological parameters using AMF1 facility during RAWEX–GVAX at ARIES, Nainital, Current Science, vol 111, issue 1, 2016.

Nandi, I., Srivastava, S., Yarragunta, Y., Kumar, R. and Mitra, D.: Distribution of surface carbon monoxide over the Indian subcontinent: investigation of source contributions using WRF-Chem. Atmospheric Environ. 243, p.117838, 2020.

Nordmann, S., W. Birmili, K. Weinhold, K. Müller, G. Spindler, and A. Wiedensohler.: Measurements of the mass absorption cross section of atmospheric soot particles using Raman spectroscopy. J. Geophys. Res. Atmos. 118, no. 21: 12-075, 2013.

Novelli, P.C., Masarie, K.a., Lang, P.M.: Distributions and recent changes of carbon monoxide in the lower troposphere. J. Geophys. Res. Atmos. 103 (D15), 19015, 1998.

Ojha, N., Naja, M., Singh, K.P., Sarangi, T., Kumar, R., Lal, S., Lawrence, M.G., Butler, T. M., Chandola, H.C.: Variabilities in ozone at a semi-urban site in the Indo-Gangetic Plain region: association with the meteorology and regional processes. J. Geophys. Res. Atmos. 117 (20), 1–19, 2012.

Olson, Michael R., Mercedes Victoria Garcia, Michael A. Robinson, Paul Van Rooy, Mark A. Dietenberger, Michael Bergin, and James Jay Schauer.: Investigation of black and brown carbon multiple-wavelength-dependent light absorption from biomass and fossil fuel combustion source emissions. J. Geophys. Res. Atmos. 120, no. 13 : 6682-6697, 2015.

Ostro, B., Tobias, A., Karanasiou, A., Samoli, E., Querol, X., Rodopoulou, S., Basagaña, X., Eleftheriadis, K., Diapouli, E., Vratolis, S. and Jacquemin, B.: The risks of acute

exposure to black carbon in Southern Europe: results from the MED-PARTICLES project. Occupational and environmental medicine, 72(2), pp.123-129, 2015.

Paige Presler-Jur, Prakash Doraiswamy, Okisha Hammond & Joann Rice.: An evaluation of mass absorption cross-section for optical carbon analysis on Teflon filter media, Journal of the Air & Waste Management Association, 67:11, 1213-1228, 2017.

Pant, P., P. Hegde, U. C. Dumka, R. Sagar, S. K. Satheesh, K. K. Moorthy, A. Saha, and M. K. Srivastava.: Aerosol characteristics at a high- altitude location in central Himalayas, J. Geophys. Res. Atmos. 111, D17206, 2006.

Park, K., Emmons, L.K., Wang, Z. and Mak, J.E.: Joint application of concentration and δ18O to investigate the global atmospheric CO budget. Atmosphere, 6(5), pp.547-578, 2015.

Petzold, A., Ogren, J. A., Fiebig, M., Laj, P., Li, S. M., Baltensperger, U., & Wehrli, C.: Recommendations for reporting" black carbon" measurements. Atmos. Chem. Phys. 13(16), 8365-8379, 2013.

Prospero, J.M., R A. Glaccum, and R.T. Nees.: Atmospheric transport of soil dust from Africa to South America, Nature, 289, 570-572, 1981.

Pruppacher, H.R., and J.D. Klett.: Microphysics of clouds and precipitation, D. Reidel publishing company, Holland, 1978.

Qin, Y., & Xie, S. D.: Spatial and temporal variation of anthropogenic black carbon emissions in China for the period 1980–2009. Atmos. Chem. Phys. 12(11), 4825-4841, 2012.

Qian, Y., Flanner, M. G., Leung, L. R., & Wang, W.: Sensitivity studies on the impacts of Tibetan Plateau snowpack pollution on the Asian hydrological cycle and monsoon climate. Atmos. Chem. Phys.11, 1929–1948, 2011.

Qian, Y., Yasunari, T.J., Doherty, S.J., Flanner, M.G., Lau, W.K., Ming, J., Wang, H., Wang, M., Warren, S.G. and Zhang, R.: Light-absorbing particles in snow and ice: Measurement and modeling of climatic and hydrological impact. Advances in Atmospheric Sciences, 32(1), pp.64-91, 2015.

Radke, L. F., P. V. Hobbs, and M. W. Eltgroth.: Scavenging of aerosol particles by precipitation, J. Appl. Meteorol, 19, 715-722, 1980.

Rajesh, T.A. and Ramachandran, S.: Characteristics and source apportionment of black carbon aerosols over an urban site. Environmental Science and Pollution Research, 24(9), pp.8411-8424, 2017.

Ram, K., Sarin, M. M., & Hegde, P.: Atmospheric abundances of primary and secondary carbonaceous species at two high-altitude sites in India: sources and temporal variability. Atmospheric Environ. 42(28), 6785-6796, 2008.

Ram, Kirpa, and M. M. Sarin.: Absorption coefficient and site-specific mass absorption efficiency of elemental carbon in aerosols over urban, rural, and high-altitude sites in India. Environmental science & technology 43, no. 21: 8233-8239, 2009.

Ram, K., Sarin, M. M., & Hegde, P.: Long-term record of aerosol optical properties and chemical composition from a high-altitude site (Manora Peak) in Central Himalaya. Atmos. Chem. Phys. 10(23), 11791-11803, 2010.

Ram, K., Sarin, M. M., & Tripathi, S. N.: Temporal trends in atmospheric PM2. 5, PM10, elemental carbon, organic carbon, water-soluble organic carbon, and optical properties: impact of biomass burning emissions in the Indo-Gangetic Plain. Environmental science & technology, 46(2), 686-695, 2012.

Ramanathan, V., Chung, C., Kim, D., Bettge, T., Buja, L., Kiehl, J.T., Washington, W.M., Fu, Q., Sikka, D.R. and Wild, M.: Atmospheric brown clouds: Impacts on South Asian climate and hydrological cycle. Proceedings of the National Academy of Sciences, 102(15), pp.5326-5333, 2005.

Ramanathan, V., & Carmichael, G.: Global and regional climate changes due to black carbon. Nature geoscience, 1(4), 221, 2008.

Rana, A., Jia, S. and Sarkar, S.: Black carbon aerosol in India: A comprehensive review of current status and future prospects. Atmospheric Research, 218, pp.207-230, 2019.

Rastogi, N., & Sarin, M. M.: Quantitative chemical composition and characteristics of aerosols over western India: One-year record of temporal variability. Atmospheric Environ. 43(22-23), 3481-3488, 2009.

Reddy, K., Phanikumar, D. V., Joshi, H., Ahammed, Y. N., & Naja, M.: Effect of diurnal variation of aerosols on surface reaching solar radiation. Journal of Atmospheric and Solar-Terrestrial Physics, 129, 62-68, 2015.

Reist, P. C.: Introduction to aerosol science, MacMillan Publishing Company, 1984.

Reist, P. C.: Aerosol Science and Technology, 2nd Edition, McGraw-Hall, 1993.

Rhodes, Martin J., ed.: Introduction to particle technology. John Wiley & Sons, 2008.

Ricchiazzi, P., Yang, S., Gautier, C. and Sowle, D.: SBDART: A research and software tool for plane-parallel radiative transfer in the Earth's Atmosphere, Bull. Am. Meteorol. Soc., 79, 2101, 1998.

Rienecker, M.M., Suarez, M.J., Todling, R., Bacmeister, J., Takacs, L., Liu, H.C., Gu, W., Sienkiewicz, M., Koster, R.D., Gelaro, R. and Stajner, I.: The GEOS-5 Data Assimilation System: Documentation of Versions 5.0. 1, 5.1. 0, and 5.2., 2008.

Rosenfeld, D., Lohmann, U., Raga, G.B., O'Dowd, C.D., Kulmala, M., Fuzzi, S., Reissell, A. and Andreae, M.O.: Flood or drought: how do aerosols affect precipitation?. Science, 321(5894), pp.1309-1313, 2008.

Saarikoski, S., Timonen, H., Saarnio, K., Aurela, M., Järvi, L., Keronen, P., Kerminen, V.M. & Hillamo, R.: Sources of organic carbon in fine particulate matter in northern European urban air. Atmos. Chem. Phys. 8(20), 2008.

Safai, P. D., Raju, M. P., Rao, P. S. P., & Pandithurai, G.: Characterization of carbonaceous aerosols over the urban tropical location and a new approach to evaluate their climatic importance. Atmospheric Environ. 92, 493-500, 2014.

Safai, P.D., Ghude, S., Pithani, P., Varpe, S., Kulkarni, R., Todekar, K., Tiwari, S., Chate, D.M., Prabhakaran, T., Jenamani, R.K. and Rajeevan, M.N.: Two-way relationship between aerosols and fog: A case study at IGI airport, New Delhi. Aerosol and Air Quality Research, 19(1), pp.71-79, 2019.

Sagar, R. Manish Naja, G. Maheswar, A. K. Srivastava: Science at High-Altitude Sites of ARIES - Astrophysics and Atmospheric Sciences, 80(4):759-790, 2014.

Sahu, L.K., Lal, S., Venkataramani, S.: Distributions of O3, CO and hydrocarbons over the Bay of Bengal: a study to assess the role of transport from southern India and marine regions during September-October 2002, Atmos. Environ. Times 40 (24), 4633–4645, 2006.

Sahu, L.K., Varun Sheel, Kajino, M., Deushi, M., Gunthe, Sachin S., Sinha, P.R., Yadav, Ravi, Pal, Devendra, Nedelec, P., Thouret, V., Smit, H.G.: Impact of tropical convection and ENSO variability in vertical distributions of CO and O 3 over an urban site of India. Clim. Dynam, 2016.

Saleh, R., Marks, M., Heo, J., Adams, P.J., Donahue, N.M., Robinson, A.L.: Contribution of brown carbon and lensing to the direct radiative effect of carbonaceous aerosols from biomass and biofuel burning emissions. J. Geophys. Res. 10,285–296, 2015.

Samset, B.H., Myhre, G., Forster, P.M., Hodnebrog, Ø., Andrews, T., Faluvegi, G., Flaeschner, D., Kasoar, M., Kharin, V., Kirkevåg, A. and Lamarque, J.F.: Fast and slow precipitation responses to individual climate forcers: A PDRMIP multimodel study. Geophys. Res. Lett. 43(6), pp.2782-2791, 2016.

Sandeep, K., R. S. Negi, A. S. Panicker, Alok Sagar Gautam, D. S. Bhist, G. Beig, B. S. Murthy, R. Latha, Santosh Singh, and S. Das.: Characteristics and Variability of Carbonaceous Aerosols over a Semi Urban Location in Garhwal Himalayas. Asia-Pacific Journal of Atmospheric Sciences 56, no. 3: 455-465, 2020.

Sandradewi, J., Prévôt, A.S., Szidat, S., Perron, N., Alfarra, M.R., Lanz, V.A., Weingartner, E. and Baltensperger, U.R.S.: Using aerosol light absorption measurements for the quantitative determination of wood burning and traffic emission contributions to particulate matter. Environmental science & technology, 42(9), pp.3316-3323, 2008.

Sarangi T., M. Naja, N. Ojha, R. Kumar, S. Lal, and H. C. Chandola.: Variability in meteorological parameters and trace gases over the central Himalayas: Observations and model simulations, Vayumandal, Vol. 38, No. 1-4, pp, 10-17, 2012.

Sarangi, T., M. Naja, N. Ojha, R. Kumar, S. Lal, S. Venkataramani, A. Kumar, R. Sagar and H. C. Chandola: First simultaneous measurements of ozone, CO and NO_y at a high altitude regional representative site in the central Himalayas, J. Geophys. Res. 119, 2014.

Satheesh, S.K., Ramanathan, V., Li-Jones, X., Lobert, J.M., Podgorny, I.A., Prospero, J.M., Holben, B.N. and Loeb, N.G.: A model for the natural and anthropogenic aerosols over the tropical Indian Ocean derived from Indian Ocean Experiment data. J. Geophys. Res. Atmos. 104(D22), pp.27421-27440, 1999.

Satheesh, S. K., V. Ramanathan, B. N. Holben, K. K. Moorthy, N. G. Loeb, H. Maring, J. M. Prospero, and D. Savoie.: Chemical, microphysical and radiative effects of Indian Ocean aerosols, J. Geophys. Res., 107(D23), 4725, 2002.

Satheesh, S. K., and J. Srinivasan: A method to estimate aerosol radiative forcing from spectral optical depths, J. Atmos. Sci., 63, 1082–1092, 2006.

Satheesh, S. K., Moorthy, K. K., Babu, S. S., Vinoj, V., & Dutt, C. B. S.: Climate implications of large warming by elevated aerosol over India. Geophys. Res. Lett. 35(19), 2008.

Satsangi, A., Pachauri, T., Singla, V., Lakhani, A., & Kumari, K. M.: Organic and elemental carbon aerosols at a suburban site. Atmospheric Research, 113, 13-21, 2012.

Saud, T., Saxena, M., Singh, D.P., Saraswati, M., Dahiya, Sharma, S.K., Datta, A. Gadi, R., Mandal, T.K.: Spatial variation of chemical constituents from the burning of commonly used biomass fuels in rural areas of the Indo-Gangetic Plain (IGP), India Atmos. Environ., 71, pp. 158-169, 2013.

Saxena, P. and Hildemann, L.M.: Water-soluble organics in atmospheric particles: A critical review of the literature and application of thermodynamics to identify candidate compounds. J. Atmos. Chem. 24(1), pp.57-109, 1996.

Schauer, J. J., Kleeman, M. J., Cass, G. R., & Simoneit, B. R.: Measurement of emissions from air pollution sources. 5. C1− C32 organic compounds from gasoline-powered motor vehicles. Environmental science & technology, 36(6), 1169-1180, 2002.

Schwarz, J.P., Gao, R.S., Spackman, J.R., Watts, L.A., Thomson, D.S., Fahey, D.W., Ryerson, T.B., Peischl, J., Holloway, J.S., Trainer, M. and Frost, G.J.: Measurement of the mixing state, mass, and optical size of individual black carbon particles in urban and biomass burning emissions. Geophys. Res. Lett. 35(13), 2008.

Seinfeld, J.H., and S.N. Pandis.: Atmospheric Chemistry and Physics-from Air Pollution to Climate Change. New York, USA, Wiley, 1998.

Sen, P.K.: Estimates of the regression coefficient based on Kendall's tau. Journal of the American statistical association, 63(324), pp.1379-1389, 1968.

Shaik, Darga Saheb, Kant, Yogesh, Mitra, Debashis, Suresh Babu,S.: Assessment of aerosol characteristics and radiative forcing over northwest himalayan region. IEEEJ. Sel. Top. Appl. Earth Obs. Remote Sens.10 (12),5314-5321, 2017.

Sharma, S., Brook, J. R., Cachier, H., Chow, J., Gaudenzi, A., & Lu, G.: Light absorption and thermal measurements of black carbon in different regions of Canada. J. Geophys. Res. Atmos. 107(D24), AAC-11, 2002.

Sharma, S.K., Choudhary, N., Srivastava, P., Naja, M., Vijayan, N., Kotnala, G. and Mandal, T.K.: Variation of carbonaceous species and trace elements in PM 10 at a mountain site in the central Himalayan region of India. J. Atmos. Chem. 77, pp.49-62, 2020.

Sharma A., Bhattacharya, A., Venkataraman, C.: Influence of aerosol radiative effects on surface temperature and snow melt in the Himalayan region, Science of The Total Environment, 810, 151299, 2022.

Shiraiwa, M., Kondo, Y., Moteki, N., Takegawa, N., Miyazaki, Y., & Blake, D. R.: Evolution of mixing state of black carbon in polluted air from Tokyo. Geophys. Res. Lett. 34(16), 2007.

Shrestha, A.B., Wake, C.P., Mayewski, P.A. and Dibb, J.E.: Maximum temperature trends in the Himalaya and its vicinity: an analysis based on temperature records from Nepal for the period 1971–94. Journal of climate, 12(9), pp.2775-2786, 1999.

Shukla, K. K., Phanikumar, D. V., Newsom, R. K., Kumar, K. N., Ratnam, M. V., Naja, M., and Singh, N.: Estimation of the mixing layer height over a high altitude site in Central Himalayan region by using Doppler lidar. Journal of Atmospheric and Solar-Terrestrial Physics, 109, 48-53, 2014.

Sheoran, R., Dumka, U.C., Kaskaoutis, D.G., Grivas, G., Ram, K., Prakash, J., Hooda, R.K., Tiwari, R.K. and Mihalopoulos, N.: Chemical Composition and Source Apportionment of Total Suspended Particulate in the Central Himalayan Region. Atmosphere, 12(9), p.1228, 2021.

Singh, T., Ravindra, K., Sreekanth, V., Gupta, P., Sembhi, H., Tripathi, S.N. and Mor, S.: Climatological trends in satellite-derived aerosol optical depth over North India and its relationship with crop residue burning: rural-urban contrast. Science of The Total Environment, 748, p.140963, 2020.

Srivastava, A. K., Ram, K., Pant, P., Hegde, P., & Joshi, H.: Black carbon aerosols over Manora Peak in the Indian Himalayan foothills: implications for climate forcing. Environmental Research Letters, 7(1), 014002, 2012a.

Srivastava, S., Lal, S., Venkataramani, S., Guha, I., Bala Subrahamanyam, D.: Airborne measurements of O3, CO, CH4 and NMHCs over the Bay of Bengal during winter. Atmospheric Environ. 59, 597–609, 2012b.

Srivastava, A. K., Bisht, D. S., Ram, K., Tiwari, S., & Srivastava, M. K.: Characterization of carbonaceous aerosols over Delhi in Ganga basin: seasonal variability and possible sources. Environmental Science and Pollution Research, 21(14), 8610-8619, 2014.

Srivastava, P., and Naja M.: Characteristics of carbonaceous aerosols in PM 2.5 derived from long-term high-resolution measurements over a high-altitude site in the Central Himalayas: Radiative forcing estimates and role of meteorology and biomass burning, Environmental Science and Pollution Research, 28, 14654–14670 , 2021.

Srivastava, P., Naja, M., Seshadri, T.R., Joshi, H., Dumka, U.C., Gogoi, M.M. and Babu, S.S.: Implications of Site-specific Mass Absorption Cross-section (MAC) to Black Carbon Observations at a High-altitude Site in the Central Himalaya. Asia-Pacific Journal of Atmospheric Sciences, pp.1-14, 2021.

Srivastava P, Naja M, Seshadri TR.: Probing the sources, diurnal variations and radiative forcing of carbonaceous aerosols using high-resolution ground-based measurements over the Central Himalayas, under review in Science of the Total Environment, 2022.

Snyder, D. C., and Schauer, J. J.: An inter-comparison of two black carbon aerosol instruments and a semi-continuous elemental carbon instrument in the urban environment. Aerosol Sci. Technol. 41(5), 463-474, 2007.

Tadeusz E. Kleindienst, Michael Lewandowski, John H. Offenberg , Edward O. Edney , Mohammed Jaoui , Mei Zheng , Xiang Ding & Eric S. Edgerton: Contribution of Primary and Secondary Sources to Organic Aerosol and PM2.5 at SEARCH Network Sites, Journal of the Air & Waste Management Association, 60:11, 1388-1399, 2010.

Tao, W. K., Li, X., Khain, A., Matsui, T., Lang, S., & Simpson, J.: Role of atmospheric aerosol concentration on deep convective precipitation: Cloud-resolving model simulations. J. Geophys. Res. Atmos. 112(D24), 2007.

Textor, C., Schulz, M., Guibert, S., Kinne, S., Balkanski, Y., Bauer, S., Berntsen, T., Berglen, T., Boucher, O., Chin, M. and Dentener, F.: Analysis and quantification of the diversities of aerosol life cycles within AeroCom. Atmos. Chem. Phys. 6(7), pp.1777-1813, 2006.

Timonen, H., Aurela, M., Carbone, S., Saarnio, K., Saarikoski, S., Mäkelä, T., Kulmala, M., Kerminen, V.M., Worsnop, D.R. and Hillamo, R.: High Time resolution Chemical Characterization of the Watersoluble Fraction of Ambient Aerosol with PILS-TOC-IC and AMS. Atmos. Meas. Tech. 3: 1063–1074, 2010.

Titos, G., Del Águila, A., Cazorla, A., Lyamani, H., Casquero-Vera, J.A., Colombi, C., Cuccia, E., Gianelle, V., Močnik, G., Alastuey, A. and Olmo, F.J.: Spatial and temporal variability of carbonaceous aerosols: assessing the impact of biomass burning in the urban environment. Science of the Total Environment, 578, pp.613-625, 2017.

Tiwari, S., Srivastava, A. K., Bisht, D. S., Safai, P. D., & Parmita, P.: Assessment of carbonaceous aerosol over Delhi in the Indo-Gangetic Basin: characterization, sources and temporal variability. Natural hazards, 65(3), 1745-1764, 2013.

Turpin, B.J. and Huntzicker, J.J.: Identification of secondary organic aerosol episodes and quantitation of primary and secondary organic aerosol concentrations during SCAQS. Atmospheric Environ. 29(23), pp.3527-3544, 1995.

US EPA.: Report to Congress on Black Carbon, https://19january2017snapshot.epa.gov/-www3/airquality/blackcarbon/2012report/fullreport.pdf, 2012.

Twomey, S.: Atmospheric aerosols, Elsevier, Amsterdam-Oxford-New York, 1977.

Tyson P.D., M. Garstang, R. Swap, P. Kallberg, and N. Edwards.: An air transport climatology for subtropical southern Africa, Int. J. Climatol., 16, 256-291, 1996.

van der Werf, G.R., Randerson, J.T., Giglio, L., Collatz, G.J., Mu, M., Kasibhatla, P.S., Morton, D.C., DeFries, R.S., Jin, Y., van Leeuwen, T.T.: Global fre emissions and the contribution of deforestation, savanna, forest, agricultural, and peat fres (1997–2009). Atmos. Chem. Phys. 10 (23), 11707–11735, 2010.

Venkataraman, C., Habib, G., Eiguren-Fernandez, A., Miguel, A.H. and Friedlander, S.K.: Residential biofuels in South Asia: carbonaceous aerosol emissions and climate impacts. Science, 307(5714), pp.1454-1456, 2005.

Venkataraman, C., Habib, G., Kadamba, D., Shrivastava, M., Leon, J.-F., Crouzille, B., Boucher, O., Streets, D.G.: Emissions from open biomass burning in India: integrating the inventory approach with high-resolution Moderate Resolution Imaging Spectroradiometer (MODIS) active-fre and land cover data. Global Biogeochem. Cycles, 20(GB2013), 2006.

Wan, X., Kang, S., Rupakheti, M., Zhang, Q., Tripathee, L., Guo, J., Chen P, Rupakheti D, Panday AK, Lawrence MG, Kawamura K.: Molecular characterization of organic aerosols in the Kathmandu Valley, Nepal: insights into primary and secondary sources. Atmos. Chem. Phys. 19(5), 2725-2747, 2019.

Wang, Y.Q., Zhang, X.Y. and Draxler, R.R.: TrajStat: GIS-based software that uses various trajectory statistical analysis methods to identify potential sources from long-term air pollution measurement data. Environmental Modelling & Software, 24(8), pp.938-939, 2009.

Wang, Y., Liu, S., Shi, P., Li, Y., Mu, C., & Du, K.: Temporal variation of mass absorption efficiency of black carbon at urban and suburban locations. Aerosol and Air Quality Research, 13(1), 275-286, 2013.

Wang, X., Gong, P., Sheng, J., Joswiak, D. R., & Yao, T.: Long-range atmospheric transport of particulate Polycyclic Aromatic Hydrocarbons and the incursion of aerosols to the southeast Tibetan Plateau. Atmospheric Environ. 115, 124–131, 2015.

Wei, J., Li, Z., Peng, Y. and Sun, L.: MODIS Collection 6.1 aerosol optical depth products over land and ocean: validation and comparison. Atmospheric Environ. 201, pp.428-440, 213, 2019.

Weingartner, E., H. Saathoff, M. Schnaiter, N. Streit, B. Bitnar, and U. Baltensperger.: Absorption of light by soot particles: determination of the absorption coefficient by means of Aethalometers." Journal of Aerosol Science 34, no. 10: 1445-1463, 2003.

Wester, P., Mishra, A., Mukherji, A. and Shrestha, A.B.: The Hindu Kush Himalaya assessment: mountains, climate change, sustainability and people (p. 627). Springer Nature, 2019.

Wexler, A.S. and Johnston, M.V.: What Have We Learned from Highly Time-Resolved Measurements during EPA's Supersite Program and Related Studies? J. Air Waste Manage. Assoc. 58: 303–319, 2008.

Wigley, T.M.L., Smith, S.J., Prather, M.J.: Radiative forcing due to reactive gas emissions. J. Clim. 15 (18), 2690–2696, 2002.

Winker, D.M., Vaughan, M.A., Omar, A., Hu, Y., Powell, K.A., Liu, Z., Hunt, W.H. and Young, S.A.: Overview of the CALIPSO mission and CALIOP data processing algorithms. Journal of Atmospheric and Oceanic Technology, 26(11), pp.2310-2323, 2009.

Winker, D.M., Tackett, J.L., Getzewich, B.J., Liu, Z., Vaughan, M.A. and Rogers, R.R.: The global 3-D distribution of tropospheric aerosols as characterized by CALIOP. Atmos. Chem. Phys. 13(6), pp.3345-3361, 2013.

Wiscombe, W.J. and Warren, S.G.: A model for the spectral albedo of snow. I: Pure snow. J. Atmos. Sci. 37(12), pp.2712-2733, 1980.

Witting, A.E., Takahama, S., Khlystov, A.Y., Pandis, S.N., Hering, S., Kirby, B. and Davidson, C.: SemiContinuous PM2.5 Inorganic Composition Measurements during the Pittsburg Air Quality Study. Atmos. Environ. 38: 3201–3213, 2004.

Wu, C. and Yu, J.Z.: Determination of primary combustion source organic carbon-to-elemental carbon (OC/EC) ratio using ambient OC and EC measurements: secondary OC-EC correlation minimization method. Atmos. Chem. Phys. 16(8), pp.5453-5465, 2016.

Wu, C., Wu, D. and Yu, J.Z.: Estimation and uncertainty analysis of secondary organic carbon using 1 year of hourly organic and elemental carbon data. J. Geophys. Res. Atmos. 124(5), pp.2774-2795, 2019.

Xia, X., Zong, X., Cong, Z., Chen, H., Kang, S., & Wang, P.: Baseline continental aerosol over the central Tibetan plateau and a case study of aerosol transport from South Asia. Atmospheric Environ. 45(39), 7370–7378, 2011.

Xu, B., Cao, J., Hansen, J., Yao, T., Joswia, D.R., Wang, N., Wu, G., Wang, M., Zhao, H., Yang, W. and Liu, X.: Black soot and the survival of Tibetan glaciers. Proceedings of the National Academy of Sciences, 106(52), pp.22114-22118, 2009.

Yao, L., Huo, J., Wang, D., Fu, Q., Sun, W., Li, Q. and Chen, J.: Online measurement of carbonaceous aerosols in suburban Shanghai during winter over a three-year period: Temporal variations, meteorological effects, and sources. Atmospheric Environ. 226, p.117408, 2020.

Yarragunta, Y., Srivastava, S., Mitra, D., Le Flochmo¨en, E., Barret, B., Kumar, P., Chandola, H.C.: Source attribution of carbon monoxide and ozone over the Indian subcontinent using MOZART-4 chemistry transport model. Atmos. Res. 227 (April), 165–177, 2019.

Yarragunta, Y., Srivastava, S., Mitra, D., Chandola, H.C.: Infuence of forest fire episodes on the distribution of gaseous air pollutants over Uttarakhand, India. GIScience Remote Sens, 1–17, 2020.

Young, S.A., Vaughan, M.A., Kuehn, R.E. and Winker, D.M.: The retrieval of profiles of particulate extinction from Cloud–Aerosol Lidar and Infrared Pathfinder Satellite Observations (CALIPSO) data: Uncertainty and error sensitivity analyses. Journal of Atmospheric and Oceanic Technology, 30(3), pp.395-428, 2013.

Yu, Y., Wang, H., Wang, T., Song, K., Tan, T., Wan, Z., Gao, Y., Dong, H., Chen, S., Zeng, L. and Hu, M.: Elucidating the importance of semi-volatile organic compounds to secondary organic aerosol formation at a regional site during the EXPLORE-YRD campaign. Atmospheric Environ. 246, p.118043, 2021.

Zanatta, M., Gysel, M., Bukowiecki, N., Müller, T., Weingartner, E., Areskoug, H., Fiebig, M., Yttri, K.E., Mihalopoulos, N., Kouvarakis, G. and Beddows, D.: A European aerosol phenomenology-5: Climatology of black carbon optical properties at 9 regional background sites across Europe. Atmospheric Environ. 145, pp.346-364, 2016.

Zhao, L., Wu, Q., Marchenko, S.S. and Sharkhuu, N.: Thermal state of permafrost and active layer in Central Asia during the International Polar Year. Permafrost and Periglacial Processes, 21(2), pp.198-207, 2010.

Zhao, Z., Cao, J., Shen, Z., Xu, B., Zhu, C., Chen, L.W.A., Su, X., Liu, S., Han, Y., Wang, G. and Ho, K.: Aerosol particles at a high-altitude site on the Southeast Tibetan Plateau, China: Implications for pollution transport from South Asia. J. Geophys. Res. Atmos. 118(19), pp.11-360, 2013.

Zotter, P., Herich, H., Gysel, M., El-Haddad, I., Zhang, Y., Močnik, G., Hüglin, C., Baltensperger, U., Szidat, S. and Prévôt, A.S.: Evaluation of the absorption Ångström exponents for traffic and wood burning in the Aethalometer-based source apportionment using radiocarbon measurements of ambient aerosol. Atmos. Chem. Phys. 17(6), pp.4229-4249, 2017.